



Theses and Dissertations

2006-07-13

Numerical Modeling of Blast-Induced Liquefaction

Wayne Yeung Lee

Brigham Young University - Provo

Follow this and additional works at: <https://scholarsarchive.byu.edu/etd>



Part of the [Civil and Environmental Engineering Commons](#)

BYU ScholarsArchive Citation

Lee, Wayne Yeung, "Numerical Modeling of Blast-Induced Liquefaction" (2006). *Theses and Dissertations*. 524.

<https://scholarsarchive.byu.edu/etd/524>

This Dissertation is brought to you for free and open access by BYU ScholarsArchive. It has been accepted for inclusion in Theses and Dissertations by an authorized administrator of BYU ScholarsArchive. For more information, please contact scholarsarchive@byu.edu, ellen_amatangelo@byu.edu.

NUMERICAL MODELING OF BLAST-INDUCED LIQUEFACTION

by

Wayne Y. Lee

A dissertation submitted to the faculty of

Brigham Young University

in partial fulfillment of the requirements for the degree of

Doctor of Philosophy

Department of Civil and Environmental Engineering

Brigham Young University

August 2006

Copyright © 2006 Wayne Y. Lee

All Rights Reserved

BRIGHAM YOUNG UNIVERSITY

GRADUATE COMMITTEE APPROVAL

of a dissertation submitted by

Wayne Y. Lee

This dissertation has been read by each member of the following graduate committee and by majority vote has been found to be satisfactory.

Date

Kyle M. Rollins, Chair

Date

T. Leslie Youd

Date

Steven E. Benzley

Date

Richard J. Balling

Date

Travis M. Gerber

BRIGHAM YOUNG UNIVERSITY

As chair of the candidate's graduate committee, I have read the dissertation of Wayne Y. Lee in its final form and have found that (1) its format, citations, and bibliographical style are consistent and acceptable and fulfill university and department style requirements; (2) its illustrative materials including figures, tables, and charts are in place; and (3) the final manuscript is satisfactory to the graduate committee and is ready for submission to the university library.

Date

Kyle M. Rollins
Chair, Graduate Committee

Accepted for the Department

E. James Nelson
Graduate Coordinator

Accepted for the College

Alan R. Parkinson
Dean, Ira A. Fulton College of Engineering
and Technology

ABSTRACT

NUMERICAL MODELING OF BLAST-INDUCED LIQUEFACTION

Wayne Y. Lee

Department of Civil and Environmental Engineering

Doctor of Philosophy

A research study has been conducted to simulate liquefaction in saturated sandy soil induced by nearby controlled blasts. The purpose of the study is to help quantify soil characteristics under multiple and consecutive high-magnitude shock environments similar to those produced by large earthquakes.

The simulation procedure involved the modeling of a three-dimensional half-space soil region with pre-defined, embedded, and strategically located explosive charges to be detonated at specific time intervals. LS-DYNA, a commercially available finite element hydrocode, was the solver used to simulate the event. A new geo-material model developed under the direction of the U.S. Federal Highway Administration was applied to evaluate the liquefaction potential of saturated sandy soil subjected to sequential blast environments. Additional procedural enhancements were integrated into the analysis process to represent volumetric effects of the saturated soil's transition from solid to liquid during the liquefaction process. Explosive charge detonation and pressure

development characteristics were modeled using proven and accepted modeling techniques.

As explosive charges were detonated in a pre-defined order, development of pore water pressure, volumetric (compressive) strains, shear strains, and particle accelerations were carefully computed and monitored using custom developed MathCad and C/C++ routines. Results of the study were compared against blast-test data gathered at the Fraser River Delta region of Vancouver, British Columbia in May of 2005 to validate and verify the modeling procedure's ability to simulate and predict blast-induced liquefaction events. Reasonable correlations between predicted and measured data were observed from the study.

ACKNOWLEDGMENTS

I wish to thank Dr. Kyle Rollins for giving me the opportunity to get involved with this exciting research endeavor; and for his continued support, recommendations and contributions to the development of this dissertation. Most of all, for his visions in pursuing new computing technology to help increase the understanding of one of nature's most destructive and devastating events – liquefaction of soil due to large earthquakes. I also appreciate the time, effort, suggestions, and recommendations offered by all members of my graduate committee.

I offer my sincere gratitude for the generous scholarships and fellowship grants provided by the College of Engineering, Department of Civil Engineering, the Civil Engineering Scholarship Society, the Ralph and Betty Rollins Family, and the T. Leslie Youd Family.

To Tom Raisor, the system administrator for BYU's Fulton Supercomputing Laboratory, I offer my gratitude for his support, patience, and professionalism. Special thanks also to my classmate Spencer Strand for providing the necessary figures and site maps associated with the May 2005 blast-induced liquefaction tests at the Fraser River Delta test site.

To my aunt Connie, I owe my thanks for the blunt comments she gave me during her son's high school graduation ceremony in 1976, which awakened my soul

and forever changed my life and attitude toward achieving my education. I also express my appreciation to the rest of my extended family and friends for their help, continual support, and encouragement they have given us throughout this educational journey.

In memory of Mrs. Stephanie Zini, who spent countless hours teaching, guiding and tutoring me during my first few years in the United States as I struggled to learn the English language.

To my parents who always believed in me, even after I had failed them many times during my adolescent years, I offer my utmost gratitude for the sacrifices and hardships they endured in order to provide me the opportunity to gain a college education. Their never-failing love, support, and encouragement throughout the years have carried me through many adversities and challenges in my life.

To my children I wish to express my gratitude, for their support and willingness to put aside their own comforts to help make their father's educational pursuit possible. I never cease to be amazed by their ability to adapt to new environments and excel in whatever they put their hearts into doing. They truly are my inspirations, my pride, and my joy.

Last, but not least, I dedicate this dissertation as an expression of my love and appreciation for my wife, Ginny, for giving up her own comfort and personal pursuits in order to support this educational endeavor. Her unceasing love, sacrifice, devotion, inspiration, encouragement, unfailing support, and best of all, her sense of humor, has made this educational journey feasible, enjoyable, and endurable.

TABLE OF CONTENTS

LIST OF TABLES	xv
LIST OF FIGURES	xvii
1 Introduction.....	1
1.1 Background.....	1
1.2 Objectives	3
1.3 Scope of Work	4
2 Review of Existing Numerical Modeling Research.....	7
2.1 Overview.....	7
2.2 Liquefaction Evaluation Through In-Situ Testing and Modeling.....	7
2.3 Available Numerical Models for Simulating Liquefaction Events.....	11
3 Baseline Numerical Model Requirements	15
3.1 Overview.....	15
3.2 Model Symmetry	15
3.3 Evaluation of Acoustic Waves and Shock Waves	16
3.4 Geometry Non-Linearity.....	20
3.5 Material Non-Linearity	22
3.6 Acceleration Measurement	24
3.7 Blast Pressure Development	24
3.8 Pore Pressure Development	25
3.9 Strain-Rate Considerations	25

3.10	Drainage and Seepage Considerations.....	26
4	General Modeling Methodology	29
4.1	Overview.....	29
4.2	Implicit Methods.....	29
4.3	Explicit Methods.....	31
4.4	Axisymmetric Linear-Superposition Simulation Procedure.....	43
4.5	Three-Dimensional Blast-Pressure Transfer Modeling Procedure.....	45
4.6	Three-Dimensional Fully-Integrated Modeling Procedure.....	48
4.7	Loading Environments.....	50
5	Hardware Considerations	61
5.1	Operating Systems	61
5.2	AMD-Athlon Windows-Based Desktop Computer	62
5.3	Intel Pentium IV Linux-Based Desktop Computer.....	63
5.4	Hewlett-Packard Unix-Based Workstation Cluster	64
5.5	SGI R-16000 UNIX Clusters	65
5.6	MarylouX Linux-Based Cluster by IBM	66
5.7	Intel Xeon 64-Bit Linux-Based Super Cluster.....	66
5.8	Hardware Performance and Limitation Summary	68
6	Model Geometry and Constraints	71
6.1	Overview.....	71
6.2	Geometry Dimensionality.....	71
6.3	Mesh Considerations.....	74
6.4	Mesh Generation Utilities.....	80
6.5	Boundary Conditions	82

7	LS-DYNA’s FHWA Soil Material Model 147	91
7.1	Overview	91
7.2	Pore-Water Pressure Definition	94
7.3	Computed and Measured Parameters.....	99
7.4	Skeleton Bulk Modulus/Volumetric Strain Factor	101
7.5	Maximum Number of Plasticity Iterations	104
7.6	Maximum and Residual Friction Angles	106
7.7	Cohesion	108
7.8	Drucker-Prager Coefficient.....	110
7.9	Eccentricity	111
7.10	Strain Rate Parameters.....	112
7.11	Plasticity Parameters.....	114
7.12	Void Formation and Initial Damage Threshold.....	117
7.13	Damage Level and Element Deletion	119
8	High-Explosive Material Model.....	121
8.1	Baseline Blasting Material.....	121
8.2	Baseline Explosive Modeling Techniques.....	122
9	Vancouver Blast-Induced Liquefaction Experiment.....	125
9.1	Overview.....	125
9.2	Site Characterization.....	127
9.3	Experiment Preparation	131
9.4	Discussion of Experiments	135
9.5	Discussion of Results.....	141
10	Discussion of Baseline Model Analysis.....	153

10.1	Overview.....	153
10.2	Fundamental Assumptions and Methodology	153
10.3	ALE Analysis Distortion and Stability Controls	158
10.4	Boundary Environments	161
10.5	Loading Environments.....	162
10.6	Model Output Interval Size Control	162
10.7	Model Development Evolution Process.....	164
10.8	Original Baseline Model.....	165
10.9	Improvements to the Original Baseline Model.....	179
11	Enhanced Baseline Model Analysis.....	201
11.1	Overview.....	201
11.2	Application of the Bulk Transition Relationship	202
11.3	Proof-of-Concept Evaluation Assumptions and Limitations.....	204
11.4	Proof-of-Concept Analysis Steps.....	206
11.5	Analysis Input Parameters	208
11.6	Blast Sequence Snap Shots	209
11.7	Pore Water Pressure Results	214
11.8	Acceleration, Velocity and Displacement Results.....	227
11.9	Pore Water Pressure Ratio and Shear Strains	245
12	Conclusions and Improvement Recommendations	251
12.1	Conclusions.....	251
12.2	Improvement Recommendations	253
	References	263
	Appendix A ANSYS® Parametric Model Development.....	271

Appendix B	Tracers and Pore Water Pressure Extraction.....	285
Appendix C	Cauchy’s Infinitesimal Strain	301
Appendix D	Baseline Tri-Level Model	311

LIST OF TABLES

Table 5-1	Baseline Model Parallel-Processing Performance Summary	67
Table 5-2	Baseline Model Computer Performance Comparison Summary	69
Table 6-1	Characteristics of Shock at Interface between Two Materials.....	86
Table 7-1	Summary of Input Parameters for *MAT_FHWA_SOIL	93
Table 7-2	Summary of Computed / Measured Input Parameters	100
Table 8-1	Hydro-dynamic and EOS Parameters for Pentex.....	124
Table 9-1	Data Capturing Device Coordinates	142
Table 11-1	Summary of Bulk Transition Input Parameters for Blast Series 3.....	208
Table 11-2	Summary of Bulk Transition Input Parameters for Blast Series 1.....	209
Table 11-3	Initial Effective Stress at Each PPT Location.....	220

LIST OF FIGURES

Figure 1-1	May 2005 Vancouver Blast-Induced Liquefaction Test Layout.....	6
Figure 3-1	Vancouver (2005) Liquefaction Test Blast Configuration	17
Figure 4-1	Single Element ALE and LaGrangian Comparison Analysis.....	39
Figure 4-2	Blast-Induced Liquefaction Example for Axisymmetric Analysis.....	44
Figure 4-3	Blast-Initiation Pressure in a Sample 3-D Wedge Model.....	47
Figure 4-4	Peak Over-Pressure Induced by Spherical Pentolite 50/50 Charges	57
Figure 6-1	Baseline 3-D Blast-Induced Liquefaction Analysis Model	73
Figure 6-2	Baseline Blast-Induced Liquefaction FEA Model Mesh	77
Figure 6-3	Enlargement of Baseline Model Cross Section and Plan Views	78
Figure 6-4	Test Instrumentation Layout and Blast-Sequence	83
Figure 6-5	Potential Eulerian Fluid Leakage Location in Wedge Models	89
Figure 7-1	Volumetric Strain vs. Pore Pressure Ratio.....	98
Figure 7-2	Summary of Skeleton Bulk Modulus (K_{sk}) Trade Study	102
Figure 7-3	Summary of ITERMX Trade Study.....	105
Figure 7-4	Summary of PHIMAX Trade Study	107
Figure 7-5	Summary of PHIRES Trade Study	107
Figure 7-6	Summary of COH Trade Study.....	109
Figure 7-7	Summary of GAMMAR Trade Study.....	113

Figure 7-8	Summary of VN Trade Study	114
Figure 7-9	Summary of Hardening Parameter (A_n) Trade Study	116
Figure 7-10	Summary of Hardening Parameter (E_t) Trade Study	116
Figure 7-11	Summary of Initial Damage Threshold (DINT) Trade Study.....	118
Figure 7-12	Summary of Void Formation Energy (VDFM) Trade Study.....	118
Figure 9-1	Composite Photo of May 2005 Vancouver Test Site.....	125
Figure 9-2	May 2005 Vancouver Test Site Map	126
Figure 9-3	CPT Data Measured at Site 1	128
Figure 9-4	CPT Shear Wave Velocity Data Measured at Site 1.....	129
Figure 9-5	Idealized Soil Profile and Properties at Fraser River Delta Site 1	130
Figure 9-6	Site 1 Instrumentation Layout.....	132
Figure 9-7	Insertion of Data Measurement Device	133
Figure 9-8	Extracted Saturated Sandy Soil Sample.....	133
Figure 9-9	Installation of Blast-Holes by Vibro-Hammer.....	134
Figure 9-10	May 2005 Vancouver Blast Liquefaction Test Layout.....	138
Figure 9-11	Installation of Explosive Charges	139
Figure 9-12	Soil Surface Before (Left) and After (Right) Blast Series 3	139
Figure 9-13	String-Potentiometer Settlement Data for Blast Series 1.....	140
Figure 9-14	String-Potentiometer Settlement Data for Blast Series 3.....	141
Figure 9-15	Accelerometer 1 Measured Time Histories	144
Figure 9-16	Accelerometer 2 Measured Time Histories	145
Figure 9-17	Accelerometer 3 and Center PPT Measurements	146
Figure 9-18	Accelerometer 4 Measured Time Histories	147

Figure 9-19	Full Duration PPT Data	148
Figure 9-20	Blast Duration PPT Data.....	149
Figure 10-1	Liquefaction Test Instrumentation Layout and Blast Sequence	155
Figure 10-2	ALE Analysis Element Expansion Limit Trade Study.....	160
Figure 10-3	Original Baseline LS-DYNA Finite Element Model.....	166
Figure 10-4	Improved Baseline LS-DYNA FEA Model.....	167
Figure 10-5	Improved (Left) and Original (Right) Baseline Model Centers.....	168
Figure 10-6	Original Baseline Pore Pressure (North PPT at Z = 38').....	174
Figure 10-7	Original Baseline Pore Pressure (South PPT at Z = 31').....	175
Figure 10-8	Original Baseline Pore Pressure (West PPT at Z = 45').....	175
Figure 10-9	Original Baseline Pore Pressure (East PPT at Z = 18')	175
Figure 10-10	Original Baseline Pore Pressure (Center PPT at Z = 25')	176
Figure 10-11	A Typical Half-Sine Function.....	192
Figure 10-12	Typical Relationship Between Bulk Modulus and Exponent.....	195
Figure 11-1	May 2005 Test Blast Order and Instrumentation Layout	203
Figure 11-2	Blast Series 3 Bottom Level Blast Wave Propagation Summary	211
Figure 11-3	Blast Series 3 Mid-Level Blast Wave Propagation Summary	212
Figure 11-4	Blast Series 3 Top Level Blast Wave Propagation Summary.....	213
Figure 11-5	Excess Pore Pressure Histories (North PPT at Z = 38 ft).....	215
Figure 11-6	Excess Pore Pressure Histories (South PPT at Z = 31 ft).....	216
Figure 11-7	Excess Pore Pressure Histories (West PPT at Z = 45 ft)	217
Figure 11-8	Excess Pore Pressure Histories (East PPT at Z = 18 ft).....	218
Figure 11-9	Excess Pore Pressure Histories (Center PPT at Z = 25 ft).....	219

Figure 11-10	Excess Pore Pressure Ratio (North PPT at Z = 38 ft).....	221
Figure 11-11	Excess Pore Pressure Ratio (South PPT at Z = 31 ft).....	222
Figure 11-12	Excess Pore Pressure Ratio (West PPT at Z = 45 ft).....	223
Figure 11-13	Excess Pore Pressure Ratio (East PPT at Z = 18 ft).....	224
Figure 11-14	Excess Pore Pressure Ratio (Center PPT at Z = 25 ft).....	225
Figure 11-15	Comparison Between Computed and Measured Acceleration Data...	229
Figure 11-16	Sample of a Full-Duration Computed Accelerations.....	232
Figure 11-17	Compressed-Duration Acceleration at Northwest Accelerometer.....	233
Figure 11-18	Compressed-Duration Acceleration at Northeast Accelerometer.....	234
Figure 11-19	Compressed-Duration Acceleration at Southwest Accelerometer.....	235
Figure 11-20	Compressed-Duration Acceleration at Southeast Accelerometer.....	236
Figure 11-21	Compressed-Duration Velocity at Northwest Accelerometer	237
Figure 11-22	Compressed-Duration Velocity at Northeast Accelerometer	238
Figure 11-23	Compressed-Duration Velocity at Southwest Accelerometer	239
Figure 11-24	Compressed-Duration Velocity at Southeast Accelerometer	240
Figure 11-25	Compressed-Duration Displacement at Northwest Accelerometer	241
Figure 11-26	Compressed-Duration Displacement at Northeast Accelerometer	242
Figure 11-27	Compressed-Duration Displacement at Southwest Accelerometer	243
Figure 11-28	Compressed-Duration Displacement at Southeast Accelerometer	244
Figure 11-29	Blast Series 3 Pore Pressure - Shear Strain Relationship	247
Figure 11-30	Blast Series 1 Pore Pressure - Shear Strain Relationship	248

1 Introduction

1.1 Background

Liquefaction is a natural phenomenon in which loose sands lose strength and act as a viscous fluid when subjected to earthquake shaking. Liquefaction and the resulting loss of shear strength can lead to landslides, lateral movement of bridge abutments and wharfs, loss of vertical and lateral bearing support for foundations, and excessive foundation settlement and rotation. Liquefaction resulted nearly \$1 billion worth of damage during the 1964 Niigata Japan earthquake (NRC, 1985 and Rollins et al., 2004), \$99 million damage in the 1989 Loma Prieta earthquake (Holzer, 1998 and Rollins et al., 2004), and over \$11.8 billion in damage just to ports and wharf facilities in the 1995 Kobe earthquake (EQE, 1995 and Rollins et al., 2004). The loss of these major port facilities subsequently led to significant additional indirect economic losses. Since damage due to “liquefied” soils during an earthquake are often substantial, understanding the mechanisms involved in the development of liquefaction during an earthquake is essential for engineers and scientists to find ways of reducing potential damage.

Currently, the susceptibility of a soil to liquefaction has been evaluated primarily based on the performance of similar soils during earthquake events. Unfortunately, field performance data is not available for all soil types and engineers are placed in a position of waiting for earthquakes to test these soils or applying subjective judgments about

expected field performance. As a result, several investigators have developed methods for evaluating field performance in-situ using approaches that both reproduce liquefaction in specific types of soil materials, and produce liquefaction in ways similar to those induced by large earthquakes. By simulating earthquake environments, one does not have to wait for a large earthquake to study liquefaction.

For example, Rathje et al. (2005) have used modified oil prospecting “vibroiseis trucks” to induce cyclic shear strains in soil profiles. Rollins et al. (2001) recently pioneered the application of explosives to produce liquefaction in saturated sandy soils. Under controlled detonation events, Rollins et al. were successful in creating liquefied soil conditions that can be used to study engineering designs, with the potential to reduce damages and casualties. Successes in Rollins et al.’s blast induced liquefaction tests have produced both new hopes, as well as more educated-questions concerning the subject of liquefaction. Questions regarding the physics (i.e. the “why’s” and the “how’s”) behind the mechanisms that produce liquefaction still need to be answered in order to achieve the level of understanding necessary to combat the damaging effects of liquefaction. For example, in order to transfer results from blast liquefaction tests to expected behavior during an earthquake event, a better understanding of the stress and strain fields produced by blasting is required.

With recent advances in computer technology, it has become more practical and economical to simulate full-scale blast testing events by computer, but the accuracy of these methods has yet to be evaluated with field performance data.

1.2 Objectives

The main objective of the dissertation titled “Numerical Modeling of Blast Induced Liquefaction” is to develop a quantitative means for assessing and simulating blast-induced soil liquefaction behaviors by computer. Pore pressure build-up during numerically simulated blasts provides the key to assessing the potentially damaging effects of soil liquefaction induced by controlled blasts. As such, success of the modeling procedure is dependent on the material model’s ability to accurately predict pore pressure build-up in the soil upon multiple and consecutive controlled blasts.

Since verifications and validations are essential in assuring an accurate representation of the desired events, data from recent blast-induced liquefaction tests conducted in Vancouver, Canada are used to calibrate the numerical model, and to help validate the proper physics that need to be accounted for in an actual event. Efforts are made to help ensure that the modeling procedure are developed as a “predictive” rather than a “matching” tool so that it may be used to predict behaviors of liquefied soil in future liquefaction tests. However, one must be reminded that every numerical model must still be calibrated and verified by actual test data. Since variability in soil properties from different locations are often significant, adjustments to parameters with respect to local conditions must be expected.

During the development of the 3-D computer-modeling procedure, the processes of calibrating, verifying, and validating the analysis tools and material model(s) occupied the majority of the time and efforts. Results from this research effort are expected to form the foundation for future developmental work in computer simulations of liquefaction and other similar geotechnical events.

In the National Science Foundation (NSF) International Workshop on Earthquake Simulation in Geotechnical Engineering held in 2001 at Case Western Reserve University in Cleveland, OH, Professor Idriss encouraged the geotechnical community to “strive to conduct physical as well as numerical simulations that are needed ... for vital and pressing issues” (Idriss, 2001). Idriss also expressed concerns on serious deficiencies in the presentations of recent numerical simulations where authors focused on presenting a great deal of analytical results from their simulations while neglecting to discuss the premises on which the results were obtained (Idriss, 2001). In preparing this dissertation, the author hopes to help address these concerns in advancing numerical simulations of soil liquefaction, while explaining in sufficient detail the assumptions, limitations, pit-falls, and “rule-of-thumbs” in obtaining acceptable and feasible numerical modeling results. Necessary elements and principles in geotechnical engineering, computer science, computational mechanics, and shock physics fields will be discussed to help clarify the rationales behind the numerical procedure developed during this research effort.

1.3 Scope of Work

The major focus of the research is on the development of a numerical procedure and its ability to predict pore pressure build-up in saturated sandy soil upon nearby multiple consecutive controlled blasts. The design of structures and foundations including piles to withstand effects of capacity reduction due to soil liquefaction are outside the scope of this research. However, one may expect that the success of this research effort can help form the foundation for future numerical modeling research involving structures and foundations placed on liquefiable soil.

The baseline blast-induced liquefaction test event to be simulated in this research effort took place in May, 2005 at the Fraser River Delta near the south end of the Massey Tunnel located south of Vancouver, B.C. The baseline test is a tri-level sequential blast event that involved 21 controlled detonations at pre-defined locations around the blast circle as summarized in Figure 1-1. It should be noted that the northern-most pore pressure transducer was designated as the north (N) sensor for reference and convenient purposes even though it does not lie parallel to the actual north direction of the test site due to rotational offset of the blast holes (see Chapter 9). This sensor referencing convention will be used through this dissertation. Chapter 9 provides a detailed description of the baseline test event.

The first five chapters of this dissertation provide information that forms the foundation for the numerical modeling of blast-induced liquefaction. Chapter 3 describes the fundamental requirements for a numerical model that has the potential to simulate a blast-induced liquefaction event successfully. Chapter 4 describes the various modeling techniques available for simulating a blast-induced liquefaction event. Chapter 5 describes the available hardware resources at BYU for extensive computational tasks.

Chapters 6 onward discuss the core of the simulation effort. Chapters 6, 7, and 8 involve the model construction, or pre-processing, aspect of the simulation process, which include descriptions of the geometry configuration, the baseline soil material model, and the explosive model. Chapter 9 provides a general overview of the blast-induced liquefaction test event to be simulated. Chapter 10 discusses in details the analysis aspect of the simulation, followed by a presentation of the results in Chapter 11. Finally, Chapter 12 presents the conclusions and recommendations of this research.

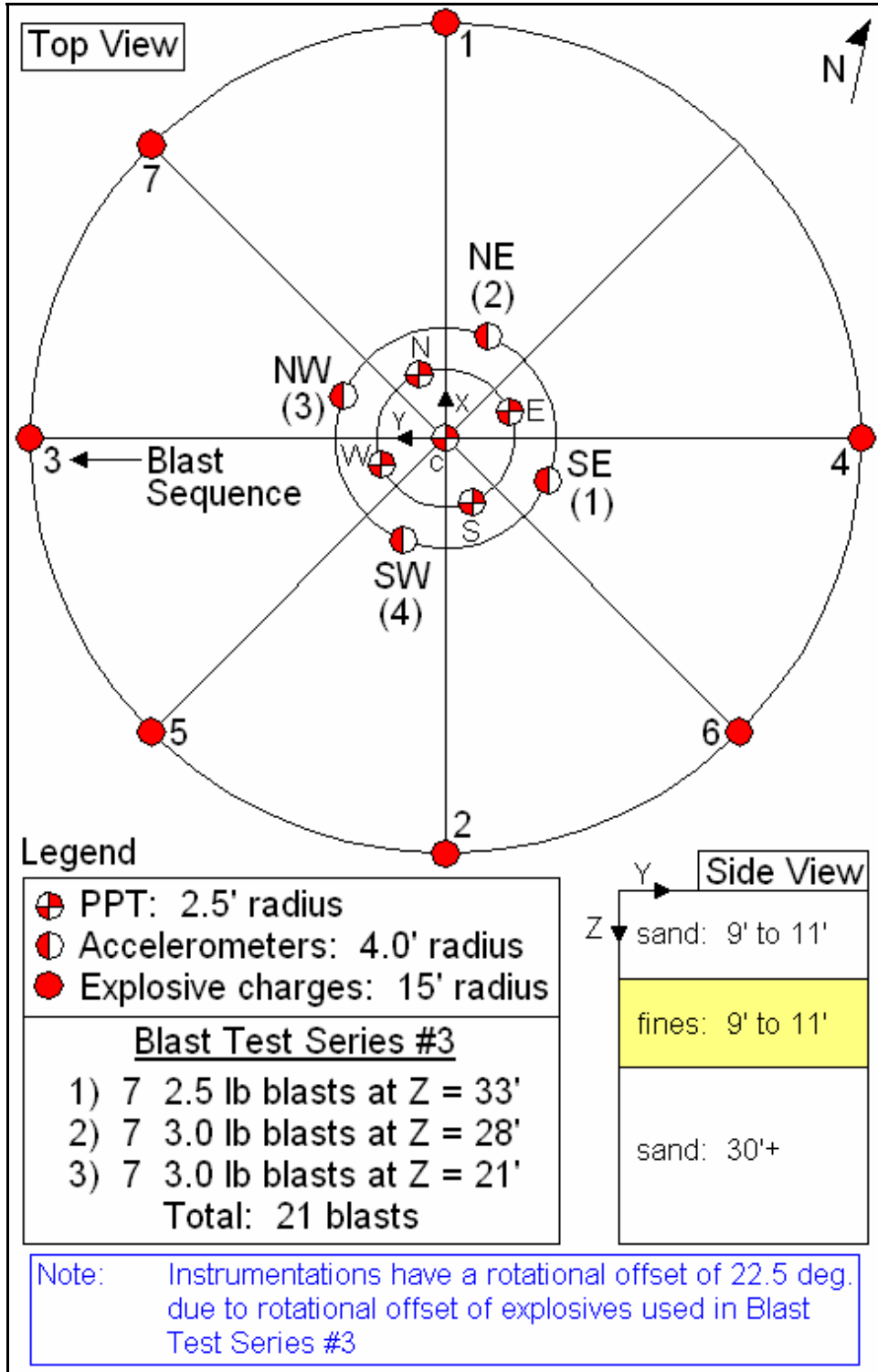


Figure 1-1 May 2005 Vancouver Blast-Induced Liquefaction Test Layout

2 Review of Existing Numerical Modeling Research

2.1 Overview

Several in-situ testing and numerical modeling techniques have recently been developed to analyze liquefaction under various experimental environments. Each technique has its own merits in accordance with their specific assumptions and limitations. The following subsections provide a brief summary of some of the major modeling techniques. Examples and details on the following as well as other modeling techniques are documented in their respective publications and articles listed in the Reference section of this dissertation.

2.2 Liquefaction Evaluation Through In-Situ Testing and Modeling

2.2.1 In-Situ Dynamic Liquefaction Model / Experiment

Rathje, Chang, and Stokoe developed a procedure for measuring liquefaction and pore pressure generation characteristics of soil from data measured in-situ (Rathje et al., 2004 and Rathje et al., 2005). The approach utilizes a large vibroseis truck to apply a vertical dynamic load adjacent to a pre-defined volume of soil deposit. Integrated sensors containing two orthogonally oriented geophones plus a pore pressure transducer are strategically placed at four corners plus the corresponding center of a vertically situated rectangular area within the soil deposit of interest. Velocities measured from the sensors

are numerically integrated to obtain displacements. Computed displacement data can then be interpolated via a surface iso-parametric approach to obtain a linear (i.e. first order) description of the displacement field across the rectangular data-measurement area.

The major limitation in the iso-parametric interpolation approach used by Rathje et al. (2004 and 2005) is that it is only applicable for small, linear, and elastic displacements within a rectangular area. As a result, it was determined that the plane element developed by Rathje et al. is not directly applicable for computing strains in the simulation of the baseline blast-induced liquefaction event for this research due to rotated orientations of the sensors. A more generalized formulation based on Cauchy's infinitesimal strain theory that allows rotated orientations was derived early in this research in preparation for potential needs for its utilization during the course of the research. Details of the derivation is presented in 0.

From the measured velocity and calculated displacement data, shear strains are computed using three different wave-propagation methods to compare against the corresponding shear strains computed by a displacement-based (DB) method. The three wave-propagation methods are plane shear wave (PSW) propagation, plane Rayleigh wave (PRW) propagation and apparent wave (AW) propagation. Shear strains (γ) in terms of particle velocity (\dot{u}) and wave propagation velocity (V) are computed by the wave-propagation methods using Equation 2-1.

$$\gamma = \frac{-\dot{u}}{V} \quad (2-1)$$

Corresponding shear strains for the displacement-based (u) method are computed from a strain definition defined in solid mechanics based on Cauchy's infinitesimal strain tensor (Fung, 1977) as shown in Equation 2-2. When applying the shear strain computations, one must recognize that shear strains (γ) expressed by Rathje et al. are in engineering strain notation (γ_{ij}), which is twice the corresponding shear strains in tensor notation (ε_{ij}) as shown in Equation 2-2.

Results of the comparison analysis and discussions of the limitations and restrictions of each method used for computing shear strains are documented in Rathje et al., 2004 and Rathje et al., 2005 and will not be presented here.

$$\begin{aligned}\varepsilon_{ij} &= \frac{1}{2} \cdot \left(\frac{\partial u_j}{\partial x_i} + \frac{\partial u_i}{\partial x_j} \right) = \frac{\gamma_{ij}}{2} && \text{when } i \neq j \\ \varepsilon_i &= \frac{\partial u_i}{\partial x_i} && \text{when } i = j\end{aligned}\tag{2-2}$$

2.2.2 Centrifuge Models

Although centrifuge models are not in the same classification of numerical modeling techniques discussed in this section, empirical equations developed to correlate centrifuge data with in-situ data do provide numerical quantification of soil liquefaction characteristics. Charlie et al. (2005) correlated centrifuge data with in-situ data and then compared the results against empirical equations developed from full-scale explosive tests by Drake and Little (Charlie et al., 2005). Drake and Little developed and documented empirical equations based on ground shock data collected from over one hundred explosive tests in a 35-year period (Drake and Little, 1983).

Results from Charlie et al. in conjunction with Drake and Little's work indicate that empirical equations correlating explosive charge mass with distance from the blast-point are valid over nine orders of magnitude of explosive masses. Some discrepancies were noticed in the correlation coefficients developed between centrifuge and prototype tests, which Charlie et al. attributed to factors such as compaction methods, degree of saturation, types of explosives, etc. Results based on research from Charlie et al. (2005) and Drake/Little (1983) provide a useful framework for defining blasting effects on velocity, stress, and acceleration as a function of explosive mass and distance from blast-point.

2.2.3 Controlled Detonation Pore Pressure Development

Gohl et al. (2001) have developed techniques for measuring in-situ liquefaction potential of sandy soils by means of controlled detonation of explosives. Their research experiment involved two decks or depth-levels of explosives strategically placed around a set of data capturing instruments which included accelerometers, pore pressure transducers (PPT) and soundex settlement gauges. The May, 2005 blast liquefaction tests conducted at the Fraser River Delta used for this research and described in Chapter 9 are in many ways similar to the approach presented by Gohl et al. (2001).

Gohl et al. suggest that their approach, which can be applied to all soil types, measures in-situ soil liquefaction potential without unnecessary soil disturbance, soil sampling for laboratory tests, and idealization of the drainage conditions of the cyclic loading as being purely undrained. Resulting characteristics due to pore pressure build-up and soil softening can be observed in situ.

Results from the experiment produced relationships involving pore water pressure magnitudes, particle velocities with respect to scaled distance, and pore pressure ratio to estimate shear strain relationships (Gohl et al. 2001). Upon completion of their experiment, a double integration was performed to derive a set of displacement time histories from the acceleration data. Small strain theory techniques similar to Rathje et al.'s approach presented in Section 2.2.1 of this dissertation was applied by Gohl et al. to estimate both component and average maximum shear strains at specific location and instance of time within a given blast pulse. Research performed by Gohl et al. provided invaluable lesson-learned information and experience for the May 2005 blast liquefaction test used for this dissertation research.

2.3 Available Numerical Models for Simulating Liquefaction Events

2.3.1 UBC Soil Liquefaction Model

In the mid-1990's, Peter Byrne and his graduate students at the University of British Columbia (UBC) developed a constitutive model known as UBCSAND for simulating soil liquefaction events (Park and Byrne, 2004). UBCSAND was designed to estimate displacements, accelerations, as well as pore water pressure generation and dissipation caused by a specified input motion. Byrne et al. incorporated UBCSAND into a 2-D explicit finite difference computer code called FLAC 2-D (Fast LaGrangian Analysis of Continua 2-D), which was developed and published by HClasca, an international civil engineering consulting and software publishing company.

UBCSAND is an effective stress based non-linear constitutive model during loading; however, the original model considered unloading as an elastic event. In 2004,

Byrne et al. incorporated a two-plane shear (rotating maximum shear and horizontal shear) capability in UBCSAND to handle “plastic unloading” and “principal stress rotation associated with anisotropic consolidation” (Park and Byrne, 2004). The concept used to account for plastic unloading is based on the mobilization of plastic deformations on a horizontal plane as a function of the initial K_0 consolidation state during simple shear loading. Rotation of principal stresses depends on the value of K_0 . At a K_0 of 1.0, the horizontal plane becomes the maximum shear plane as soon as horizontal shear stress is applied. When the value of K_0 is 0.5, the maximum shear plane rotates from 45° toward a horizontal plane as horizontal shear stress is applied. Eventually an approximate horizontal failure plane is produced. Detailed descriptions and sample results of the model are documented in Park and Byrne (2004). This improved soil liquefaction model known as UBCSAND2 was also incorporated into FLAC.

Byrne et al. applied the UBCSAND model implemented in FLAC to perform 2-D numerical predictions of liquefactions in sand under dynamic centrifuge tests (Byrne et al., 2004a and 2004b). In Byrne’s evaluation, a considerable effort was devoted to show that densification at depth contributes to the apparent limitations on liquefaction at depth observed in some centrifuge tests.

During the Canadian Liquefaction Experiment (CANLEX) program, both University of British Columbia and University of Alberta conducted 2-D finite element analyses using FLAC and PISA, respectively, to model centrifuge tests (Byrne et al., 2000). Details and descriptions of the CANLEX program and its analysis results are documented in five CANLEX reports (Robertson et al., 2000a and 2000b; Byrne et al., 2000; and Wride et al., 2000a and 2000b).

2.3.2 PGI's Single-Charge 2-D Blast-Induced Liquefaction Model

Blair Gohl of PGI (Pacific Geodynamics Inc.) applied the commercial explicit finite element code LS-DYNA to simulate a 2-D axisymmetric, single-blast-induced liquefaction event in soil material (Gohl, 2005). The LaGrangian model applied by PGI utilized existing LS-DYNA's Piecewise Linear Plasticity Model 24 and Geologic Cap Model 25. As in most commercially available material models, defining the proper input parameters is the most challenging task involved in an analysis. PGI applied an iterative procedure to a single-element model in order to calibrate the necessary material parameters against cyclic simple shear test data. Due to the lack of pore-water-pressure computation capabilities in both Model 24 and Model 25, PGI applied strain-softening techniques to approximate liquefaction following a critical strain level. According to Gohl in a discussion during the Fraser River blast-induced liquefaction tests that took place in May of 2005, blast pressure for the PGI model was generated by a TNT-equivalency air-blast approximation approach available in LS-DYNA. Insufficient published information is available on the performance and accuracy of PGI's 2-D axisymmetric LS-DYNA model.

2.3.3 Taylor's Effective Stress Material Model for Saturated Soils

Paul Taylor of Sandia National Laboratory developed an effective soil material model for CTH, an Eulerian shock-physics code published by Sandia (Taylor, 2004 and Bell et al., 2005). Taylor's model accounts for pore pressure development as a function of water saturation level defined by the user. Effective stress is computed from total stress and pore water pressure. Taylor's model was specifically developed for short duration, high magnitude impulsive loading environments similar to blast or earthquake

induced liquefaction environments. Drainage and water seepage effects in saturated soils subjected to short duration impulsive loads are often negligible. As such, Taylor's model does not consider seepage.

Specific advanced features in Taylor's model cannot be described here due to security restrictions set forth in the Sandia software agreement. Based on a preliminary evaluation of the theory and capabilities behind Taylor's model, it shows tremendous potential and possibilities for simulating blast-induced liquefaction events. Unfortunately, both Taylor's model and the corresponding CTH code where the model was implemented are "export controlled". Therefore, potentials and possibilities for applications and international collaborations in earthquake research using Taylor's model are very limited.

2.3.4 FHWA's LS-DYNA Soil Material Model 147

Brett Lewis of APTEK, Inc., a U.S. Federal Highway Administration (FHWA) contractor, developed an LS-DYNA soil material model that accounts for geometric non-linearity, material non-linearity (plasticity), and pore water pressure development (Lewis, 2004). This is the baseline material model used for the current dissertation research. Specific features of this soil material model, its input parameters, and application research will be provided in Chapter 7 of this dissertation.

3 Baseline Numerical Model Requirements

3.1 Overview

The ability to simulate an event successfully under pre-defined environments is directly related to one's ability to understand the problem at hand, as well as his or her ability to recognize and apply the proper tools at the right place and at the right time. Therefore, it is vitally important to first define the problem and the corresponding conditions necessary for a successful simulation prior to making a first attempt to solve the problem. This section of the dissertation defines the fundamental modeling requirements for simulating a blast-induced liquefaction event.

3.2 Model Symmetry

Model symmetry is essential in maintaining analytical feasibility. For most engineering problems, taking advantage of both geometric and loading symmetry is critical to the probability of completing the tasks within time and budgetary constraints. However, there are exceptions when symmetry cannot be applied due to pre-defined and / or unexpected circumstances.

Typically, a single detonation (or blast) is an axisymmetric event where the shock waves and blast pressures propagate outwardly from the point of detonation. Although multiple explosive charges detonated simultaneously in a horizontal circular pattern is not

axisymmetric, planes of symmetry can often be defined to help reduce the complexity of the event to be modeled numerically.

The 2005 Vancouver blast-induced liquefaction test used for this research consisted of sequential blasts from 21 explosives set at 3 depth levels (21 ft, 28 ft and 33 ft) as shown in Figure 3-1. The blast pattern and sequence with respect to the locations of the accelerometers and pore pressure transducers (PPTs) are also presented in Figure 3-1. No explosive charges were installed at the North-East blast hole due to an unplanned single-hole blast test conducted in that test hole prior to the actual sequential test series. For a sequential blast order with one of the eight blast holes not being used as shown in Figure 3-1, there is no symmetry in the blast pattern or the blast order. Therefore, a full 3-D non-symmetrical numerical model is required to represent the actual event accurately.

3.3 Evaluation of Acoustic Waves and Shock Waves

When a load is applied to a solid material, the solid material dissipates the energy generated by the applied load through deformations and/or rise in temperature. Under a dynamic loading environment, mass inertia and material damping also play an important role in defining the response characteristics of the material. An impulsive environment is present when a load with a short duration is applied. Impulsive loads can either be singular (i.e. impact) or cyclic / repetitive (i.e. earthquake).

In an impulsive environment, materials propagate the applied load via compressive and shear waves. Solid materials can transmit both compressive and shear waves whereas liquids and gases can only transmit compressive waves due to their

inability to support shear. Waves that propagate in a solid continuum can be classified into two categories: elastic acoustic waves and shock waves.

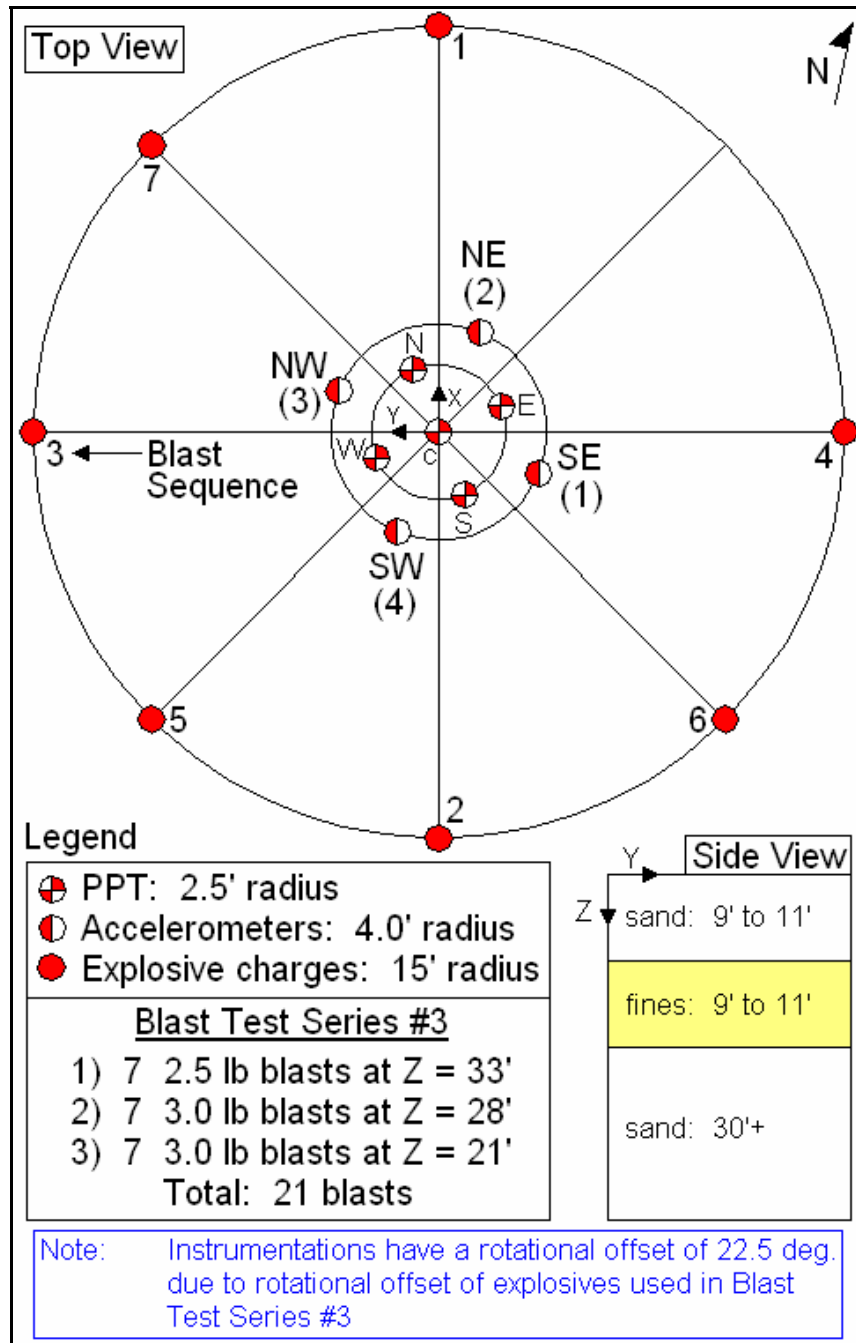


Figure 3-1 Vancouver (2005) Liquefaction Test Blast Configuration

In engineering, acoustic waves are sometimes mistakenly referred to as shock waves, partly due to terminology differences among the various fields of engineering. One should notice, however, that there are distinctions between elastic acoustic waves and shock waves. The types of waves propagated by a material depend on the material's strength with respect to the severity of the applied load.

If a solid material remains completely within its elastic limit when subjected to an impulsive load, then the waves that propagate outwardly from the loading source through the material medium are acoustic sound waves. When the material begins to yield and exhibits combined elastic-plastic behaviors, both acoustic sound waves and shock waves exist in the material. However, if the material exhibits behaviors that are completely within its plastic region (i.e. plastic deformations are much greater than elastic deformations), then the only type of wave that can propagate from the material is a shock wave (Lee, 2003 and Cooper, 1996).

During an earthquake, waves transmitted from the source are typically a combination of acoustic sound waves and shock waves as a function of distance from the source and the corresponding strength of soil materials. Since soil materials are relatively "weak" in comparison to high strength materials such as metals or fiber composites, significant plastic deformations and fractures are frequently observed during earthquakes. As such, waves generated by earthquakes are often classified as shock waves, or a combination of acoustic and shock waves. An important point to remember is that plastic deformations in non-continuous, non-homogenous cohesionless soils have different characteristics and, therefore, different responses than the corresponding plastic deformations found in continuous materials such as metals and plastics.

Fractures (or separation of adjacent particles) take place with small deformations in cohesionless soil materials. Therefore, sound wave transmissions in plastically deformed or fractured cohesionless soil do not propagate in the same way as plastically deformed metals. In general, waves transmitted in soil materials encounter alternating high and low impedance jumps or dips as they travel from solid soil particles to air (or water) voids followed by more soil particles. One can expect greater energy dissipation for wave propagation in non-homogeneous soil materials due to the impedance jumps and dips than in continuous, homogeneous materials such as metals.

In a solid continuum, characteristics of an elastic acoustic wave are defined by its sound speed with respect to the shear modulus (G), bulk modulus (K) and density (ρ) of the respective material. Sound speeds of elastic compressive and shear waves are expressed by Equation 3-1 below (Bolt, 1993).

$$c_c = \sqrt{\frac{K + \frac{4}{3} \cdot G}{\rho}} \qquad c_s = \sqrt{\frac{G}{\rho}} \qquad (3-1)$$

Unlike elastic acoustic waves, shock waves are significantly more difficult to evaluate than elastic acoustic waves. In a shock, the front is a discontinuous jump with a shock velocity (U). The original states of a solid particle's velocity (u), along with the material's density (ρ), internal energy (E), and pressure (p), suddenly change from a non-shock environment to a shock environment via a discontinuous jump across the shock front. The result is five unknowns that must be solved by five equations. The first three equations are theoretically described by the conservation of mass, the conservation of

momentum, and the conservation of energy, which together are known as the Rankine-Hugoniot jump equations (Lee, 2003 and Cooper, 1996).

The fourth equation required to evaluate a shock is defined by an empirical relationship known as the Hugoniot. The Hugoniot is defined by experimentally relating shock velocity or pressure to particle velocity or specific volume of the material. Results of experimental data are typically expressed in terms of an equation-of-state and/or other forms of shock (i.e. detonation) properties as required by specific analysis tools used to evaluate the shock.

The fifth or final equation required to evaluate a shock can be defined by applying appropriate and problem specific relationships (i.e. boundary, constitutive, and thermodynamic conditions) to the shock environment of interest.

The most challenging aspect in evaluating a shock is the definition of the input parameters and the conditions required to describe the event at hand. Descriptions of input parameters used to simulate the blast-induced liquefaction will be provided in later sections of this dissertation.

3.4 Geometry Non-Linearity

Detonation events involve extremely high magnitude (i.e. 1,000,000+ psi) and very short duration (i.e. microseconds to milliseconds) impulsive forces that initiate motions which propagate outwardly as shock waves from the loading source. At such high magnitude and short duration, materials immediately adjacent to the blasting source do not behave in the same manner as one would expect when subjected to finite, quasi-static type loads based on Hooke's law.

In many cases, energy from the blast causes the adjacent solid material to increase in temperature and behave like “molten” materials that “flow” as liquid to exhibit significant geometrically non-linear behaviors. However, it is vitally important to realize that from studies of both heat transfer and physics, temperatures in solid materials adjacent to a blast typically do not have sufficient time (i.e. microseconds to milliseconds) to reach their melting point. As such, the apparent liquid behaviors described above are **not** caused by melting of the materials (Walters and Held, 2003). Instead, solid materials adjacent to a high-explosive detonation are simply being pushed aside by the sudden and extremely high pressure from the blast, thereby exhibiting “apparent” liquid behaviors as they “flow” away from the blast point (Walters and Zukas, 1989).

Solid ductile materials such as metals form jets, slugs and particulates with tremendous penetrating energy when subjected to adjacent detonation events. Brittle orthotropic / anisotropic materials such as graphite fiber composites “shatter” under identical detonation environments (Lee, 2003). Soil is a material that is formed by “fragmented” or “non-continuous” particles with air- and water-filled voids which behave somewhere in between a ductile and a brittle material.

Soft soil materials with low material sound speed typically exhibit significantly greater damping and shock-attenuation characteristics than hard materials such as metals. Since compressive waves can travel faster in water than in solid soil particles due to greater compressibility (in terms of bulk modulus) in soils, water can react much faster to shock waves than soil particles. Therefore, water often becomes the “pressure carrier” in saturated cohesionless soil when subjected to impulsive loads such as blasts or

earthquakes. Cohesion found in fine materials such as clay and silt is often sufficient to “lock” adjacent particles together to form a continuous mass, which may also provide sufficient resistance against water flow between soil particles. Inhibited or discontinuous flow of water reduces its ability to transmit shock waves and compressive loads. Therefore, cohesive soils are less likely to liquefy as cohesionless soils under identical impulsive environments.

Due to current limitations on modeling discontinuous or particulate materials, soil particles are typically treated as a solid continuum using their “averaged” reactive characteristics to represent their bulk behaviors. Since a solid continuum cannot separate as readily as particulates, some inherent geometric non-linearity errors can be expected in modeling soil materials. Nevertheless, geometric non-linearity plays an important role in defining the characteristics of soil materials adjacent to detonation environments. Analytical tools used to evaluate a blast-induced liquefaction event must be able to handle significant and localized geometry non-linearity, particularly in the immediate vicinity of the blast charges.

3.5 Material Non-Linearity

As described in Section 3.4 above, pressure due to a blast event propagates in the form of shock waves outwardly into the surrounding materials. The ability for the pressure generated by the detonation event to propagate and to attenuate is a function of the surrounding materials. The softer and less dense the material, the greater the corresponding damping characteristics, material compliance, the time required to travel through the material (i.e. slower material sound speed), and plastic damages or energy dissipations in the material. Since the dispersion of energy from a shock in a material is

accomplished through deformations, displacements and heat, greater shock attenuation is expected in soft materials than stiff materials.

In addition to large geometric non-linearity, solid materials adjacent to explosives upon detonation are also subjected to severe plastic deformations and material damages, thereby resulting in the propagation of shock waves. In such regions, both geometric (large deformations) and material (plastic flows) non-linearity are significant and must be accounted for in numerical modeling. As shock waves propagate away from the loading source, attenuations often result in a transformation from almost a pure shock wave at the loading source to an elastic acoustic wave at some distance away from the same loading source. Therefore, one can focus material non-linearity near the blasting source with nearly elastic behaviors in the bulk of a half-space soil mass. The size of the plasticity influence zone from a given blasting point is a function of the charge mass, the corresponding amount of energy it generates upon detonation, and the soil material's strength characteristics.

One must keep in perspective that the focus of a blast-induced liquefaction experiment is to simulate the effects of a large earthquake within a small, manageable, and pre-defined region due to economic, safety, feasibility, repeatability, and other reasons. The amount of explosives used in an experiment is typically sized only to produce sufficient energy to cause the soil in region of interest to liquefy. Therefore, the total energy produced by a blast-induced liquefaction experiment is substantially (i.e. orders of magnitudes) smaller than the corresponding energy produced by a large earthquake. As such, the plasticity influence zone of a blast-induced liquefaction

experiment is significantly smaller than the corresponding plasticity influence zone of a large earthquake.

3.6 Acceleration Measurement

The ability to extract crucial acceleration, velocity and displacement results at locations of interests within the numerical model is important in order to provide a direct comparison against measured data. There are two ways to extract acceleration, velocity, and displacement data from an explicit (shock physics) finite element analysis.

First, one can extract nodal displacements, velocities, and accelerations from the numerical model. This approach is the most common in the engineering community. The limitation of this approach is the inability to extract results at exact locations of interest, versus at nodal locations of specific elements. One can, however, extract results from all surrounding nodes and apply some sort of weighted or non-weighted averaging scheme to interpolate the results for the locations of interests.

Second, one can extract nodal displacements, velocities, and accelerations from “tracer points” that are fixed in space at locations of interest. Tracers are available only for Eulerian and/or Arbitrary-Lagrangian-Eulerian (ALE) analyses, which will be discussed in Section 4.3 of this dissertation. Appendix B also provides a detailed explanation of tracers and their functionalities.

3.7 Blast Pressure Development

Proper definitions of blast pressure as input loading environments for a numerical analysis are essential for an accurate simulation of a blast-induced liquefaction event. Shock duration (or pulse width), magnitude and frequency are several important factors

in the consideration of blast-pressure definitions. For example, the difference between a blast-pulse width of 0.5 milliseconds and 1.0 millisecond of the same magnitude may seem trivial in quasi-static analysis; however, it is vitally important in defining the proper shock physics and the corresponding shock wave propagation characteristics in the numerical model of interest. Doubling the blast-pulse width in many cases can completely alter materials' responses, thereby resulting in erroneous results. More details on the approach to modeling blast-pressure development will be provided in Section 4.7.

3.8 Pore Pressure Development

The most fundamental requirement in determining liquefaction characteristics of a saturated cohesionless soil material is the ability to describe pore water pressure development within the material to be subjected to large impulsive and/or cyclic loading environments. There are multiple definitions and approaches in defining pore pressure development within a soil material. Lewis (2004) and Taylor (2004) are examples of two different approaches being used in describing pore pressure development within numerical models. The accuracy and appropriateness of each approach is a function of the corresponding soil materials and their applications.

3.9 Strain-Rate Considerations

In highly impulsive loading environments such as detonations, very high strain rate accompanied by very high magnitude shock waves emanate from the blasting source across the materials adjacent to explosive charges. Shock waves can induce extremely damaging forces that can alter the normal and expected behaviors of any materials along their path. Therefore, under highly impulsive loading environments, materials often do

not behave as one would expect under quasi-static environments. Material stiffnesses often increase along with the corresponding applied stresses induced by shock waves propagating from the impulsive loading source. As a result, it is vitally important to account for rate dependent behaviors when evaluating materials subjected to highly impulsive environments to avoid erroneous or misleading results.

Similar to pore-pressure development considerations, several approaches are available for simulating strain rate effects. One approach to account for strain rate effects in geomaterials was proposed and implemented into LS-DYNA by Yvonne Murray. Murray developed a two-parameter Devaut-Lions viscoplastic algorithm which basically performs a parametric interpolation between the elastic trial stress (i.e. stress beyond yield surface) and the inviscid stress (stress on the yield surface with negligible viscosity effects (Murray, 1997)). Murray's approach to account for strain rate in geo-materials (Murray, 1997) was incorporated by Lewis into his effective stress material model for LS-DYNA (Lewis, 2004). Chapter 7 of this dissertation describes the assumptions and approaches in considering strain rate effects being used in the baseline numerical model.

3.10 Drainage and Seepage Considerations

Drainage and seepage are typically not an issue in a blast environment as the rate of the loading input is significantly faster than the rate of water seepage and dissipation. However, if the explosive charge is to be detonated near a free surface where cratering due to the blast(s) can be observed, then the path of least resistance is through the free surface where excess pressure generated by detonations can easily dissipate. In the case of the May 2005 Vancouver blast-induced liquefaction test, charges were placed at 21+ feet below ground surface and beneath an 8 to 10 feet layer of fine cohesive material. As

such, drainage and seepage in such an environment for the duration of blasts is not expected to be an issue. Therefore, undrained condition can be assumed for the modeling of the May 2005 Vancouver blast-induced liquefaction event.

4 General Modeling Methodology

4.1 Overview

One of the most important aspects of a numerical modeling study is selection of the most appropriate method for determining the solutions of the problem at hand. This section presents a general description of numerical methods available for evaluating the blast-induced liquefaction event of interest and the rationale for selecting the methods that were used in this study.

4.2 Implicit Methods

The implicit method involves the solution to Newton's law of motion (Equation 4-1), typically by means of the construction and solution via triangulation or inversion of stiffness matrices. Details on implicit method's theory and formulations are presented in many finite element texts such as Bathe (1982), Belytschko et al. (2000), and Zienkiewicz (2000a, 2000b, 2000c).

$$F(t) = [K] \cdot u + [c] \cdot \dot{u} + [m] \cdot \ddot{u} \quad (4-1)$$

The non-linear implicit method iterates toward the convergence of loads (i.e. force, pressure, moment etc.) based on given material constitutive relationships. Time

duration of applied loads is generally not a critical issue since implicit solutions excel in quasi-static, small strains, and some non-impulsive dynamic (i.e. vibrations, elastic stability etc.) environments. Model constraints are critical in implicit method to avoid “small pivots” or “rigid body motions” caused by either ill-conditioned or singular stiffness matrices.

Element refinements are generally recommended for areas of high stress gradients. However, a balance must be maintained between element refinement and analysis run time to ensure feasibility and acceptable costs in terms of time and CPU / disk usage requirements. One should realize that the relationship between run time and model size is non-linear. The amount of time required to solve the problem by the implicit method often increases at a faster rate than the rate of increase in the model size. For large models with significant mesh refinements, out-of-core solvers may be required for the solution of the corresponding large stiffness matrices. Numerous schemes to re-order and solve large sparse stiffness matrices have been developed to improve the performance of matrix solutions. Double precisions are generally standard in implicit solutions to minimize numerical round-off errors often associated with the solution of stiffness matrices.

Implicit methods are very popular with most commercial engineering and many aerospace companies due to their versatility in solving a large range of small strain, quasi-static, and some dynamic problems. Typical commercial implicit finite element tools available in the market include ANSYS, MSC/NASTRAN, ABAQUS, ADINA, ALGOR, NISA, COSMO-M, PLAXIS, PCAMAT, LS-DYNA/Implicit etc.

While implicit methods are well suited for solving quasi-static problems, detonations and similar types of impulsive or shock environments are not suitable nor efficient for implicit methods due to time sensitivity; shock wave generation / propagation; large strains / large deformations; and potential rigid body kinematics and flexible body dynamic motions often observed in the region around the explosive charge(s).

4.3 Explicit Methods

4.3.1 Overview

Software performing analyses using the explicit methods are sometimes referred to as “hydro-codes” due to their ability to evaluate highly impulsive environments with greater displacements and deformations than their implicit counterparts. Instead of assembling and solving stiffness matrices via triangulations or matrix inversion techniques as in the implicit method, explicit methods perform a “time march” or “time integration” for solutions of the problem at hand. Solution at a given time step is based on the results obtained for the previous time step plus the results computed from the current incremental time value. Since solutions are based on simple arithmetic from one time step to the next, numerical precision due to round-off errors is generally not as much of an issue as in the implicit method for short duration problems. Detailed theoretical background on the explicit method can be located in publications such as Belytschko (2000) and Hallquist (1998).

Many of the explicit solvers (i.e. LS-DYNA) utilize single-precision computations for faster analysis cycle time. Furthermore, single-precision performed on

new 64-bit based machines (i.e. Athlon 64, Intel's EM64T Xeon etc.) are as accurate as double-precision solutions computed from an equivalent 32-bit machine.

Stability of explicit solutions controls the maximum time step size per iteration. It is common to see thousands of time steps for a one-millisecond time duration of loading solutions. Long duration (i.e. seconds) or quasi-static problems using explicit methods are typically not as efficient as implicit methods due to the number of time steps required (i.e. millions to hundreds of millions) in order to arrive at the desired results. Accumulation of numerical round-off errors and numerical instability can be an issue for long duration runs using explicit methods.

Unlike implicit methods, smaller elements do not necessarily improve the accuracy of the results. In fact, time-step size is inversely proportional to element size. In an explicit finite element model, the smallest element controls the amount of time required to complete the analysis of the entire model. One may observe that two explicit models with identical number of elements but with different element sizes result in significantly different amounts of time to complete the respective analyses. In some cases, differences in time required to complete the analyses can be in terms of several orders of magnitude. All it takes is one small element or one degenerate element in the model to increase the run time significantly. More details on this subject matter are presented in Chapter 10 of this dissertation.

Explicit solutions are also susceptible to abrupt change in sizes among adjacent elements, as well as excessively large (or small) element aspect ratio. This is especially true in high-energy shock wave analyses. Since time step sizes are based on the shortest distance between two nodes within an element, abrupt changes in element size and /or

aspect ratio may be detrimental to the results of the model. For example, an element with an aspect ratio of 20 to 1 in a blast analysis will take 20 time steps for shock waves to propagate in the long direction of the element versus a single time step in the short direction. As such, deformations in the near end of the shock wave may have initiated and dissipated well before the far end even feel the effects of the same shock wave. Such a scenario may cause premature failure of the element as well as erroneous results. It is generally a good practice to maintain the adjacent element sizes and individual element aspect ratio to no more than a factor of four, although a factor between one and two is highly preferred. However, sometimes it is not possible to maintain such tight element size differences and aspect ratios due to one reason or another. In such cases, engineering judgment becomes important in the development of the model.

Since explicit solutions are based on incremental results computed on finite time steps, pressure / force equilibriums are not checked rigorously for convergence as in the implicit method. Therefore, it is more likely to see pressure / force oscillations induced element instabilities in explicit solutions than in implicit solutions. However, these oscillations can often be controlled or minimized by adjusting time step size and the corresponding hourglass control parameter as described in Section 4.3.4.

Boundary constraints in explicit analyses are not nearly as restrictive as implicit stiffness methods. Small pivotal issues relating to rigid body motions are not an issue in explicit methods. Therefore, explicit methods are well suited for rigid-body kinematics, flexible-body motions / dynamics and unconstrained problems subjected to impulsive loading environments.

There are two general categories to solutions in explicit methods: LaGrangian and Eulerian. Other explicit solution approaches such as Arbitrary-LaGrangian-Eulerian (ALE) are combinations of the LaGrangian and the Eulerian methods.

4.3.2 LaGrangian

The Explicit LaGrangian method deals with the observation of stationary particles from the reference viewpoint of a moving particle in terms of material coordinates. “The material coordinate labels a material point: each material point has a unique material coordinate, which is usually taken to be its spatial coordinate in the initial configuration of the body” (Belytschko et al., 2000). LaGrangian method employs a deformable mesh where nodes and elements move with the material. Typical models are defined to represent deformable structures subjected to dynamic and / or impulsive loading environments. In general, LaGrangian solutions can be very accurate, economical, and rapid in terms of solution time when applied properly. With careful planning and modeling techniques, complex problems with over 100,000+ elements subjected to highly impulsive and short duration (i.e. a few milliseconds) environments can be solved accurately using a personal computer (PC) in a few hours.

The LaGrangian method is typically used for impact and general shock wave propagation problems with limited deformations and mesh distortions. Structural response to impulsive environments is an example of an application well suited for LaGrangian solutions.

4.3.3 Eulerian

The Eulerian method deals with the observation of moving particles passing by a stationary reference view point in terms of a spatial coordinate in the current

configuration. “A spatial coordinate specifies the location of a point in space” (Belytschko et al., 2000). Eulerian method employs a fixed finite element mesh where nodes and elements are fixed in space. Material within an element or a cell can flow into other elements or cells. Therefore, Eulerian materials are not restricted to stay within its initially defined element or cell boundaries. The Eulerian method is well suited for liquid / gaseous materials, or solid materials that “flow” like liquid when subjected to blast or high velocity impact environments (i.e. shape charge, warhead detonations, missile impacts, etc.). Typical models are defined to represent large deformations under highly impulsive loading environments, especially in situations where LaGrangian mesh distortions become an issue to successfully completing an analysis of interest.

Solutions based on the Eulerian method are significantly more computational intensive and time consuming than the LaGrangian method. Accuracy can also be of concern especially when multi-material mixing is involved. The explicit Eulerian method often utilizes a multi-phase approach known as the “Split Operator Technique” (SOT) to obtain solutions rather than directly solving the more complex Navier-Stokes equations as done in implicit computational fluid dynamics (CFD) analyses (Souli, 2000).

In the multi-phase approach, the physics of the problem is solved first by the LaGrangian method in a deformable mesh. The process continues for as long as mesh deformations / distortions are “reasonable”. When the mesh begins to distort severely, the Eulerian advection phase is then activated by first transforming the deformed LaGrangian mesh into a flow-pattern of a fixed Eulerian mesh, followed by solutions of the conservation equations (mass, momentum and energy) in Eulerian forms. During the

Eulerian advection process, instead of computing element deformations, materials are transported from one element into adjacent elements in a fixed grid.

For fluid materials, advections involve the solutions of mass, momentum and energy equations. Stresses are computed from velocity results. For solid materials, in addition to mass, momentum and internal energy, advection of stress components and plastic stresses are performed to obtain results for the next time step. During the advection process, averaging of materials are performed for each element cell, followed by a reversed mapping of the materials back into a LaGrangian mesh (Souli, 2000) for further LaGrangian analysis. The multi-phase process described above is repeated until the analysis is completed. The final deformed mesh is then mapped onto the final “flow” pattern in a fixed Eulerian mesh.

It is during the Eulerian advection process that most numerical errors occur. For example, during the advection process, as soon as a material from one element begins to enter into an adjacent element with a different material, the originating material is smeared across the receiving element by the averaging algorithm. Smearing induced by the averaging / smoothing process takes place in Eulerian analysis because it is presently infeasible to accurately track and separate multiple materials within a given element. Obviously, the more materials involved in the averaging process within a given element, the greater the potential for errors.

Since the more complex advection and smearing do not take place in the LaGrangian method, the LaGrangian method is inherently simpler, faster, and more accurate. If numerical errors become a major concern in an Eulerian analysis, one can always refine the mesh in order to reduce numerical errors. It should be remembered,

however, that a finer mesh causes an increase in run time. Therefore, experience and proper engineering judgments are necessary to ensure an acceptable balance between run time and accuracy.

Although the Eulerian method is not as accurate as the LaGrangian method for solid materials in many cases, the most compelling reason behind the popularity of its usage is its stability for large deformation problems. In this research, two Eulerian solvers were evaluated in terms of their shock physics capabilities, as required to simulate a blast-induced liquefaction event in undrained conditions where seepage effects are negligible throughout the time duration of interest. The two solvers evaluated were Livermore Software Technology Corporation's (LSTC's) LS-DYNA and Sandia National Laboratory's (SNL's) CTH. LS-DYNA is a commercially available FEA hydro-code with LaGrangian, Eulerian, ALE, Smooth Particle Hydro-dynamics (SPH) and meshless analysis capabilities. CTH is an Eulerian based hydro-code developed by Sandia National Laboratories for the evaluation of detonations, high-velocity impacts, radiation and other high magnitude, short duration impulsive environments.

4.3.4 Arbitrary LaGrangian – Eulerian (ALE)

Although the LaGrangian method is simpler, faster and more accurate than Eulerian methods, it is susceptible to a phenomenon known as “hourglassing” when excessive load and/or deformations are present in the deformable structure of interest. Hourglassing is a stability issue which occurs when two opposing nodes in a quadrilateral or brick element cross over each other, resulting in an inversion or a twist of the element's surface into an hourglass shape. Software such as LS-DYNA also provides multiple hourglass control schemes one can apply in accordance with the type of analysis

at hand. These hourglass control schemes generally function well within the limits and assumptions specified in the corresponding documentations (Hallquist, 2003).

Additionally, one of the most straightforward approaches to reduce hour-glassing problems is to sub-divide a given load increment into multiple smaller load increments by reducing the corresponding solution time steps. However, sub-dividing time steps can increase the total solution run time significantly. Therefore, this sub-dividing time step approach is recommended only when the range of time being sub-divided represents a small fraction of the total time duration to be evaluated, or when the sub-dividing processes do not result in a major increase in total solution run time.

In cases where the range of time to be sub-divided represents a significant portion of the total run duration, one can apply the Arbitrary-LaGrangian-Eulerian (ALE) method of solution to help stabilize deformable structures experiencing hour-glassing symptoms. ALE combines the accuracy of the LaGrangian method while taking advantage of the stability in the Eulerian method. The major trade-off in using ALE over LaGrangian is the added complexity, which sacrifices both run time and numerical accuracy. In ALE, Eulerian computations are applied only when necessary. Results for an ALE analysis are always presented in the deformed LaGrangian format. Sometimes it is difficult to tell the difference in results between a LaGrangian analysis and an ALE analysis, especially with LaGrangian problems where hourglass behavior is not an issue.

Figure 4-1 shows a typical example of the stability improvement of ALE over the corresponding LaGrangian analysis suffering from hourglass symptoms. The example consists of a one-inch cube element of soil subjected to a uniform cyclic pressure (multiple loading / unloading cycles) of 120 psi across all element faces. The element on

the left shows a nice and uniform compressive deformation pattern based on the ALE method of solutions. However, the element on the right shows a typical “hourglassing” issue one may encounter after a few cycles of identical cycle of compressive load identical to those to which the element on the left was subjected. As mentioned previously, there are hourglassing schemes available in software such as LS-DYNA that can help “reduce”, but not necessarily eliminate, the severity of such unsightly and unstable issues. When all else fails in the attempt of analyzing a model using the LaGrangian method, one should at least attempt to perform an Eulerian or an ALE analysis to solve the problem at hand.

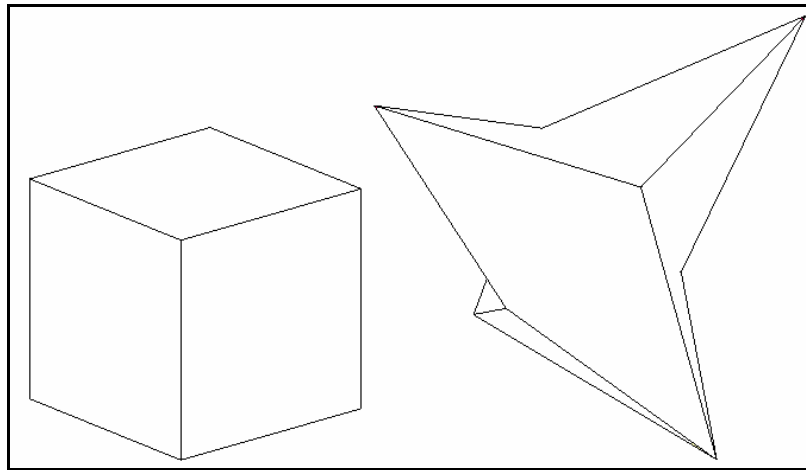


Figure 4-1 Single Element ALE and LaGrangian Comparison Analysis

A concern that is often encountered in ALE analysis is exhibited during the transformations of an Eulerian flow pattern into a deformed LaGrangian mesh. Finite elements are discrete approximations of “smooth” fluid boundary in an Eulerian field. As such, flow pattern jaggedness in a fixed Eulerian mesh is often observed. During the

transformation of an Eulerian flow pattern into a deformed LaGrangian mesh, such jaggedness may induce undesirable results. To address the jaggedness issue, various smoothing or boundary reconstruction options are generally available in Eulerian solvers.

4.3.5 Fluid-Structure Coupling

There are circumstances where fluid (or a structural material with fluid-like behaviors such as a shape charge or fully liquefied sand) interacts directly with adjacent deformable structures (i.e. buildings, piles, and foundations) in an impulsive environment. Traditional explicit analyses typically can only represent such types of environments in a very limited fashion. To accurately simulate the interactions, one must account for both fluid and structural behaviors. Coupled fluid-structure analysis, if performed properly, can provide solutions to simulate events such as fully liquefied soil interactions against adjacent foundations, piles, and/or structures of interest.

In a fluid-structure analysis, fluids (or structures with fluid-like behaviors) are modeled using the Eulerian method while solid structures are modeled with the LaGrangian method. Interactions between Eulerian and LaGrangian materials are coupled together by special two-way Eulerian-LaGrangian constraints similar to “contact elements” used in solid mechanics. There are inherent difficulties in performing fluid-structure analysis due to the additional complexity in defining interactions between Eulerian and LaGrangian methods. Significant increase in complexity, time, and costs are the main detractors to performing a fluid-structure analysis at the present level of technology unless there are sufficient justifications for its use. A blast-induced liquefaction event, by itself, does not require fluid-structure interactions to be modeled. However, when piles and foundations are added to a blast-induced or earthquake-induced

liquefaction event, fluid-structure analysis might be warranted to represent accurately the structural responses of the piles and/or foundations subjected to interactions against liquefied soil or water.

4.3.6 Smooth Particle Hydrodynamics

Recent development (past four to five years) in particle hydrodynamics has led to the increasing popularity of smooth particle hydrodynamics (SPH) analysis method. SPH, also known as special particle hydrodynamics or spherical particle hydrodynamics, is a unique approach in modeling particulate materials such as sand. Unlike finite element methods, SPH do not require “discrete” element meshes to be constructed. Instead, the structure(s) of interest are represented by “particles” with finite “space of influence” surrounding the corresponding particles. Interactions are modeled using contact-like methodology. Unfortunately, the number of particles required to represent complex structures has limited the applicability of SPH among typical industrial and commercial users. Advances in computing technology and hardware capabilities can potentially make it feasible within the next few years for SPH to develop widespread usage in place of, or in addition to, traditional finite element analyses.

4.3.7 Meshless Analysis of Solid Continuum

Meshless analysis method is one of the new analysis technologies looming on the horizon that can perform evaluations of local deformations within a structure without having to discretize the geometry into “finite elements”. Several approaches are currently under development by national laboratories, universities, and commercial finite element companies. Sandia National Laboratories’ EMU is a meshless peridynamic

solver that allows for the modeling of fractures and cracks anywhere within a structural body without discrete restrictions of finite elements (Silling, 2005).

Normal partial differential equations (PDE) describing the behaviors of a structure do not apply when encountering a fractured surface or discontinuity. Special boundary techniques (i.e. ignoring the discontinuity by geometry smoothing techniques) are required to treat discontinuities. This is especially true with soils and other geo-materials where fractures and discontinuities are common and are randomly located. New approaches such as peridynamic are being developed to address the issues of randomly located fracture surfaces.

The basis of a peridynamic approach is to reformulate the appropriate PDE such that the equations become applicable to everywhere in a structural body regardless of discontinuities (Silling, 2005). The basic concept of “following the path of least resistance” is applied directly in a peridynamic solver to simulate the propagations and development of cracks with random orientations and sizes. As a result, fractures in materials are created and propagated autonomously.

Unfortunately, fundamental principles applied in peridynamic are currently still in the developmental stage. Once developed, however, the peridynamic approach could possibly be very effective in modeling the “random” fracture characteristics of cohesionless soil during liquefaction process.

4.4 Axisymmetric Linear-Superposition Simulation Procedure

4.4.1 Overview

The simplest approach in modeling a sequential blast-induced liquefaction event is the axisymmetric linear-superposition approach.

4.4.2 Assumptions and Limitations

Several fundamental assumptions are necessary for the axisymmetric linear-superposition approach. First, blast effects from a single charge are assumed to be emitted from a central source located at a pre-defined point along the central axis of an axisymmetric frame of reference. Second, material characteristics are assumed to be within the linear, elastic range for the superposition method to be valid. It should be noted that this assumption is not appropriate in the neighborhood of the blast source due to high localized deformations induced by sudden and intense magnitude blast loads. Since analysis of detonations in cohesionless soils are focused mainly on the study of soil's dynamic responses due to blast waves, linear approximations of soil behaviors are generally acceptable at regions away from the blasting source due to low and diminishing deformations with respect to distance from blast source.

4.4.3 Description of Approach

In this approach, the user models the detonation of a single-charge at a pre-defined soil depth using axisymmetric element(s) to represent the radial and longitudinal outward propagations of shock waves from the corresponding central axis of the vertically placed explosive charge. Once results are obtained from the single blast axisymmetric analysis, subroutines can be developed to extract the desired results at

specific locations and/or distance from the blast point for superposition computations as a function of time, and in accordance with the blast pattern of interest.

For example, Figure 4-2 shows a 15 ft radius blast circle with an explosive charge placed at the north, east, south and west points of the circle. Let's assume that the location of pore pressure measurement as shown in Figure 4-2 is at 4 feet east of the center of the blast circle. One can compute the distance from the center of each explosive charge to the center of the measurement point. With distances from the explosive to the measurement point computed, one can then extract the corresponding pore-pressure time history results from the axisymmetric analysis at horizontal locations from the explosive center using the computed distances. Next, one would shift each time history in accordance with the distance required for the load to transmit from the current explosive to the measurement point. Followed by a linear superposition of the time-shifted pore-pressure time histories to produce the final time history of interest.

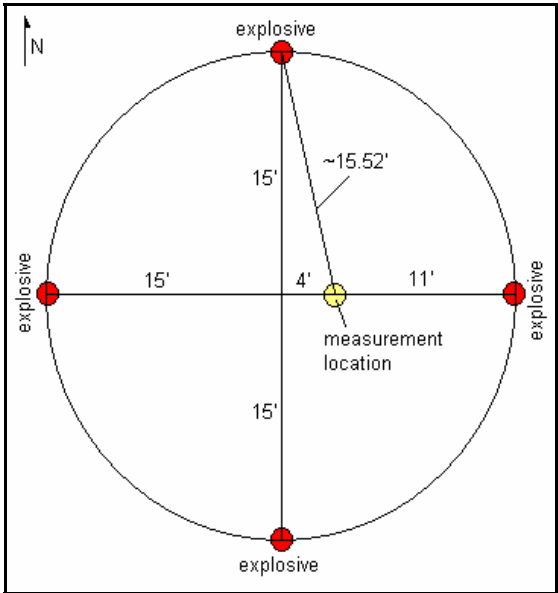


Figure 4-2 Blast-Induced Liquefaction Example for Axisymmetric Analysis

The major limitation of this simple axisymmetric approach is its inability to account for shock wave interactions due to shock collisions when charges are being detonated in a rapid pattern (i.e. milliseconds apart between detonations). Furthermore, depth and non-symmetry effects from blast points to measurement locations are difficult to apply in the axisymmetric approach due to simplification assumptions. Finally, any plastic characteristics observed from the results can potentially invalidate the results.

4.5 Three-Dimensional Blast-Pressure Transfer Modeling Procedure

4.5.1 Overview

In cases where an axisymmetric model cannot accurately represent the actual blasting event due to reasons such as non-symmetrical geometry and/or loading environments, a 3-D model must be utilized. Three-dimensional models often increase the complexity, overhead costs, and run time of an analysis significantly. In fact, sometimes it is not feasible to incorporate explosive charges in the 3-D model due to budgetary, time and other constraints. In such cases, 3-D blast-pressure transfer techniques can be employed to achieve the analysis objectives that will also satisfy project constraints. The 3-D blast-pressure transfer techniques are simply a generalization and an extension of the blast-pressure transfer portion of the axisymmetric superposition approach. Rather than assuming the blast pattern to be axisymmetric, the 3-D techniques can account for blast effects that are non-symmetrical, or partially symmetrical around the center vertical axis of the blast circle.

4.5.2 Assumptions and Limitations

The most fundamental assumption for the 3-D blast-pressure transfer approach is that it is valid only for linear, elastic, small strain regions. As in the axisymmetric superposition approach, the 3-D blast-pressure transfer method is likely to produce erroneous results in regions that are in close proximity to detonations due to expected geometric and material non-linearity induced by highly impulsive blast loads.

In cases with many detonation points with different detonation initiation times, the 3-D blast-pressure transfer can cause the inputs to be excessively large due to the number of input pressure time histories involved for each detonation point. Bookkeeping and time delays / shifts for various blast initiation times can be monumental. As with any approach, there can be a point where one may encounter a diminishing return in the amount of time saved by this approach versus the amount of additional time required to manage the additional input overhead costs. Sound engineering judgment is essential in determining the effectiveness of employing the 3-D blast-pressure transfer method.

4.5.3 Description of Approach

Similar to the axisymmetric superposition approach, the 3-D blast-pressure transfer method takes numerical results from a single, 3-D detonation analysis and maps its blast-pressure time-history profile to a larger global soil model as pressure inputs.

Analyses were conducted during the early stage of this research to evaluate the merits of the 3-D blast-pressure transfer method. Figure 4-3 illustrates a typical moving pressure front in a sample 3-D single-blast, pressure-generation wedge model at time shortly after initiation of blast. There are significant technical difficulties involved in the transferring of blast-pressure time-history profiles. Section 4.7.2 provides a more

detailed discussion on how to transfer blast-pressure profiles from a single blast model to a multi-level sequential-blast model using the blast-pressure transfer method, as well as the difficulties and limitations involved in the pressure transferring process.

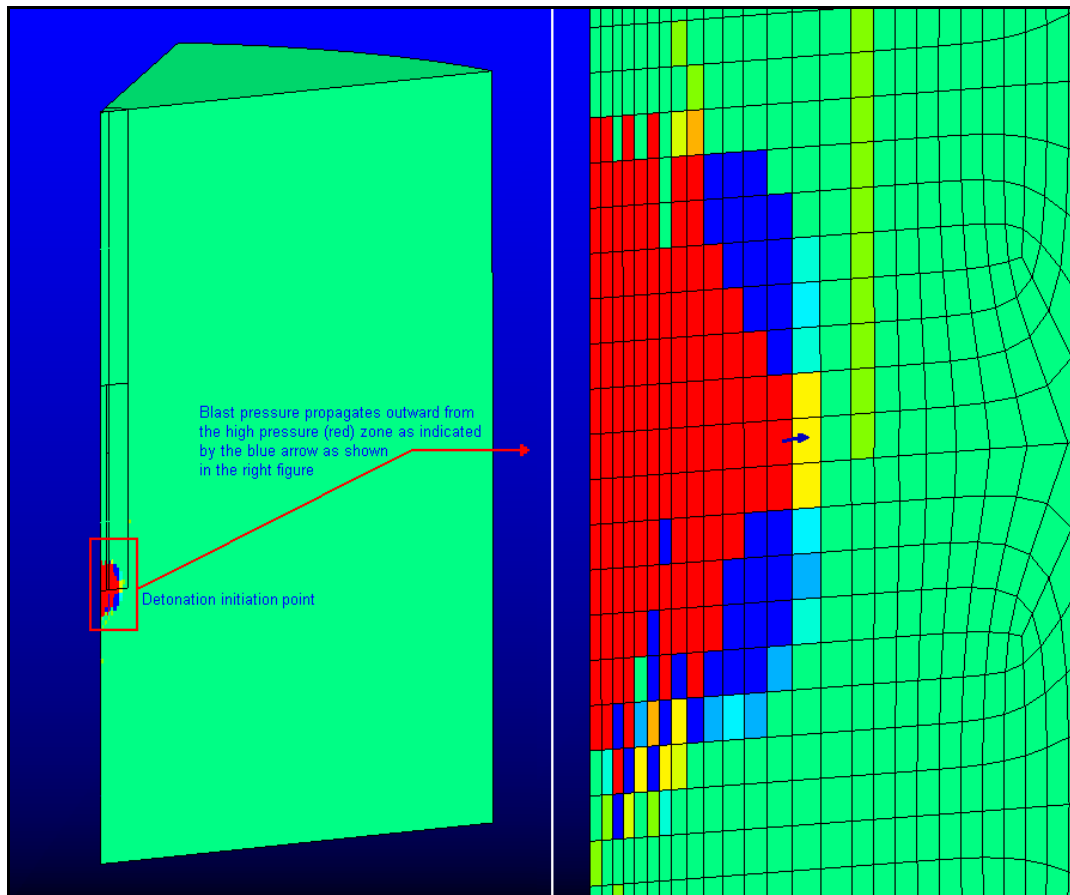


Figure 4-3 Blast-Initiation Pressure in a Sample 3-D Wedge Model

Upon evaluations of the technical difficulties in transferring blast-pressure time-history profiles within a reasonable amount of time, it was determined that the 3-D fully integrated modeling approach presented in the next section would be more appropriate and cost-effective for this research effort.

4.6 Three-Dimensional Fully-Integrated Modeling Procedure

4.6.1 Overview

The 3-D fully integrated modeling approach is the most generalized approach to be described in this dissertation, and is the baseline approach used to simulate the 2005 Vancouver blast-induced liquefaction event. It is recommended especially for a non-symmetrical model with non-symmetrical loading and/or boundary environments. However, for circumferentially symmetrical or simpler model, it may be more cost effective to apply either the axisymmetric superposition or the 3-D blast-pressure transfer methods.

4.6.2 Assumptions and Limitations

The major assumption involved in the fully integrated method is in the approach being used to model the explosive materials and the interactions between the explosive materials and their adjacent soils. The first and most common approach is to integrate the blast material with the adjacent soil materials as a single model with multiple materials. This approach assumes that nodes along the interface between explosives and the surrounding soil co-exist as “common” nodes. Shear, moment and normal loads are transferred among all adjacent materials. The major advantage of this approach is its simplicity and cost effectiveness. Limitations of this approach include the inability for the explosive materials to pull-away from or slide along the adjacent soil materials. Additionally, pressures, stresses and strains along the soil – explosive material interface are averaged. As long as the results to be evaluated are not along or adjacent to the soil /

explosive interface, results produced by this approach are reasonable and the procedure is cost-effective in terms of run time and modeling effort.

The second approach is to define the explosive materials separately from the surrounding soil materials. In this approach, interactions between the explosive materials and the adjacent soil materials are defined using contact and sliding interface elements. Sometimes LaGrangian-Eulerian fluid-structure coupling parameters are used in place of contacts. This approach, if done correctly, can produce more realistic results than the integrated approach described above; however, the more realistic results are often offset by the additional costs and complexity involved in the development of the model, model run time, and disk / memory requirements. The rule of thumb to be applied is “simplicity” whenever possible. Complex models may improve accuracy of an analysis; however, in most cases, the added accuracy alone is often insufficient reason to offset the additional time and costs involved in achieving it.

There is insufficient evidence indicating that the second approach involving more complex and time-consuming contact or fluid-structure interactions as described could produce significantly more accurate results for the blast-induced liquefaction event. As such, the first approach, or the integrated modeling approach, described in this section was employed for its simplicity, cost effectiveness and acceptable accuracy.

4.6.3 Description of Approach

The 3-D fully integrated modeling approach includes the modeling of explosive materials in the global soil model. Detonations of the explosives materials in a pre-defined sequence and pattern were conducted to generate the input blast-pressure necessary to trigger dynamic response of the corresponding soil materials to be evaluated.

The pre-defined 3-D blast sequence and configuration do not necessarily have to be in any specific orders or in any symmetrical fashion. As a result, the 3-D fully integrated modeling is very flexible and applicable for most configurations.

There are several approaches in modeling the detonations of the explosives materials for the generation of the input blast-pressure load to be applied to the soil materials of interest. The following section provides an overview of the most commonly used approaches in defining input blast-pressure environment through the modeling of explosive material detonations.

4.7 Loading Environments

4.7.1 Overview

There are many approaches in defining blast loads. From the basic approach of defining a blast pressure-time history to the sophisticated approach of modeling the explosives and their corresponding detonations, each approach has its own merits and limitations. By far, the most challenging aspect in defining a blast load in a model is the definitions of the proper explosive parameters and therefore, the proper loading environment. Four of the most common blast-load definition approaches are discussed in the following subsections.

4.7.2 Blast-Pressure Time History Representation and Limitations

The most straightforward approach in defining blast characteristics in a computer model is the direct definition of a blast-pressure time history. Explosives materials are typically not modeled in this fashion due to the difficulties involved in obtaining the proper blast-pressure time history as the input to the problem at hand. However, in some

cases, the direct pressure history approach can be advantageous in terms of run time improvements, especially for sequential blasting with multiple “small” charges (i.e. charges that occupy very small space relative to the total volume of the material modeled). When “small” charges are used in a sequential blast simulation, charges in the model that have not yet been detonated must be included in the computation of the controlling time step size. Time step size in an explicit model is controlled by the size of the smallest edge of all elements, the corresponding sound speed (or time required to travel) across the same edge, and its material stiffnesses (i.e. bulk, shear or tensile moduli). In a large model with “small” explosives, properties of the “non-detonated” explosives can often produce the smallest time steps, which must be used to avoid numerical instability. By not having to model the “small” explosives, direct entry of the blast pressure-time history often results in significantly faster analysis run time.

There are limitations associated with the direct definition of the blast pressure-time history. First, defining the proper blast pressure-time history is the most fundamental yet difficult requirement, especially when dealing with commercial blasting materials using identical charge configurations of interest. Pressure time histories from blasting vendors are difficult to obtain. However, one can potentially obtain the explosive parameters from the vendor, followed by computations to estimate the proper blast pressure-time history for the configuration at hand. In many isotropic materials under quasi-static environments, slight changes in mechanical properties (i.e. modulus) do not necessarily produce significantly different results. However, explosive materials’ detonation characteristics are rather sensitive to their detonation parameters such as material density, detonation pressure / velocity / energy, etc. Changes in detonation

parameters often result in noticeable shock characteristics, especially dealing with fragmentations and penetration events. Therefore, ensuring that the proper blast pressure-time history is being applied is essential to the success of a shock propagation analysis.

Second, once the pressure-time history is determined, one must determine from the detonation velocity of the blasting material the proper time when the blast-pressure will reach a specific element where the pressure is to be applied. This is crucial especially when dealing with element sizes in large units (i.e. multiple inches, feet, meters etc.). A separate pressure time history may be necessary for each element to account for the varying pressure magnitudes and initiation time as a function of the distance between element center and blast point. This requirement is necessary because detonation pressure, unlike static pressure, propagates rapidly in time and distance. A few milliseconds may appear to be “a short time”, but it can significantly alter the shock interactions and propagation profiles near the detonation point, resulting in erroneous material behaviors and responses.

4.7.3 Air-Blast Scaling Representations and Limitations

It is common to represent an explosion by applying an equivalent TNT blast pressure profile utilizing air-blast theory as inputs to a system subjected to nearby detonations. Baker (1973) provides the fundamental theory and background in properly defining air-blast effects as inputs to analysis. The Navy’s Handbook on Explosion Effects and Properties, Part I, edited by Swisdak, M. M. (1975) provides an extensive procedure and detailed discussion in defining air-blast theories and approaches used by

the U.S. Department of Defense (DOD). The U.S. Department of Energy (DOE) has also published many documents in the subject of air-blasts.

The most common form of scaling utilized in air-blast theory is the “cube root” scaling formulated by B. Hopkinson in 1915 (Cooper and Kurowski, 1996), which is commonly referred to as the Hopkinson scaling. In the Hopkinson scaling, the scaled distance Z is defined as a function of the total weight W or detonation energy E of the explosive in terms of TNT equivalency, and the distance R between the center of a spherical explosive and the point of observation as shown in Equation 4-2.

$$Z = \frac{R}{W^{\frac{1}{3}}} = \frac{R}{E^{\frac{1}{3}}} \quad (4-2)$$

The cube root in the denominator is derived from the scaling of volume and density of the explosive material. For a spherical explosive object, the volume is in a cubic form of the radius of the sphere, hence the cube root exponent is used when converting to an equivalent TNT weight or energy. For a long cylindrical explosive column, one often applies the circular area per inch of cylindrical column height. Since circular area is a square instead of a cubic function, some scaling approaches may apply a “square root” instead of a “cube root” of the weight or energy, implying that the scaling is performed using the circular cross-section area of an explosive column per unit height.

Hopkinson scaling is one of many similar approaches in defining equivalent TNT air-blast pressure generation techniques. Many of these approaches utilize some sort of cubic or square function along with some empirically derived multipliers. The differences in the scaling functions are results of variations in scaling found in different

explosives with respect to TNT. Factors that influence the accuracy of each air-blast scaling method include explosive material density (ρ_o), size, detonation or Chapman-Jouget (CJ) pressure (P_{CJ}), detonation velocity (D), detonation energy (E), chemical constituents, elevation of blasts, blast confinements, potential multi-phase transitioning characteristics, and other detonation and thermo-chemical related behaviors.

Computing the equivalent TNT values can be tricky due to the variations in characteristics of different explosive materials and the number of variables (such as those shown above) involved in the estimation process. Cooper and Kurowski (1996) show a peak over-pressure curve due to TNT blasts at sea level as a function of Z that helps define the effects of air-blast induced over-pressure using a scaling method that is a variation of the Hopkinson method. In defining the shock waves in air, Cooper and Kurowski (1996) suggested the following relationship (Equation 4-3) as an approximate approach to compute the equivalent TNT weight

$$W_{TNT_equivalent} = W_{explosive} \cdot \frac{\left(\frac{P_{CJ}}{\rho_o} \right)_{explosive}}{\left(\frac{P_{CJ}}{\rho_o} \right)_{TNT}} \quad (4-3)$$

There are limitations associated to the various air-blast scaling approaches. Some of the more common limitations include the following assumptions:

1. A constant atmospheric pressure is applied at a specific elevation (i.e. sea level). The higher the elevation, the smaller the over-pressure generated by the air-blast.

2. Rate-dependent effects are typically ignored.
3. Ideal explosive characteristics are assumed.
4. Baseline or reference TNT is at a specific density. It should be noted that variations of TNT's (or other explosives') densities can significantly alter the corresponding detonation properties.
5. Blasts occur in perfect light-density, air-filled atmospheric conditions with no solid, fluid, or gaseous obstacles in between the blast source and the observation point.

Air-blast theory is adequate for generating input blast-induced over-pressure for an object at some distance from the blast-source, with nothing but air in between them. Typically, applications include blast-effects on structures, roadside blast effects on vehicles etc. The air-blast approach is inappropriate for direct applications of explosives embedded in totally saturated soils, where water and solid soil particles are the predominant materials, without adjustments to the approach to account for soil and water. These adjustments are required because both water and solid soil particles can transmit shock waves at significantly greater rates with greater shock impedance and less compressibility than air. Denny (1993) provides additional insights of the important properties and characteristics of air and water.

4.7.4 Submerged Blast Pressure Representation and Limitations

Since the air-blast approach is inappropriate for direct application of embedded blasts in totally saturated soils, one potential alternative is to apply a submerged (i.e. underwater) blast representation to generate pressure for the blast-induced liquefaction event. The Navy's Handbook on Explosion Effects and Properties, Part II, edited by

Swisdak, M. M. (1978) provides an extensive procedure and detailed discussion in defining underwater-blast theories and approaches used by the Department of Defense (DOD). The main approach discussed in Swisdak (1978) also accounts for effects of water depth, bubble formation, sea-floor reflections, etc., many of which are not directly applicable to embedded blasts in fully saturated soils.

Cooper and Kurowski (1996) applied the following empirical equation presented by R. H. Cole in 1948 to estimate peak shock pressure at any “underwater” distance from a submerged blast source.

$$P = K \cdot \left(\frac{W^{\frac{1}{3}}}{R - R_o} \right)^{\alpha} \quad (4-4)$$

In Equation 4-4, P is the peak shock pressure with units of psi; W is the explosive weight with units of pounds; R_o is the radius of a spherical charge with units of inches; α is an explosive constant with a value typically between 1.12 to 1.16 for different explosives; and K is an explosive constant which has a limited availability in “open” literatures. However, Cooper and Kurowski (1996) suggested that the value of K maybe estimated from the heat of explosion (ΔH_{exp}^o) expressed in units of kilo-calorie/gram for most explosives as shown in Equation 4-5.

$$K = 1.5 \times 10^5 \cdot (1 + \Delta H_{\text{exp}}^o) \quad (4-5)$$

Figure 4-4 shows a comparison of the peak submerged over-pressures induced by detonating a 1.0-lb, 2.5-lb, and 3.0-lb spherical Pentolite 50/50 explosives as a function of distance from the respective charge using Equations 4-4 and 4-5. Since the distance between any explosive charge and the corresponding blast-hole edge in the May 2005 Vancouver liquefaction test is less than 1 ft, Figure 4-4 shows that the minimum peak over-pressure is at least one million pounds per square inch (psi). Millions of psi peak over-pressure at a short distance from an explosive charge is a commonly observed magnitude.

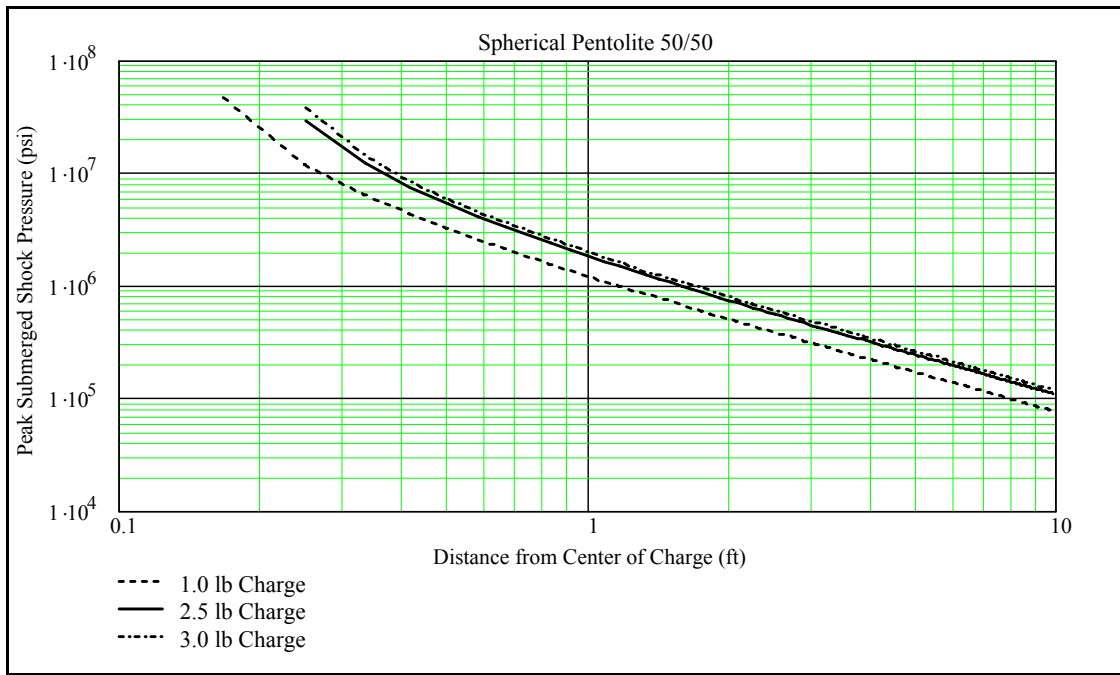


Figure 4-4 Peak Over-Pressure Induced by Spherical Pentolite 50/50 Charges

However, one should note that a blast-induced over-pressure such as those shown in Figure 4-4 is a transient, highly impulsive underwater load that lasts only a very small fraction of a second. Therefore, one must not treat the peak pressure as quasi-static

pressure environment, which at the pressure magnitudes shown in Figure 4-4 will certainly induce damage at several orders of magnitudes greater than would be expected and observed in an actual blast.

When dealing with saturated soils where soil particles and water co-exist with one another, significant damping accompanied by rises and drops of shock impedances with noticeable amount of energy loss can be expected. As such, one must account for the soil/water mixture induced damping effects while ignoring certain effects documented in the Navy Explosive Handbook such as bubbling and sea-floor reflections that are not expected to occur in saturated soils.

4.7.5 Blast-Material Representation and Limitations

One of the many capabilities of explicit analysis software available today is the ability to model directly the detonation process of explosive materials using empirically derived detonation properties, mechanical constitutive relationships, and equations of state. Section 3.3 presented an overview of shock wave propagations, which require the solutions of five unknown from five independent equations. These equations are derived from the conservation of mass, energy, and momentum, the Hugoniot that relates shock velocity or pressure to particle velocity or specific volume of the material, and the equations of state (EOS) for the explosive materials of interest. The user is responsible to define the proper inputs for the development and solution of the five equations in order to model the detonation process successfully. Kerley (2001) and his former colleagues at Sandia National Laboratory have developed an extensive set of EOS for various hydrodynamic applications.

Depending on the model selected by the user, inputs to the analysis representing the explosive materials typically include mechanical, hydrodynamic, and detonation properties such as density, detonation velocity, CJ pressure, bulk modulus, shear modulus. Additionally, the user must also enter the EOS to define the pressure-volume relationship of the explosive material(s) at hand. The trickiest aspect of the input definition process is the choice of EOS.

One of the most widely used EOS for modeling explosive materials is by Jones, Wilkins, and Lee known as the JWL EOS (Walters and Held, 2003). There is a variant version of the JWL EOS known as the JWLB EOS that was enhanced by E. Baker of the US Army Research Laboratory (Walters and Held, 2003). Equation 4-6 provides the basic form of the JWL EOS, which defines pressure (P) as a function of internal energy per initial volume (E) and the current relative volume (V).

$$P = A \cdot \left(1 - \frac{\omega}{R_1 \cdot V}\right) \cdot e^{-R_1 \cdot V} + B \cdot \left(1 - \frac{\omega}{R_2 \cdot V}\right) \cdot e^{-R_2 \cdot V} + \frac{\omega \cdot E}{V} \quad (4-6)$$

In Equation 4-6, the variables A , B , R_1 , R_2 and ω are input parameters for specific explosives known as the JWL coefficients. JWL coefficients for many explosives can be obtained from textbooks, published papers, and documents from government agencies and national laboratories such as the LLNL Explosives Handbook (Dobratz and Crawford, 1985).

Coefficients in the JWL EOS are derived from cylinder tests, which can be a deterrent for the acceptance in applying the JWL EOS for detonation analyses. Depending on the organizations and/or national laboratories involved, some researchers

may prefer other EOS formulations such as BKW EOS proposed by Becker, Kistiakowsky, and Wilson (Mader, 1998). Given that EOS for other formulations are not as widely available as JWL in both commercial and many government developed hydrocodes, along with the greater availability of the corresponding JWL coefficients, JWL has been used extensively to successfully model detonations for numerous DOD and DOE applications. Therefore, the JWL approach has been chosen as the baseline EOS for describing the pressure-volume relationship of the explosive used for this research.

5 Hardware Considerations

High fidelity simulations are very computationally intensive. Development of software technology including material models and modeling drivers must be concurrent with the development of hardware technology in order to produce a feasible and a successful simulation within both time and cost constraints. The previous section of this dissertation described the latest software technology required and used to simulate blast-induced liquefaction. This section presents a discussion of the choice of operating systems associated with the hardware; hardware configurations required and available for this dissertation research; and a summary of performance comparisons and limitations among the different systems.

5.1 Operating Systems

Most of the commercial numerical modeling software systems are available on multiple operation systems including Microsoft Windows XP, Linux, and UNIX. Computational speed and efficiency issues are among the major considerations for determining which operating system is more appropriate for the application at hand.

In early 2002, while performing research in the aerospace and defense industry, the author of this dissertation evaluated LS-DYNA Version 960's performance with several LS-DYNA jobs on two identical Intel Pentium IV machines manufactured by Dell, Inc. The first machine was running under Microsoft Windows XP (Professional

version) operating system, and the other with Red Hat Linux 9.0. The machine with the Linux operating system outperformed the XP system by 25% to 30% in terms of computation time. Two of the long duration runs on the XP systems encountered system crashes that required reboot and restart of the respective jobs after approximately 24 hours of clock time. Every one of the Linux jobs ran to completion without problems. Differences in results between the two machines were well within expected computational errors.

Based on experience with greater computational efficiency and operational reliability for long duration jobs, the author chose the Linux operating system over Windows XP for longer duration computations performed for this research. However, due to the availability of software under Microsoft Windows, post-processing of the results was conducted remotely on a Windows-based machine as described below.

5.2 AMD-Athlon Windows-Based Desktop Computer

A Hewlett-Packard AMD-Athlon 2800 (~2.1 GHz) Windows XP-based machine with one giga-bytes (GB) of PC2700 double-data-rate (DDR) random access memory (RAM) was used to prepare this dissertation and process analysis results. This AMD-Athlon box also served as the central hub for submitting and monitoring analyses performed remotely on the Linux and UNIX computer clusters on BYU campus. A 128-MB NVIDIA GeForce FX-5200 graphics accelerator with a Hitachi 160-GB (7200 rpm) EIDE hard-drive were installed on the AMD Athlon box for graphical processing and mass data storage and manipulations.

For compatibility and ease of communications with BYU's UNIX and Linux clusters, the Cygwin Linux emulator by GNU (Free Software Foundation) was installed

to post-process LS-DYNA analysis results in a Linux-like environment. Additionally, secured copy (scp) file transfer software and secured shell (ssh) terminal emulation software as recommended by BYU's IT department were installed for two-way communications with the analysis computer clusters on BYU campus.

Results from each LS-DYNA run was "tarred" (grouped) and "gzipped" (compressed) on the respective Linux or Unix system, then "scp" to the AMD Athlon box for post-processing and preparation for insertion into this dissertation. Post-processing of LS-DYNA analysis results were conducted using LS-PREPOST by LSTC, publisher of LS-DYNA. Throughout the research, the NVidia graphics card provided excellent graphical performance at a resolution of 1280 pixels by 1024 pixels on a 17" monitor. Significant advancements of computer technology within the past few years have made it possible to process giga-bytes of data and to complete this dissertation within a reasonable amount of time.

5.3 Intel Pentium IV Linux-Based Desktop Computer

Technology on desktop computers has evolved exponentially in recent years. A common desktop computer produced within the past two years can rival the speed of "supercomputer" used for intensive computations within the past two decades. Most desktop computers today have "clock speed" running in the neighborhood of high two to mid three giga-hertz (GHz). As such, many of today's numerical simulations can be performed effectively and efficiently on a desktop computer.

The most important aspects of a desktop computer for computationally intensive simulations are CPU speed, amount of memory available, memory's access speed, amount of disk space, and disk access speed. Graphical performance and throughput are

important mainly for the pre- and post-processing portions of an analysis. The bottleneck of a large analysis is often controlled by the input to and output from (i.e. I/O) the hard disk drive in the form of “virtual memory.” As such, configuring sufficient in-core memory is extremely important in minimizing, if not eliminating, the need for “virtual memory” during computations. Experience has shown that most carefully planned explicit finite element analyses with up to 250,000 elements have acceptable performance with only 1GB of internal memory.

Due to budgetary constraints, a Linux-based desktop computer manufactured by Dell, Inc. with a minimum configuration was used for a majority of the preliminary analyses performed for this research. The CPU box consisted of an Intel Pentium IV processor running at 3.2 GHz; 1-GB of internal memory with a 400 MHz front-side bus speed; an 80-GB Enhanced IDE hard disk drive; and a 128-MB ATI Radeon graphical processing card for pre- and post-processing. The CPU’s hyper-threading capability was turned off to maximize individual analysis throughput. Hyper-threading capability consists of logic to split the CPU internally for X number of processes, with each process utilizing approximately 1/X amount of CPU resources simultaneously. By turning off the hyper-threading capabilities of the CPU, one effectively converts the computer into a dedicated single-process device that runs at maximum performance for a single long-duration task.

5.4 Hewlett-Packard Unix-Based Workstation Cluster

During the earlier stage of the research, several performance evaluation-based analysis jobs were conducted remotely on BYU’s Hewlett-Packard (HP) Unix-based workstation-cluster using CITRIX and SSH terminal emulation software systems. An

analysis-performance evaluation between the HP workstations and the “Linux box” described in the previous section was conducted in the early stage of the research. Several identical test runs were submitted concurrently on the “Linux box” described in the previous section as well as the HP workstations. The minimally configured “Linux box” outperformed the HP workstations by a factor between 2.5 and 4.0. This is largely due to the Linux box’s newer and higher performance microprocessor that was dedicated for a single analysis run. Additionally, HP workstations also have greater overhead in order to serve multiple users from multiple disciplines. As a result, the author decided to use the HP workstations as “test-beds” for parameter sensitivity runs made in preparation for long duration analyses.

The HP workstations were perfect choices for using ANSYS’ Prep7 pre-processor to generate the 3-D finite element models due to easy accessibility, availability, and ease of usage. All models used in the research were generated by ANSYS on the HP workstations. Each ANSYS model was transferred to the AMD-Athlon Windows-based machine for translation into LS-DYNA models.

5.5 SGI R-16000 UNIX Clusters

BYU has three Silicon Graphics Inc. (SGI) 64-bit RISC-architecture UNIX based clusters known as Marylou, Marylou1, and Marylou2 for analyses. Marylou is a SGI Origin 3900 cluster with 128 MIPS R16000 processors running at 700 mega-hertz (MHz). Marylou1 is a SGI Origin 350 cluster with 15 MIPS R16000 processors running at 800 MHz. Marylou2 is a SGI Origin 3800 cluster with 32 MIPS R12000 processors running at 400 MHz and 32 MIPS R14000 processors running at 600 MHz. The SGI clusters were configured to run LS-DYNA and other high performance commercial and

personal applications. Unfortunately, the author was unable to get the baseline soil-material model running successfully among the SGI clusters during initial tests and evaluations. As a result, the SGI clusters were utilized only for evaluating stability of LS-DYNA without the baseline soil materials.

5.6 MarylouX Linux-Based Cluster by IBM

The MarylouX cluster at BYU consists of an IBM 1350 Linux cluster with 256 Pentium 32-bit Xeon processors running at 2.4 giga-hertz (GHz). Due to some undetermined difficulties in getting hydro-codes such as LS-DYNA running successfully on MarylouX, analysis for this dissertation were performed on BYU's other computer clusters.

5.7 Intel Xeon 64-Bit Linux-Based Super Cluster

A new 630 dual-processing node (1260 CPU's) Intel EM64T Xeon Linux-based super-computing cluster manufactured by Dell, Inc. known as Marylou4 was installed during the summer of 2005, just in time for the long duration runs required for this dissertation research. After conducting several performance analysis runs, it was determined that a single-processor job on Marylou4 ran approximately twice as fast as the Intel Pentium IV based Linux box as described in Section 5.3, which makes it the fastest computer-cluster available on the BYU campus.

An extensive parameter sensitivity study was performed on Marylou4 with the new soil material model to determine the proper input parameters. The study was aimed toward minimizing the material model's instability, and improving the corresponding convergence rate. Details from the sensitivity study will be discussed in Chapter 7.

To determine the parallel-processing efficiency of the baseline soil material model in LS-DYNA, several identical test runs were conducted on Marylou4 using 1, 2 and 10 CPU's. Table 5-1 shows a summary of the parallel-processing performance of the baseline soil-material model obtained from test runs conducted on the Marylou4 Dell/Linux supercomputing cluster.

Table 5-1 Baseline Model Parallel-Processing Performance Summary

Number of CPU's	Number of Analysis Cycles	Normalized Run Time Metrics
1	55460	1.000
2	55460	0.878
10	55460	0.785

Table 5-1 shows that the analysis using 10 CPU's on the Dell Linux cluster only runs approximately 21% and 11% faster than identical runs utilizing only 1 CPU and 2 CPU's, respectively, which is disappointing. There are several "potential" reasons why the performance of multiple-cpu runs are not "up-to-par" as expected based on greater number of processors, including:

1. Although LS-DYNA itself has been "parallelized" for multi-processor runs, the baseline soil-material model itself is unlikely to have been parallelized since it has only been incorporated into LS-DYNA in recent months. The "serialization" effects become more prominent when multiple "non-parallelized" iterations within the soil model are required for large deformation / plasticity convergence and stability purposes. Parallelization requires extensive and additional coding to divide-up computation tasks for

multiple-processors. Unless the material model developer is keen on parallelizations, most new material models are not likely to be optimized for multi-processor runs.

2. The task scheduler for the newly installed Marylou4 Dell / Linux cluster may not be optimized or “fine tuned” for commercial multi-processor runs.
3. Task load assignment and memory / disk access wait-time among the various processing nodes may not be evenly distributed such that processors that can complete their tasks quickly have to wait until the rest of the processors have completed their respective tasks.
4. Network communication speed may potentially be a source of bottleneck in parallel computing.

One must realize that the multi-processor run performance evaluated above is for a 3-D LS-DYNA analysis of a blast-induced liquefaction event utilizing the new soil material model available in LS-DYNA. It may not be applicable to other analyses using other material models and / or solvers. Analyses using other material models may perform differently depending on how much the material model itself has been optimized for multi-processor runs, and how much “fine-tuning” has been performed on the corresponding computer cluster.

5.8 Hardware Performance and Limitation Summary

In summary, a performance comparison of various machines available at BYU for a 3-D LS-DYNA analysis for the simulation of a blast-induced liquefaction event is listed below in order of computation speeds:

1. Marylou4 – Dell / Linux cluster as described in Section 5.7.

2. Dell Pentium IV single processor Linux box as described in Section 5.3.
3. HP UNIX-based Desktop computers as described in Section 5.4.
4. SGI Origin computer cluster as described in Section 5.5.
5. IBM / Linux cluster as described in Section 5.6.

Table 5-2 summarizes the single-processor speed performance of each computer used for an identical 3-D blast-induced liquefaction analysis.

Table 5-2 Baseline Model Computer Performance Comparison Summary

Computer Platform	Normalized Speed Metrics
Marylou4 Linux Cluster	1
Dell Pentium IV Linux Box	0.5
HP Workstations	0.1 – 0.2

It should be noted that the above performance summary are specific to the tasks described in this dissertation. Actual performance for other applications may vary in accordance with the optimizations and other conditions assumed and applied to the specific analytical procedures involved.

6 Model Geometry and Constraints

6.1 Overview

The first of several steps in a successful high fidelity numerical modeling analysis deals with the analyst's ability to accurately define the baseline model's geometry and the corresponding boundary constraints. Proper geometric definitions of a model typically help minimize computation errors as well as run time. Appropriate boundary constraints help secure accurate results from the analysis of interest. This chapter provides detailed descriptions of the assumptions, approaches, and limitations of the geometry and boundary constraints applicable to the baseline blast-induced liquefaction model.

6.2 Geometry Dimensionality

The baseline event to be simulated is a 3-D, tri-level sequential and non-symmetrical blasting event conducted in May, 2005 at the south end of the Massey Tunnel along the Fraser Rive Delta region of Vancouver B.C. The most appropriate analysis method for simulating an event consisting of a series of highly impulsive controlled-blasts is the explicit time-march approach as discussed in Chapter 4 of this dissertation.

Commercial 3-D explicit analysis tools available at BYU include LS-DYNA, ABAQUS-Explicit, and CTH. Since CTH is an export-controlled software tool published

by DOE's Sandia National Laboratories, it is not readily available for simulating events that potentially have international implications without having to obtain special permissions and authorizations for exportation from DOE. Both LS-DYNA and ABAQUS have 3-D implicit, as well as explicit, capabilities. However, LS-DYNA is currently the only commercial software available in the industry with a full spectrum of explicit methods including LaGrangian, Eulerian, ALE, coupled Eulerian / LaGrangian fluid-structure, SPH and meshless analysis capabilities. Therefore, LS-DYNA has been selected as the baseline solver for the modeling of the blast-induced liquefaction event.

The baseline analysis consisted of a 3-D LS-DYNA analysis model. Each explosive charge was modeled as an embedded explosive utilizing JWL EOS and high explosive (HE) modeling techniques commonly used for aerospace and defense applications. Multiple layers of soil materials found in the Massey Tunnel site as described in previous soil investigations (i.e. the Canadian Liquefaction Experiments, or CANLEX, project) are modeled in the baseline analysis. Chapter 0 includes a comprehensive listing of published references available for the CANLEX project.

Figure 6-1 illustrates a transparent representation of the blast-induced liquefaction model used for analyses conducted for this dissertation research effort. The model is shown from the south-southeast perspective looking toward the northwest direction of the test site. Each of the blasting-holes has its location, with respect to the center of the blast-circle, marked above it. For the baseline event, charges were not installed in the NE blasting-hole due to its use for a prior evaluation blast. The origin of the baseline model is located in the top surface at the center of the blasting-circle with x-axis points to the north, y-axis points to the west, and z-axis points upward. Other similar models were

also developed for comparison and evaluation purposes during the course of the research, most of which will be presented in the respective sections of this dissertation.

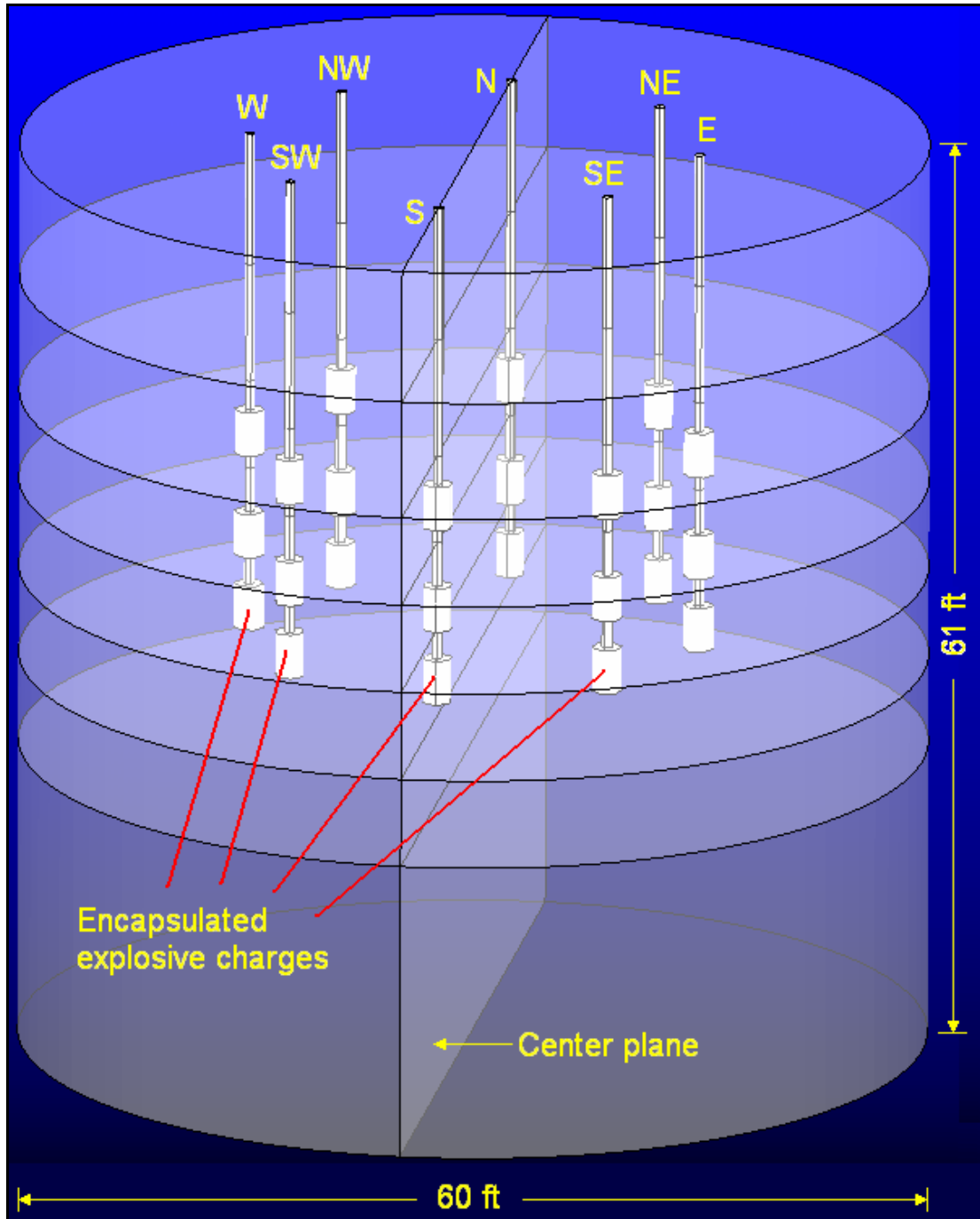


Figure 6-1 Baseline 3-D Blast-Induced Liquefaction Analysis Model

6.3 Mesh Considerations

6.3.1 Overview

Explicit analyses with short duration, high magnitude impulsive loads are sensitive to mesh degeneracy, high (or low) element aspect ratio, and sudden changes of adjacent element sizes. A discussion of each of these issues applicable to the baseline model is presented in the following subsections.

6.3.2 Element Degeneracy

Element degeneracy occurs when two or more nodes of a finite element are merged into a single node, causing a reduction in the number of normal element edges. The finite distance between two nodes involved in a merge or an element-degeneration becomes zero, resulting in the time required to travel between the merged nodes to an infinitesimal amount. When the time step approaches zero, it causes the overall analysis run time to increase accordingly. Therefore, element degeneracy is a serious issue in explicit analyses since it significantly impacts the overall analysis run time by as much as orders of magnitude in many cases. These problems can turn a perfectly feasible analysis into an infeasible analysis simply by pushing the time constraint typically associated with a project to or beyond its limit.

Careful planning has been incorporated into the development of the baseline blast-induced liquefaction analysis model so that no element degeneracy is allowed nor observed during the model design and construction process. Every element in the baseline model is a 3-D solid hexahedral, or brick, element with a minimum edge length requirement incorporated into the meshing process. By establishing a minimum element

edge requirement during the meshing process and carefully overseeing the entire meshing process, one can be confident of generating a model without element degeneracy. Figure 6-2 shows the latest version of the finite element mesh used for the baseline 3-D tri-level sequential blast-induced liquefaction model. Figure 6-3 shows the corresponding enlarged cross-section and top view of the baseline model for clarification purposes.

6.3.3 Element Aspect Ratio

Section 4.3 provided a general overview of the effects of excessive element aspect ratio. Avoidance of excessive element aspect ratio is much simpler in theory than in practice, especially for analyses that are constrained by time, cost, and model size. For the baseline blast-induced liquefaction model, the mesh has been generated with a predefined constraint of no more than a 4 to 1 (or 1 to 4) element aspect ratio.

The worst aspect ratio occurs at each explosive column where the vertical height to horizontal width ratio is close to the self-imposed aspect ratio limit. This is done intentionally to accommodate the dominant horizontal expansions of the explosive elements during the detonation process. Since the explosive materials are vertical cylinders, as soon as detonations are initiated, explosive elements undergo significant horizontal and some vertical expansion, thereby reducing the vertical to horizontal element aspect ratios rapidly. If the original or starting explosive element aspect ratio is closer to 1.0, the rapid horizontal expansions during detonation are likely to push the deformed elements' aspect ratios outside the desirable range upon detonation. This is a good example where adequate planning must be employed to account for effects at both before and after loading events have taken place.

The major technique used to generate the model while attempting to satisfy all “good-mesh” modeling constraints was to subdivide the 3-D model into modules for individually controlled meshes, followed by assembling the modules into a final 3-D model. Multiple iterations were conducted before reaching a final mesh configuration acceptable for the baseline blast-induced liquefaction analysis. This procedure resulted in the mesh shown in Figure 6-2 and Figure 6-3. It should be noted that Figure 6-2 and Figure 6-3 are screen snap-shots of the baseline model’s respective graphical display. As such, each of the views as shown has slightly different scales, in addition to errors induced by screen display’s pixel round off. It is not recommended for dimension scaling across different views. However, dimensions shown in the figures do provide some perspectives for the size of the model in the respective view.

6.3.4 Abrupt Changes in Adjacent Element Sizes

It is generally not a good practice to have significant size differences among adjacent elements. This is especially true in the explicit Eulerian method where averaging and advection in regions with abrupt changes in element sizes may artificially induce excessive numerical error. Although such issues do not have as great of an impact in LaGrangian analyses, it is still advisable to avoid abrupt element size differences among adjacent elements in order to minimize potential errors during shock-wave propagation and transmission.

As with element aspect ratio, the baseline model was produced with a restriction of no more than a 4 to 1 (or 1 to 4) ratio of adjacent element sizes everywhere in the model except for explosive elements and their immediate neighbors.

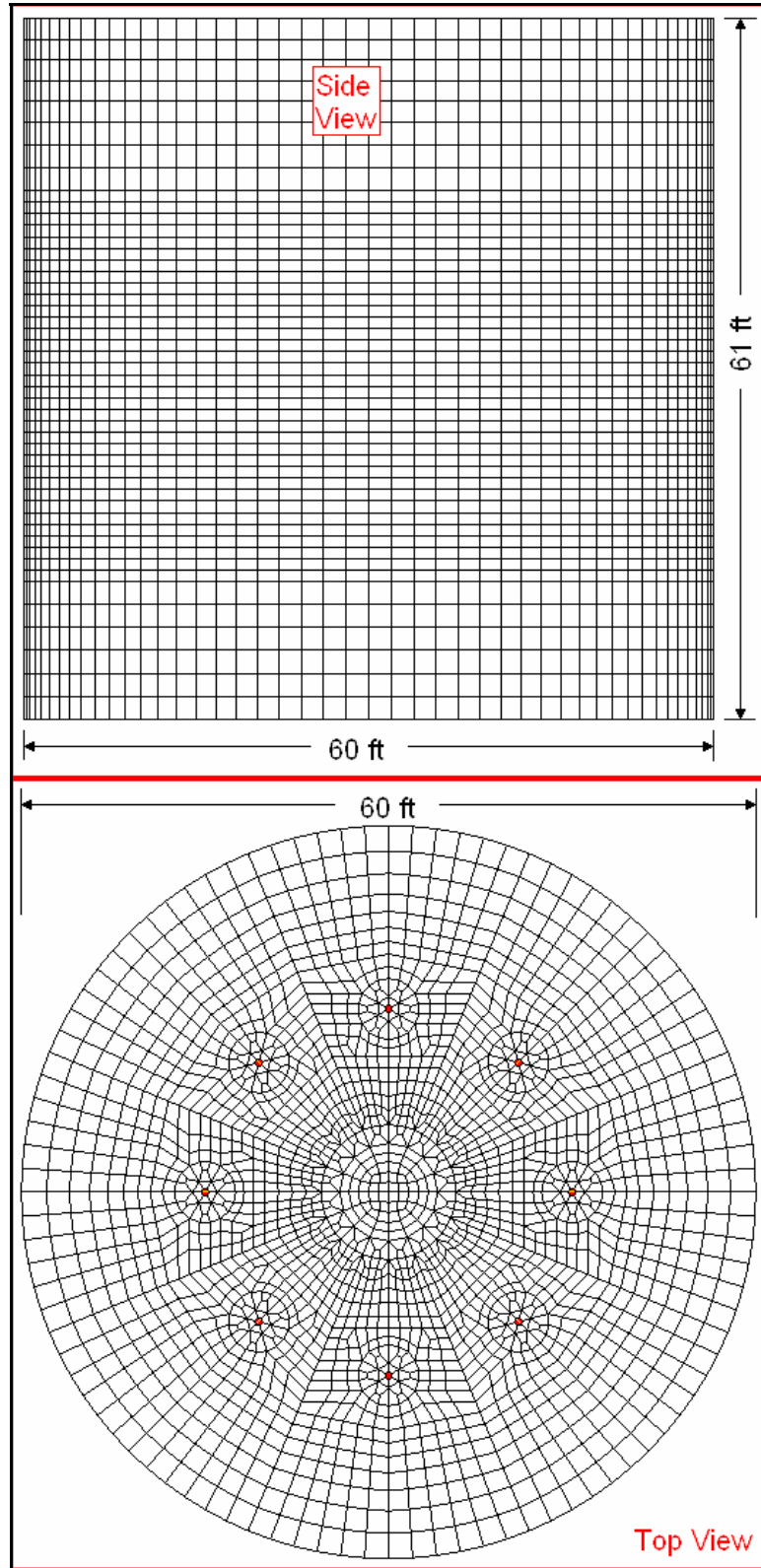


Figure 6-2 Baseline Blast-Induced Liquefaction FEA Model Mesh

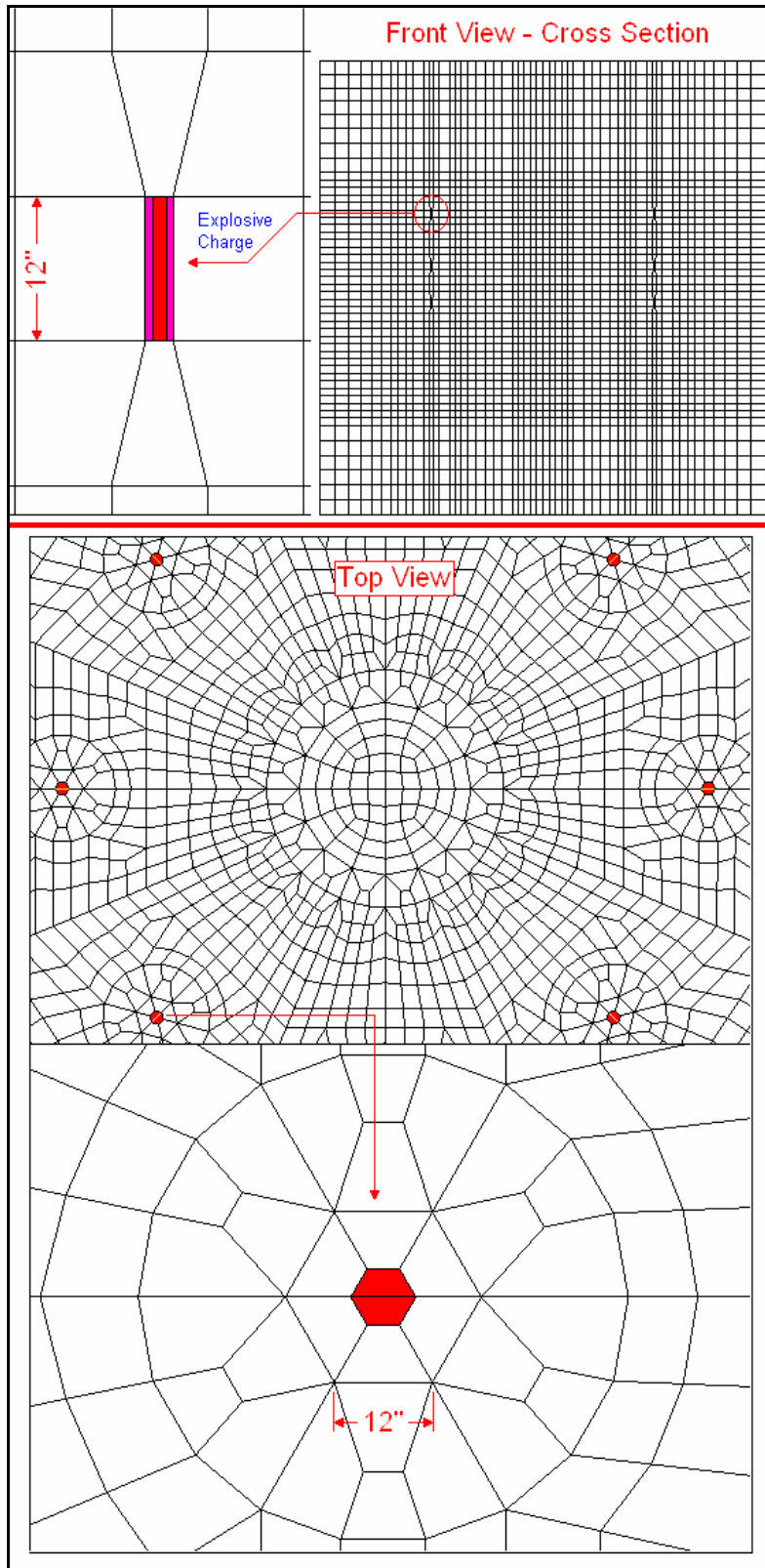


Figure 6-3 Enlargement of Baseline Model Cross Section and Plan Views

An aspect ratio smaller than 4 to 1 is more desirable for most analyses; however, due to limitations imposed on the model size by the pre-processing software, it is simply not feasible to obtain better than a 4 to 1 ratio while producing sufficient details around the “small” explosive charges that are embedded in the analysis model.

Prior to detonation, the original or starting explosive element widths are much smaller than the adjacent element widths to accommodate the horizontal expansion experienced by the explosive elements during detonations as described in Section 6.3.3. Similar to aspect ratio issues, should the elements adjacent to explosives have widths similar to those of the explosive elements, they would be distorted into unacceptable shapes during detonations, resulting in erroneous results and greater potential for hourglass-induced crashes.

6.3.5 Mesh Sizes

The baseline tri-level sequential blast-induced liquefaction model shown in Figure 6-2 has a diameter of 60 feet and a height of 61 feet. With the radius of each explosive element less than 4 inches, it is technically challenging to construct a reasonably sized 3-D model that also satisfies the non-degeneracy, good element aspect ratio, and gradual element size change requirements. The baseline model shown in Figure 6-2 consists of element edge widths between about 4 inches wide to approximately 2 feet, with a gradual transition of adjacent element sizes except at explosive column regions as described in Section 6.3.3.

6.4 Mesh Generation Utilities

Although LS-DYNA has a powerful post-processor for digesting analysis results, it lacks a good pre-processor for constructing analysis models. During the early stage of the research, with help from Dr. K. Merkley of ElemTech, an attempt was made to apply Sandia's CUBIT hexahedron mesh generator under ElemTech's Beta version graphical user interface (GUI) to mesh the baseline model. The effort was short lived due to the following reasons:

1. Output from CUBIT was not available for LS-DYNA at the time without having to develop a custom translator for converting CUBIT's Exodus or neutral format output to LS-DYNA.
2. During the course of testing the software's GUI by constructing a replica of the actual 3-D model, the software crashed or "locked up" eight times in the course of a one-hour period. To be fair to the GUI developers, the version of CUBIT's GUI was one of the first, if not the first, beta-test release of the software that has not yet been rigorously tested.

Without a stable pre-processor, the modeling effort's progress was halted temporarily until it was discovered that ANSYS, a commercial implicit FEA code with a pre-processor called PREP7, was available for research usage through BYU's Fulton Supercomputing Laboratory. Further investigation revealed that an academic version of ANSYS was installed on the HP UNIX desktop cluster with a model size limitation of 125,000 nodes. Furthermore, ANSYS has a translator that can be used to translate ANSYS model data into LS-DYNA input format.

After initial validation and model generation tests of the ANSYS software on the HP system, ANSYS' PREP7 finite element pre-processor was selected to perform the baseline blast-induced liquefaction analysis' model generation process. Since the model size limitation was discovered early in the model development phase, special attention was given to ensure that the baseline model would remain within ANSYS' restriction. Because of the precautionary measures, the original baseline model consisted of 120,089 nodes with 114,560 hexahedral (brick) elements, which is approximately 96% of the model size limit imposed by the academic version of ANSYS available at BYU. During the research process, the original baseline model was enhanced and improved for process run time and minimization of numerical instabilities observed in the original baseline model. Refinements made to the original baseline model not only improved the run time by nearly an order of magnitude (i.e. from ~42 days down to ~5 days), it also improved the corresponding volume coverage, numerical stability, and element uniformity while reducing the overall model size. Chapter 10 of this dissertation provides a detailed description of the enhancements and improvements made to the original baseline model. The final baseline model consists of 103,537 nodes with 99,072 hexahedral elements.

An advanced script language in PREP7 known as the "ANSYS Parametric Design Language" (APDL) was applied to construct the baseline model parametrically. Appendix A provides an overview of the APDL capabilities in ANSYS' PREP7 pre-processor, as well as an overview of the evolutionary process used to develop the baseline model.

6.5 Boundary Conditions

6.5.1 Overview

Boundary conditions are essential components for a successful analysis. Each analysis is uniquely defined for the evaluation of a specific geometry subjected to a specific set of loading and boundary environments. As such, boundary conditions are problem and model dependent. The baseline model represents a large mass of soil encompassing a circular blasting-region and the corresponding instrumentations. Two regions within the baseline soil model as shown in Figure 6-1 and Figure 6-2 may potentially require the definitions of boundary conditions: The exterior surfaces (top, circular side, and bottom), and interior “radial-axial” oriented planes at mid-way between adjacent explosives due to symmetry. The following sections document the rationale behind the definitions of boundary conditions used in the baseline model.

6.5.2 Symmetry

From the geometry standpoint, the baseline model as shown in Figure 6-1 and Figure 6-2 is not axisymmetric due to “discrete” blast locations at 45° intervals around the circumference of the blast circle. However, it is symmetrical every 22.5° around the circumferential (or X-Y) direction. As a result, a 22.5° pie-shape wedge model is typically sufficient for a simultaneous blast environment.

Figure 6-4 shows the blast-pattern (solid circular dots) and blast-sequence (number adjacent to each solid circular dot) of the baseline liquefaction test conducted in May 2005 at the Fraser River Delta region just south of the Massey Tunnel. Since no explosive was placed at the north-east blasting hole (between hole #1 and hole #4), a non-

symmetrical loading environment was created. Along with a tri-level sequential blasting pattern as shown in Figure 6-4, a full 3-D non-symmetrical analysis is necessary to represent the actual blasting event in a realistic manner. Therefore, a circular or pie segment symmetrical model with symmetry boundary conditions cannot be used in the baseline model analysis.

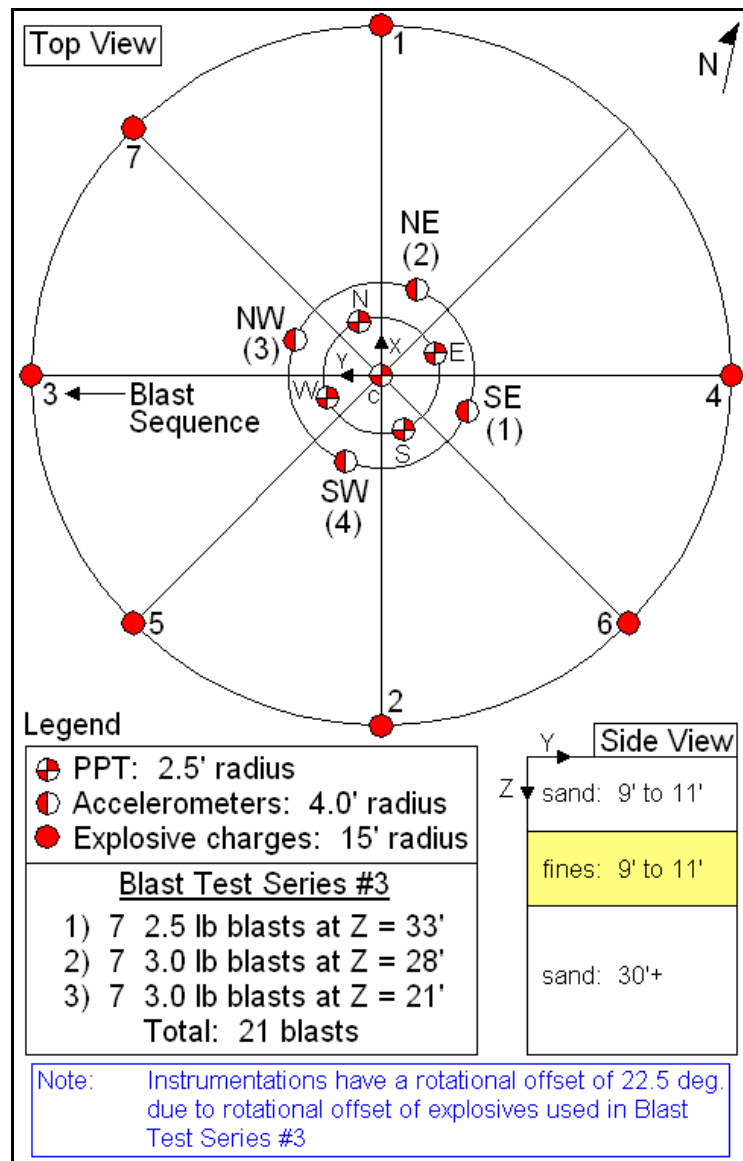


Figure 6-4 Test Instrumentation Layout and Blast-Sequence

6.5.3 Infinite or Non-reflecting Boundary Constraints

Exterior surfaces of the baseline model shown in Figure 6-1 and Figure 6-2 are direct interfaces to the “outside world” with respect to the model. Therefore, one must consider the boundary conditions along those surfaces in order to simulate the actual environments encountered in the field. Prior to defining the proper boundary conditions along these exterior surfaces, the concept of shock impedance is a prerequisite to help explain the rationale behind the boundary conditions to be defined.

Shock impedance Z is defined as the product of material density ρ_o and shock velocity U as shown in Equation 6-1. For a given shock velocity, the greater the material density, the greater the corresponding shock impedance.

$$Z = \rho_o \cdot U \quad (6-1)$$

When a propagating shock front encounters an interface (i.e. exterior surfaces of the baseline model), its characteristics change in accordance with the impedance differences it encounters at the interface. An accepted method in classifying the impedance differences between the “shock-origination” (or “incident”) material and the “new material” along the interface is based on shock impedance ratio as shown in Equation 6-2. Shock impedance ratio r_z is defined as the impedance of the “new” material Z_2 divided by the impedance of the “incident” material Z_1 .

$$r_z = \frac{Z_2}{Z_1} \quad (6-2)$$

When a shock travels across an interface from a high impedance (or high density) material into a low impedance (or low density) material, the corresponding impedance ratio is less than one. An extreme case where the impedance ratio is approximately zero occurs when a shock crosses from a high impedance material into free space, or air. In such a case, twice the displacement with zero stress is transmitted across the interface where air has effectively zero stiffness or stress resistance against the incoming shock.

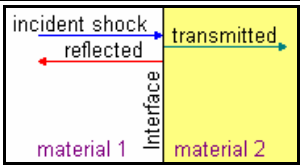
When a shock travels across an interface from a low impedance (or low density) material into a high impedance (or high density) material, the corresponding impedance ratio is greater than one. An extreme case where the impedance ratio approaches infinity (∞) occurs when a shock encounters a rigid wall, or a symmetry boundary along the material interface. In such a case, twice the incident stress with zero displacement is transmitted across the interface.

An impedance ratio is equal to one when a shock travels through an interface between two materials with identical impedances, which are the same as if the shock is traveling through an infinite medium consisting of a single, homogeneous material. If the shock continues to propagate through an infinite medium, then 100% of its displacement and stress are transmitted, with nothing reflected back. In such a case, the shock will maintain its magnitude indefinitely in a perfectly incompressible, undamped medium with zero internal friction or resistance. However, realistic materials such as soils have frictional resistance, damping characteristics, and are always compressible to a certain degree. Therefore, attenuation of shock (i.e. energy loss) is expected with respect to distance from the source of shock as well as time. Table 6-1 summarizes the characteristics of a shock when it arrives at an interface. To achieve equilibrium at the

interface, the sum of incident and reflected shock values must equal to the corresponding transmitted value as explained previously.

Table 6-1 Characteristics of Shock at Interface between Two Materials

Impedance Ratio (r_z)	Displacement Amplitudes δ			Stress Amplitudes σ		
	Incident	Reflected	Transmitted	Incident	Reflected	Transmitted
0	δ	δ	2δ	σ	$-\sigma$	0
1	δ	0	δ	σ	0	σ
∞	δ	$-\delta$	0	σ	σ	2σ

	<p>References: Kramer, 1996 and Cooper, 1996</p>
---	--

With the shock impedance concept introduced, one can now discuss the proper boundary conditions to be applied to the baseline model. First, the top surface of the model represents the ground surface in the field. The ground surface in the field is exposed to ultra-light density and highly compressible air, which is effectively a “free” end condition. A shock wave entering the top surface from below will essentially transmit displacement but not stresses into the free end, or air. Therefore, the impedance ratio is expected to be nearly zero. In such a case, symmetry boundary conditions do not apply along this surface. In fact, no boundary condition is necessary along the top surface of the baseline model.

The circular or circumferential side and bottom surface of the model represent an “infinite” medium where shock waves continue to propagate without reflections of both stresses and displacements. Attenuation is expected with respect to the damping

characteristics of the soil materials. If the circular side and the bottom surface are treated as interfaces with free air, then full displacements along with stresses at full magnitudes in the opposite directions are reflected along these surfaces, which is not what one would expect to take place in an “infinite” medium. On the other hand, if symmetry conditions are applied, then full stresses along with full displacements with opposite directions are reflected via “rarefaction” waves, causing collisions against incoming waves, resulting in a localized rise in stresses and displacements along the plane normal to the direction of wave collision, which is a phenomenon known as “spalling”. This is not what one would expect to take place in a shock traveling along an “infinite” medium. Therefore, neither symmetry boundary nor free boundary conditions are appropriate along the circumferential side and bottom surface of the model.

The most appropriate boundary condition available that can be applied along the circular side and bottom surface of the baseline model is a special boundary condition known as “impedance matching.” Unlike traditional constraints where displacements and / or rotations are fixed, “impedance matching” does not rigidly restrain displacements. Instead, equations and conditions are defined internally within the solver to represent an infinite medium. In other words, the model’s material impedance along the interface is computed and applied as the impedance of the “virtual material” adjacent to the interface and outside the model where the shock waves are to be transmitted. In this manner, an infinite medium is simulated wherein zero stress and zero displacement are reflected, while full stress and displacement are transmitted into a “virtual” space. Unlike symmetry boundary conditions, the displacements one would expect to occur in an actual infinite-medium do develop along surfaces with “matching impedance” boundary

conditions. This phenomenon can be misleading or misunderstood since it may not be intuitively obvious, especially to analysts only familiar with quasi-static, implicit finite element analysis where the capability of “matching impedance” does not exist. One must examine the results via simple, verifiable models in order to comprehend this advanced boundary definition feature designed specifically for the evaluations of shock propagations within an infinite or semi-infinite (i.e. half-space) entity and environments..

The major limitation of “matching impedance” is that it does not apply to regions encountering excessive deformations and/or plasticity such as regions immediately adjacent to high explosive blasts. With that in mind, the circular side and bottom surfaces of the baseline model were extended to distances sufficiently far away from the immediate blast zones in order to avoid, or at least minimize, potential “impedance matching” errors.

6.5.4 Eulerian Fluid Leakage Prevention

During the early stages of this research, wedge models were developed to represent single blasts for generating blast pressures to be applied to the full 3-D soil model. It was during this early stage of the research that a phenomenon known as Eulerian fluid leakage was observed along the center axis of the wedge or pie-shape models as shown in Figure 6-5.

While the cause of the leakage is simple, explainable, and easy to repair, the effect of the leakage is enormous. In LS-DYNA, angled symmetry boundary conditions are defined by vectors. Each of the X, Y, and Z direction is an orthogonal component of the vector. Symmetry boundary conditions along a surface are obtained by mapping a linear relationship among X, Y, and Z components to allow sliding while exercising

normal constraints along a specific slanted plane where the boundary conditions are to be applied. Therefore, in the global Cartesian coordinate system, slanted symmetry is nothing more than tying the horizontal displacements to the vertical and out-of-plane displacements via a linear relationship. This works fine except at the center axis where two edge planes of the wedge model intersect. At this location, slight computation errors can sometimes induce unbalanced constraint transformations, resulting in slight motions (or “leakage” in Eulerian terms) to be initiated along the center axis. In a time march solution approach, these minor errors may allow velocity vectors to develop and magnify with respect to time, eventually causing a major loss of the internal forces and energy, resulting in a phenomenon known as “leakage”.

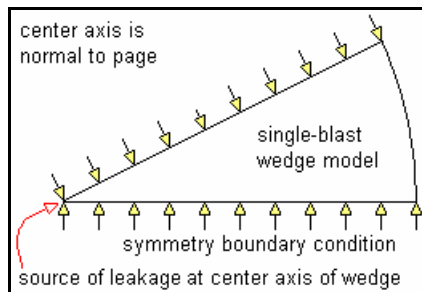


Figure 6-5 Potential Eulerian Fluid Leakage Location in Wedge Models

To eliminate the leakage problem, one can simply apply full horizontal and vertical constraints along the center axis of a wedge model. By so doing, all planar displacements are set to zero without the potential of computation errors induced by transformations. Since the full 3-D baseline model does not contain symmetry constraints along the center axis, “leakage” issues (at least in the context described above) do not exist in the model along the center axis.

7 LS-DYNA's FHWA Soil Material Model 147

7.1 Overview

The baseline soil material model chosen for the analysis is LS-DYNA's *MAT_FHWA_SOIL (or *MAT_147) material model developed by Brett Lewis, formerly of APTEK, Inc., for the Federal Highway Administration (FHWA) in 2004 (Lewis, 2004). Upon evaluation of existing and available soil material models suitable for simulating a blast-induced liquefaction environments, two models that satisfy most of the requirements are LS-DYNA's *MAT_FHWA_SOIL model and CTH's Geo-Effective Stress model from Sandia National Laboratories. Although CTH has the ability to treat both solid (pre-liquefaction) phase and liquid (liquefied) phase of the soil materials separately in an integrated and sophisticated manner, its export-controlled policy limits its applicability for commercial applications. CTH analysis results would be difficult to present in an open forum.

LS-DYNA's *MAT_FHWA_SOIL model was developed with support from the Federal Highway Administration (FHWA). During the research and development of *MAT_FHWA_SOIL, Lewis conducted a detailed review of all existing soil models in LS-DYNA to determine if an existing model could be extended, or if a completely new model would be required which would account for pore water pressure build-up and the resulting changes in soil properties. A summary of Lewis' findings is presented in the

*MAT_FHWA_SOIL users manual (Lewis, 2004). Lewis concluded that existing models were inadequate. As a result, he developed a new soil model that accounts for excess pore-water pressure while including failure, damage, and strain rate effects.

Lewis' approach to modeling pore-pressure effects is based on a modified Mohr-Coulomb based failure theory coupled with relationships that account for moisture-effects; a pore-water pressure algorithm; strain hardening/softening relationships; and Yvonne Murray's geo-material rate dependency equations (Lewis, 2004 and Murray, 1997). Lewis' approach does not separately treat the solid and liquid phases of the soil materials as in Taylor's Geo-Effective Stress model (Taylor, 2004). When coupled with the ability to model detonations, LS-DYNA's *MAT_FHWA_SOIL model is the most feasible and readily available material model for a first attempt to evaluate soil liquefaction potential during controlled blasts.

The subsections that follow explore the development of input parameters used for the baseline *MAT_FHWA_SOIL model. Additional discussions on capabilities, assumptions, and limitations of the *MAT_FHWA_SOIL model are presented in the LS-DYNA 970 Users Manual (Hallquist, 2003), *MAT_FHWA_SOIL Model Theory/Users Manual (Lewis, 2004), and the *MAT_FHWA_SOIL Model Evaluation Report (Reid and Coon, 2004).

As with any material model for specific solvers and purposes, the most challenging and time consuming task is the definitions of the input parameters. Many of the input parameters are not well defined by the author or the evaluators due to limited data or background information indicating the appropriate values to be applied (Reid and Coon, 2004). To help reduce the uncertainties involved in the definitions of the input

parameters, extensive sensitivity or trade studies were conducted to determine the effects of the major parameters. These trade studies forms the basis for inputs to the baseline model used for the evaluations of blast-induced liquefaction events. Table 7-1 provides a summary of the input parameters required for the *MAT_FHWA_SOIL model.

Table 7-1 Summary of Input Parameters for *MAT_FHWA_SOIL

MID	Material ID*	RO	Density of soil
NPLOT	Plotting option*	SPGRAV	Specific gravity
RHOWAT	Density of water	VN	Viscoplasticity parameter (Strain-rate enhanced strength)
GAMMAR	Viscoplasticity parameter (Strain-rate enhanced strength)	INTRMX	Maximum number of plasticity iterations
K	Soil's bulk modulus	G	Soil's shear modulus
PHIMAX	Peak shear strength angle (friction angle) in radians	AHYP	Coefficient A for modified Drucker-Prager Surface
COH	Cohesion or shear strength at zero confinement (overburden)	ECCEN	Eccentricity parameter for third invariant effects
AN	Strain hardening % of phimax where non-linear effects start	ET	Strain hardening amount of non-linear effects
MCONT	Soil's moisture content (0 - 1)	PWD1	Parameter for pore water effects
PWKSK	Skeleton bulk modulus (set to zero to eliminate effects)	PWD2	Parameter for pore water effects on effective pressure (confinement)
PHIRES	Min. internal friction angle residual shear strength in radians	DINT	Volumetric strain at initial damage threshold
VDFM	Void formation (fracture) energy	DAMLEV	Level of damage resulted in element deletion (0 – 1)
EPSMAX	Maximum principal failure strain	* Value has no effects on analysis results	
Note: Model units in pound-force, inches and seconds			

The following sub-sections present an overview of how the *MAT_FHWA_SOIL model handles pore-water pressure, followed by discussions on the computations and trade studies conducted for the development of input parameters used for the baseline soil model.

7.2 Pore-Water Pressure Definition

Equation 7-1 shows the relationship between pore-water-pressure (u) and volumetric compression strain (ε_v) used by Lewis for the *MAT_FHWA_SOIL model (Lewis, 2004).

$$u = \frac{K_{sk}}{1 + K_{sk} \cdot D_2 \cdot n_{cur}} \cdot \varepsilon_v \quad (7-1)$$

There are three parameters defined in Equation 7-1 that need consideration. The first parameter n_{cur} is the current porosity due to air void (Murray, 2005). For partially saturated soil, the constant value of D_2 is defined as a function of Skempton's pore-water pressure parameter B , soil porosity n , degree of saturation S , and soil bulk modulus K as shown in Equation 7-2. For saturated soils, n_{cur} equals zero. It follows that regardless of the value of the constant, D_2 , pore-water pressure (u) as shown in Equation 7-1 is linearly proportional to the volumetric compression strain (ε_v) by K_{sk} , which is defined as the skeleton bulk modulus of the soil material.

$$B = \frac{1}{1 + n \cdot \frac{K_{sk}}{K}} \quad D_2 = \frac{1 - B}{B \cdot K_{sk} [n \cdot (1 - S)]} \quad (7-2)$$

When the computed D_2 value is inserted into Equation 7-1, the algorithm iterates on the n_{cur} parameter as a function of volumetric strain corresponding to the volume of

the air-voids (ε_{air}), and the total volumetric compression strain (ε_v) as shown in Equation 7-3, resulting in a basically linear relationship.

$$n_{cur} = \max[0, (\varepsilon_{air} - \varepsilon_v)] \quad (7-3)$$

$$\varepsilon_{air} = n \cdot (1 - S)$$

In summary, the pore-water pressure build-up algorithm used for the *MAT_FHWA_SOIL model is a linear model which assumes a monotonic increase of pore-water pressure u with respect to volumetric compressive strain (ε_v). When the computed pore-water pressure (u) is divided by the initial mean vertical effective stress (σ'_v) of the soil material at the depth of interest, a quantity used to measure the soil's progression towards liquefaction known as the excess pore-water pressure ratio (R_u) results as shown in Equation 7-4. A soil liquefies when R_u reaches 1.0. Since R_u is a function of u , the resulting ε_v vs. u relationship remains linear.

$$R_u = \frac{u}{\sigma'_v} \quad (7-4)$$

A monotonically increasing linear relationship for describing the development of excess pore water pressure in a solid soil mass is a first order representation of the soil's response to loads. However, it may not truly represent what really happens in saturated soil as it progresses towards liquefaction. When a mass of saturated soil is subjected to high magnitude impulsive loads, stresses and strains increase monotonically in a linear or

non-linear fashion, resulting in excess pore pressure build-up until liquefaction occurs, or until applied loads dissipate. Since pressure is a volumetric instead of a distortional entity, corresponding stresses act in the normal direction against each soil particle.

As pore-water pressure increases beyond the confining pressure pre-existing in the soil prior to load application, solid soil particles are no longer in constant direct-contact with one another to transfer loads among the particles. Without support from adjacent soil particles, solid particles within the soil mass become statically unstable as they lose their abilities to transfer and carry loads, thereby producing an “apparent” macroscopic soil softening effect. When this happens, water in the soil takes over as the load-carrying and load-transferring medium.

Since shear (stress) resistance in water is negligible, one often observe large flow-distortions / deformations associated with liquefied soil mass in directions of least-resistance (i.e. unconstrained or with negligible confinements). As excess pore water pressure dissipates in liquefied soil, solid soil particles resume contacts with their neighboring particles, resulting in an increase of shear or friction resistance against flow-distortions. This increase of shear resistance due to increasing solid particle contacts as excess pore pressure dissipates is typically viewed as an increase in or recovery of the overall shear strength of the soil mass. When shear resistance increase to or beyond destabilizing shear loads, equilibrium occurs within the soil mass and displacements subside.

The “numerical quantities” of effective stresses in liquefied soils are either zero or slightly negative, based on the convention that compressive stress is positive in soil materials. In the liquefied stage, it matters not whether effective stresses in solid soil

particles equal to or less than zero. All that matters is that loads are now being carried by the water, while the “free” solid soil particles are considered to have failed, or become ineffective. This scenario causes the liquefied soil mass to behave more like a viscous liquid than a solid mass as the corresponding shear (stress) resistance is greatly reduced. In many cases, shear resistance in liquefied soil maybe considered as negligible, especially when the soil mass begins to flow. Such behaviors reflect the potential needs for separate treatments of the solid phase and the liquid phase of a soil mass during liquefaction.

To improve the ability to predict solid-particle behaviors of saturated sandy soils upon liquefaction, enhancements to the pore-pressure vs. volumetric strain relationship are necessary. An enhanced pore-water pressure algorithm is proposed to combine the iterative equation used by *MAT_FHWA_SOIL model for updating bulk modulus of the combined soil / water mass (K) with Equations 7-1 and 7-2, resulting in the iterative set of equations as shown below. In fully saturated soil, the constant D_2 has no effects on pore-water pressure u .

$$K_{i+1} = \frac{K_i}{1 + K_i \cdot D_1 \cdot n} \tag{7-5}$$

$$u_i = \frac{K_i}{1 + K_i \cdot D_2 \cdot n_{cur_i}} \cdot \varepsilon_{v_i}$$

The following example illustrates the functionality and demonstrates the effects of the proposed change discussed above. For the May 2005, Vancouver blast tests, Dr. Gerber and Dr. Rollins estimated the maximum volumetric strains observed during

liquefaction ($R_u \sim 1$) in fully saturated soil to be approximately 3%. Based on the estimated volumetric strain and a rough estimated average pre-load effective stress of 115 kPa or 16.7 psi (Robertson et al., 2002), Equation 7-5 with an iterative value of bulk modulus K was used to generate a ε_v vs. R_u curve as shown in Figure 7-1. The value of D_1 was estimated to be 3.19E-05 per psi by iterations. As stated earlier, the value of D_2 does not affect the curve shown in Figure 7-1. Therefore, a value of zero was assumed for D_2 .

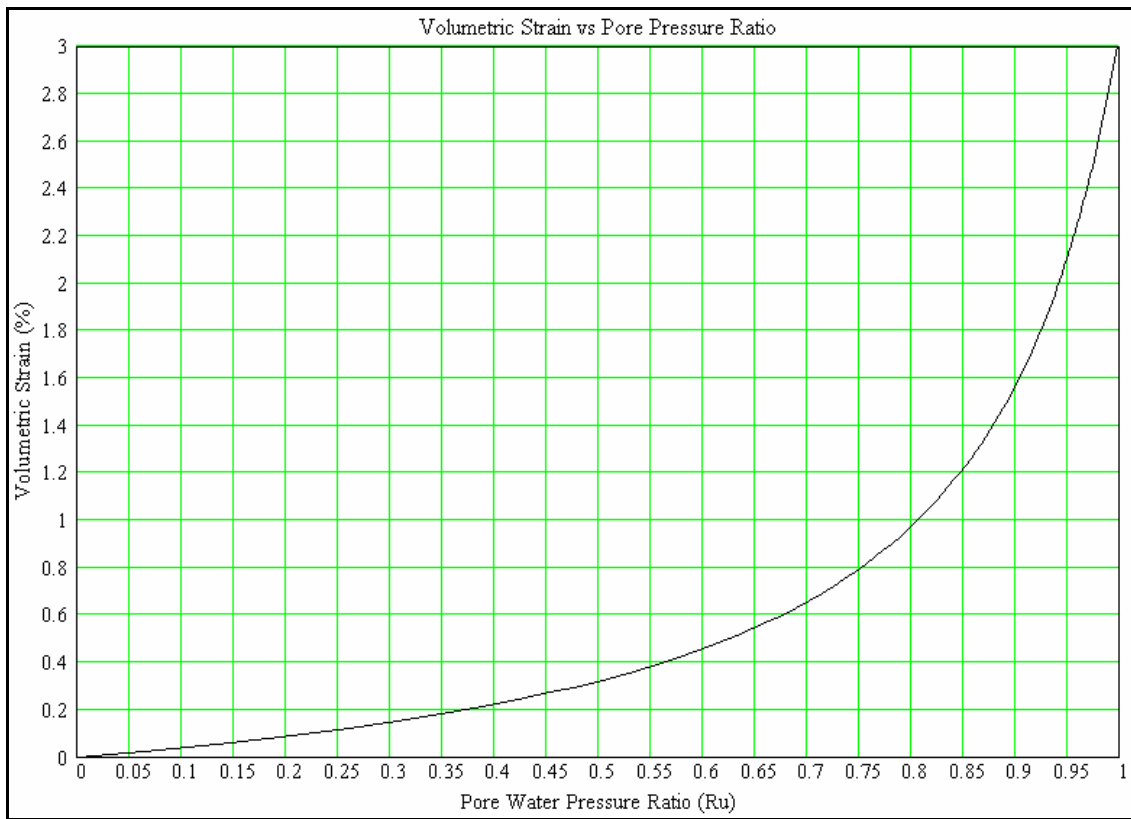


Figure 7-1 Volumetric Strain vs. Pore Pressure Ratio

The volumetric strain vs. pore-water pressure ratio curve shown in Figure 7-1 is consistent with the trend of what one would expect to take place in soil during the process

of liquefaction. As the pore pressure ratio (R_u) increases from zero, strain increases monotonically. As R_u approaches one, corresponding volumetric strains increase asymptotically, indicating that the soil mass' decreasing ability to resist stresses by manifesting itself in the form of increasing displacements, or strains. The overall trend of the curve is also consistent, in magnitude and shape, with published results such as those shown by Lee (1974). It should be noted that relative density of soil affects the shape of the curve shown in Figure 7-1, which is a generic curve for demonstrating effects due to the proposed change from a constant bulk modulus to an iterative bulk modulus during a soil's liquefaction process. Unfortunately, the *MAT_FHWA_SOIL model was not readily available for enhancements and updates. As such, the author was unable to implement and validate the proposed enhancement to the volumetric strain vs. pore-water pressure relationship in the baseline model during the course of this research.

7.3 Computed and Measured Parameters

Several input parameters were derived based on typical table values or computed using published methods and available data as noted in Table 7-2. Table 7-2 provides a summary of the general input parameters used as inputs to the analyses. It should be noted that properties for saturated clay were estimated due to lack of available data. Parameters with an "*" as shown in Table 7-2 were based on information or methods documented in the Canadian Liquefaction Experiment, or CANLEX (Robertson et al., 2000a and 2000b).

Table 7-2 Summary of Computed / Measured Input Parameters

Unit weight of water, γ_w	62.4 pcf	Soil: Poisson's ratio ν	0.25
Soil: Bulk modulus K^*	4697 psi	Soil: Shear modulus G^*	2818 psi
Soil: Young's modulus E^*	7045 psi	*** Water: Bulk modulus K_w	320 ksi
e (saturated sand)*	1.00	* e (partially saturated)	0.97
γ (saturated sand)**	115 pcf	** γ (partially saturated sand)	91 pcf
G_s (saturated sand)	2.684	G_s (partially saturated sand)	2.684
w (saturated sand)	37.3%	w (partially saturated sand)	7.0%
S (saturated sand)	1.00	S (partially saturated sand)	0.19
n (saturated sand)	0.50	n (partially saturated sand)	0.49
γ (saturated clay)**	118 pcf	G_s (saturated clay)	2.78
w (saturated clay)	36.0%	S (saturated clay)	1.0
n (saturated clay)	0.50	e (saturated clay)	1.0

* Values based on CANLEX and standard published data and/or methods.

** Values estimated by Prof. K. Rollins (08/05/2005)

*** Typical bulk modulus of water

Bulk, Shear and Young's Moduli

$$K = k_K \cdot P_A \cdot \left(\frac{\sigma'_m}{P_A} \right)^m \quad G = k_G \cdot P_A \cdot \left(\frac{\sigma'_m}{P_A} \right)^n \quad E = \frac{9 \cdot G \cdot K}{3 \cdot K + G}$$

Porosity n , Specific Gravity G_s , Water Content w , and Degree of Saturation S

$$n = \frac{e}{1 + e} \quad G_s = \frac{\gamma \cdot (1 + e)}{\gamma_w} - e$$

$$w = \frac{n \cdot \gamma_w}{\gamma - n \cdot \gamma_w} \quad S = \frac{w \cdot G_s}{e}$$

where $\sigma'_m = 115kPa = 16.7psi$

$k_K = 300$

$k_G = 180$

$m = n = 0.5$

$P_A = 1$ atmosphere

Based on suggested values for Fraser River and "similar" Syncrude sand per CANLEX project.

References: Robertson et al., (2000); Byrne et al. (2000); Das (2002)

7.4 Skeleton Bulk Modulus/Volumetric Strain Factor

One of the “not so well defined” parameters in the *MAT_FHWA_SOIL Users Manual is called the skeleton bulk modulus constant K_{sk} (Lewis, 2004; Reid and Coon, 2004), which the author of the model defined as the “bulk modulus for soil without air voids” (Lewis, 2004). The soil model’s Evaluation Report suggested that the value of K_{sk} be approximately two orders of magnitude less than the corresponding value of the bulk modulus K , with a clause which stated that “the authors are unaware of any physical testing or theoretical means for determine specific recommended value for PwKsk” (Reid and Coon, 2004). In the context being defined by Lewis and being used by Reid and Coon, along with uncertainties described by Reid and Coon (2004), K_{sk} appears to be used as a volumetric strain factor with a suggested range of values obtained iteratively by analysis. Hence, the parameter K_{sk} would be more appropriately termed as the “volumetric strain factor” rather than skeleton bulk modulus to minimize potential confusions with the bulk modulus K . Meanwhile, to be consistent with the material model’s manuals, the term skeleton bulk modulus is used throughout the discussions in this dissertation, with an understanding that there are uncertainties involved with the definition of K_{sk} . Nevertheless, the actual context of K_{sk} as a volumetric strain factor was applied for the baseline analyses.

The variable Pwksk is applied in LS-DYNA to represent K_{sk} . With so much uncertainties concerning K_{sk} in the soil model’s manuals, a trade study was conducted to determine the effects of K_{sk} in a blast-induced liquefaction analysis and its influence on the baseline soil model’s stability and convergence. The trade study consisted of a single charge baseline model with input parameters pre-determined either by default or by

recommendations from published documents. Variations of the value of K_{sk} were applied for multiple analysis runs. Figure 7-2 provides a summary of pore-water pressure results from the K_{sk} trade study.

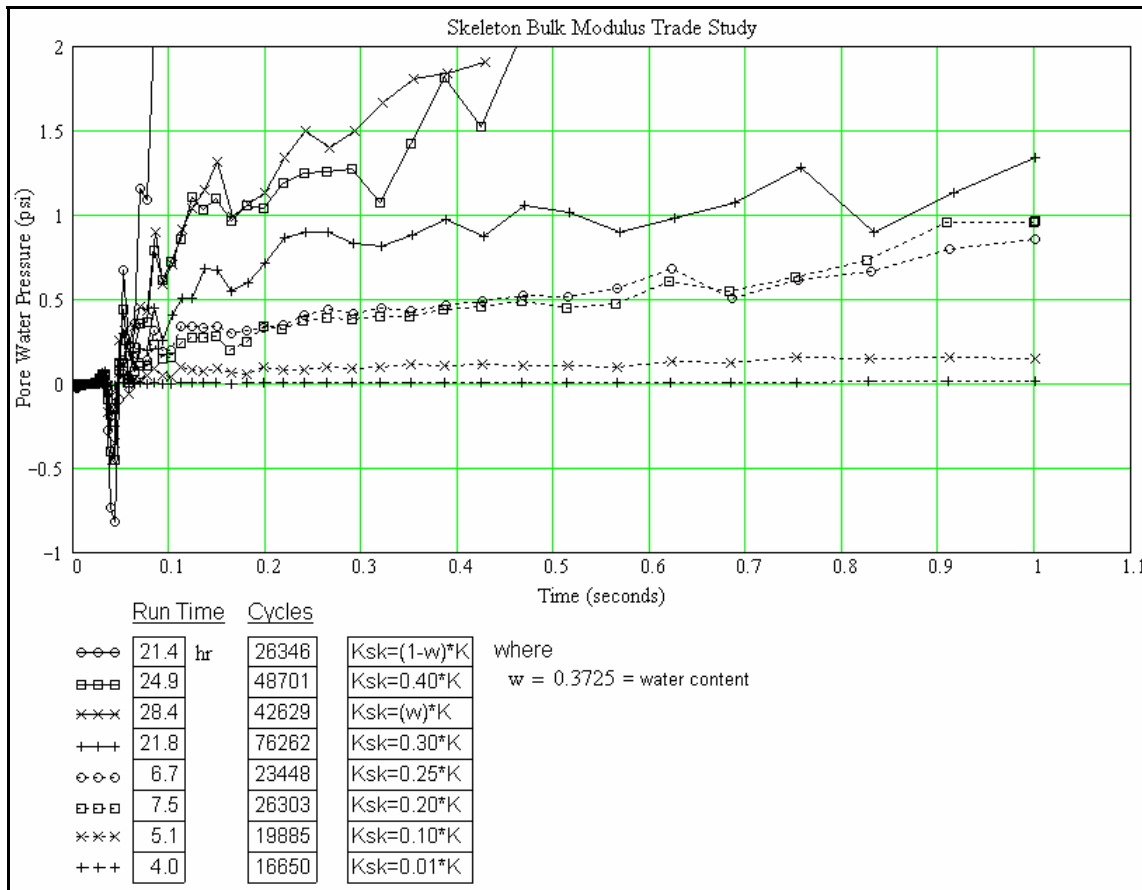


Figure 7-2 Summary of Skeleton Bulk Modulus (K_{sk}) Trade Study

Run time and number of analysis cycles to accomplish the analysis for each run performed in the trade study are also shown in Figure 7-2 for evaluating stability and convergence of the corresponding runs. The trade study originally started with a K_{sk} value equal to the corresponding bulk modulus K value. The run diverged rapidly and

crashed early in the analysis. Results for the $K_{sk} = K$ run were not recorded due to its premature failure.

The K_{sk} value was then adjusted to a percentage of K equivalents to the complement of the soil water content percentage, or 62.75%, as a starting point. Run time, number of analysis cycles, and the pore-water pressure were extracted, computed, and recorded for comparisons against other runs. As the value of K_{sk} gets smaller, the corresponding run time and number of analysis cycles required to complete the tasks drop significantly. The trade study stopped at a K_{sk} value equals 1% of, or 2 orders of magnitudes smaller than, the corresponding bulk modulus K where there is negligible pore pressure build-up as shown in Figure 7-2.

From the results of the trade study under a blast loading environment, appropriate and stable values of K_{sk} appear to lie somewhere between 1 to 20% of the corresponding bulk modulus (K) value. One should note that the appropriate range of K_{sk} values might change under loads with significantly slower application rates. At 20% of the K value or above, one begins to see oscillatory behaviors, increasing analysis iterations and run time, as well as divergence characteristics during the solution process. On the other hand, if the suggested value of K_{sk} is at ~1% of the value of K , one may not obtain sufficient pore-water pressure build-up in the model for proper determinations of liquefaction potentials. Therefore, it is recommended that for maximum stability, reasonable run time, and reasonable amount of pore-water pressure build-up that the value of K_{sk} to be in the range of 5% to no more than 20% of the corresponding value of the material bulk modulus K . One may need to step through an iterative procedure during actual analysis in order to calibrate the actual value of K_{sk} .

Determinations of the input parameters via trade studies were strictly based on physics, analysis stability, convergence, run time, number of analysis cycles required to complete the task, and reasonableness. Individual parameter trade studies are for obtaining “ball-park” figures of input parameters. Fine-tuning of the parameters was performed when all individually determined parameters had been selected, compiled, and combined in a single analysis run. Optimization techniques (i.e. the genetic-algorithm approach) currently under research by Professor Richard Balling at BYU may improve the process in determining appropriate values for the input parameters.

7.5 Maximum Number of Plasticity Iterations

The plasticity algorithm implemented in the *MAT_FHWA_SOIL model is based on a modified Mohr-Coulomb method utilizing a hyperbolic fit to the yield surface. At zero shear strength (i.e. on the pressure axis), the modified surface is a smooth surface which avoids a sharp discontinuity typically associated with Mohr-Coulomb revolving cone yield surface as described in the Theory / User Manual (Lewis, 2004). Solution convergence of the plasticity algorithm is based on an iterative process. A trade study on the maximum number of iterations (ITERMX, spelled INTRMX in the LS-DYNA 970 Users Manual) to determine a recommended (i.e. local optimal) number of plasticity algorithm iterations should be used in the baseline analysis. Figure 7-3 shows a summary of the INTRMX trade study.

In Figure 7-3, the run with a maximum of 1000 iterations defined for ITERMX was terminated prematurely at approximately 0.35 seconds due to the excessive number of hours projected to complete the remaining analysis. For plastic analysis, it is generally a good idea to allow sufficient convergence iterations for reliable and accurate results.

However, the number of iterations is directly proportional to the amount of time and the number of analysis cycles required completing the analysis as shown in Figure 7-3. A balance must be maintained between the number of plasticity iterations allowed and the run time. Based on the results presented in Figure 7-3, it appears that an ITERMX value between 10 and 20 is most reasonable for a blast-induced liquefaction analysis.

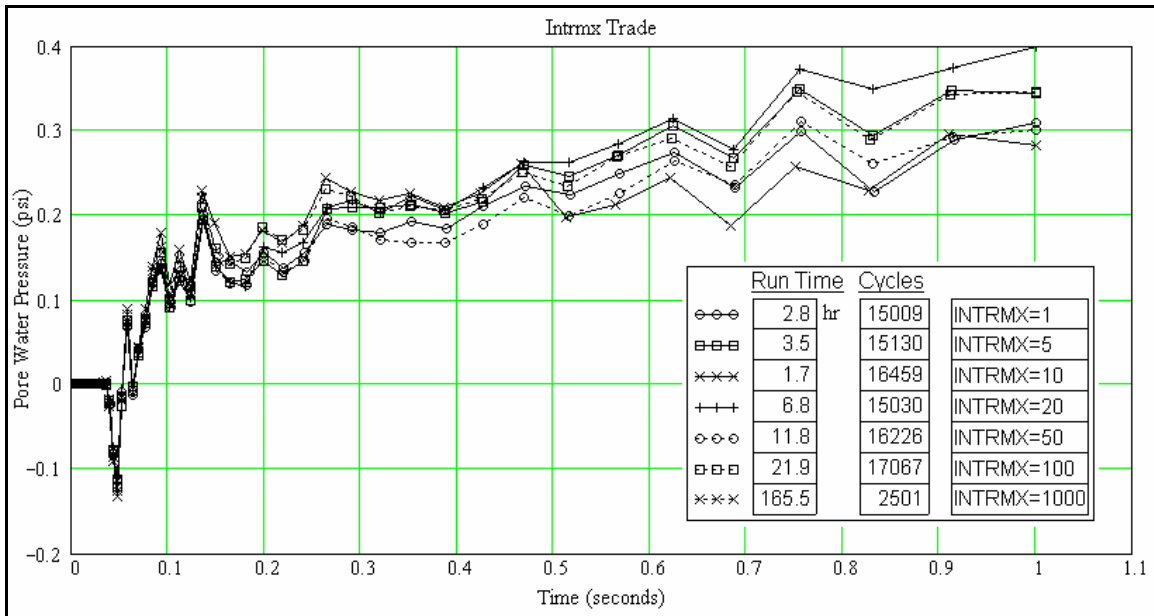


Figure 7-3 Summary of ITERMX Trade Study

A value of 20 seems to be near the point of “diminishing returns” where additional iterations will only increase the run time without any gain in accuracy. Values at or above 20 are not recommended due to the amount of additional time required to accomplish the same analysis. Both authors of the Theory/Users Manual and the Evaluation Report recommended that a value of 10 for ITERMX is a good starting point for most analysis utilizing the *MAT_FHWA_SOIL model (Lewis, 2004; Reid and Coon, 2004).

7.6 Maximum and Residual Friction Angles

The angle of internal friction (ϕ) is the inclination of the shear strength envelope which helps define the relationship between shear and normal stresses. Authors of the Evaluation Report recommended a maximum allowable internal friction angle (PHIMAX or ϕ_{\max}) of 63° to be used for cohesionless soil. Although results are not expected to alter significantly, the angle of 63° still appears to be too high for sandy soils. After consulting with Professor Rollins and CANLEX reports, a value of 35° was assigned to PHIMAX for the analysis. A trade study was conducted to determine the effects of PHIMAX and the results of the trade study are summarized in Figure 7-4. As one would expect, variations of the maximum allowable internal friction angle, or PHIMAX, do not alter the results or the run time / cycles of the analysis significantly. According to Professor Rollins, it is a somewhat subjective call to specify the actual value of PHIMAX. For the baseline analysis, a value of 35° was assigned to the PHIMAX parameter per recommendation from Prof. Rollins.

The residual friction angle (PHIRES) is the angle that defines the slope of the failure envelope, which quantifies the residual strength once shear failure has initiated. The developer of the *MAT_FHWA_SOIL model recommended a value between 0 and 0.001 radians for PHIRES (Reid and Coon, 2004). Since measured data was not readily available to determine the actual values for PHIRES, a trade study was performed on the value of PHIRES and its results presented in Figure 7-5. Although changes due to the variations of PHIRES are not alarming, greater variations in results are observed when PHIRES drops below 11° . At a value above 15° , results appear to stabilize.

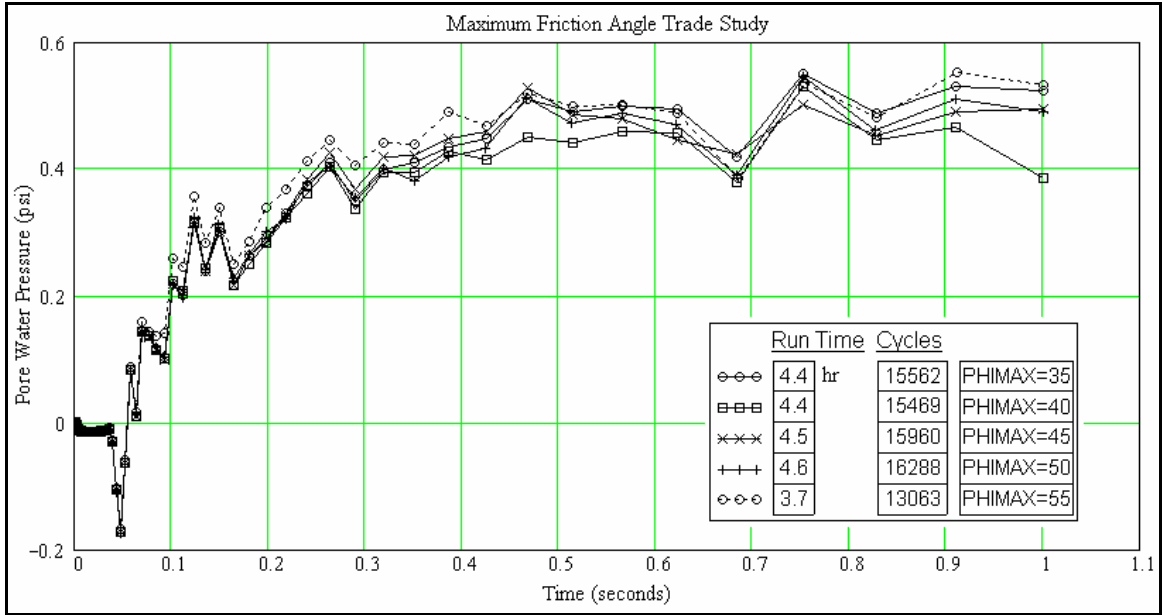


Figure 7-4 Summary of PHIMAX Trade Study

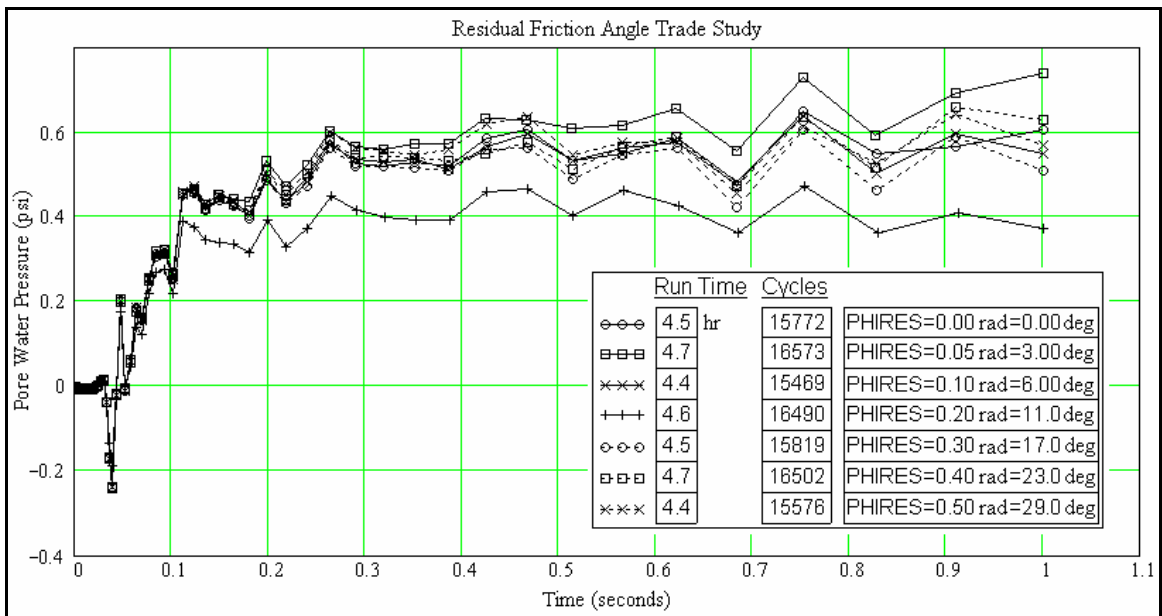


Figure 7-5 Summary of PHIRES Trade Study

According to Prof. Rollins, the residual angle typically does not reduce to zero. In fact, the residual angle is generally not much smaller than the original friction angle in loose to medium dense sand. Upon consulting with Prof. Rollins, a value of 30 deg (0.5236 radians) was selected for PHIRES.

7.7 Cohesion

The standard definition of cohesionless soil is just what the name implies: zero cohesion. However, the plastic algorithm implemented for the *MAT_FHWA_SOIL model require an increasing number of iterations to converge as the value of the cohesion (COH) approaches zero. At a COH value of zero, the number of iterations required for the plasticity routines to converge is likely to exceed the number of iterations defined in INTRMX (see Section 7.5). From the analysis feasibility standpoint, the soil model's Evaluation Report recommended to set a small value of 6.2E-06 GPa, or 0.8992 psi, for the COH parameter. The recommended value “appears to be close enough to zero, but still allows the plasticity routines to converge relatively rapidly” (Reid and Coon, 2004). A trade study was conducted to evaluate the effects of the parameter COH. Figure 7-6 shows a summary of the COH trade study. One can readily see from Figure 7-6 that as the value of COH approaches zero, the number of cycles and run times increase. As the value of COH becomes zero, the yield surface approaches a discontinuity, causing the plasticity algorithm to have difficulties in converging to an acceptable solution as described in the Evaluation Report (Reid and Coon, 2004).

Figure 7-6 shows that the overall results do not vary significantly among the different values of cohesion (COH) as long as the COH value remains small. As COH increases beyond unity, delays in failure due to cohesion effects causes excessive

distortions in localized regions near sources of high magnitude loads even though the number of plasticity iterations in terms of cycles and run time decreases. A balance must be maintained between the avoidance of excessive element distortion due to high COH and excessive run time due to near-zero COH. The recommended value of 0.8992 psi was chosen for the baseline analysis since it does appear to be stable with acceptable run time, yet it is sufficiently close to zero to avoid excessive element distortions.

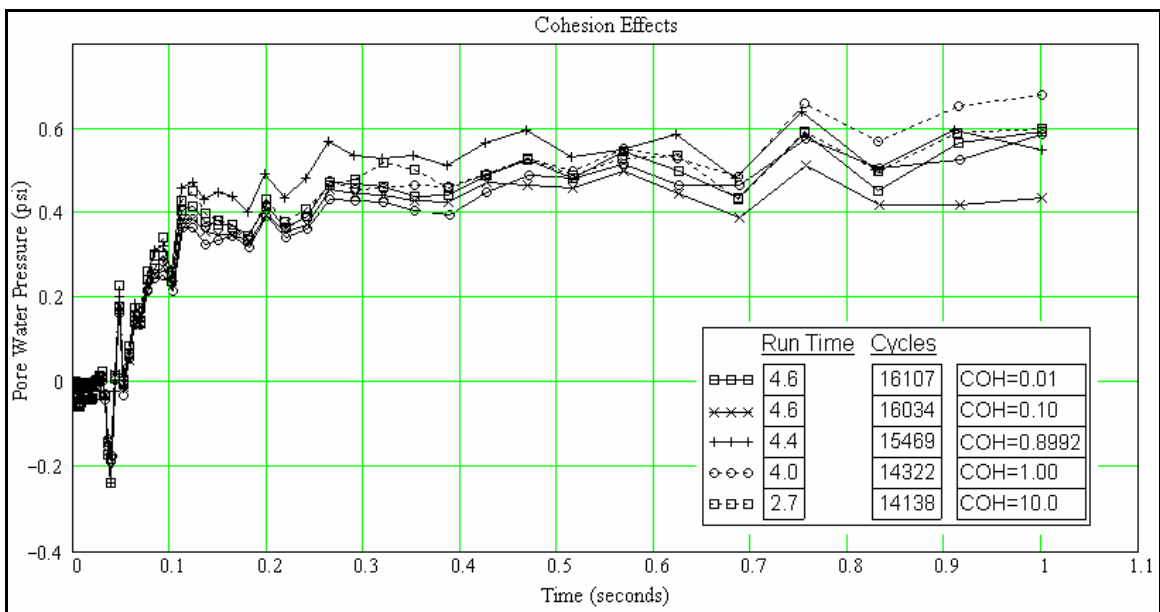


Figure 7-6 Summary of COH Trade Study

The clay layer between the partially saturated sandy layer above it and the fully saturated sandy layer underneath it at the Fraser River test site is not well characterized. Vast uncertainties on the properties of the clay layer remain to be answered. Due to the lack of properties on the clay layer at the Fraser River site, a value of 2 psi was assumed for COH after consulting with Professor Rollins. The COH value of the clay layer was originally assumed 10 psi, which seemed excessive, but with no actual data against the

excessiveness, an evaluation was conducted. Upon review the deformed geometry, the 10-psi COH value was deemed too excessive in causing undesirable distortions in elements adjacent to the blast materials. Significant discontinuities between the clay layer and the sandy layers were observed which did not appear to be a natural phenomenon. As a result, the COH value for the clay layer was adjusted to 2 psi, which appears to be reasonable since it is slightly more than twice the assumed cohesion for the sandy material, yet it is sufficiently small to avoid significant element distortions under blast loads.

7.8 Drucker-Prager Coefficient

In the standard Mohr-Coulomb approach, the failure surface converges to a vertex, or a point of discontinuity, where convergence at such point becomes difficult and time consuming to achieve. Drucker-Prager developed an inscribed cone that provides an approximation of the vertex singularity with a smooth transition curve. The baseline soil model's Evaluation Report discusses in fair detail concerning the Drucker-Prager yield surface approach summarized here. The replacement of the vertex singularity with a smooth transition curve resulted in faster plasticity convergence with fewer iterations and improved numerical stability.

AHYP is the Drucker-Prager coefficient that provides a description of the smoothing results at or near the point of singularity in the Mohr-Coulomb failure surface. At $AHYP = 0$, the original Mohr-Coulomb surface develops, along with the singularity associated with the Mohr-Coulomb failure surface's vertex.

When the value of AHYP is large, the hyperbolic smoothing algorithm causes the fitted surface to deviate from the original Mohr-Coulomb failure surface. Authors of the

Evaluation Report suggested that a reasonable value of AHYP could be obtained when it is set to a value between 0 and a computed value using Equation 7-6 (Reid and Coon, 2004).

$$0 \leq AHYP \leq \frac{c}{20} \cdot \cot(\phi) \quad (7-6)$$

For example, for cohesion c of 0.8992 psi and a maximum internal friction angle of 45° , the maximum suggested value of AHYP based on Equation 7-6 is 0.045 psi or $3.1E-7$ GPa.

7.9 Eccentricity

The parameter ECCEN is defined as the “material input parameter describing the ratio of triaxial extension strength to triaxial compression strength” for the third invariant (J_3) of the stress deviator function defined by Klisinski (Lewis, 2004). Klisinski’s function is an enhanced yield surface in the deviatoric plane based on the original Mohr-Coulomb surface function (K) as shown in Equation 7-7.

$$K(\theta) = \frac{4 \cdot (1 - e^2) \cdot \cos^2 \theta + (2 \cdot e - 1)^2}{2 \cdot (1 - e^2) \cdot \cos \theta + (2 \cdot e - 1) \cdot \sqrt{4 \cdot (1 - e^2) \cdot \cos^2 \theta + 5 \cdot e^2 - 4 \cdot e}} \quad (7-7)$$

$$\text{where } \cos 3\theta = \frac{3 \cdot \sqrt{3} \cdot J_3}{2 \cdot \sqrt{J_2^3}}$$

The value of ECCEN (or e in Equation 7-7) is between 0.5 and 1.0. The standard circular-cone Mohr-Coulomb yield surface is produced when ECCEN equals 1, and a triangular yield surface is formed when ECCEN equals to 0.55. The model developer suggested an ECCEN value of 0.7 for a reasonably smooth surface without over-smoothing the corners of the yield surface. For the baseline analysis, the ECCEN was assigned to 1.0 for a standard circular-cone Mohr-Coulomb yield surface.

7.10 Strain Rate Parameters

Yvonne Murray developed a two-parameter Devaut-Lions viscoplastic algorithm for geo-materials (Murray, 1997). Lewis implemented Murray's two-parameter algorithm in the soil model to account for potential rate dependent effects. Murray's algorithm performs a parametric interpolation between the elastic trial (stresses beyond yield surface) stress and the inviscid (stresses on the yield surface with negligible viscosity effects) stress to obtain the viscoplastic stress as shown in Equations 7-8 through 7-10.

$$\bar{\sigma}_{vp} = (1 - \zeta) \cdot \bar{\sigma} + \bar{\sigma}_{trial} \quad (7-8)$$

$$\zeta = \frac{\eta}{\Delta t + \eta} \quad (7-9)$$

$$\eta = \left(\frac{\dot{\gamma}_r}{\dot{\varepsilon}} \right)^{\frac{V_n-1}{V_n}} \quad (7-10)$$

The parameters GAMMAR (γ_r) and VN (V_n) represent a viscosity parameter and a viscosity exponent, respectively. Rate enhanced strength effects are disabled when GAMMAR equals to zero, independent of the value of VN. Due to uncertainties in selecting the appropriate values for GAMMAR and VN, trade studies were conducted to improve understandings of the effects due to these two parameters. Figure 7-7 and Figure 7-8 summarize results from the respective GAMMAR and VN trade studies.

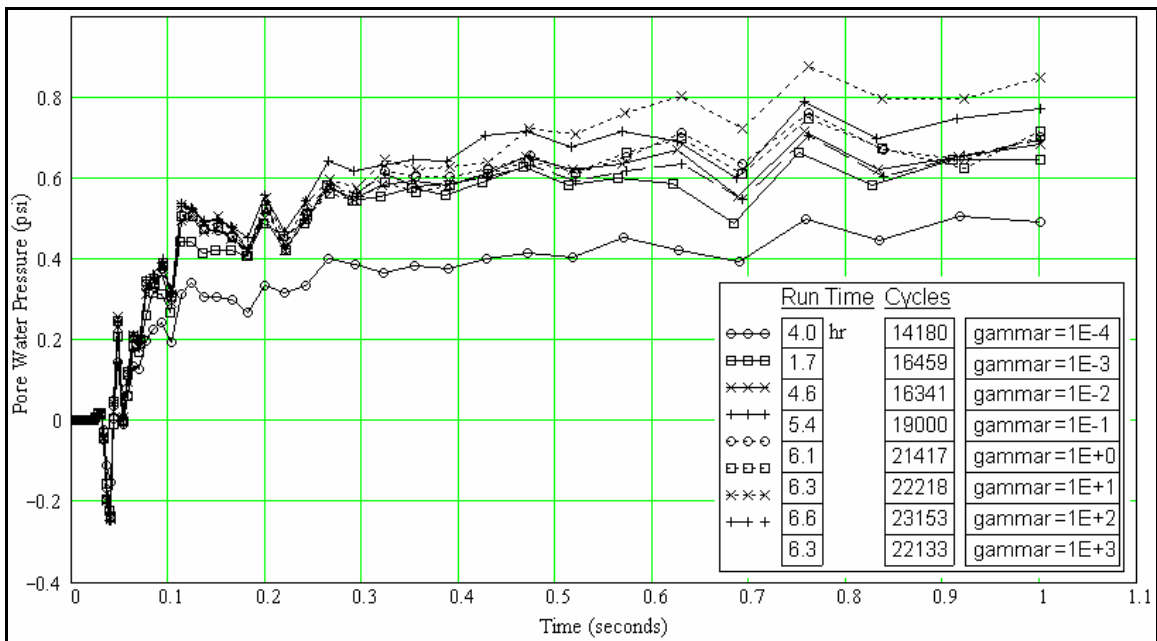


Figure 7-7 Summary of GAMMAR Trade Study

Results from the GAMMAR trade studies show stable and consistent trends for results obtained using GAMMAR values ranging from 1.0E-04 to 1.0E+03. It appears that the magnitude of the pore pressure is proportional to the value of GAMMAR. The time and number of cycles to complete the analysis, however, appears to be inversely proportional to the value of GAMMAR. If measured data is not available in determining

GAMMAR, then the selection of the appropriate values is largely subjective toward the analysis run time and pore pressure magnitudes.

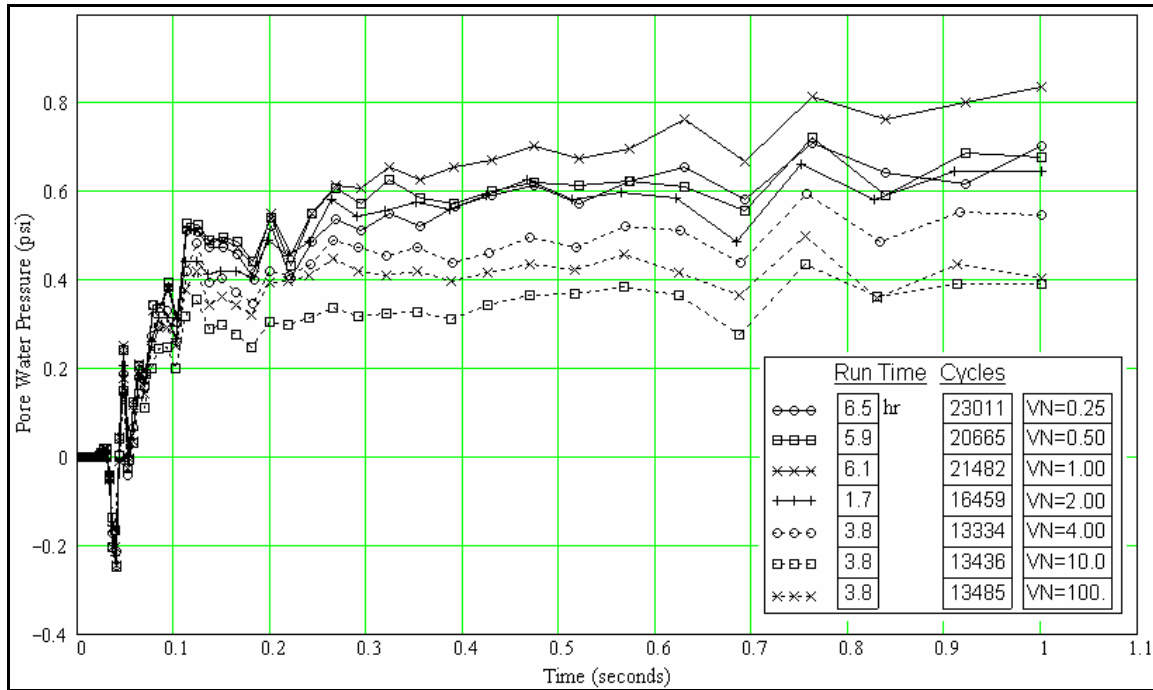


Figure 7-8 Summary of VN Trade Study

Results from the VN parameter trade study shows that the amount of pore pressure generated and the time and number of cycles required to complete the analysis are inversely proportional to the corresponding value of VN. The larger the VN value, the less pore pressure is generated with faster run time and less analysis cycles. Stability does not appear to be an issue for both GAMMAR and VN parameters.

7.11 Plasticity Parameters

To simulate non-linear plastic hardenings of the soil, the friction angle increases with respect to the effective plastic strain as shown in Equation 7-11. Two parameters

that control the strain hardening effects are A_n and E_t . E_t is the amount of non-linear plastic strain hardening desired. According to the Evaluation Report, “ A_n ” is a fraction of the maximum friction angle when hardening begins and has a value between 0 and 1, inclusive (Reid and Coon, 2004). It was not certain prior to the trade studies, how the model would handle calculations when A_n in the denominator of Equation 7-11 was equal to 0. One of the runs for studying effects of A_n was assigned a zero value to the A_n parameter just to determine the effects of a zero value. It appears from the results that there is internal logic in the soil model to circumvent a floating-divided by zero issue when A_n equals to zero. However, the Users Manual does recommend the range of 0 and 1 with only 1 is inclusive (Lewis, 2004).

$$\Delta\phi = E_t \cdot \left(1 - \frac{\phi - \phi_{init}}{A_n \cdot \phi_{max}} \right) \cdot \Delta\varepsilon_{eff_plastic} \quad (7-11)$$

Trade studies were conducted on the parameters A_n and E_t . Results of the trade studies are shown in Figure 7-9 and Figure 7-10. Pore pressure results vary significantly as the value of E_t changes. Run time is shortest when E_t equals 0 whereas the friction angle does not increase with respect to strains. However, one would expect at least some degree of plasticity hardening to take place under high magnitude short duration impulsive loading, especially at regions near the blast. As such, the value of E_t should not be zero in a blast environment. Variations of pore pressure induced by different values of A_n are not as dramatic as the corresponding variations for different values of E_t .

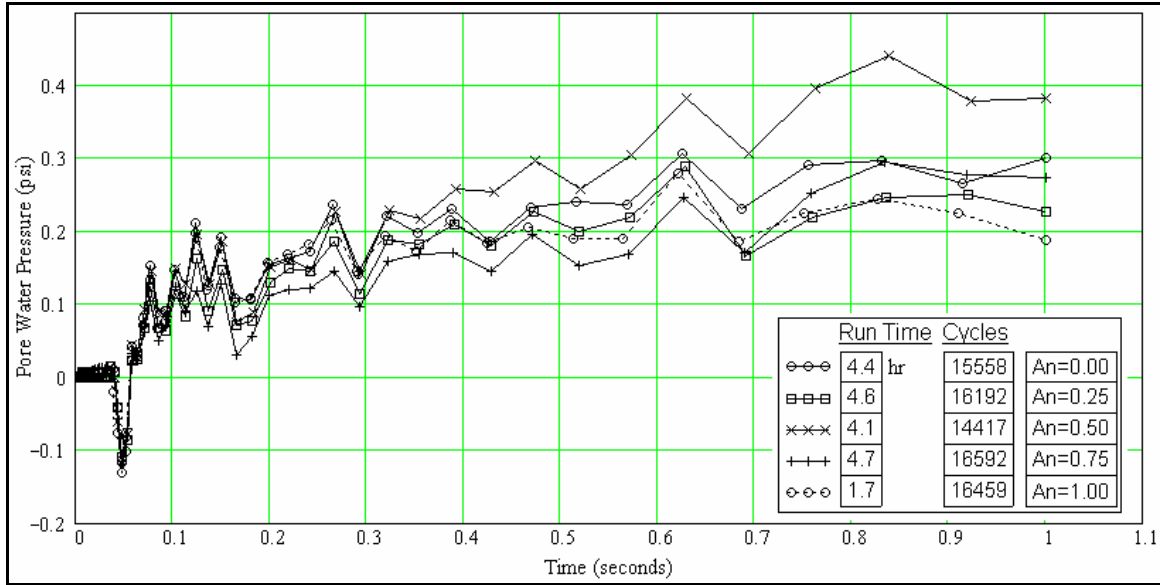


Figure 7-9 Summary of Hardening Parameter (A_n) Trade Study

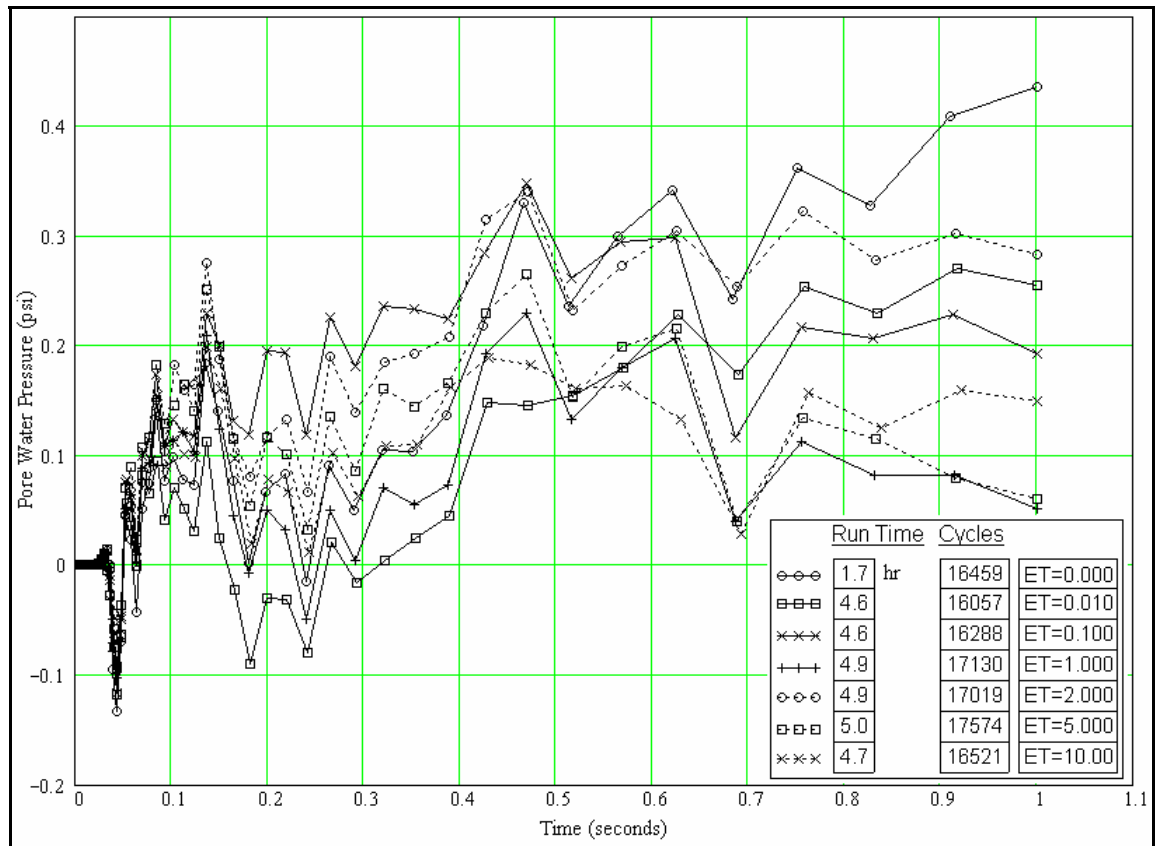


Figure 7-10 Summary of Hardening Parameter (E_t) Trade Study

Authors of the Evaluation Report expressed that they are “unaware of any physical testing or theoretical means for determining the recommended values for A_n and E_t ” (Reid and Coon, 2004). Test models and Developer’s recommendations as shown in the Evaluation Report do not account for plasticity hardening (i.e. $E_t = A_n = 0$). Therefore, selection of values for A_n and E_t can be challenging due to subjectiveness.

7.12 Void Formation and Initial Damage Threshold

The parameter DINT (ξ_0) represents the volumetric strain when damages in the soil initiate whereas VDFM represents the soil’s void formation (or fracture) energy. VDFM is nothing more than the area under the softening region of the pressure-volumetric strain curve times the cube root of the element volume. Authors of the soil model’s Evaluation Report stated that they “are unaware of any physical testing or theoretical means for determining the recommended values for VDFM or DINT” (Reid and Coon, 2004). Trade studies for the development of VDFM and DINT parameters were conducted. Figure 7-11 summarizes the results of the trade study for DINT while Figure 7-12 summarizes the results of the trade study for VDFM.

In the DINT trade study, run/cycle time improves noticeably as DINT increased to 0.1. Analysis stability, convergence, and results do not vary significantly with respect to several orders of magnitude changes in the value of DINT. As such, choice of DINT value is subjective based on personal preferences when insufficient data are available to specify the exact value of DINT. Similar characteristics as DINT is noticed in the VDFM trade study except when VDFM equals to 0, in which case the run / cycle time and more noticeable oscillatory and divergence behaviors are observed. Similar to DINT, selecting a value for VDFM is subjective when no data is available.

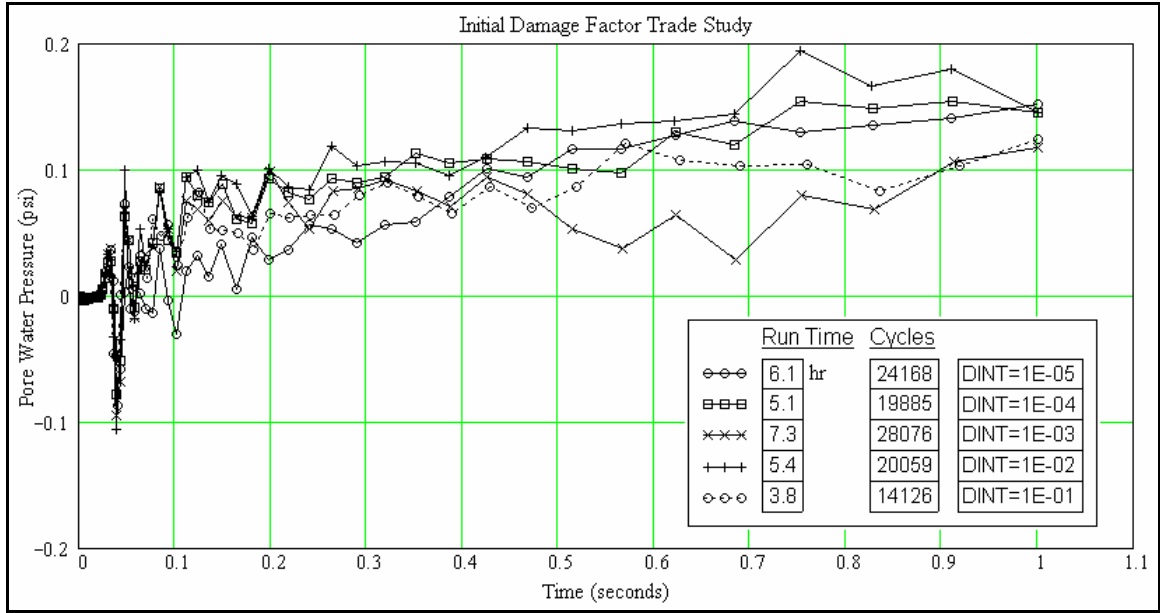


Figure 7-11 Summary of Initial Damage Threshold (DINT) Trade Study

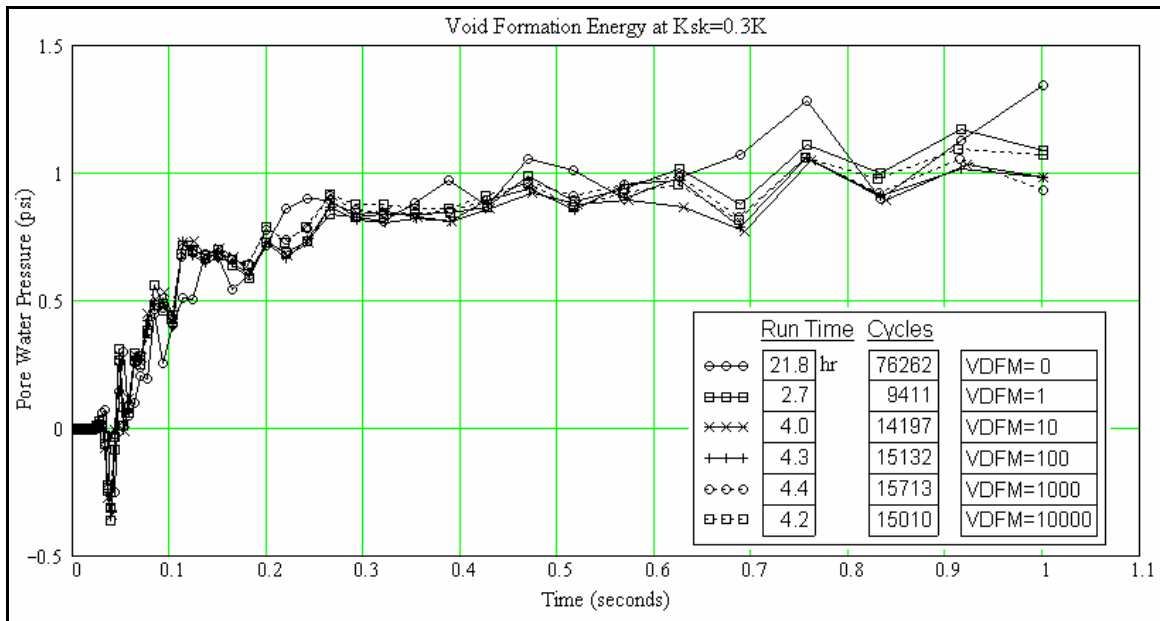


Figure 7-12 Summary of Void Formation Energy (VDFM) Trade Study

7.13 Damage Level and Element Deletion

Damage level (DAMLEV) is the percentage of material damage where the element can be deleted from analysis. Another parameter called EPSMAX specifies the maximum principal failure strain when the element can be deleted. Unlike implicit finite element analyses designed for quasi-static type environments, element deletion without careful considerations can be detrimental to explicit hydro-code analyses.

In an explicit hydro-code analysis, deleting an element in which there are non-trivial internal energy and loads remaining within the element is equivalent to a sudden removal, or application, of an impulsive load with zero time increment. The results are a shock wave generated by the sudden change that propagates through the model, causing numerical instability and, in most cases, erroneous results, as well as crashes. Therefore, element deletion is generally not recommended in an integrated continuum model in a shock wave analysis without seriously considering the consequences of doing so. Authors of the Evaluation Report also recommended against element deletion due to numerical instability reasons as described (Reid and Coon, 2002).

A scenario where the removal of elements is potentially safe to do so is in fragmentation or impact analyses where individual fragments as modeled are in free and random motions, and the likelihood of interactions among fragments are negligible. In such a case, elements representing individual fragments can safely be deleted without inducing undesirable shock waves and numerical instability.

To turn off the element deletion scheme, a value of 0 is assigned to DAMLEV, in which case the corresponding value of EPSMAX is ignored in the analysis. As such, the default value of 1 was assigned for EPSMAX as a “place holder.”

8 High-Explosive Material Model

8.1 Baseline Blasting Material

Several commercially available explosives can be used for blast-induced liquefaction experiments. Kinepak and Dyno Xtra were two of several explosives chosen for previous tests conducted at locations such as the Treasure Island in the San Francisco Bay (Ashford and Rollins, 2000 and Lane, 2000). Pentex, a commercial form of Pentolite 50/50 explosives, was selected as the baseline explosive for the May 2005 Vancouver blast-induced liquefaction test due to its availability and suitability as recommended by the professional blasters hired to perform the task. Pentex is typically used as a booster for small bomblets in military applications (Carleone, 1993) and for other commercial applications. It has excellent water resistance characteristics, which is essential for embedded placement in saturated soils below the ground water table.

Pentolite 50/50, or Pentex, is an organic explosive compound with approximately 50% Pentaerythritol Tetranitrate (an aliphatic or non-benzene based nitrate ester explosive known as PETN), and 50% Trinitrotoluene (aromatic or benzene based explosive known as TNT). According to the Material Safety Data Sheet (MSDS) published by Orica (2002) for Pentex, the amount of PETN in Pentex can vary from 50 to 70%. The corresponding amount of TNT can also vary between 30 and 50% (Orica Brazil Inc., 2002). Typical detonation properties for Pentex boosters including density,

detonation velocity, and detonation pressure are 1.7 grams/cc, 7.5 km/sec, and 255 kbar, respectively. One should note that detonation properties for most explosive materials often vary among different references published by different manufacturers due to variations in the explosive grade, consistency, density, and the amount of PETN and TNT used in the manufacturing process.

8.2 Baseline Explosive Modeling Techniques

Section 4.7 describes the common techniques used to model a detonation process. The direct explosive material modeling approach described in Section 4.7.5 is the baseline approach chosen for the simulation of the blast-induced liquefaction event. The direct approach uses LS-DYNA's High Explosive Burn model (HEBm) with default options of combined programmed and beta burn, which allows the high explosive material to behave as an elastic perfectly plastic material prior to detonation.

The HEBm uses a pre-defined lighting (or detonation initiation) time and location for each explosive to allow users the flexibility of modeling simultaneous or sequential blasts. The actual detonation time for each element is the summation of the corresponding lighting time, and a time offset computed from the distance between the detonation initiation point and the element center divided by the element's detonation velocity.

Once detonation begins, the HEBm treats the detonation products as gas instead of solid in order to simulate the actual detonation process. Pressure – volume relationship of the HEBm then follows the characteristics specified by the corresponding equation of state (EOS) defined for the HEBm. Two sets of inputs are required to properly define the HEBm: hydrodynamic or detonation properties and the EOS.

During the model development phase when using LaGrangian or ALE methods of analysis, care must be taken to ensure that elements adjacent to explosives are several times larger than the explosive elements to allow for expansions of the explosives during detonation. This can also help reduce the potential for “hourglass” related failures or crashes. The size difference requirement mentioned above is not necessary when using the Eulerian method due to its fixed or non-deformable mesh.

8.2.1 Hydro-dynamic Parameters and Equation of State

Hydro-dynamic input parameters (or detonation properties) define the fundamental detonation and mechanical characteristics of the explosive material modeled by the HEBm, while the equation of state (EOS) defines the high explosive (HE) material’s pressure – volume relationship.

Table 8-1 summarizes both the hydrodynamic input parameters and the corresponding JWL EOS parameters used to simulate the detonation process of Pentex (50/50) HE material.

There are several sets of hydrodynamic properties and EOS parameters available from the literature for different PETN / TNT proportions and compositions. Properties shown in Table 8-1 are average and typical published data for a Pentex composition with 50% PETN and 50% TNT as was indicated by the blasting professionals at the Fraser River Delta test site. One should note that the parameters listed in Table 8-1 have been converted from published units of measurement to units consistent with those used in the analysis model.

Table 8-1 Hydro-dynamic and EOS Parameters for Pentex

Hydro-dynamic (Detonation) Parameters for 50% PETN / 50% TNT Composition*					
Density $\left(\frac{\text{pound_force} \cdot \text{s}^2}{\text{in}^4}\right)$	Detonation (C-J) Pressure (psi)	Detonation (C-J) Velocity (in/sec)	Detonation Energy (psi)	γ	TNT ** Equivalency
1.572E-04	3.698E+06	2.965E+05	1.175E+06	2.78	1.12
JWL Equation of State Parameters for 50% PETN / 50% TNT Composition*					
A (psi)	B (psi)	C (psi)	R1	R2	Ω
7.846E+07	1.359E+06	1.498E+05	4.5	1.1	0.35
* Parameters converted to units consistent with those used in the analysis model.					
** Based on detonation energy to explosive density ratio method (Cooper, 1996).					
<u>References</u>					
Anderson (1993), Cooper (1996), Dobratz and Crawford (1985), and Orica Canada Inc. (2003) .					

9 Vancouver Blast-Induced Liquefaction Experiment

9.1 Overview

Three blast-induced liquefaction experiments were conducted in May 2005 at the Fraser River Delta near the south end of the Massey Tunnel located south of Vancouver, B.C. Figure 9-1 shows a composite photo of the test site with respect to the south end of the Massey Tunnel. On the left side of the photo is the south entrance of the Massey Tunnel under the Fraser River, south of Vancouver, B.C. A white truck operated by ConeTec for performing CPT tests is located just to the right of the double tree-trunk in the center section of the photo. Figure 9-2 presents the site map produced by Spencer Strand, a PhD student involved in the experimental aspects of the blast-induced liquefaction tests conducted at Fraser River Delta location during the summer of 2005.



Figure 9-1 Composite Photo of May 2005 Vancouver Test Site

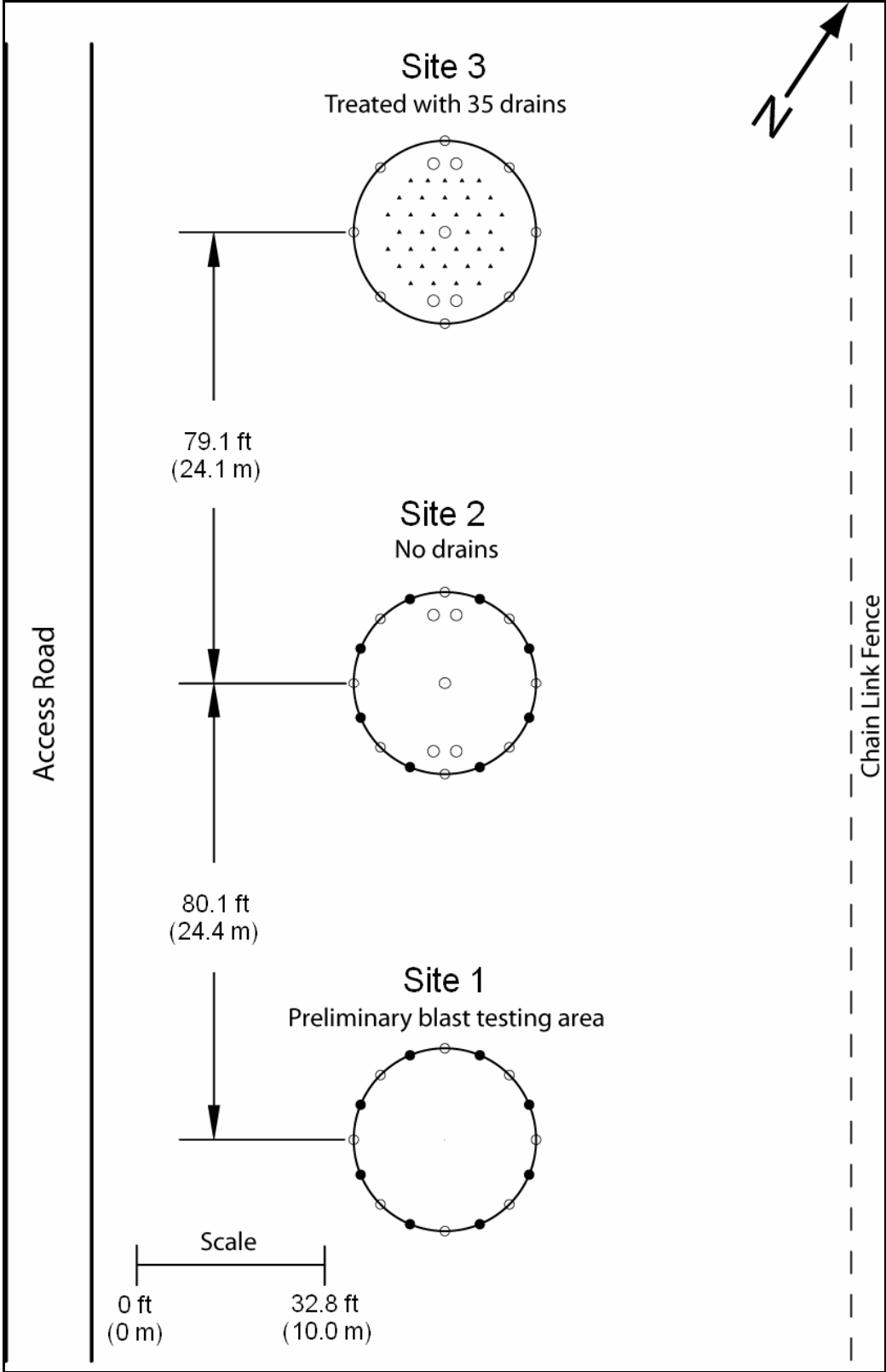


Figure 9-2 May 2005 Vancouver Test Site Map

This section provides a general overview of the experiments and results related to this numerical modeling research and the results. Professor Rollins and Spencer Strand are in the process of preparing a detailed test report documenting the process of all experiments conducted at Fraser River Delta during the summer of 2005.

9.2 Site Characterization

The first step in preparation for the blast experiments was to perform site characterization, which includes on-site inspections, CPT tests, and ground survey to determine locations and orientations of the blast circle and for the placement of instrumentation.

Three CPT's and a geophone test for seismic characteristics assessment were conducted at each of the three test sites as shown in Figure 9-2. Meanwhile, ground survey of the sites was conducted simultaneously to determine locations and orientations of the blast circle and instrumentation. Sites 2 and 3 were reserved for tests conducted in mid to late summer of 2005 that included piles and other equipments for projects unrelated to this numerical modeling research. Data for this research were measured from Site 1 where blast-tests were conducted in May 2005 without additional in-ground foundation and structural components. CPT data measured from the Fraser River Delta Site 1 are summarized in Figure 9-3. The corresponding shear wave velocity data are presented in Figure 9-4. A summary of soil properties with respect to depth at Site 1 as prepared by Spencer Strand is presented in Figure 9-5. Strand's data were prepared near the completion of this dissertation. Due to differences in averaging, interpolation, and interpretation techniques, differences between data computed by Strand and input data prepared during the early stage of this research as shown in Table 7-2 can be expected.

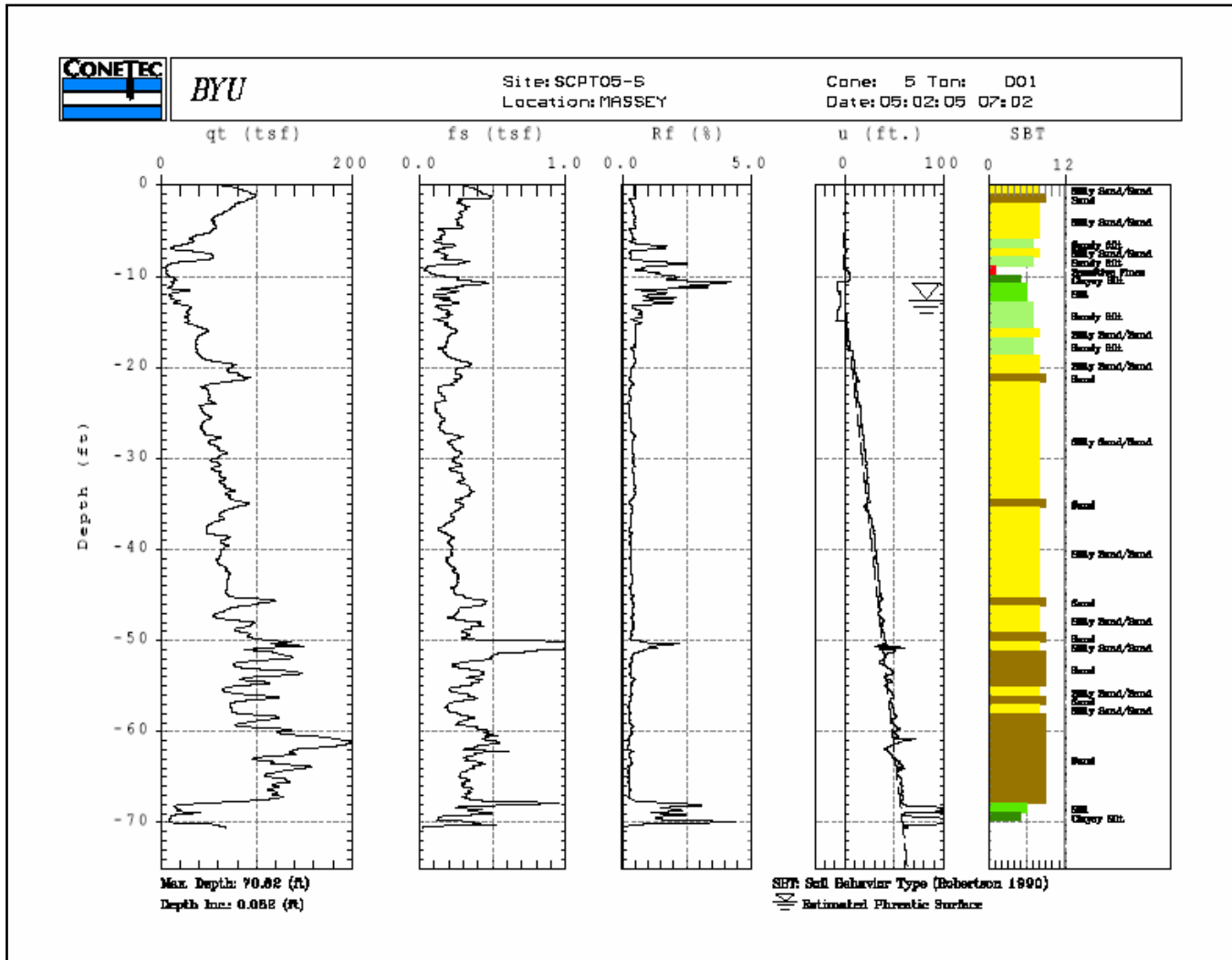


Figure 9-3 CPT Data Measured at Site 1

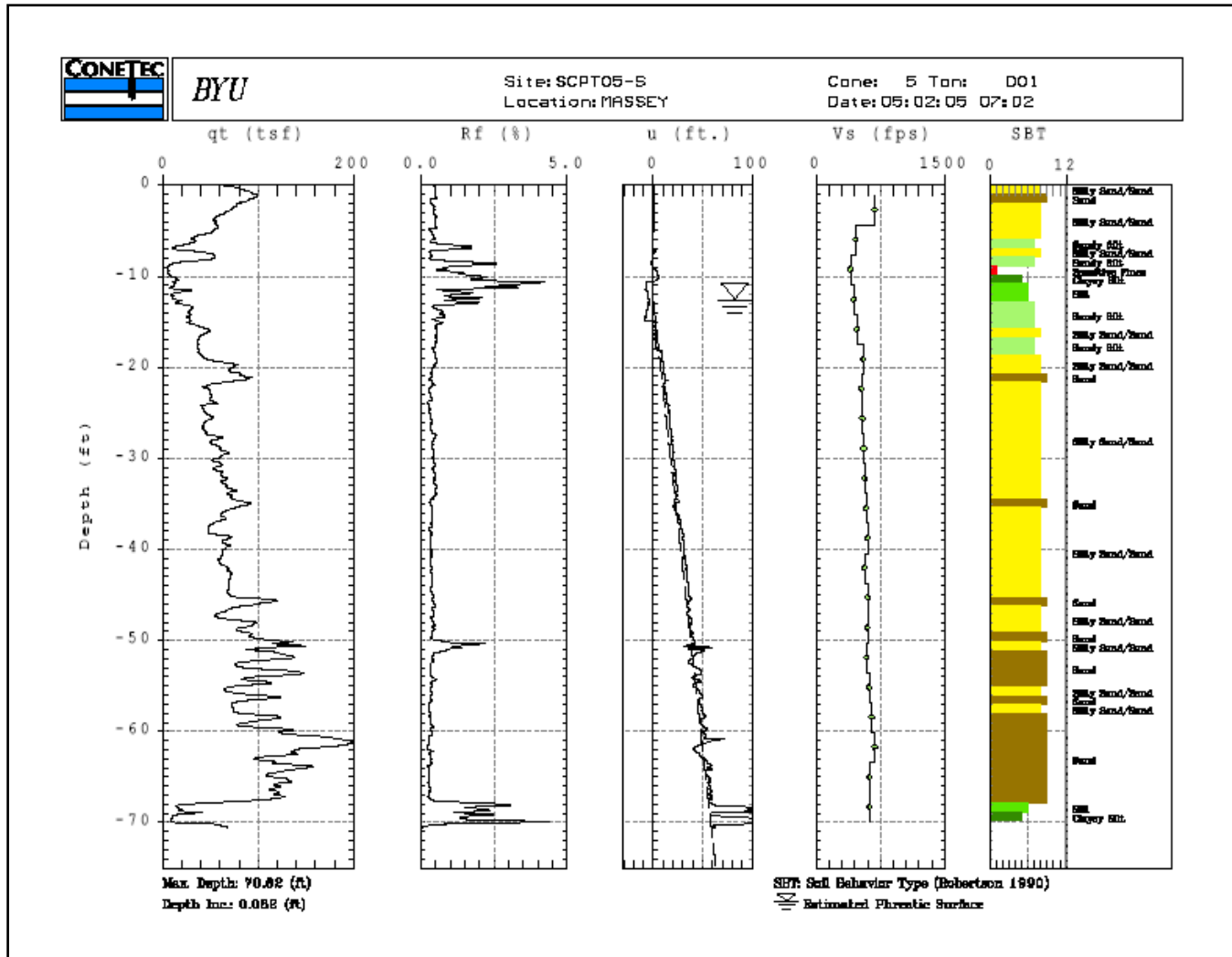


Figure 9-4 CPT Shear Wave Velocity Data Measured at Site 1

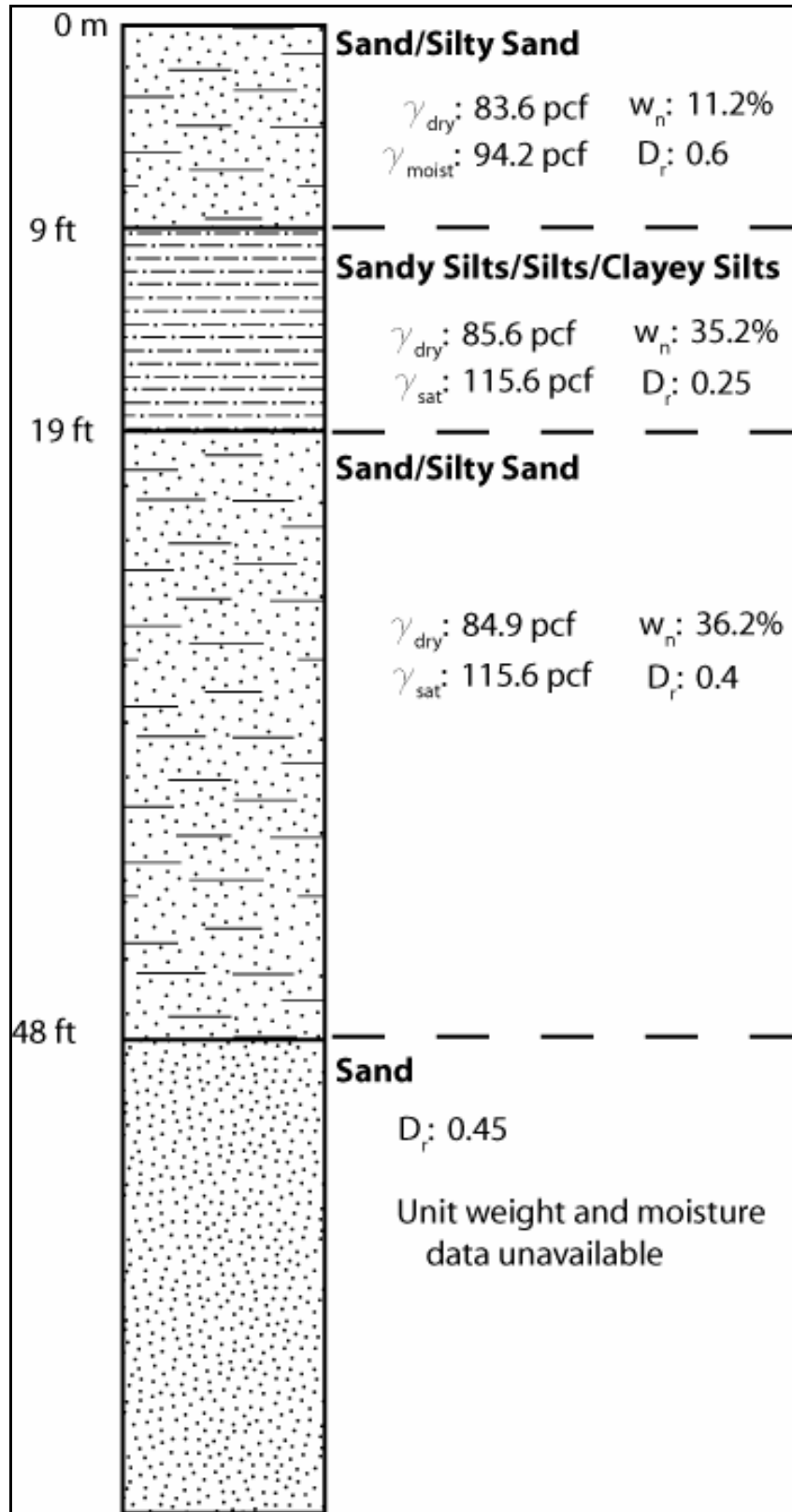


Figure 9-5 Idealized Soil Profile and Properties at Fraser River Delta Site 1

9.3 Experiment Preparation

Acceleration and pore water pressure data measured from tests conducted at Site 1 located at the south end of the site map shown in Figure 9-2 provided the validation basis for this numerical modeling research. Figure 9-6 as prepared by Spencer Strand shows the locations of the accelerometers and pore pressure transducers around the 15-ft radius blast-circle in Site 1. The center of this 15-ft radius blast-circle was located in the region between the white truck near the center of the photo shown in Figure 9-1 and the white van at the right side of the same photo. The white van shown at the right end of Figure 9-1 was the mobile data acquisition station with auxiliary power provided by a portable generator nearby.

The water table was determined by the CPT tests to be located at a depth somewhere between 9 ft to 12 ft, depending on the time and day due to tidal fluctuations known to occur at the test site. A drilling rig was used to drill and install pore pressure transducers and accelerometers at specific locations and depths around the center axis of the corresponding blast circle as shown in Figure 9-6. For each measurement device, a hole was drilled to the appropriate depth, followed by the placement of the measurement device to the bottom of the drilled hole as shown in Figure 9-7. Once the bottom of the hole was reached, the driller then activated the drilling rig to push the measurement device approximately 1 ft into the soil beneath the bottom of the drilled hole to ensure that the device was securely set in place. A bentonite slurry mix was added into the hole during the drilling process to prevent the drill hole from collapsing. After instrument installation, holes were completely backfilled with the slurry. A saturated sandy sample was extracted from one of the drill holes as shown in Figure 9-8.

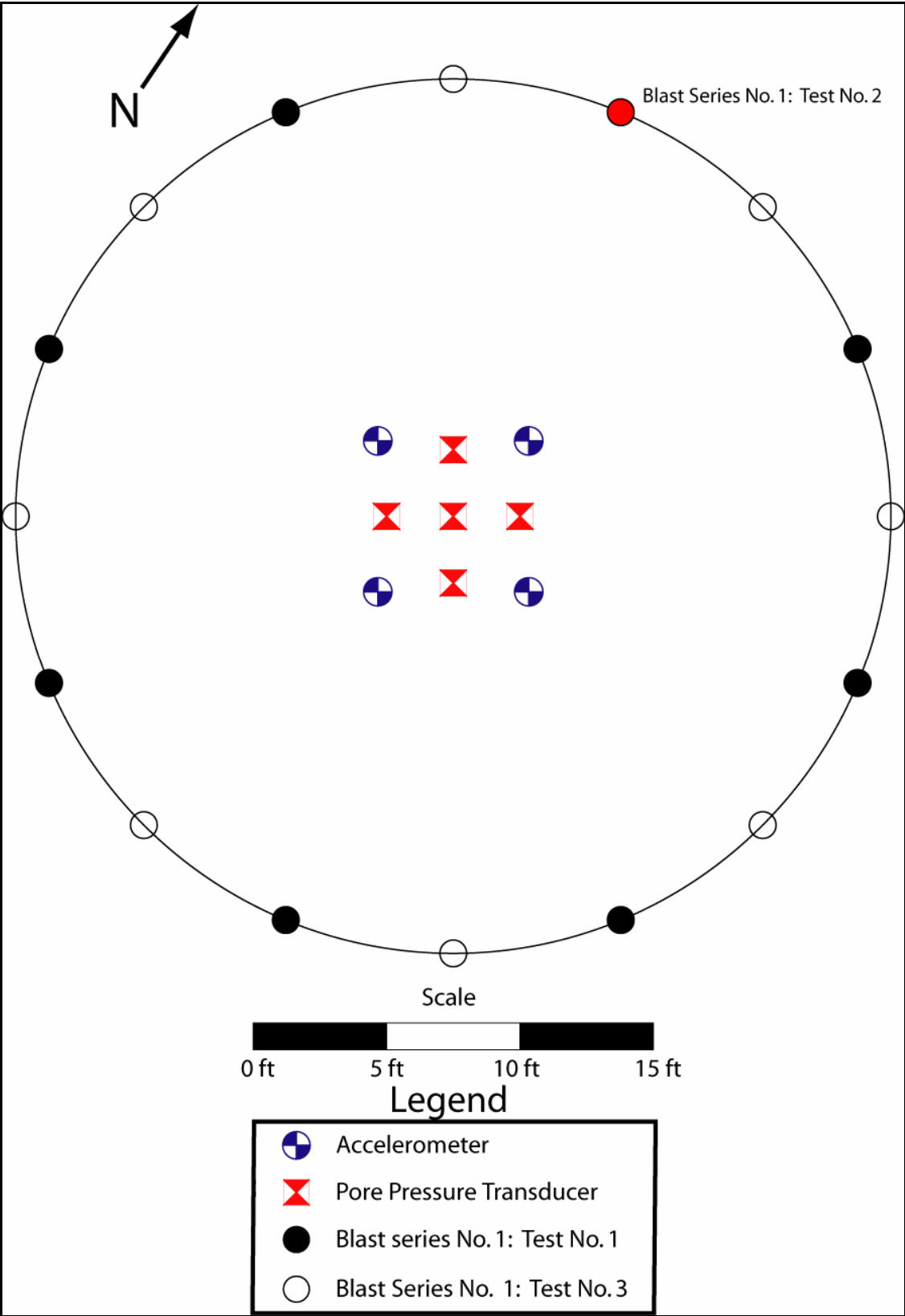


Figure 9-6 Site 1 Instrumentation Layout



Figure 9-7 **Insertion of Data Measurement Device**



Figure 9-8 **Extracted Saturated Sandy Soil Sample**

Upon completion of the CPT tests and the installation of the data capturing devices, eight blast-holes for a first test series and eight additional blast-holes for a second test series were installed using a crane-mounted vibro-hammer and steel mandrel as shown in Figure 9-9. A corrugated plastic drainpipe with an end plate attached was inserted inside the steel mandrel. The mandrel then pushed against the end plate and vibrated the drainpipe into the ground. Finally, the mandrel was extracted leaving the drainpipe in place. Difficulties in controlling the horizontal swaying motions at the top of the steel mandrel were encountered during the insertion process as shown in Figure 9-9. As a result, most of the blast-holes were installed in a slanted position at an angle of approximately 3° to 6° from the vertical axis (see Figure 9-9), resulting in a horizontal offset at the bottom of the blast hole by as much as 2 to 4 feet.



Figure 9-9 Installation of Blast-Holes by Vibro-Hammer

While inserting the southwest hole of the blast circle, the vibro-hammer was unable to push the steel pipe mandrel to the desired maximum depth of 33 feet below grade for the explosives to be placed in that hole. Upon consulting among team members, it was decided that the explosive charges in that hole would be placed at 20, 25, and 29.5 feet depths rather than 21, 28, and 33 feet depths originally planned.

The charge-depth offsets for the southeast blast-hole induced difficulties in meshing a numerical model represented by discrete elements, while both avoiding element warpage/distortions, and satisfying the maximum model size limitations of the pre-processing software. Furthermore, different explosive depths induced different shock pattern behaviors and interactions in the saturated sandy soils. As such, a direct comparison between a physics-based analysis and the measured data was not feasible to accomplish within a reasonable amount of time. Therefore, this study focuses on the last blast-series although analyses were performed for both charge detonations.

9.4 Discussion of Experiments

Originally, two test series were planned for the evaluation of liquefaction potentials at the Fraser River test site. Both test series consisted of 3 levels (or decks) of blasts at depths of 21, 28 and 33 feet, with 8 explosives evenly spaced at 45° increments around the circumference of the blast circle per level, resulting in a total of 24 charges to be detonated per test series.

Modifications to the explosive placement depths for the first blast series were necessary in order to include the southeast blast-hole that did not achieve sufficient depth during the insertion process. Depths in the southeast hole were 20, 25, and 29.5 feet instead of the pre-specified values of 21, 28, and 33 feet as described previously in

Section 9.3. The first series of blasts consisting of 24 charges with one pound of Pentex (Pentolite 50/50) explosive per charge was conducted with no surface evidence of liquefaction observed. This was verified by pore water pressure ratio computed from the pore pressure transducer data. It should be noted that the first test series was intentionally used low charge weights to avoid excessive build-up of pore water pressure. This testing program was designed to determine the charge weights necessary to gradually induce liquefaction over the course of 16 to 20 seconds as an earthquake might do rather than to immediately produce liquefaction as had been done in previous experiments (Ashford et al., 2004).

Following the first blast series, it was determined that additional explosives were required to induce liquefaction. Eight more blast-holes were installed around the same blast-circle at an offset angle of 22.5° from the first eight blast holes.

Prior to the installation of the explosives for the second test series, Dr. B. Gohl of Pacific Geodynamics recommended that a single charge with 2.5 lbs of Pentex explosives should be tested by itself at one of the blast-holes. His recommendation was to ensure that the additional explosive mass did not damage any of the pore pressure transducer in the ground as he had experienced in the past with similar charge weights and sensors. Per Dr. Gohl's recommendation, the northeast blast-hole for the next test series was chosen for a test blast using a single 2.5-lb Pentex charge. This single-charge blast became the "new" test 2. No damage was observed among any of the sensors due to the single-charge blast.

Following the single-charge test, installation of the explosive charges for test series 3 were placed in the seven blast holes shown in the bottom half of Figure 9-10.

Figure 9-11 shows one set of the explosive charges being placed into a blast-hole by the professional blaster hired for the liquefaction tests. With the northeast blast-hole used for test 2 disabled, test series 3 had a non-symmetrical blast-pattern around the circumference. Furthermore, a decision to increase the explosive weight from 2.5 lb to 3.0 lb was made after the installation of the bottom level of charges. Therefore, the final configuration consisted of 2.5 lb charges at the bottom level (at a depth of 33 feet) for 7 blast holes, followed by 3.0 lb charges at the middle (28 feet depth) and top (21 feet depth) levels for 7 blast holes each, resulting in a total of 21 set of charges. Charges were detonated one at a time with a 1-second delay between detonations. The blast sequence began with the charges on the bottom level and then moved upwards. The order of detonation for each level is designated in Figure 9-10.

At approximately blast number 17 (third charge detonation on the top level), fountains of water and minor sand boils were observed within the blast circle, providing a visual indication that soil liquefaction had occurred, although the extent of the liquefaction was not yet known at the time. Figure 9-12 shows a before and after photo in the proximity of the blast-circle and liquefied zone. The photo on the left was taken one day before the tests and the photo on the right was taken between one to two hours after blast series 3. One can easily notice the amount of ground settlements that had taken place after blast series 3.

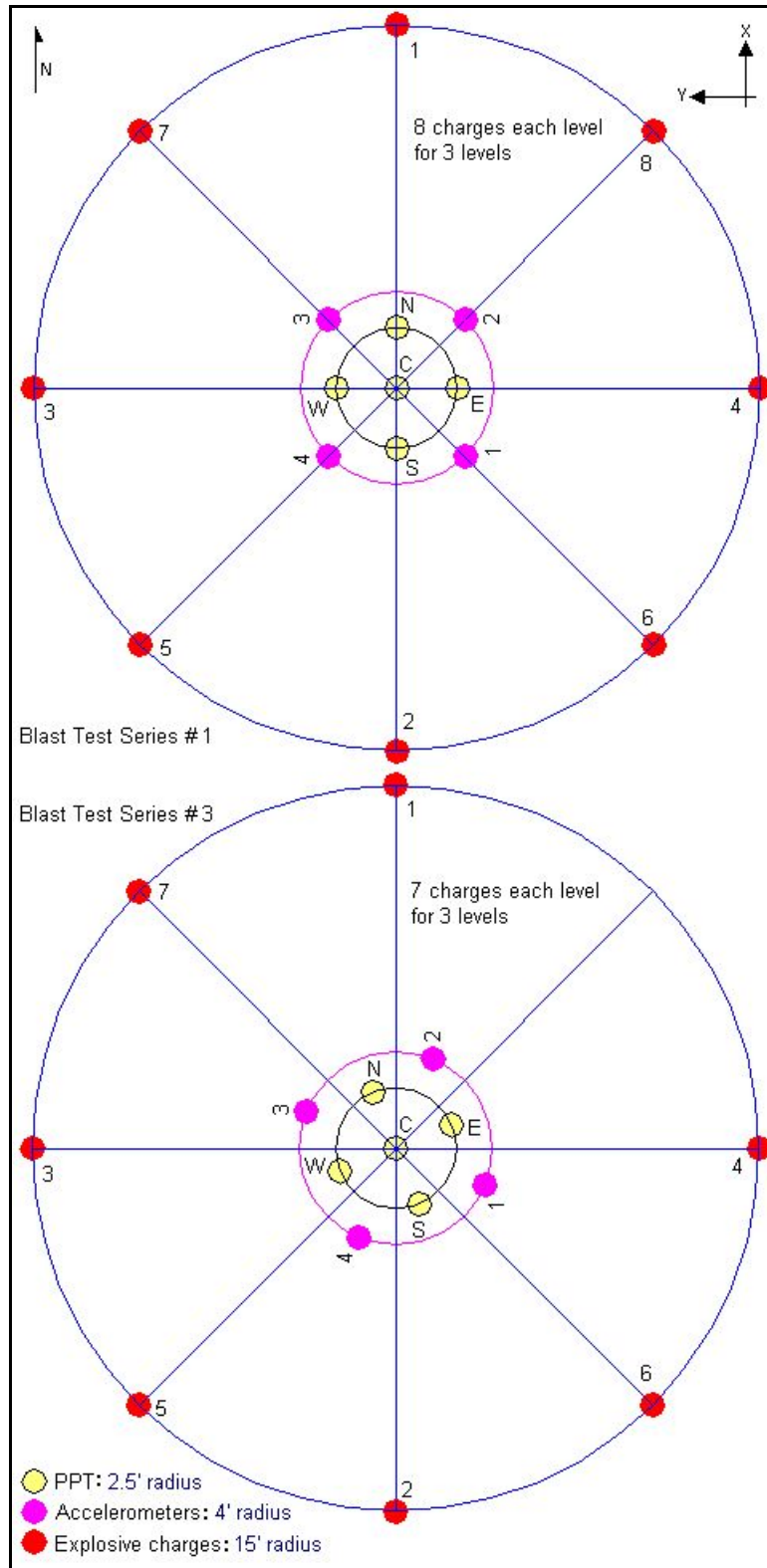


Figure 9-10 May 2005 Vancouver Blast Liquefaction Test Layout

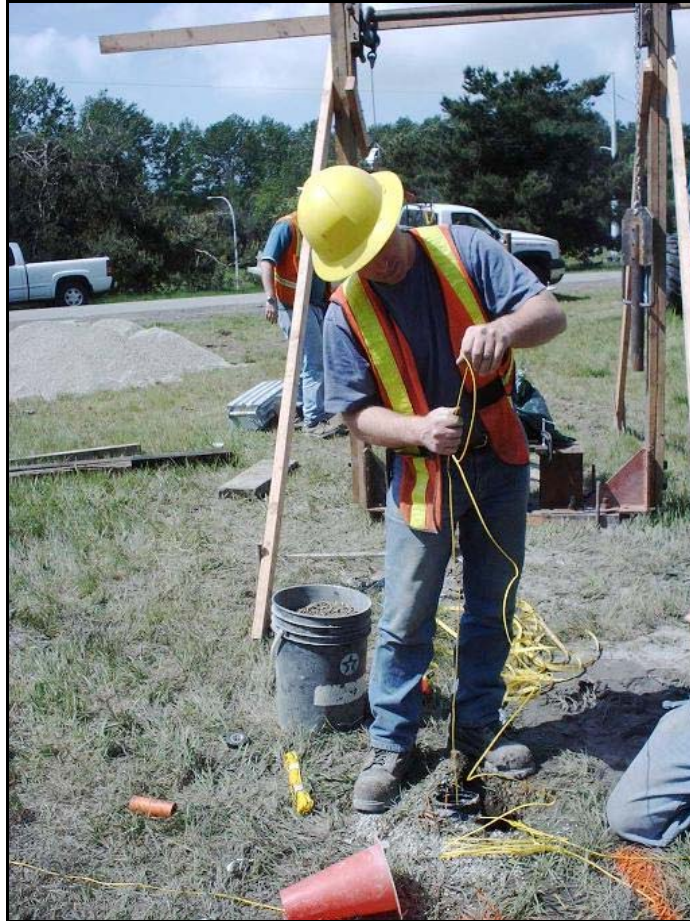


Figure 9-11 Installation of Explosive Charges



Figure 9-12 Soil Surface Before (Left) and After (Right) Blast Series 3

Figure 9-13 and Figure 9-14 show the settlements measured by string-potentiometers during blast series 1 and blast series 3, respectively. Although liquefaction was not produced during blast series 1, settlement of over 3 inches developed within 10 minutes after the blasts as pore water pressure dissipated. In contrast, the liquefaction produced by blast series 3 resulted in about 12 to 14 inches of settlement within about 10 minutes after the blasts. As a result, the maximum post-blast ground settlement within the blast circle for blast series 3 is approximately four times the corresponding amount of settlement from blast series 1.

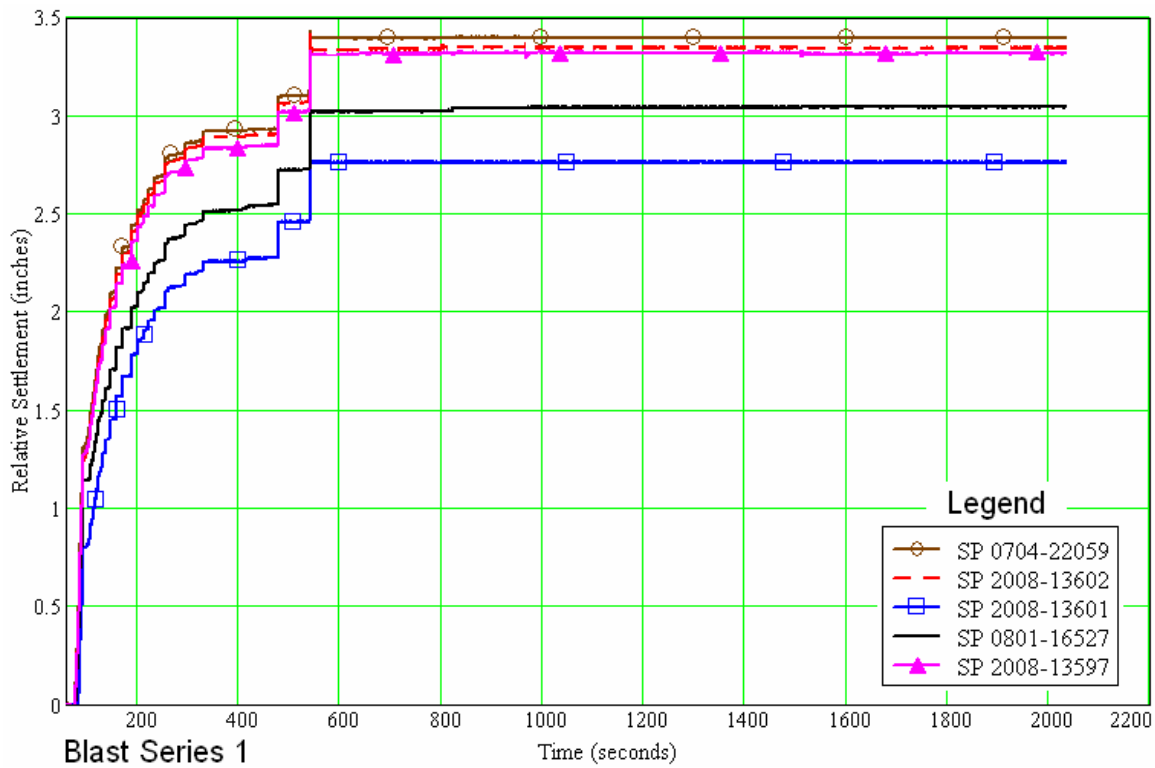


Figure 9-13 String-Potentiometer Settlement Data for Blast Series 1

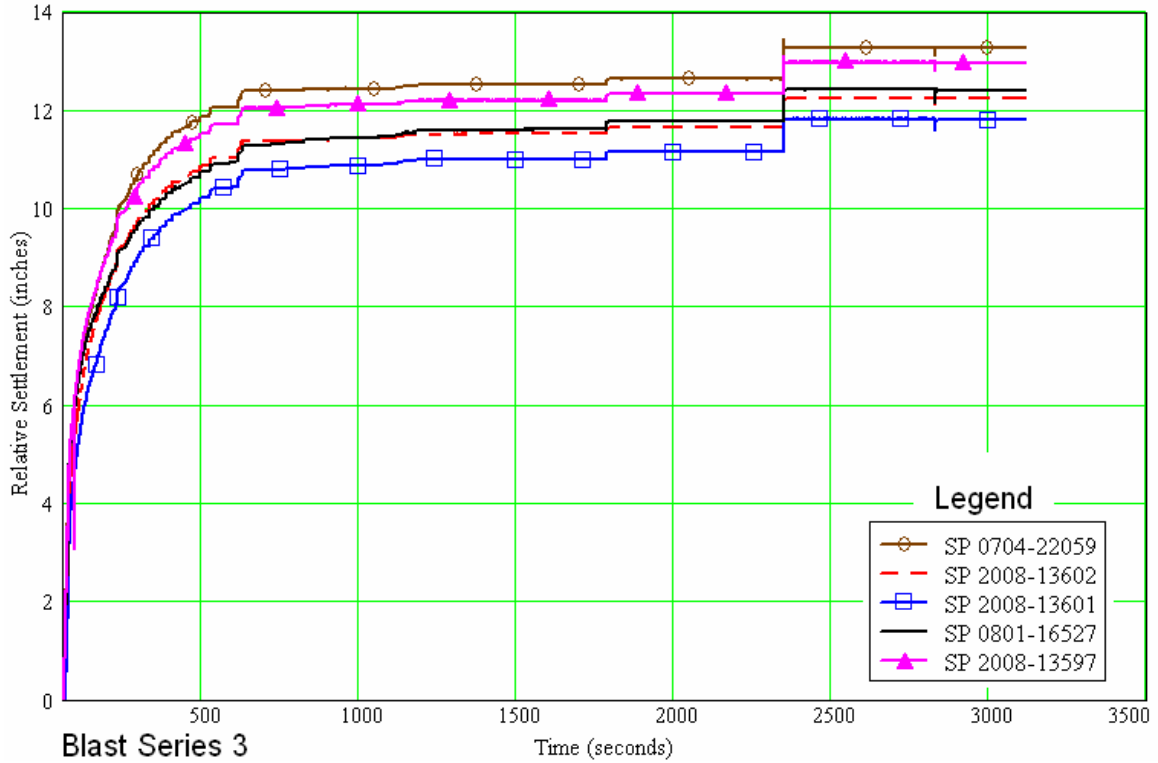


Figure 9-14 String-Potentiometer Settlement Data for Blast Series 3

9.5 Discussion of Results

Acceleration and pore-pressure time histories were measured respectively by accelerometers and pore-pressure transducers (PPT) embedded at pre-specified locations and depths within the blast circle. The location of each accelerometer is specified by measurements in three orthogonal (or X, Y, and Z) directions. During the installation, the positive X, Y and Z directions of each accelerometer were aligned in the respective north, west, and vertical directions relative to the blast circle. Four accelerometers and five PPT's were installed for the blast tests. Figure 9-10 shows the locations of both in-ground accelerometers and PPT's with respect to the blast circle, while Table 9-1 presents the corresponding coordinates of the respective in-ground sensors. Coordinates shown in Table 9-1 are in typical geotechnical conventions where +Z direction is

downward from ground surface. Given that +X is to the north, it follows that +Y in Table 9-1 is to the east. Transformations to the global FEA modeling coordinates are necessary prior to incorporating the coordinates listed in Table 9-1 into a FEA model to avoid erroneous results.

Table 9-1 Data Capturing Device Coordinates

Data Capturing Device and Location	X (ft)	Y (ft)	Z (ft)
Pore Pressure Transducer 859105 (North)	2.5	0	38
Pore Pressure Transducer 883032 (South)	-2.5	0	31
Pore Pressure Transducer 859120 (West)	0	-2.5	45
Pore Pressure Transducer 859215 (East)	0	2.5	18
Pore Pressure Transducer #856610 (Center)	0	0	25
Accelerometer (NW)	2.83	-2.83	25
Accelerometer (NE)	2.83	2.83	25
Accelerometer (SW)	-2.83	-2.83	25
Accelerometer (SE)	-2.83	2.83	25
<u>Important Note</u>			
Coordinates shown in table are with respect to center of blast circle and are based on typical geotechnical convention: +X to the north, +Y to the east, and +Z down from ground surface. This is different from the typical FEA coordinate system used for the numerical model, which is +X to the north, +Y to the west and +Z up from ground surface.			

During a routine check of instrumentations prior to blast series 1, Dave Anderson, the BYU Civil Engineering Test Laboratory Manager in charge of data acquisitions at the test site, discovered that the Z direction acceleration of accelerometer 3 had stopped functioning for some undetermined reason. A decision was made to replace the “dead” high-speed data input channel with data inputs from the center PPT for capturing an additional set of high-speed pore water pressure data. As a result, only X and Y acceleration data were obtained from accelerometer 3.

Figure 9-15 to Figure 9-18 present acceleration time histories captured by accelerometers 1 to 4, respectively, in the X, Y, and Z directions for both blast series 1 and series 3. An identification for each blast in each of the bottom, middle, and top levels is given in the X acceleration figure, with projection (dash) line down to the corresponding Y, Z and pore pressure figures.

Figure 9-17 shows the X and Y acceleration data recorded for both blast series 1 and series 3. Pore water pressure data captured for both blast series 1 and series 3 were recorded as shown at the bottom of Figure 9-17 in place of accelerometer 3's Z acceleration, which malfunctioned prior to tests as explained previously. The data acquisition system channels used for capturing accelerometer (and one PPT) data had an approximate data sampling rate 19,000 samples per second. All other channels used for PPT data were at a significantly lower approximate rate of 20 samples per second.

Figure 9-19 shows the full-duration PPT measured data for both blast series 1 and blast series 3, illustrating the amount of time required for pore-water pressure to return to approximate normal static levels prior to blasts. Figure 9-20 shows the pore-pressure histories corresponding to the duration of the blasts. The total amount of explosive charge used for blast series 1 was 24 lbs, whereas the total amount of explosive charge used for blast series 3 was 59.5 lbs, which is almost 2.5 times the amount used in blast series 1. Although the total explosive charge amount used in blast 3 is ~2.5 times (or 250 %) greater than blast 1, the corresponding peak pore water pressure for blast 3 is only about 50% greater than blast 1.

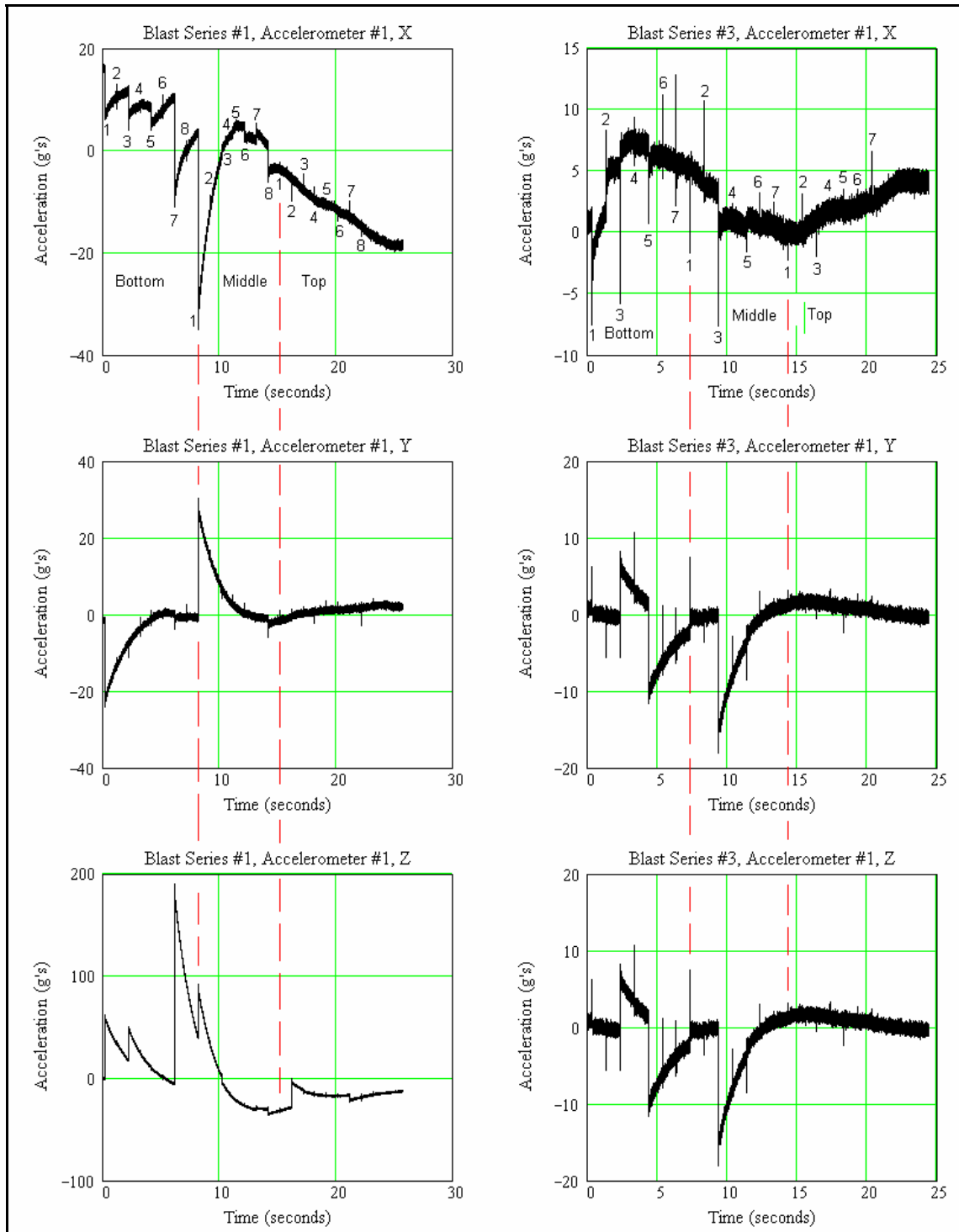


Figure 9-15 Accelerometer 1 Measured Time Histories

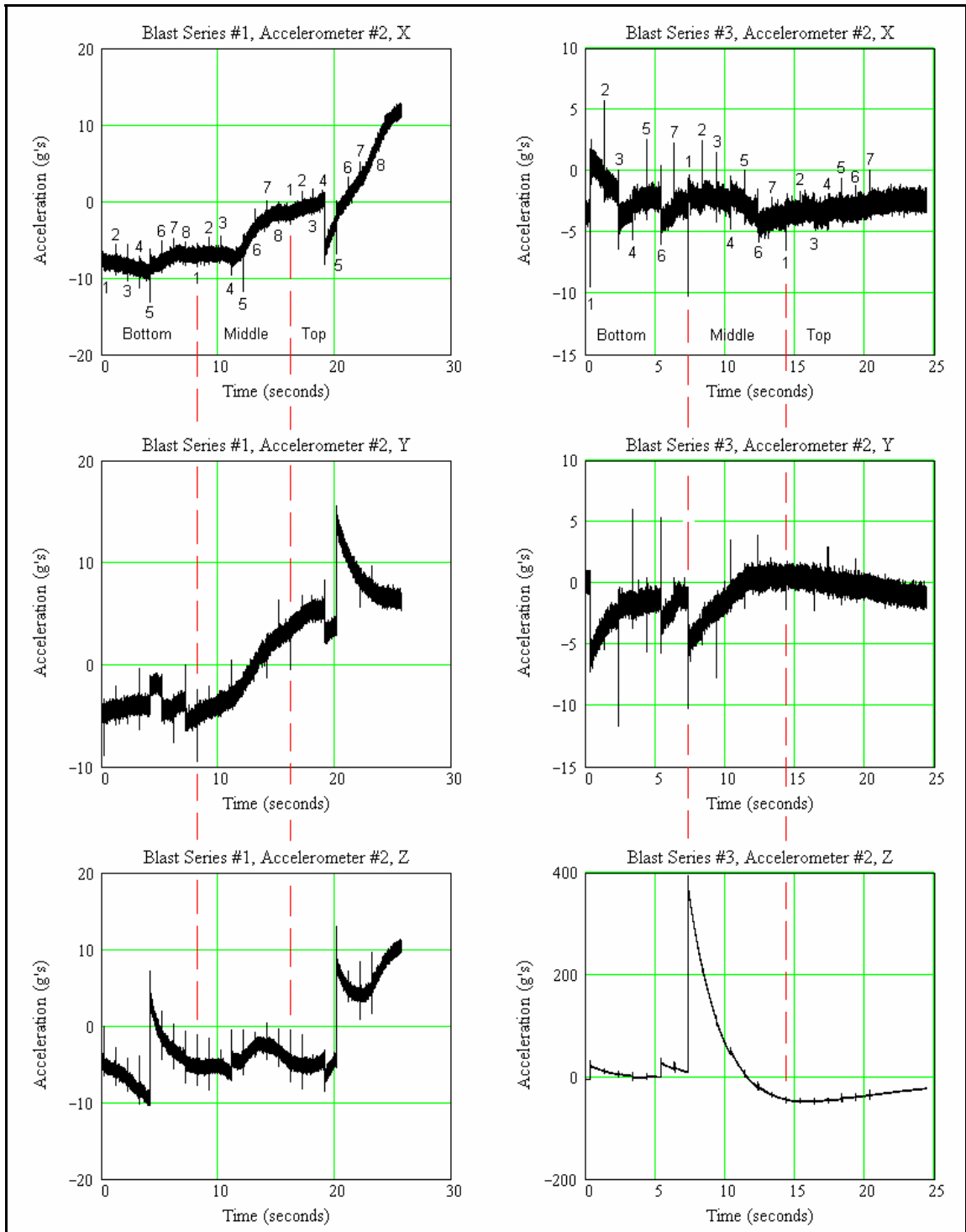


Figure 9-16 Accelerometer 2 Measured Time Histories

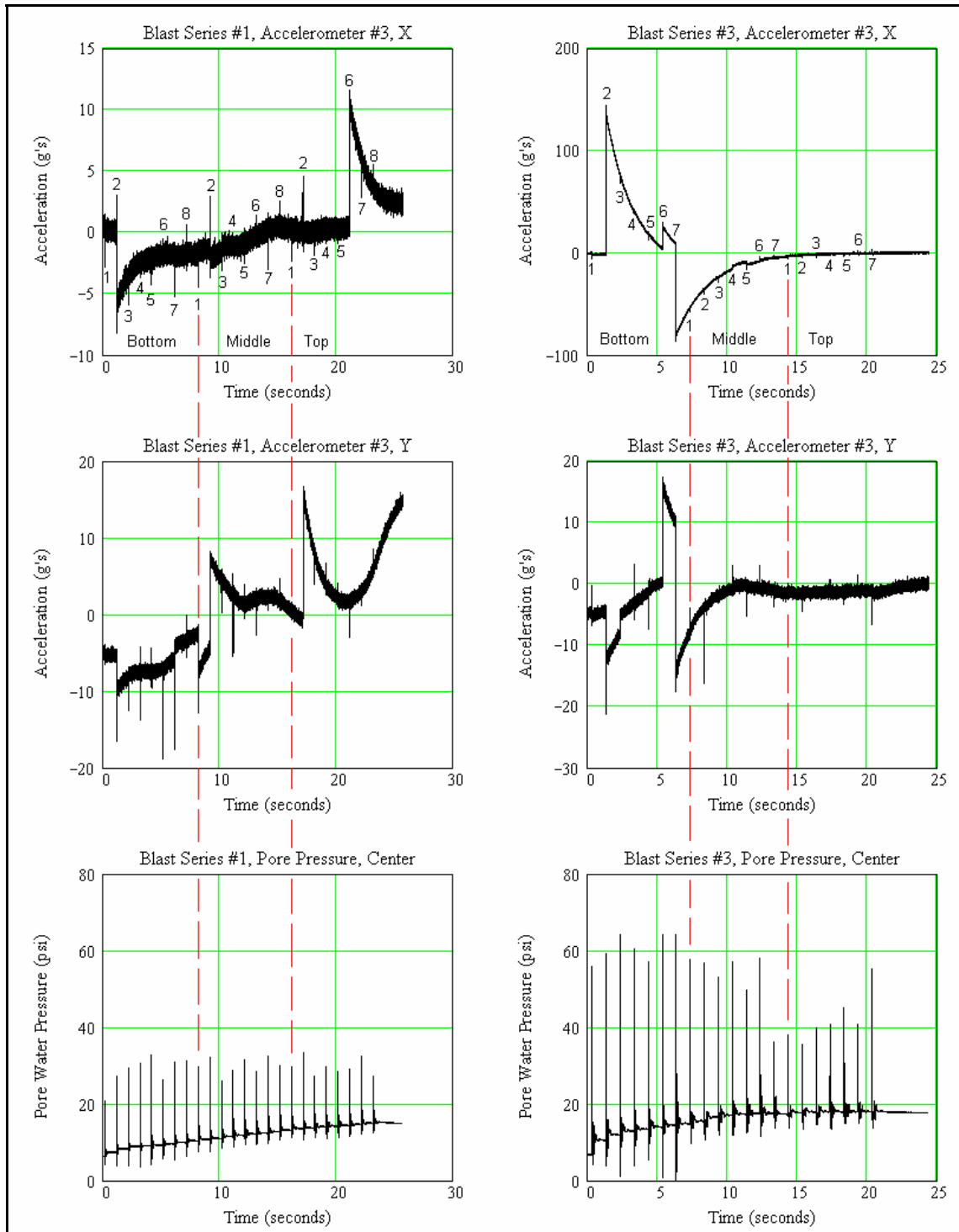


Figure 9-17 Accelerometer 3 and Center PPT Measurements

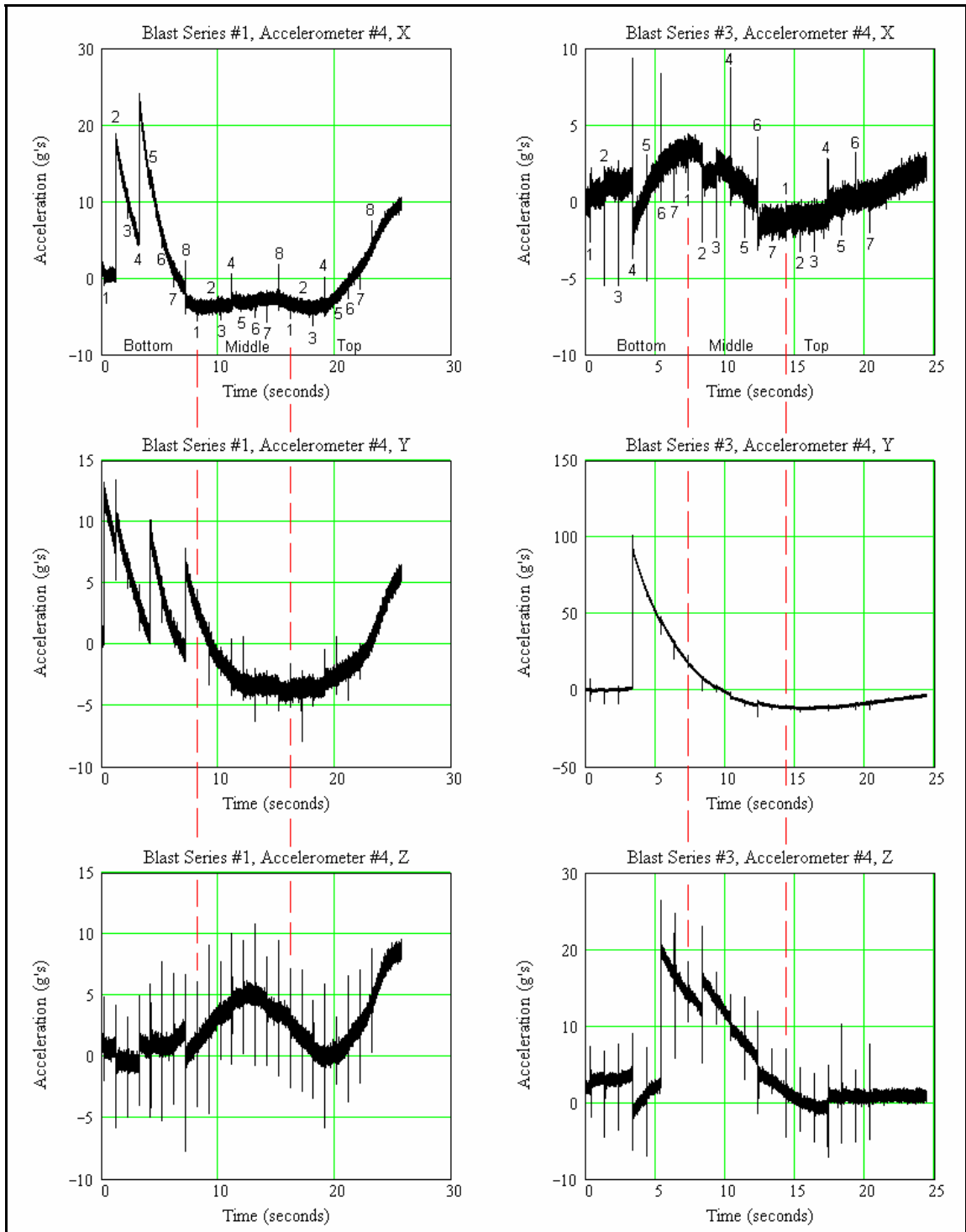


Figure 9-18 Accelerometer 4 Measured Time Histories

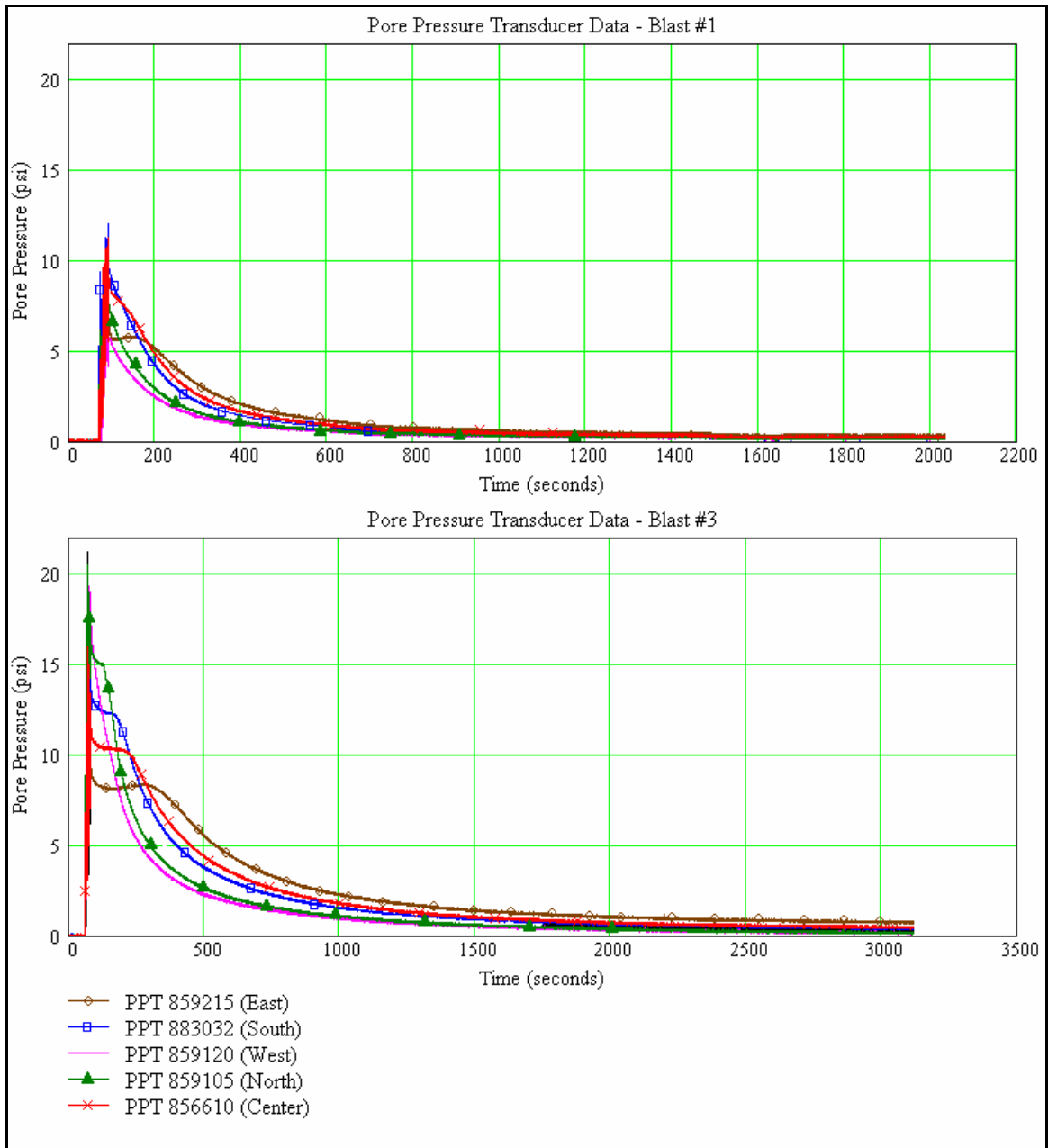


Figure 9-19 Full Duration PPT Data

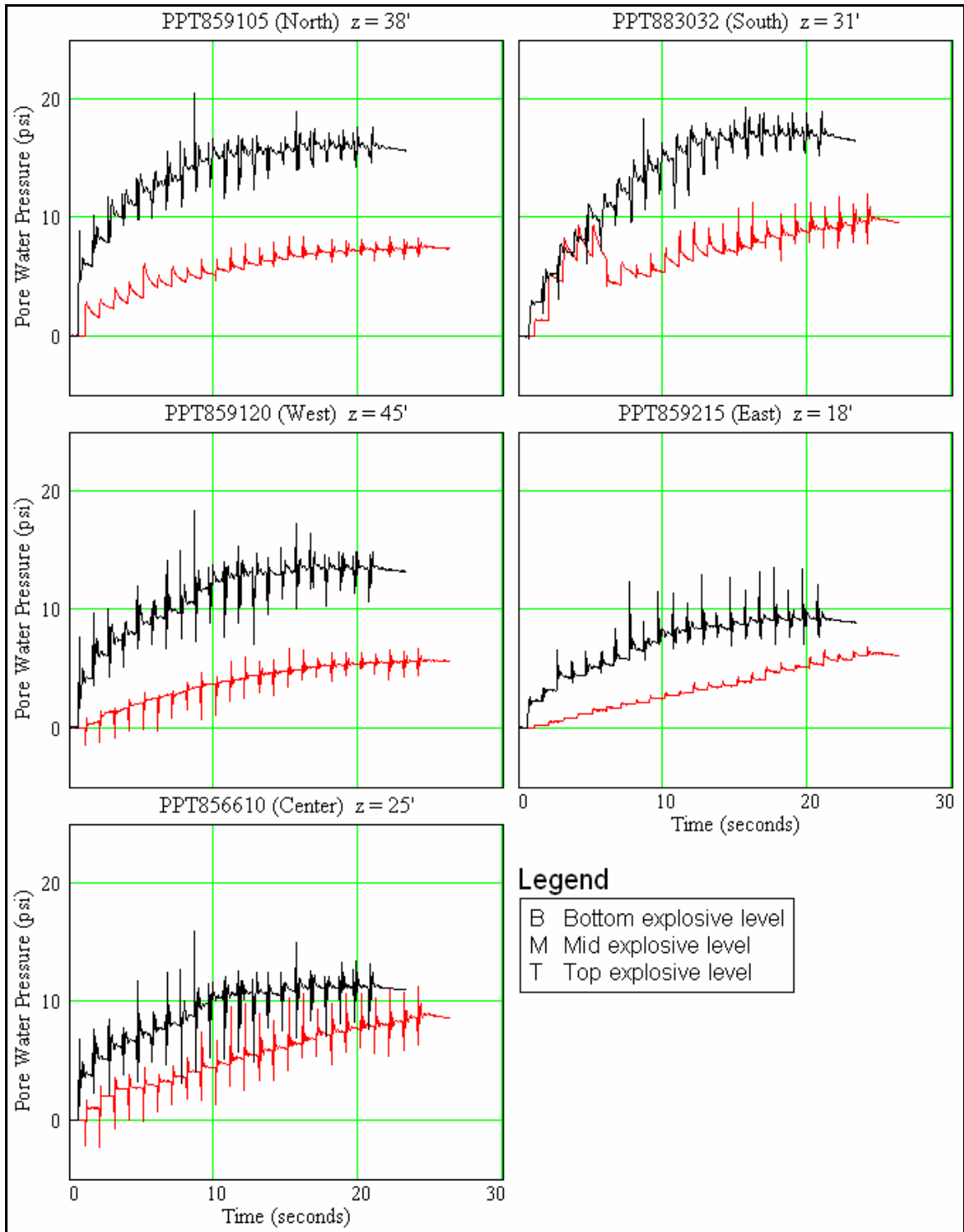


Figure 9-20 Blast Duration PPT Data

Acceleration data as shown in Figure 9-15 to Figure 9-18 cannot be used directly to compute velocity and displacement via numerical integration schemes due to the apparently random jumps and magnitude shifts along each time history. Magnitude-offset or drift adjustment schemes (Chang, 2002) that are designed for noise filtration of test data and drift reduction can provide some conditioning relative to the acceleration data. However, they were not sufficient to permit successful numerical integration to obtaining reasonable velocity and displacement results. This inability in conditioning the data mainly stems from the acceleration curves that are either positive or negative pulse dominant, rather than a balance between positive and negative pulses. Positive (or negative) dominant accelerations produce large positive (or negative) displacements, implying that the ground itself is in motion (i.e. moving away relative to the surrounding soil regions). Such displacements are unrealistic due to restraints induced by semi-infinite medium of soil materials in all but the vertically upward direction.

It is also somewhat puzzling how the accelerometers responded mainly in one direction when the shock waves hit without a similar rebound in the opposite direction before oscillating back to zero, considering that the instruments remained in place afterward. Characteristics such as those unshifted or unfiltered data shown in Figure 9-15 through Figure 9-18 appeared as though they are induced by excessive noise, over-damping, insufficient recovery rate from a “capacitor discharge” of data signals, or other undetermined reasons. Further investigations are recommended to resolve the issues prior to future experiments. In summary, several potential sources that may have contributed to the uncharacteristic magnitude shifts in the unfiltered acceleration data, as well as those observed in the south PPT as shown in Figure 9-20, are:

1. Accelerometer's measurement range is much greater than measured. The noise level in high-magnitude data measurement devices may be too high for low-magnitude applications. Sensitivity of the devices for capturing low magnitude data may not be sufficient with respect to the corresponding noise level.
2. Saturated sandy soil at the test site has much greater variability than expected, causing differential reactions at locations of data capturing devices that become sources for localized motions.
3. Blast orders may not be as specified, resulting in jumps and shifts that are not synchronized with expected blast orders.
4. Slanted blast holes with noticeable horizontal and corresponding vertical offsets for the locations and depths of the explosive materials (see Figure 9-9) can create potentially undesirable and non-symmetrical pressure distributions and shock interactions in the saturated sandy soil. At fixed data capturing locations, blast-waves may be much higher (or lower) than expected with respect to the distance offset from the planned locations of the blasts.
5. Accelerometers and PPT's were pushed into saturated sandy soils at the bottom of drilled holes that were filled with a thick, slurry compound. For a sequential blast series, the shock waves from the first (one or more) blasts may open up the soils surrounding the sensor sufficiently for the viscous fluid to seep into gaps adjacent to the sensor. A viscous mix adjacent to the sensor can form a "dampening" barrier layer around the devices for subsequent blasts. This may explain why most of the horizontal (X and Y) accelerations

observed in blast series 3 were smaller than acceleration peaks recorded from blast series 1 even though significantly more explosives were used for blast series 3..

6. If stiff, saturated sand particles, rather than the viscous slurry mix, moved into the sides of the sensors, then the sand layer may compact during the settlement period after blast series 1. Under such a scenario, greater, instead of smaller, accelerations from blast 3 would be transmitted into the measurement devices due to greater stiffnesses in the compacted sand. Since it is uncertain when and where item 5 or item 6 could or did occur, some degree of randomness can be expected.

There could potentially be other reasons that are not listed here which may also contribute to the behaviors in the measured data as discussed. However likely or unlikely, resolutions, improvements, and development of greater understanding to minimize such data responses are warranted for future applications.

10 Discussion of Baseline Model Analysis

10.1 Overview

The previous chapters of this dissertation discussed the requirements, trade studies, approaches, and conditions assumed in developing a numerical model to simulate blast-induced liquefaction, followed by an overview of the Vancouver experiments to be evaluated. This chapter summarizes and organizes information discussed for the development of the baseline numerical models. Chapter 11 presents a detailed discussion of the baseline analysis and its results. Conclusions and recommendations for the research are presented in Chapters 12.

10.2 Fundamental Assumptions and Methodology

As discussed in Chapter 9, faulty blast-hole depths installed in test-series 1 induced additional complexity, run time, significant initial element warpage, and changes in locations/directions of shock wave interactions. As such, one can expect errors and differences to be observed in a direct comparison between theoretical/predicted results using uniformly placed explosives against test data measured in faulty blast-hole depths. Since the misplacements of explosive depths occurred in only one out of eight blast-holes, one expected a minimum of 10 to 15% errors can be observed in the predicted results from an analysis with uniformly placed explosives against the corresponding

measured data. Therefore, the baseline modeling effort were developed based on calibrations against results from blast series 3 where uniformly placed explosives were installed. Nevertheless, analysis representing test-series 1 was conducted and compared against the corresponding measured data in spite of the misplacements of the explosives for future references and completeness of this research effort.

In the analysis for blast series 3, there were three blast levels with 7 explosives per level embedded into the baseline model, resulted in 21 controlled blasts as described in Chapter 9. Explosive charges in the bottom level were 2.5 lbs each, whereas the corresponding charges in the middle and top levels were 3.0 lbs each.

In the May 2005 Vancouver blast experiment, detonations of the charged were spaced at 1-second intervals. Bottom level explosive charges were detonated sequentially around the circumference of the blast circle in the order as shown in Figure 10-1, followed by the detonations of the middle and upper levels of explosive charges in the same blast sequence around the circumference of the blast circle.

The event time needed to simulate a tri-level, 21-charge sequential blasts is at least 22 seconds. For explicit analyses used to simulate shock physics events, a 22+ seconds event time can appear as “eternity” since each time step in an explicit blast analysis is typically in the order between microseconds (10^{-6} seconds) and nanoseconds (10^{-9} seconds). Additionally, neither the blast layout configuration nor the corresponding blast sequence is symmetrical around the center of the blast circle. Therefore, symmetry boundary conditions cannot be applied to simplify the analysis task.

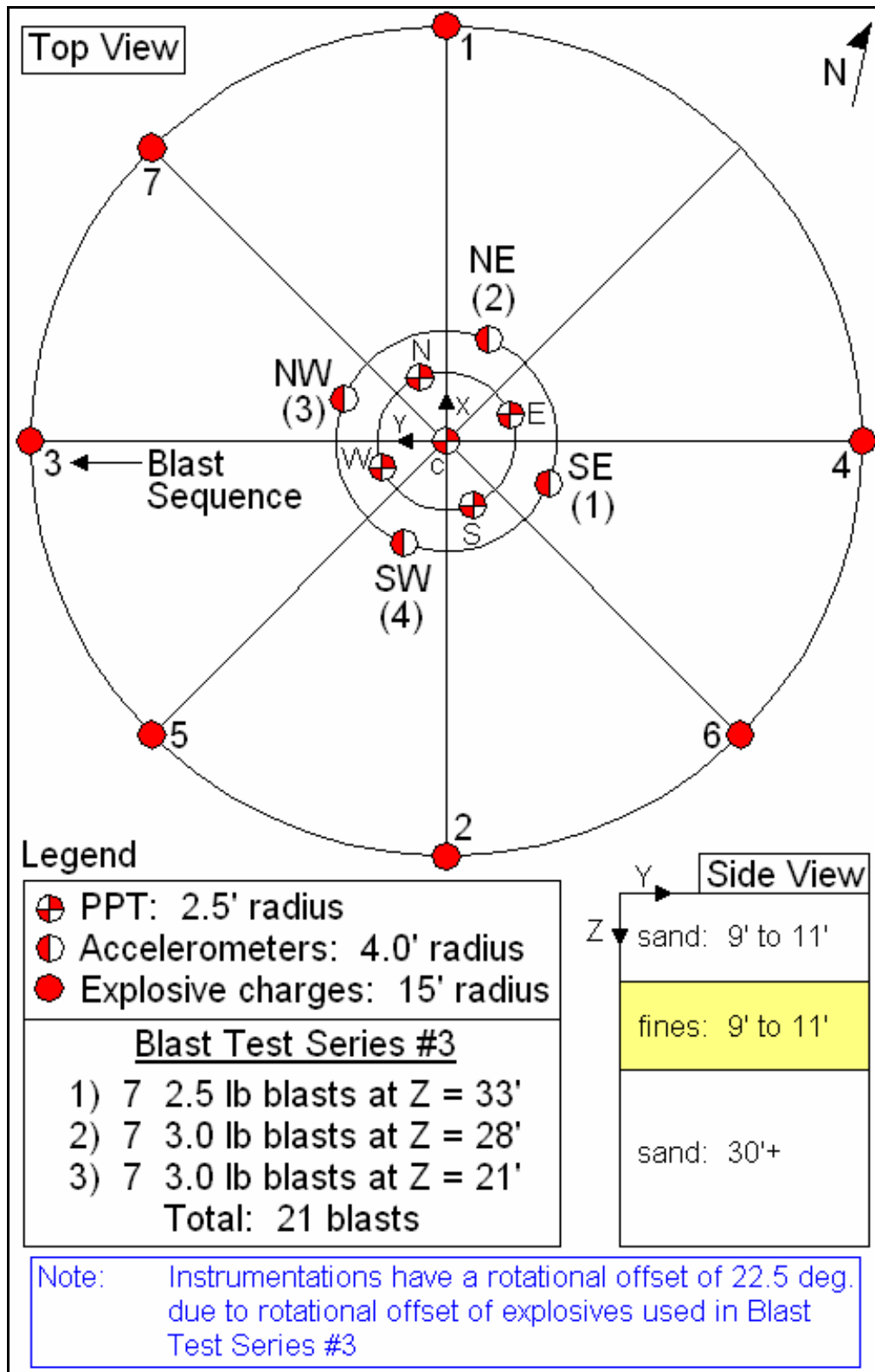


Figure 10-1 Liquefaction Test Instrumentation Layout and Blast Sequence

At the beginning of the research, the author estimated based on test runs that it would take a clock time over 200 days to perform one simulation analysis of a full 22+ seconds event duration. Furthermore, every additional complication over and beyond the long duration issues at hand can potentially render the evaluation process more infeasible to complete within a reasonable amount of time. Since multiple analysis runs were expected to calibrate the necessary input parameters, something had to be done to increase the feasibility of the analysis effort. Therefore, extra effort was made throughout the research to reduce the required run time, as well as to balance the complexity of the model and analysis approach against process feasibility and accuracy. It should be noted that every simplification or assumption applied to the analysis was carefully examined to ensure sufficient conservatisms and to minimize potential errors.

One of the earliest steps used to increase both analytical feasibility and success was to focus on shortening the total run time. After carefully examining preliminary single-blast test run results and the measured test data, the author observed that the transient portion of each controlled blast typically subsided within 0.2 seconds upon detonation. Therefore, analysis for each blast beyond 0.20 seconds of event duration consisted of mainly steady state oscillations and after-effects from the corresponding controlled detonation. It followed that one of the potential simplifications that could be made was to account for only the transient effects by reducing the simulated blast interval time from 1 second to 0.2 seconds. This event-duration reduction process resulted in a nearly 5-fold decrease of analysis run time from 200+ days to approximately 42+ days. Although the 42+ days analysis run time is still too long for any potential iterative process required to calibrate input parameters, the run time reduction caused the analysis

tasks to become more manageable, and provided greater probabilities for successful completion of the research within a reasonable amount of time. Therefore, the author adopted this blast-interval reduction approach while concurrently searching for ways to further reduce the analysis cycle time.

In order to properly compare against measured data at a blast interval of 1 second, results subsequent to the first blast were “stretched” by 0.8 seconds along the time domain at the end of each 0.2 seconds blast-interval and at moment just before the initiation of the next blast when transient effects has or nearly subsided. This process essentially ignores the negligible steady state oscillatory effects between 0.2 seconds and 1 second of event time between blasts by replacing it with a pre-determined, horizontal line across the time domain. Since the transient effects are in most cases much more significant and observable than the corresponding steady state oscillatory motion, the duration reduction process described here produces a much more simplified and feasible analysis approach.

LS-DYNA, a widely accepted commercial explicit and implicit finite element analysis (FEA) based hydro-code for the evaluations of shock physics problems, was the baseline solver. The Arbitrary LaGrangian-Eulerian (ALE) method was chosen originally for the solutions of the blast-induced liquefaction evaluations because of its general ability to achieve LaGrangian method’s accuracy, combined with Eulerian method’s stability. However, due to the excessive “per analysis” run time (i.e. 42+ days) described above, and unexpected computational instability issues encountered while using the baseline soil material model, the original baseline model was completely overhauled and refined midway through the research. Additionally, a change in analysis

method from ALE to the simpler LaGrangian approach was applied as a part of the overhaul process to further reduce complexity and run time without noticeable reduction in accuracy and stability. The overhaul process resulted in an additional reduction in analysis run time by nearly an order of magnitude without sacrificing noticeable numerical accuracy and stability. Details of the analysis' evolution and overhaul process will be presented later in this section.

Other fundamental limitations to the baseline numerical model used for this research have been presented in the previous chapters of this dissertation; they will not be repeated here.

10.3 ALE Analysis Distortion and Stability Controls

Early in the research while performing test runs using the ALE method of solutions, convergence difficulties were observed due to numerical instabilities, and excess deformations / distortions at regions immediately adjacent to explosive materials. Two analysis options could be applied to reduce the distortions and the corresponding instabilities associated with high magnitude impulsive loads.

First, a small "sacrificial" region with low compressibility (i.e. high bulk modulus) can be placed directly adjacent to the explosive materials for load transfer purposes. This sacrificial region can typically be modeled with high bulk materials such as water or solid material consisting of some sort of weighted average bulk modulus of water and soil. If the sacrificial region is sufficiently small and the regions where responses are to be observed are adequately far from the blast region, then the sacrificial region approach is a viable approach with negligible errors (i.e. $< 1\%$) as demonstrated by single blast test runs performed early in the research. Applying water or water/soil

mixed sacrificial region is suitable for fully saturated soils adjacent to explosive materials, especially when one is uncertain on whether just water or some sort of water / soil mixtures are surrounding the explosive materials in the field.

Second, the element expansion limit (EXPLIM) for ALE analyses can be set to increase the frequency of Eulerian advections while reducing the amount of LaGrangian motions allowed in between advection steps. The EXPLIM parameter is defined in *ALE_REFERENCE_SYSTEM_GROUP, one of LS-DYNA's ALE analysis definition commands. This EXPLIM parameter is not applicable to LaGrangian analyses. Determination of the value for EXPLIM can be challenging without considering effects of convergence, numerical instabilities due to excess element distortions, and mesh motions in between advections. A parameter that deals with mesh motions which interrelate with EXPLIM is the PRTYPE parameter in the same LS-DYNA command. The PRTYPE parameter allows users to specify the type of motion reference system (i.e. Eulerian, LaGrangian, etc.) to be applied for an ALE analysis. According to an email communication with the author of the Eulerian and ALE capabilities in LS-DYNA, PRTYPE "has nothing to do with the advection itself, it has to do with the mesh motion, and how to move the mesh before advection" (Souli, 2005).

Both the sacrificial region and the element expansion limit approaches were applied to the original baseline model. For the sacrificial region option, an iterative approach on the bulk modulus of the small sacrificial region was applied until numerical instabilities were subsided sufficiently for the analysis to continue without crashing due to excessive element distortions. As for the element expansion limit, a trade study was

performed to evaluate the effects of setting allowable element expansion and shrinkage for the LaGrangian steps. Figure 10-2 summarizes the trade study's results.

As the value of EXPLIM drops below 1.20, the number of analysis iterations increase substantially, indicating that convergence is the controlling factor at this end of the spectrum. Toward the end of 1 second, the analyses have trouble maintaining convergence.

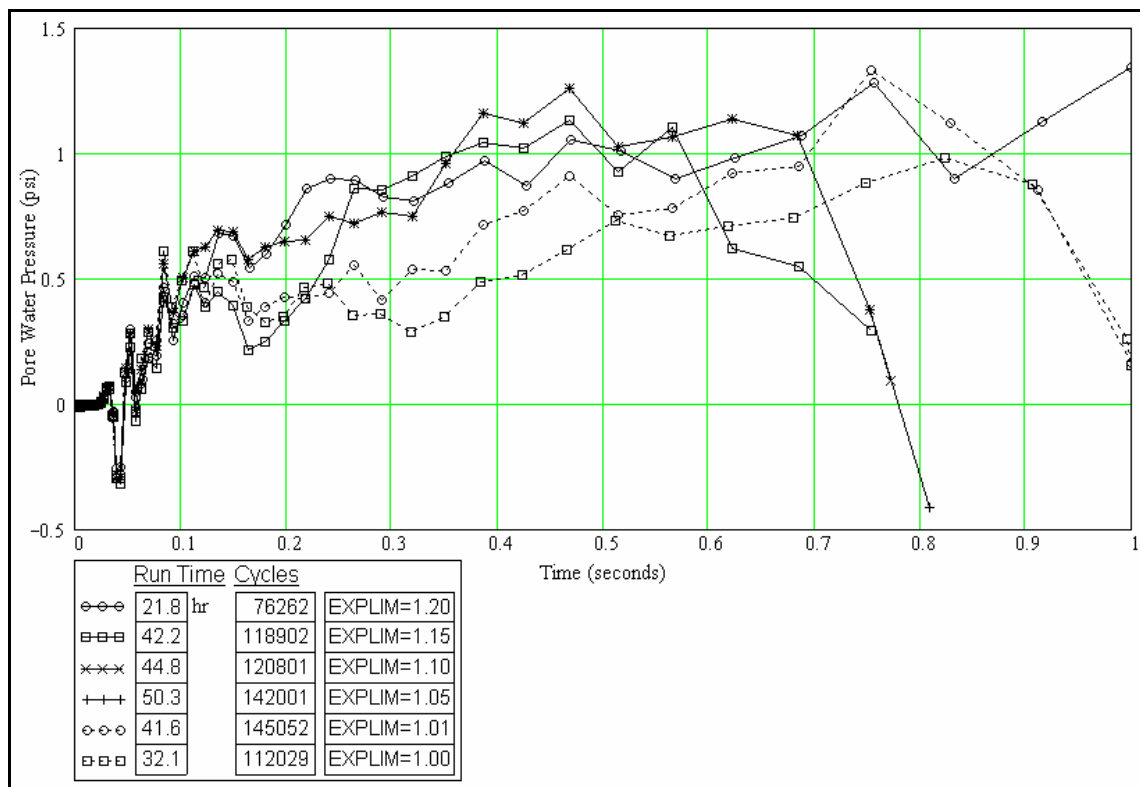


Figure 10-2 ALE Analysis Element Expansion Limit Trade Study

On the other hand, as the value of EXPLIM increase beyond 1.20, increasing numerical instabilities due to excessive element distortions resulted in pre-mature crashes of the analysis runs. As such, results for runs made with an EXPLIM value greater than

1.20 are not included in Figure 10-2. An EXPLIM value of 1.20 appears to be reasonable for the simulation of the blast-induced liquefaction analysis. One must realize that the appropriate value of EXPLIM changes in accordance with multiple factors including load application rate, materials, etc. As such, small test runs similar to those performed in this dissertation research are highly recommended prior to running a large, long duration analysis.

10.4 Boundary Environments

As discussed in Section 6.5.3, the baseline half-space model assumes that its top surface is exposed to air while sides and bottom of the model are continuous indefinitely. As such, top of the model is unconstrained, simulating the ability for pressure to escape into air (which is a medium with negligible shock impedance with respect to solid soil particles and water). Sides and bottom of the baseline model cannot be represented by symmetry constraints as one may consider in implicit analysis due to “reflections” of blast-induced shock waves that can be detrimental to the structural integrity of the model. Potential for erroneous results can also be expected if symmetry or normal constraints are applied along the sides and bottom surfaces of the model.

A special boundary condition exclusive for explicit analyses called impedance matching is most appropriate for surfaces of a model or interfacing infinite continuum with materials identical to those modeled along the interface. As explained in Section 6.5.3, impedance matching is not a constraint as one envisions in implicit analysis; it simply matches the shock impedances along an interface to prevent shock waves from reflecting back into the model or dissipating into thin air, thereby preventing undesirable results. Deformations/displacements do occur in impedance matched boundary surfaces

as in infinite media subjected to highly impulsive and high magnitude loading environments.

10.5 Loading Environments

Applied blast-loads for the baseline model were generated by embedded-explosives utilizing the widely accepted JWL programmed burn EOS, with additional hydrodynamic properties defined for the baseline explosive material. The explosive material available and used for the May 2005 Vancouver blast-induced liquefaction test was Pentex (Pentolite 50/50). Properties of Pentex were readily available from multiple published sources as discussed in Chapter 8.

10.6 Model Output Interval Size Control

During the earlier stage of the research, it was discovered that in order to capture the spikes (or transient effects) throughout the simulation of a 21-blast series, a minimum output result saving interval of approximately 10 microseconds (i.e. 10^{-6} seconds) or less is necessary. At an result output interval of 5 microseconds, the 21-blast analysis would require over 400 gigabytes (GB) of disk space, which is neither cost effective nor feasible to do within a reasonable amount of time and with finite resources. Furthermore, it is neither practical nor a good engineering practice to retrieve so much output data. Although LS-DYNA has the ability to allow variable data saving increments, it is difficult to estimate the arrival time of shock waves due to variable time delays induced by multiple, concurrent and non-equal distance from each location of instrumentation to each blast source. After careful considerations and prioritization of the most important aspects of the analysis, it was determined that the most significant feature of the results to

focus and to capture is the overall trend of the pore pressure build-up characteristics. As long as one can see the distinction of each burst pulse and the overall shape of the pore pressure build-up, one can determine the merits of the numerical model without having to know the absolute peak value of each blast pulse spike. Additionally, the actual magnitude of each blast-induced spike is not critical in modeling the development of soil liquefaction.

Pressure spikes are typically high frequency responses to impulsive loads, or “pings.” Data capturing devices function at discrete, or non-continuous, time interval. Since transient responses generally occur at high frequencies with noticeable variabilities due to various reasons, digital data instrumentations seldom capture complete peaks of spikes throughout a multi-load event. In other words, the absolute peak of each pulse more often than not falls in between two successive data recording instances. As a result, there is no assured way to capture the absolute peak of each spike. With that in mind, it was determined from the beginning of the research that the data capturing rate would be set to intervals that would limit the total amount of output disk space to within 5 to 7 GB, preferably less than 5 GB, for both feasibility and processibility reasons. The amount of disk space required for results is controlled by both the model size and the resulting capturing intervals.

For the final baseline model used to simulate blast series 3 with 21 blasts, the result output interval is approximately 0.01 seconds in order to maintain a limit of 5GB for outputs. The 0.01 seconds interval is significantly wider in time than 5 to 10 microseconds. As such, some dilution of high frequency responses can be expected, especially toward the end of the blast series where cumulative numerical round-off in the

time domain (i.e. current simulation time in seconds while time steps continues to be in between micro- to nano-seconds) becomes more apparent. This occurrence is another reason why explicit analysis typically deals with short (i.e. milliseconds), impulsive events.

While a wider output interval has the potential of not being able to view the complete spike characteristics in the results, spike characteristics are indeed captured in the actual analysis itself since the maximum time step required for stable solutions under blast environments is below 3 microseconds. A typical time step for the final baseline analysis ranges from 2 microseconds down to tens of nanoseconds, which is more than adequate to capture most transient blast effects.

In summary, blast induced spikes are captured in actual analysis due to small explicit analysis time steps of less than 3 microseconds that are required for stability reasons. Although spikes are captured in the analysis, probabilities for displaying them during post processing are remote due to the much larger output interval (i.e. 0.01 seconds) required to maintain reasonable and manageable disk space consumption for each analysis run. Nevertheless, since the expected width of a spike pulse is approximately a few milliseconds, some portions (especially in the case of the earlier blasts in the series) of a majority of the spikes can be expected to be observed in the output of the analysis.

10.7 Model Development Evolution Process

Early in the research process, significant effort was expended to avoid issues such as hexahedral element degeneracy that are known to stumble many explicit FEA. Both the original baseline model as shown in Figure 10-3 and the final (or improved) baseline

model as shown in Figure 10-4 were developed without any degenerate elements. Figure 10-5 shows the fundamental differences in the center sections between the original and the final baseline models.

The original baseline model has the appearance of multiple degenerate element wedges around the center axis of the model. Pie-wedges were generated by ANSYS' automatic quad meshing tools for every 22.5° wedge entity around the circumference of the blast circles. Therefore, each of the pie-wedge shape elements was indeed a quadrilateral element. In the final baseline model, the pie-wedge shape elements were replaced by more refined hexahedral (brick) elements to reduce interpolation and extrapolation errors.

The following subsections describe the rationale and processes behind the modifications in modeling and methodology approaches, which transformed the original baseline model into the final baseline model, along with the corresponding assumptions, limitations and methodology.

10.8 Original Baseline Model

As described in earlier sections of this dissertation, the original baseline model was developed using ANSYS' PREP7 FEA Pre-processor. ANSYS was chosen for its parametric model development capabilities. The original baseline model consisted of 120,089 nodes and 114,560 hexahedral (i.e. brick) elements as shown in Figure 10-3. The educational / research version of ANSYS available at BYU's Fulton Supercomputing Laboratory has a size restriction of 125,000 nodes. As such, the model was designed to stay within the limitations imposed by ANSYS.

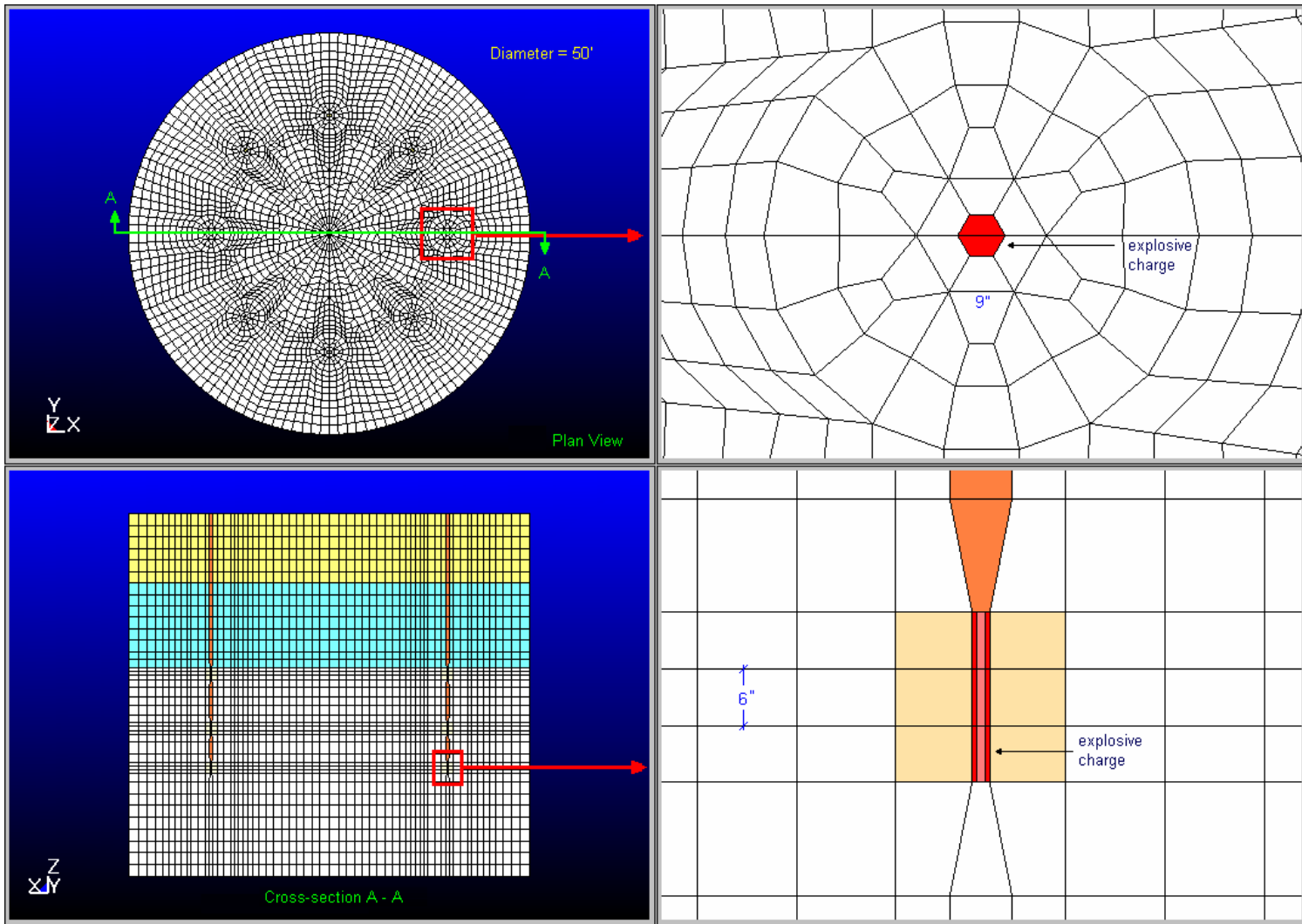


Figure 10-3 Original Baseline LS-DYNA Finite Element Model

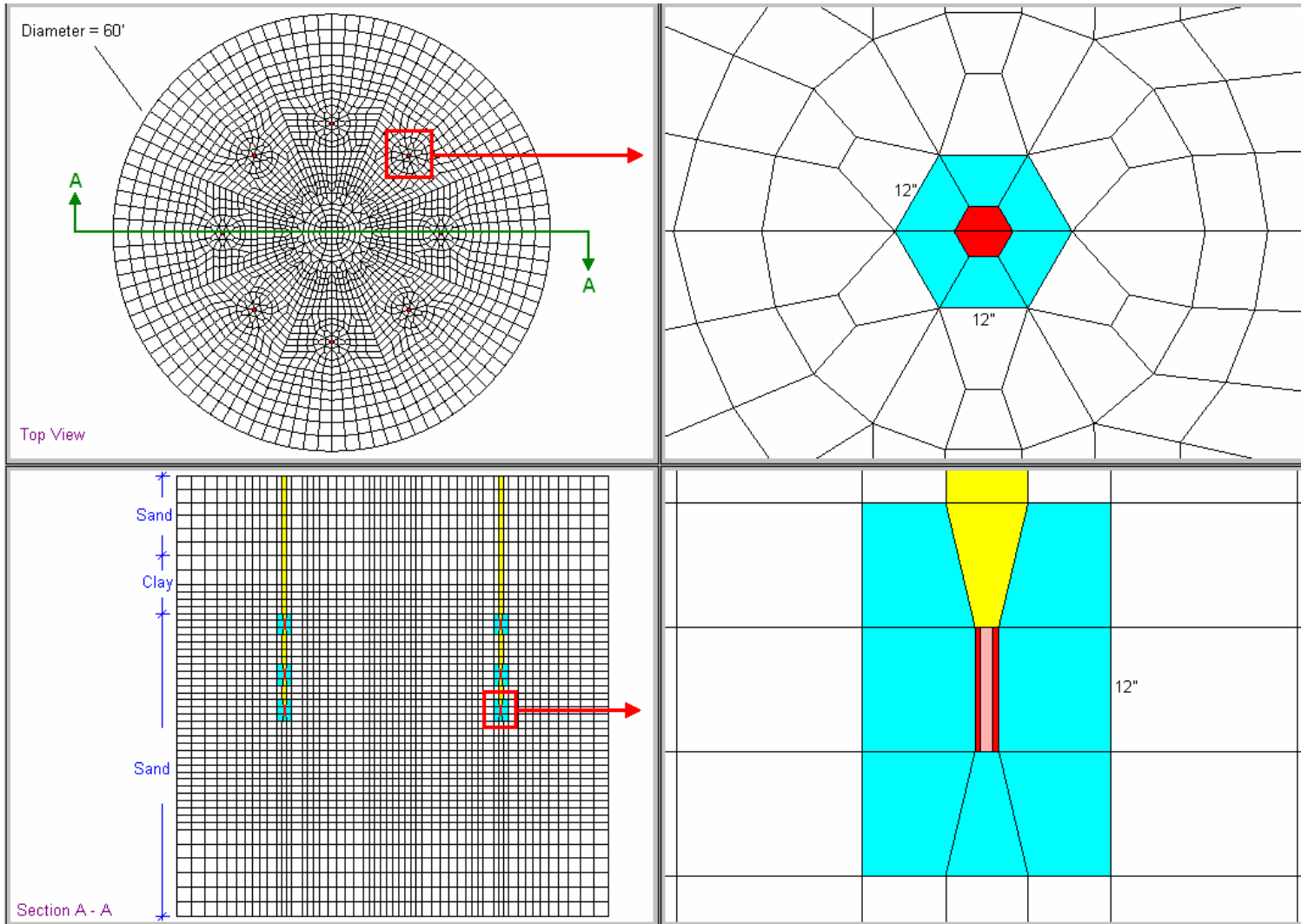


Figure 10-4 Improved Baseline LS-DYNA FEA Model

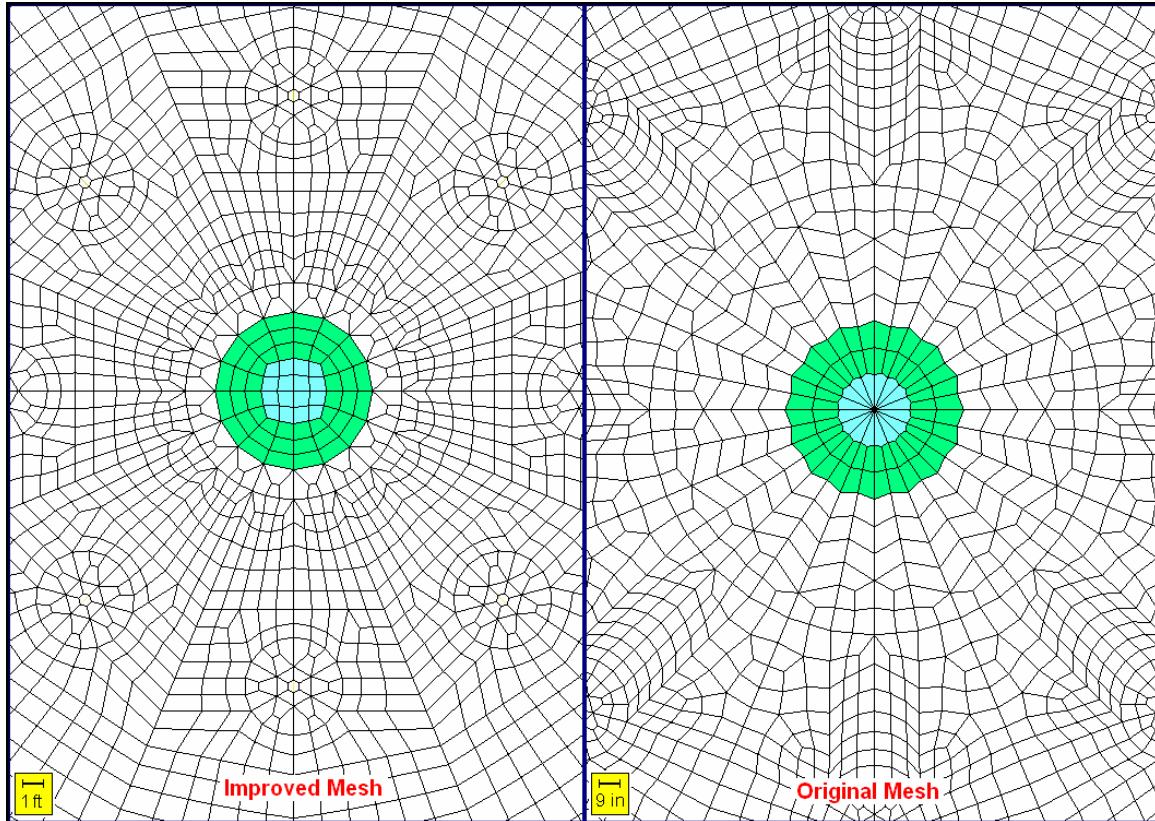


Figure 10-5 Improved (Left) and Original (Right) Baseline Model Centers

10.8.1 Assumptions, Limitations and Expectations

The original baseline model was a 3-D cylindrical half-space FEA model, which contained eight identically sized blast holes that are spaced at 45° uniformly around the circumference of the pre-specified blast-circle as shown in Figure 10-3.

Actual locations of the instrumentations placed in-situ for the capturing of pore water pressure and acceleration data were unknown during the development of the original baseline model. Therefore, the model was built with the assumption that actual placements of instrumentations were not likely to coincide with nodal locations within the model. Interpolations and extrapolations would be required to obtain results at desired locations corresponding to positions of instrumentations. Custom C/C++ routines

were developed to extract the closest nodes to the locations of instrumentations from the input deck. Appendix B provides a description and the listing of the custom routines developed to extract nodes from an input deck.

During subsequent field placement of instrumentation, there were difficulties in achieving vertically aligned blast holes as shown in Figure 9-9. Therefore, non-trivial amounts of horizontal and vertical offset (up to an estimated amount of 2 ft) in the locations of explosives could have resulted. Since quantitative means of measuring the directions, straightness, and tilt angles of blast holes were not available, some discrepancies between modeled and measured performance can be expected. Additionally, issues associated with random jumps, and magnitude shifts, in the measured acceleration and pore pressure data as discussed in Chapter 9 caused additional concerns during the early stage of the research regarding the ability to simulate such environments.

The original baseline model has uniformly sized and strategically placed explosives. One should not expect a uniformly designed numerical model to match exactly the random characteristics of the test data due to controllable or uncontrollable influences and/or factors such as those described in the previous paragraphs. The goal of the simulation is to provide a global overall view of the event with acceptable degrees of accuracy, consistency and repeatability. As such, the ability to predict the overall or global characteristics of liquefaction development remains the fundamental requirement for the numerical model.

Appendix D presents the analysis input control decks for the baseline tri-level sequential blast model used to instruct LS-DYNA how to perform a blast-induced liquefaction analysis using commands summarized in this section of the dissertation. The

corresponding geometry decks for the baseline models containing ~100,000 nodes and ~100,000 elements are not presented in this dissertation due to their excessive length.

10.8.2 Run Time Issues

The analysis cycle time of the original baseline model for simulating a tri-level, 21 sequential-blast event running on BYU's Marylou4 Linux cluster was approximately 42+ days. Although the 42+ day run-time represented a significant reduction from the original estimate of 200+ days as described earlier, it was still unacceptable when multiple analysis runs were required to calibrate some of the less well-defined input parameters. Additionally, risks involved in long duration runs were especially high during the research due to many uncertainties involved in monitoring and maintaining a newly installed Marylou4 large-scale supercomputing cluster. Many unexpected crashes and "bugs" were encountered during the initial "break-in" period upon installation of the Marylou4 system. As such, constant evaluation was necessary to develop additional approaches that would further reduce the analysis cycle time.

10.8.3 Physics Based Accuracy and Convergence Issues

To help explain the bulk modulus and pore pressure effects considered in the baseline model analysis, a quick review of mechanics of materials is first presented.

Bulk modulus is a measure of resistance against volumetric compression. Compressibility is the inverse of volumetric resistance. Therefore, the greater the bulk modulus, the smaller the compressibility. Since water has a very high bulk modulus, it has very low compressibility. Hence water is sometimes referred to as "incompressible" even though technically, water can still compress under high pressure. Incompressibility of a material is also directly related to the Poisson's ratio of the material. The greater the

compressibility of a material, the smaller the Poisson's ratio between 0 and 0.5. A material with a Poisson's ratio of 0.5 is considered an incompressible material. For a nearly incompressible material (i.e. rubber), the Poisson's ratio is typically between 0.48 and 0.50. Water is generally considered as an incompressible material. Therefore, it is an accepted engineering practice to assume the Poisson's ratio for water to be 0.5, which is typically as a frame of reference since, technically, Poisson's ratio has neither physical meaning nor applicability for water or other viscous liquid.

On the other hand, sand has a significantly smaller bulk modulus; hence, a much greater compressibility than water. As such, one would expect the Poisson's ratio to be significantly smaller than that of water, or 0.5. Since sand consists of small solid particles that are not integrally tied to one another, shifting and non-uniform movements are expected during compression as each particle tries to resituate itself to maximize surrounding support in achieving its own state of equilibrium. The modeling of independent movements of sand under load is a monumental task that is currently infeasible to perform. As such, the average bulk characteristics of the sand are typically utilized to represent the overall macroscopic behaviors as explained earlier in this dissertation, with the understanding that there are known and acceptable errors associated with the macroscopic representation of the material.

Bulk modulus (K) is a function of average compressive volumetric stress (P) and volumetric strain (ε_v) as shown in the following equation (Popov, 1976). An analogous expression can be applied to shear modulus.

$$K = \frac{-P}{\varepsilon_v} \quad (10-1)$$

The negative sign in Equation 10-1 indicates that volumetric stress is in compression. The variable P is commonly referred to as uniform pressure. When a tri-axial compressive load is applied to a material, a total stress σ is induced due to bulk and shear resistance of the material. Total stress is comprised of two components: volumetric and distortional. The volumetric component produces normal compressive stresses whereas the distortional component produces shear stresses. Pressure is defined as the average of the normal principal stresses (i.e. the portion of the normal stress component that do not produce distortions). Imbalances in normal stress are manifested in the form of combined normal and shear stresses. The amount of volumetric change in the material is controlled by bulk modulus K as shown in Equation 10-1, while the amount of distortion in the material is controlled by shear modulus G in a form analogous to Equation 10-1.

In order to understand the physics behind the pore water pressure build-up process, one needs to examine Equation 10-1 more closely. From the physical standpoint, Equation 10-1 states that for a given material with a constant K (i.e. sand or water alone), an increase in volumetric strain must be accompanied by an increase in pressure in order to obtain the same pressure-to-strain ratio that produces the constant bulk modulus value.

Now from a slightly different perspective or interpretation, a decrease in bulk modulus K as shown in Equation 10-1 implies a decrease of pressure in the numerator, an increase of volumetric strain in the denominator, or a combination of both. In other words, more compressible (i.e. smaller bulk modulus) sand produces either less pressure or greater volumetric strain, or a combination of both, than less compressible water.

These characteristics align with what one would observe in actual environments. An analogous explanation can be deduced for shear modulus, shear stress and shear strain. This basic understanding of bulk and shear behaviors forms the basis for the pore pressure development behaviors in saturated sand (i.e. sand-water mixture) to be described in the following paragraphs.

At the beginning of the research, it was clear that the analysis must account for the roles of both solid and liquid phases during the liquefaction process. However, the author was uncertain as to how both solid and liquid effects could be modeled simultaneously without having to develop a custom solid to liquid dual phase model similar the one developed by Paul Taylor for CTH (Taylor, 2004). As a result, the author determined to use the assumptions made by Lewis for the baseline *MAT_FHWA_SOIL material model (Lewis, 2004) in conjunction with UBC's sand bulk and shear moduli computation procedures (Byrne and Park, 2003) to perform several preliminary simulations. This was done with the hope that results from the preliminary runs would provide insight on how to best proceed with the research. Since the baseline material model *MAT_FHWA_SOIL by itself was not designed to account for dual phase phenomenon (i.e. both solid and liquid), it can only use the single constant bulk modulus supplied by the user. For example, if the bulk modulus of sand is supplied, then the pore pressure build-up is based uniquely on the properties of the sand. Since sand is more compressible, less pressure and/or greater volumetric strains than water can be expected as described earlier. Therefore, one would expect that the baseline material model to consistently under predict the pore pressure build-up and over predict volumetric deformations (i.e. strains).

Figure 10-6 through Figure 10-10 show the pore water pressure prediction using the original baseline model with unmodified solid soil parameters as defined by Lewis (2004). The *MAT_FHWA_SOIL material model assumes that the same bulk and shear moduli for the solid components are used throughout the liquefaction process. As described in the previous paragraph, although pore pressure development is accounted for in the model, it does not explicitly account for any bulk resistance from the water within the sand-water mixture. Without bulk support from water in the soil mass, it seems likely that the model will always under predict pore “water” pressure build-up, as one readily observes in Figure 10-6 to Figure 10-10.

Pressure is related to volumetric compressive stress as explained earlier. In an undrained environment, the greater the bulk modulus (or the smaller the compressibility), the greater the pore pressure. Since water has a significantly greater bulk modulus than sand, one must account for bulk effects from water in order to consistently and accurately predict pore water pressure development in saturated sand.

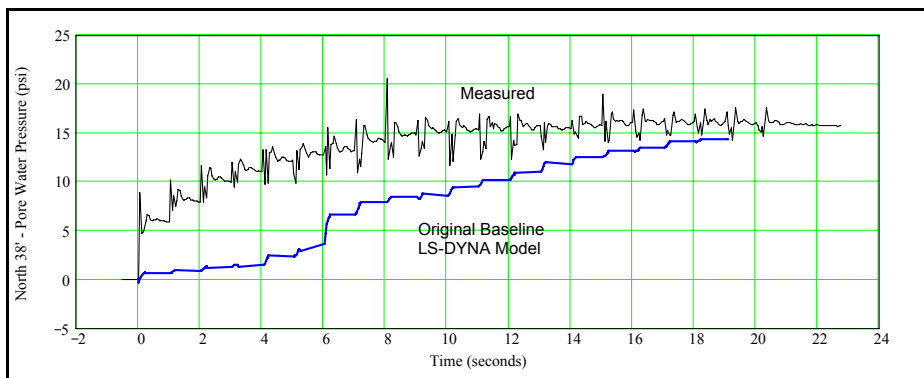


Figure 10-6 Original Baseline Pore Pressure (North PPT at Z = 38°)

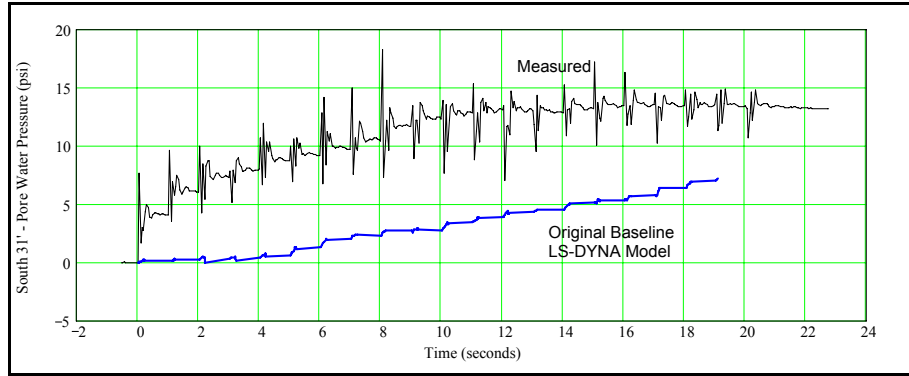


Figure 10-7 Original Baseline Pore Pressure (South PPT at Z = 31')

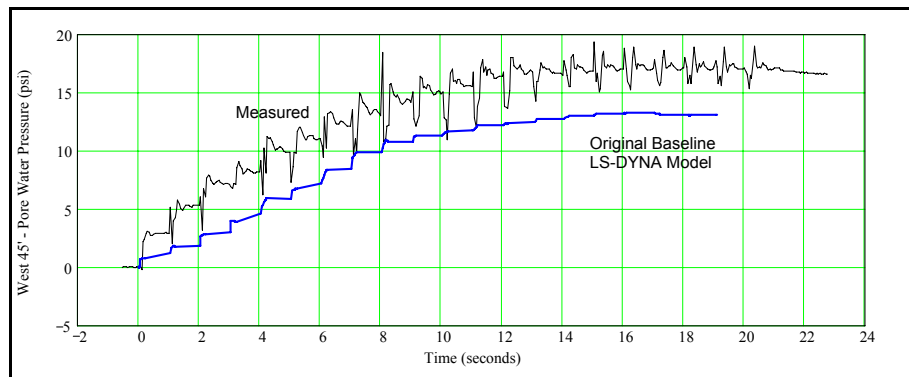


Figure 10-8 Original Baseline Pore Pressure (West PPT at Z = 45')

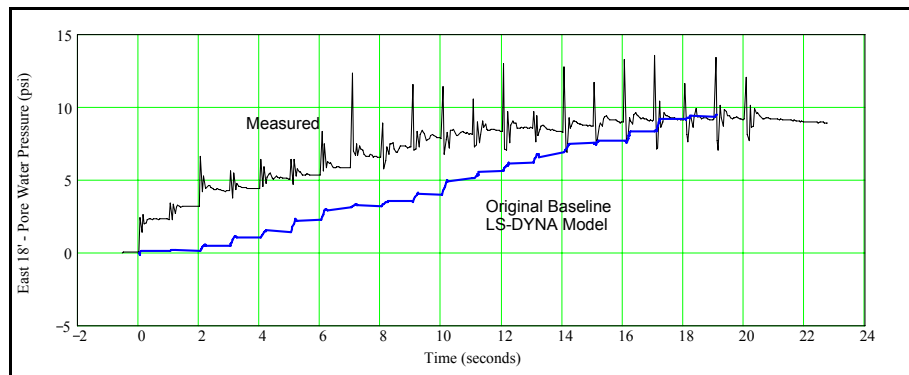


Figure 10-9 Original Baseline Pore Pressure (East PPT at Z = 18')

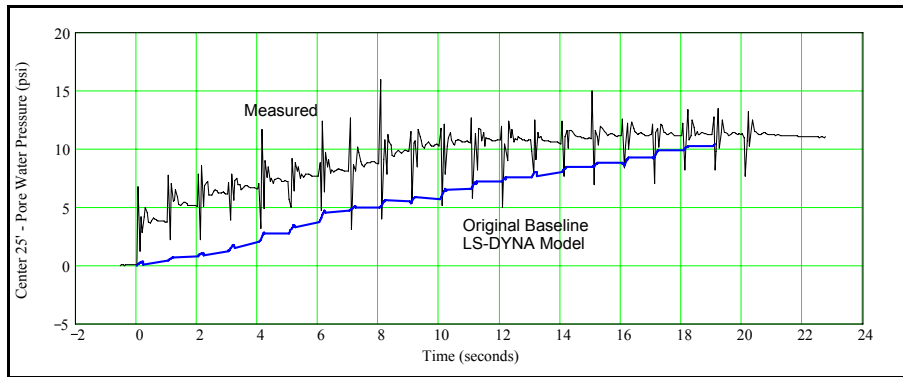


Figure 10-10 Original Baseline Pore Pressure (Center PPT at Z = 25')

Also from the results of the preliminary runs, one can readily see that a majority of the predicted results exhibit linear or near linear pore pressure build-up characteristics as discussed in Chapter 7 of this dissertation. Although linear pore pressure build-up behavior was expected due to theoretical limitations in the material model, several unexpected and disturbing behaviors were observed in the results, which led to the overhaul of the analysis approach.

First, the uncharacteristic “jump” observed in the North PPT location at approximate time of 6.0 seconds as shown in Figure 10-6 was first thought to be caused by a phenomenon known as spalling that was induced by the collisions of shock waves. After examining the results and the timing of the shock waves traveling through the soil mass, it was determined that the jump was induced by interpolation / extrapolation related errors rather than collisions of shock waves.

Second, there was no initial pore pressure jumps in the analysis results as expected and observed in the measured data. The initial jump is induced by a sudden shock from the first detonation when solid sand particles in regions of interest are still able to receive support from neighboring sand particles. This behavior can only occur

when water has not yet taken over as the volumetric load carrier. Water does not take over as the primary load carrier at the beginning of the load because water can initially increase its volume to alleviate pressure increase by “molding” itself through cracks and gaps via seepage within the soil mass. In an in-situ sandy soil environment, it is improbable to have a perfectly (i.e. 100%) undrained environment due to the porous nature of the solid materials. Therefore one can expect some initial dilution of water volume via seepage and gap fillings although it is difficult to quantify the actual amount in an in-situ environment.

Water cannot build up pore pressure or provide resistance against volumetric compression as long as it can escape or dilute at a higher rate than pressure application. Furthermore and more importantly, water has a significantly higher bulk modulus than sand. As such, the corresponding sound speed of water is much greater than sand, resulting in a much greater response time against incoming loads than sand. During a blast event, blast pressure at or near the high explosive blasting source typically exceed 1,000,000 psi that comes and goes in terms of microseconds to milliseconds. At such high amplitude and short duration, experience has shown that materials, liquid or solid, that are adjacent to or very near the blasting source exhibit behaviors that cannot be accounted for nor explained using standard elastic material laws such as Hooke’s law. Simply said, blast pressure essentially pushes everything out of its path. The higher the ability to respond to income loads (i.e. material with higher bulk), the faster it is pushed out of the way. This is especially true with materials that exhibit low shear resistance such as water, which can dilute by molding itself to whatever surrounding environments it encounters.

On the other hand, sand has a very low bulk modulus in comparison with water. The corresponding sound speed as a function of the bulk modulus per Equation 3-1 is significantly lower than water. Therefore, sand has a very slow response to incoming load relative to water. In other words, it cannot “move out of the way” as quickly as water. Resistance in sand is initially mobilized until water settles in to start producing its own resistance against incoming loads. With the significantly softer bulk (i.e. compressibility) characteristics of solid sandy particles, much greater initial volumetric strains relative to water can be expected and observed. Since pressure is directly proportional to volumetric strains for a given material (i.e. constant K), greater initial pressure jumps can be expected in a confined solid soil mass than in a confined and nearly incompressible water mass. Therefore, technically, the soil material model should be able to model the initial jump condition observed in test.

There are several potential reasons that would cause the material model’s inability to predict the initial jump of pressure when only sand properties are being applied. The first possibility would be induced by mistakes in the input parameters. Interpolations and extrapolations near the wedge elements may induce undesirable effects. Potentially, the model can also be missing one or more elements of physics in the formulation of the baseline soil material model. Reasons such as these necessitate a complete review of the analysis and modeling processes.

Third, predicted pore pressure curves for all but the west location have a slightly concave upward or linear shape rather than a concave downward shape as observed in test data. With concave upward shapes, one can deduce that pore water pressure will

continue to climb within foreseeable time durations without leveling off as expected and observed in the measured data.

Fourth, every pore water pressure curve computed by the original baseline model under-predicts the actual pore water pressure build-up during the blast series. Although adjustments to input parameters can be made to increase the predicted results in order to approximate the amplitude of the measured results, the shapes of the predicted curves as well as the model's inability to predict the initial jump indicate that there is little hope of providing a reasonable prediction using the original baseline model in the "as-is" conditions.

10.9 Improvements to the Original Baseline Model

In view of the issues discussed above, a decision was made to completely overhaul the original baseline model and analysis approach specifically to address known issues. Prior to the start of the overhaul process, a detail evaluation was conducted to clearly identify the issues to be addressed and potential solutions to be incorporated during the process.

Three major objectives for improvement were identified. First, the analysis cycle time must be resolved and reduced to a more acceptable and feasible level (i.e. no more than 1 week) in order to allow multiple iterations required for calibrating input parameters within a reasonable amount of time. Second, potential stability and convergence issues including extrapolation/interpolation induced errors must be addressed to minimize errors. Third, it had to be determined if any elements of physics were missing in the original baseline model analysis approach that would result in such noticeable deviations between predicted and measured results. With at least some of the

issues that were identified, the next logical step would be to derive an approach which resolved the issues and then to test that approach in the baseline model. The following subsections provide detailed descriptions for each of the reasons identified as contributors to the issues at hand, followed by improvements made to the model as an attempt to resolve these issues.

10.9.1 Run Time Issues

In order to reduce the existing run time in the analysis of the original baseline model, one must understand the source of the run time issues. Several options were identified from the original baseline model analysis that would potentially allow faster analysis cycle time.

1. Some undesirable numerical oscillations were observed in the ALE results in regions of interest. Experience has shown that undesirable oscillations in the results plus excessive run time are good indications that the model's plasticity and other non-linear algorithms may be having trouble converging to proper solutions. Potentially, there may be unidentified and unresolved issues between LS-DYNA's ALE solver and the newly added *MAT_FHWA_SOIL material model since the final release of the material model has not been tested using ALE (Lewis, 2004). Such issues are likely to reduce the model's ability to converge while increasing the number of internal iterations throughout the course of the analysis.
2. The LaGrangian method is known to be faster in solution process time within LS-DYNA than either the ALE or the Eulerian methods. However, simple models tested in the beginning of the research had shown that LaGrangian

method was encountering hourglassing issues that could also cause the analysis to have difficulties converging to proper solutions. Experience has also shown that simple test models may not always represent true behaviors of a full-scale model due to potential errors introduced by the assumptions used to obtain the simplified models. As such, one should never “completely” eliminate options that were indicated by simple models to be potentially problematic without testing them in a full-scale model as a last resort when other supposedly viable options have been exhausted. In this case, the LaGrangian method that showed potential hourglass problems in a simple model may never encounter the same issues in a full-scale model.

3. Although the original baseline model has a “clean” mesh, remeshing the center pie-wedge elements with high aspect ratios is likely to reduce numerical oscillations due to potentially excessive averaging of interpolated and extrapolated results along the center axis of the model. By eliminating the pie wedges, one can also reduce the smearing effects of non-symmetrical blast waves, thereby reducing potential errors. One can expect that more uniformly spaced and sized elements can also contribute to a reduction in run time.
4. A smaller model can be an option to achieve faster analysis cycle time. However, it was determined early on that a large half space model is required in order to accurately simulate the non-symmetrical blast event. Therefore, one cannot expect a significant reduction in model size without sacrificing analysis accuracy. Nevertheless, some areas for improvement in the original

model were identified that could help improve the analysis solution process while potentially resulting in some observable reduction in model size.

5. The baseline model can be organized to ensure that all locations of instrumentation are coincidental with nodal locations within the model, thereby eliminating the needs for tracer results as well as unnecessary extrapolations, interpolations and averaging of results from neighboring nodes. This approach can both increase the accuracy and reliability of the analysis while reducing analysis cycle time as well as memory and disk space requirements.

10.9.2 Stability and Convergence Issues

The disturbing side effects of interpolations and extrapolations induced errors that were manifested as jumps and shifts in results such as those shown at six seconds in Figure 10-6. Evaluating results along the “wedge-like” elements around the center axis of the baseline model revealed that results near the mentioned elements exhibited abnormal and unpredictable oscillatory behaviors as described previously. Significant jumps and shifts were observed in multiple locations near the center regions.

The research also revealed that a major contributor to the unpredictable phenomenon observed in the center regions of the original baseline model was due to the averaging of interpolated and extrapolated results near the axis of the model. Results among 32 wedge-like elements around the center axis of the model as shown in Figure 10-3 and Figure 10-5 exhibited uncharacteristic behaviors. Past experience has shown that averaging of neighboring interpolated and extrapolated results of elements around an axis was not an issue in symmetrically and uniformly loaded cases. However, when

shock waves are being applied non-symmetrically around the center axis, it appears that averaging of many high-aspect ratio elements around the center axis skewed and over-smear the results. The skewing and over-smearing produced jumps, shifts and other undesirable behaviors in the outputs. These behaviors often lead to excessive plasticity and geometric non-linearity iterations, causing longer than necessary analysis cycle time while producing less than desirable accuracy. Fortunately, wedge-element issues can easily be addressed by reorganizing the model.

10.9.3 Original Model's Physics Issues

During liquefaction, support from adjacent solid sandy particles diminishes as water pressure builds up and begins to take over as the primary load carrier. This transferring of load support from solid sandy particles to a liquid medium is hereafter referred to as a transition process. To properly simulate the development of liquefaction within a saturated soil mass in an undrained or confined environment, one must account for the effects resulting from the transition process. The original baseline model “as-is” cannot account for transition effects due to limitations of the theory used in the model. Therefore, enhancements must be made to the model to account for transitional effects. To define a relationship that describes the solid and liquid transitional behaviors during liquefaction, review of the phenomenon, and the corresponding physics involved in the process are warranted.

Since microscopic descriptions of the behavior of every sand particle within a large soil mass are neither practical nor feasible to perform at the present time, solid sandy soil particles are typically modeled as a compressible mass continuum in the

macroscopic level rather than a particulate material in the microscopic level as described in Section 10.8.3.

To account for frictional and interlocking behaviors of sandy particles within a soil continuum, finite bulk (K) and shear (G) moduli are defined from the macroscopic or overall behaviors of the soil mass observed in a laboratory or some sort of controlled in-situ environments. Magnitudes of both bulk and shear moduli for sandy soils are typically low (i.e. $< 10,000$ psi) in comparison with normal solid continuum materials such as metals or plastic. Since sandy materials are noticeably compressible as described in Section 10.8.3, the corresponding Poisson's ratios for solid sandy materials are typically in the range of 0.15 to 0.25. However, when combined with water in an undrained environment, the sand and water mixture can exhibit a much higher "apparent" Poisson's ratio (i.e. 0.3 to 0.4) due to pressure-resistance contributions from the "nearly" incompressible water in the undrained environment. This is another reason why the inclusion of water effects is important in the evaluation of the development of liquefaction in saturated sand. Typical mechanical properties used for the analysis were presented previously in Table 7-2.

Water is nearly incompressible (i.e. high bulk modulus as shown in Table 7-2 and a nearly 0.5 Poisson's ratio) with negligible ability to resist shear or distortional loads (i.e. shear modulus G is zero or negligible). Therefore, the combined sand and water medium might be treated as a composite material where the water can carry large compressive loads while the sandy soil can carry limited shear and a significantly smaller portion of the compressive load through bearing and frictional contacts. As explained earlier in Section 10.8.3, basic mechanics of materials tell us that pressure (i.e. average

normal stress) is induced by volumetric resistance while shear stresses are induced by distortional resistance. As a mass is deformed under increasing compressive and shear loads, increases in both volumetric and distortional effects are expected and observed. As long as there are imbalances in individual component load magnitudes, there will always be combinations of both volumetric and distortional effects. Nevertheless, in a pure uniform pressure environment where all components of loads are equal in all directions, only volumetric effects are observed. An analogous scenario can be deduced for distortional effects.

Since it is improbable to observe pure volumetric, or pure distortional, load applications and responses in an in-situ environment, volumetric effects almost always accompany shear effects in an in-situ environment. As such, the interrelations between volumetric and distortional effects have the potential to cause one to conclude that distortions induce volumetric effects or vice versa. To minimize confusion, one should consider volumetric and distortional effects separately.

When solid soil particles are in full contact and in equilibrium, any additional load (in excess of the pre-existing load while in equilibrium conditions) that would cause localized disturbances can be transferred from solid particles to adjacent solid particles via direct bearing contact and friction. Normal contact forces cause pressure in the soil particles while frictions from contacts induce shear. When adjacent solid particles are separated and no longer in contact, solid particles can no longer transmit normal and frictional forces among themselves and water takes over as the carrier against bulk or volumetric effects. Meanwhile, the overall distortional (shear) resistance diminishes due to water's inability to resist shear, as well as the loss of particle-to-particle contact and

friction. The transferring of load resistance from solid soil to water often appears to occur instantaneously.

In the physical world, however, it is not possible to have instantaneous (i.e. $\Delta t = 0$) applications of load within a material or instantaneous transfer of loads between adjacent materials as explained in Section 10.8.3. However, some may assume, or have assumed, that the transferring event takes place instantaneously when analyzing soil behavior in quasi-static environments. This is a valid assumption for quasi-static environments because transient effects are often negligible from a long-term perspective. However, in an explicit or shock environment, an assumption of instantaneous load magnitude change can produce undesirable shock waves rippling through the model, thereby producing erroneous results. Every transition of load carrying resistance between adjacent materials requires a finite amount of time or duration to complete its course. Therefore, some sort of mathematical relationship must be derived to account for non-instantaneous transitioning process.

To determine the proper mathematical relationship for describing the bulk transitioning process, one must first understand the mechanisms, magnitudes and effects behind the input parameters to be included in the process. The following example illustrates the ideas behind the thought process employed in developing the bulk transition relationship. For illustration purposes and ease of comprehension, material properties are discussed in terms of approximate orders of magnitude.

The baseline sandy material from Fraser River Delta has an estimated bulk modulus (K) $\sim 5,000$ psi and a shear modulus (G) $\sim 3,000$ psi as shown in Table 7-2. The corresponding Poisson's ratio (ν) using Equation 10-2 derived from basic mechanics of

materials (Popov, 1976) is ~ 0.25 . On the other hand, the bulk modulus of water is in the order of 320,000 psi. Water has a negligible ability to resist shear (i.e. G is negligible). As such, the corresponding Poisson's ratio computed from bulk and shear moduli is ~ 0.5 , which also indicates that water is nearly incompressible.

$$\nu = \frac{3 \cdot K - 2 \cdot G}{2 \cdot (3 \cdot K + G)} \quad (10-2)$$

As cyclic loads are applied to a liquefiable soil, apparent degradations in both bulk and shear modulus are observed in the solid soil, representing the solid soil's decreasing ability to resist volumetric and frictional (or shear) stresses. In other words, the solid soil's compressibility increases with respect to increasing cyclic load frequency and magnitude. This "softening" phenomenon is produced by the loss of contact, hence friction, among adjacent solid particles due to an increase in pore water pressure that separates the soil particles from one another. In summary, the loss of contacts in solid soil particles allows the solid particles to flow within the saturated soil mass, resulting in a loss of both volumetric and distortional resistance due to the increasing inability to transmit normal and shear forces via contacts. Therefore, one observes that loose saturated sand becomes more compressible with less resistance to shear (i.e. small shear modulus) as it approaches liquefaction.

While solid soil particles lose their ability to transfer load, water increases its shares of volumetric load carrying responsibility. As a result, during the transition process, the bulk modulus of water becomes more influential in the soil-water mixture while the influence of the bulk modulus of solid soil diminishes. The transition from the

bulk modulus of solid soil to that of water results in an apparent increase in the bulk modulus of soil-water mixture in a undrained or confined state. Once the bulk resistance of water begins to take over, the corresponding Poisson's ratio increases rapidly and asymptotically toward 0.5 in accordance with Equation 10-2. Analogous effects can be observed in the shear modulus degradation process.

Although the combination of increasing bulk resistance and decreasing shear resistance does induce a faster transition process from solid soil to water during liquefaction, the combined effects diminish rapidly as Poisson's ratio approaches 0.5 asymptotically. In order to account for both increasing bulk resistance and decreasing shear resistance, one must also consider the rate of change for both variables. There are infinitely many combinations one can choose when both variables are involved in the process. As such, the complexity involved in studying the effects of both bulk and shear can be extremely expensive and time consuming.

To reduce the complexity of demonstrating the existence and the importance of the soil to liquid bulk modulus (or shear modulus) transition in modeling liquefaction, the transition of only one variable is studied in this research. Since bulk resistance is significantly more dominant in water than shear resistance, and the transition process of interest goes from solid to water, bulk modulus has been selected as the variable for demonstrating the solid-water transition concept.

10.9.4 Bulk Modulus Transitional Relationship

Transition from solid bulk resistance to liquid bulk resistance is not an instantaneous process as described in Sections 10.8.3 and 10.9.3. A mathematical relationship can be derived to describe the transitional process, which process is

described in detail in this section of the dissertation. The original idea that formed the foundation used to develop the mathematical representation of the polymorphic phase change process from solid to liquid in this research was inspired by Paul Taylor's development of the multi-phase effective stress model (Taylor, 2004). Taylor's model (2004) includes two sets of equations of state (EOS) to account for the transition from solid to liquid as pore water pressure increases in the soil material.

During the initial instant at or before shocks are applied, both bulk and shear resistance of the soil-water composite are primarily due to the soil particles' soil-to-soil contacts. While it is true that water has a significantly greater bulk modulus which allows it to react and transmit compressive shock waves at a significant greater rate than the corresponding soil particles, it has negligible shear resistance against distortional deformations. When compressive loads are applied to water without full confinement, it will deform continuously until full confinement is achieved or the applied load has dissipated (Souli, 2000). As such, in a soil-water mixture subjected to sudden shocks, water can momentarily delay pressure increase by spreading and remolding itself across voids (or gaps) between sand particles as discussed in Section 10.8.3. This water spreading or remolding process, induced by negligible shear resistance in water, follows paths of least resistance as water tries to seek refuge or relief from applied pressure.

Meanwhile, sandy soil particles are able to provide temporary support against normal and shear stress through particle contacts due to its slower reactions to rapid loading as discussed in Section 10.8.3. As such, it results in momentary resistance of the blast load. With a small bulk modulus, sandy soil particle can exhibit greater volumetric

deformations associated with the increase in applied pressure than water, thereby producing an apparent initial “jump” in volumetric deformations and pressure.

Once the volumetric expansion limit has been reached, and an apparent undrained condition has arrived when all paths of least resistance (or escape) have either been exhausted or jammed, pore water pressure begins to build up. The time necessary for pore pressure to actually begin to increase noticeably depends on how porous the soil is and how readily water can redistribute or spread itself across the neighboring regions.

Now as pore pressure builds up in the water, it causes neighboring sand particles to separate from their adjacent particles, resulting in loss of contacts among solid particles. Again, a complete separation of solid particles from contacting their neighboring particles takes a finite amount of time to occur. The length of time required for the separation to occur is a function of how compact the soil is before loading; the soil permeability; how fast the soil particles are able to respond to applied loads; how rapid the load is being applied; and how rapid volumetric strains increase in the material. It is the separation of sandy particles from one another that gives the apparent increase in compressibility of the sandy soil as the soil approaches a liquefied state.

When sufficient time (i.e. milliseconds) has passed since the first encounter of the initial shock wave, shear and bulk resistance in the soil begin to build-up as the saturated soil mass begins to “relax” and reaches equilibrium in a more “compact” state. If no subsequent shocks are applied, the pore water pressure will eventually subside or dissipate, and particle-to-particle contacts will reestablish. Soil particles will then resettle until equilibrium is reached.

However, when multiple follow-on shocks are being applied before the soil-water mixture can reconstitute, subsequent shocks would induce greater pore pressure, further reducing the solid soil particles' ability to resist shear and compression due to loss of contacts. Meanwhile, the soil-water mixture, in an effectively undrained state, would exhibit increasing bulk resistance against volumetric strain as it approaches asymptotically toward its fully liquefied state where water becomes the primary source for bulk resistance. Such is the case observed in the measured test data where an initial jump in excess pore water pressure is observed, followed by an asymptotic approach toward liquefaction (i.e. $R_u = 1.0$) in a concave downward manner as shown in Figure 9-20. The degree of concave downwardness is directly related to the amount of energy produced by the loading source and the rates of bulk and shear transition from solid to liquid. The greater the loading energy as well as the bulk and shear transition rates, the faster the soil reaches its full liquefaction state.

While it is true that saturated sandy soil under a layer of fine grained material such as clay in an in-situ environment behaves as though it is in an undrained environment during an earthquake, its initial behavior when the first shock wave arrives is drastically different from its behavior when subjected to subsequent shocks for reasons just explained in the previous paragraph and in Section 10.8.3. Therefore, one cannot assume that the initial bulk resistance against incoming blast waves is solely controlled by water in the soil.

Excess pore pressure is a function of volumetric strain and the corresponding bulk modulus of the material. Recall from Section 10.8.3, for a given bulk modulus, the higher the volumetric strains, the greater the pore pressure until full liquefaction (i.e. $R_u =$

1.0). By the same token, the greater the bulk modulus, the greater the resistance to volumetric compression manifests in the form of volumetric stress as induced by uniform pressure. Therefore, smaller volumetric strains are observed for greater bulk modulus. From the observation that water is nearly incompressible (i.e. with negligible volumetric strains under compression in a confined state), the amount of increase in volumetric strain due to subsequent shock loads reduces as water becomes increasingly dominant in a soil during liquefaction under undrained conditions. Since pore pressure is directly related to the volumetric strain, reductions in the increase of volumetric strain due to subsequent shocks and increasing bulk modulus cause the pore water pressure to taper off toward a horizontal asymptote as the soil liquefies. A family of proposed functions appear to be able to describe the transition of bulk modulus from solid to liquid during the liquefaction process. These functions are based on a half-sine pulse between $-\pi/2$ and $\pi/2$ as shown in Figure 10-11.

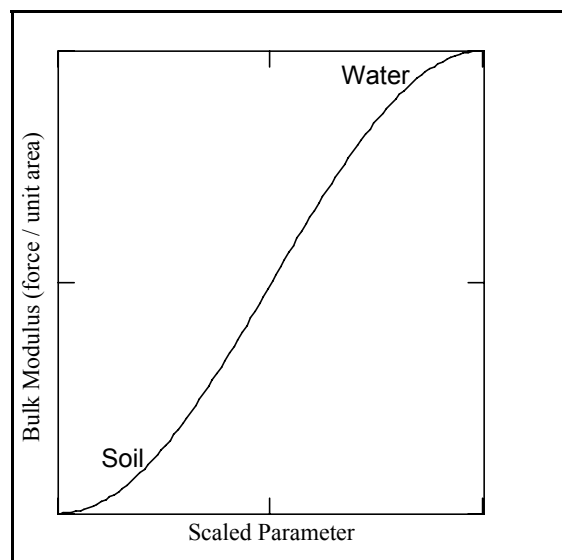


Figure 10-11 A Typical Half-Sine Function

The lower ordinate of the curve shown in Figure 10-11 associates with the initial bulk behavior of solid soil particles in the soil-water composite, whereas the upper ordinate relates to the bulk behaviors of water, which becomes dominant in liquefied state. The curve as shown in Figure 10-11 describes the transitional volumetric (or bulk) load carrying characteristics between solid soil particles and water. The scaled parameter along the abscissa is the independent variable of interest used to compute the corresponding bulk modulus for the next time step in the analysis. This independent variable relates the current state of average volumetric stress and the initial effective overburden stress to the current bulk modulus via a pre-specified mathematical function to be defined in the following paragraphs. The current state of computed average volumetric stress (or pressure) is necessary in order to define the present ability of the soil in resisting volumetric pressure being developed in the soil in response to applied impulsive environment.

Since the transition of the composite bulk modulus from solid soil to water spans orders of magnitudes, the corresponding half-sine relationship describing the transition would be most appropriate in the log domain in order to provide a more uniformly weighted liquefaction process across the data region of interest. A general form of the baseline half-sine function developed during the research for the simulation of solid to liquid bulk transition is defined by the following equation.

$$\log(K_s) \leq \log(K) = \log(K_s) + \Delta K \cdot \sin\left[\zeta^n \cdot \frac{\pi}{2}\right] \leq \log(K_w) \quad (10-3)$$

$$\Delta K = \log(K_w) - \log(K_s) = \log\left(\frac{K_w}{K_s}\right)$$

Where:

K is the bulk modulus of the soil-water composite mixture in psi ($K_s \leq K \leq K_w$)

K_s is the “constant” average bulk modulus of the soil in psi (Table 7-2)

K_w is the “constant” bulk modulus of water in psi (Table 7-2)

ζ is a parameter that relates the current state of stress to the soil’s bulk modulus

n is the exponent that controls how rapidly the bulk modulus transition takes place

Equation 10-3 is simply a line fit in log scale with the abscissa being a half-sine function instead of a single variable such as X . The “Y-intercept” is the sand material’s constant bulk modulus value; the slope of the equation is the difference between bulk modulus of water and the bulk modulus of sand. Since the soil’s average bulk modulus and the bulk modulus of water are both known quantities readily available from textbooks, handbooks, laboratory and/or in situ measured data as shown in Table 7-2, the only parameters requiring definitions are ζ and n . One must be reminded as discussed in Section 7.4 that the average bulk modulus (K_s) is a definitive measure of the soil’s bulk resistance, whereas the skeleton bulk modulus (K_{sk}) used in the constitutive model is an abstract pore pressure multiplier which value is selected iteratively during model calibration (Reid and Coon, 2004).

The unitless parameter ζ is defined as the ratio of the average principal (i.e. volumetric) stress computed by the current analysis iteration divided by the initial effective overburden stress. At the lower bound value of 0.0 (i.e. prior to application of loads), Equation 10-3 returns K_s . At the upper bound value of 1.0 (i.e. full liquefaction), Equation 10-3 returns K_w , indicating that water in the soil has become the primary load

carrier. By bounding the bulk modulus value between sand and water, the equation effectively defines only the transitioning region.

The exponent n defines the rate at which the transition process occurs. The value of n is inversely proportional to the rate of change from solid to liquid. At a low value of n (i.e. $n < 0.5$), a rapid transition takes place. On the other hand, a high value of n (i.e. $n > 0.5$) produces a more gradually increasing transition trend as shown in Figure 10-12.

$$n = f \cdot z_r^3 \cdot \frac{d}{w^3} \quad (10-4)$$

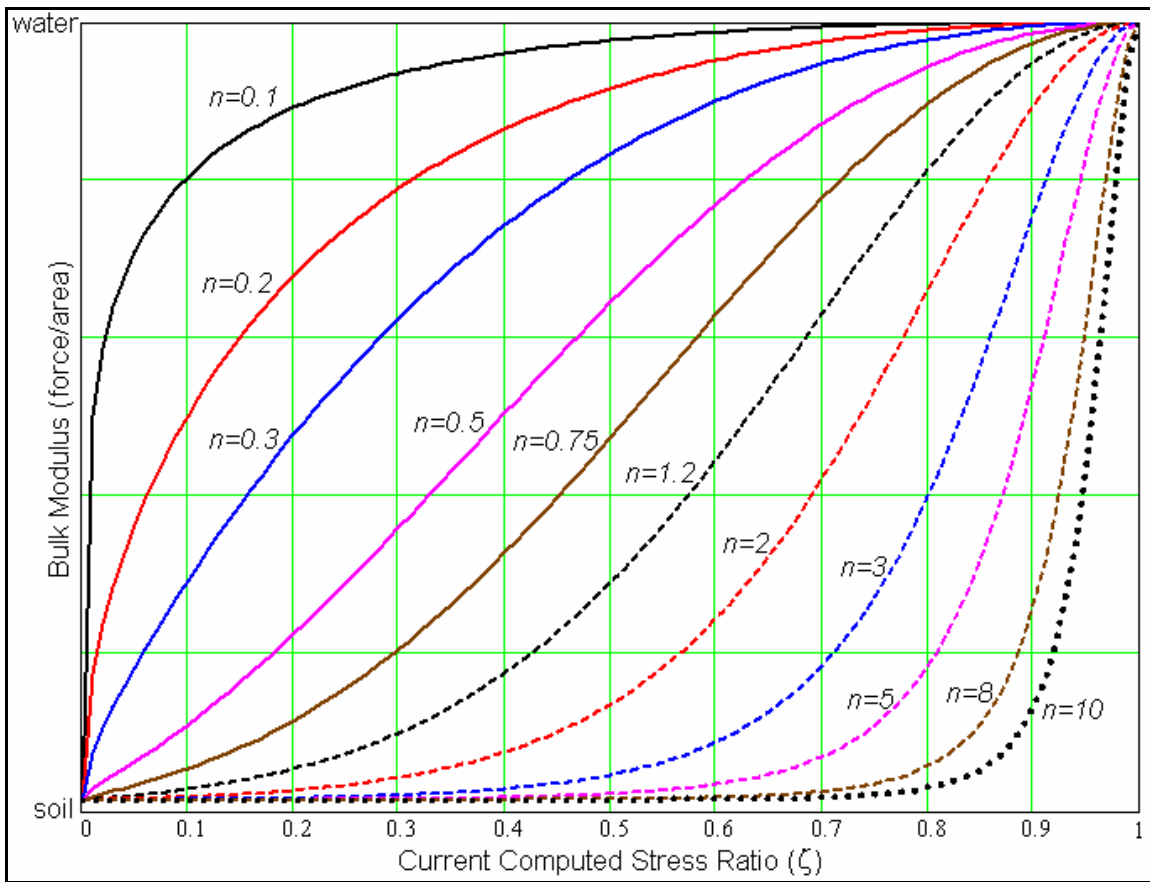


Figure 10-12 Typical Relationship Between Bulk Modulus and Exponent

It is proposed that these inversely proportional trends can be characterized by the ratio of distance to the blast source (d) over the average explosive weight (w) in a form similar to that shown in Equation 10-4. Effects of depth (z_r) and a factor of uncertainty (f) are also considered in the equation. TNT equivalency is typically applied to the weight of the explosive being used so that a frame of reference for the amount of energy produced by the explosive of interest is provided. Detailed explanations on the development of the parameters in Equation 10-4 are presented in the following paragraphs.

The d to w ratio implies that an increase in distance from the blast source and/or a decrease in explosive weight leads to a more gradual bulk modulus transition (larger n value). On the other hand, when the explosive charge increases or when the observation point is approaching the blast source (i.e. $d \rightarrow 0$), a smaller n is resulted. The smaller the n value, the faster the water takes over as the primary load carrier in the soil upon detonation, resulting in a more rapid transition of bulk modulus from soil to water. Sample bulk modulus transition curves for a large range of exponent n values are shown in Figure 10-12.

From fundamental principles of explosive engineering, the scaling factor for the amount of energy produced in a blast is typically a cube-root function of explosive weight to reflect volumetric effects (Cooper, 1996). However, in some cases, a square root, instead of a cube root, scaling factor is used to represent the volume of a very long cylindrical blast source where the areas at both ends are negligible in comparison with the surface area around the circumference of the long cylinder. The May, 2005 Vancouver blast series for this research utilized short stubby explosive charges where the end surface

areas of each explosive are not negligible. Therefore, it is more appropriate to apply a cube-root explosive weight in the denominator of the distance to average explosive weight ratio for a more accurate representation of the exponent n .

The parameter d represents the distance from the observation point to the location of the blast source. Since there are three levels of explosives with 7 charges per level around a blast circle, a weighted average of the blast distance is defined to reduce the complexity and bookkeeping efforts for each explosive charge and instrumentation point. Each instrumentation point and each blast source point are located around a concentric circle about the central axis as shown in Figure 10-1. As such, the average horizontal distance from each blast point to each instrumentation point is approximately the same as the blast circle radius. Average vertical distance between each charge to each instrumentation point is the corresponding difference in depth. An equivalent (or weighted centroidal) depth (z_{eq}) can be defined as shown in Equation 10-5 in terms of the depth (z_b) and average charge weight (w) of each explosive. Again, a cube-root function in explosive weight is used to represent volumetric effects.

$$z_{eq} = \frac{\sum \left(z_b \cdot w^{\frac{1}{3}} \right)}{\sum w^{\frac{1}{3}}} \quad (10-5)$$

With the equivalent depth of the explosives so defined, the distance from the explosives (as a family) to each observation or instrumentation point can be defined in

terms of blast circle radius (r_{bc}), equivalent explosive depth (z_{eq}) and the depth of each instrumentation point (z_i) as shown in Equation 10-6.

$$d = \sqrt{r_{bc}^2 + (z_{eq} - z_i)^2} \quad (10-6)$$

During the course of the research, it was observed that effects of depth pivoted about the equivalent depth. Depth effects for observation points above z_{eq} appear to be minor and relatively constant in comparison with points at increasing depth beyond z_{eq} . However, at depths below the equivalent explosive depth z_{eq} , the depth plays an important role in the development of pore pressure in the May 2005 Vancouver blast test. A closer examination of the depth effects further revealed that the effects for points below z_{eq} is non-linear. After careful study of the predicted results in LS-DYNA relative to the measured results, it appears that the influence of depth on the sine exponent n is a cubic function rather than a cube-root function. One may theorize that volumetric pressure with respect to depth plays an important role in defining the depth effects. Whatever the cause may be, further study of depth effects is recommended for future research. Meanwhile, unitless depth effects z_r appear to be reasonably estimated by the following relationships.

$$z_r = c \quad \text{for} \quad z_i \leq z_{eq} \quad (10-7)$$

$$z_r = \frac{z_i}{z_{eq}} \quad \text{for} \quad z_i > z_{eq}$$

The constant c for depth effects applied in this research was assumed to be 1.0, which basically neglect the minor depth effects at locations above z_{eq} .

Another challenging task in developing the bulk transition relationship is to define the uncertainty factor f , which is a unitless product of TNT equivalent factor, calibration errors, and uncertainties relating to the computation method being used to obtain the TNT equivalency factor. The unit of f is the inverse of the units defined in the d to w ratio, or $\text{pound}^{0.33}/\text{ft}$ in order to have unit consistency for the sine exponent n . All units used in this research for the development of the bulk transition effects are in English units.

One should note that a factor of uncertainty is necessary due to noticeable differences in the energy produced by the same explosive formulation with slight variations in density and proportions of ingredients. Some variability is due to thermo-dynamic and chemical reactions during explosive burns while other variability results from external factors such purity of ingredients and surrounding environments. Furthermore, TNT equivalency values are typically used to reference the amount of energy that the explosive of interest can produce. There are many methods available for computing TNT equivalency values as described in Section 4.7. Each method produces non-trivial differences in TNT equivalent weight. Therefore, a factor of variation and uncertainty (f) is warranted to account for these differences.

The actual value of the factor of uncertainty depends upon the explosive material being used. Since a factor of uncertainty f is applied, one can either apply the TNT equivalency value directly to the explosive weight, or lumped as a cubic value into f . A cubic value is used due to the cube-root weight of the explosive in the denominator of the d to w ratio. The latter approach is preferred to allow easier identification of the actual

explosive weight being used in the equation. Sometimes it is difficult to tell whether the applied average explosive weight used in the equation is correct when a TNT equivalency value is used instead of actual explosive weight. Finally, due to limited availability of explosive material properties, one should expect to perform analysis iterations in order to calibrate the factor of uncertainty f .

An important point, which one must recognize, is that the bulk modulus relationship defined in Equation 10-3 does not imply that there are physical changes of individual bulk characteristics in the solid soil particles or in the water during liquefaction. Instead, the relationship simply implies that when a soil begins to liquefy under excessive pore pressure induced by large impulsive loads, the bulk modulus behavior of the overall soil-water mixture is shifting from sand to water. The numeric quantities shown in the equation are nothing more than a way to represent the event occurring in the soil-water mixture rather than an implication of physical transformations of individual water or solid particles within the soil mass.

10.9.5 Bulk Transition Relationship's Proof of Concept

In order to properly apply the proposed bulk transition relationship as shown in Equation 10-3, the baseline *MAT_FHWA_SOIL material model must be modified to allow internal updates of the bulk modulus based on pore pressure computed from the previous time step. Since the material model's source code is not readily available, a demonstration of the concept was conducted using LS-DYNA's restart capabilities to allow updates to bulk modulus for each blast. Chapter 11 provides complete details on the baseline analysis conducted to demonstrate the validity and applicability of the proposed bulk transition relationship discussed in this section of the dissertation.

11 Enhanced Baseline Model Analysis

11.1 Overview

The analysis using the final baseline model (Figure 10-4) with bulk enhancements is a tri-level sequential-blast evaluation of liquefaction development, which simulates blast series 3 of the May 2005 Vancouver blast-induced liquefaction experiment. The baseline test consisted of 7 explosive charges per level for 3 blasting-levels located at depths of 21 feet, 28 feet and 33 feet. Blasting began at the bottom level working upward toward the top level in the per-level sequence as shown in Figure 11-1. A detailed discussion of the baseline analysis is presented in the following subsections.

Upon completion of the blast series 3 analysis, the same baseline model that was calibrated for blast series 3 was applied to simulate blast series 1 of the May, 2005 Vancouver blast-induced liquefaction experiment. Blast series 1 consisted of 1 lb of explosives placed in each of the 24 pre-designated locations, with the exception of the northeast blast hole's depth misalignment as discussed in Chapter 9. Although blast series 1 has a non-uniform depth misalignment in one of eight blast holes, an analysis using uniformly placed explosives can still provide valuable information in support of the proposed bulk transition enhancements' ability to predict the trend and overall liquefaction behaviors. One should note that minor errors and discrepancies can be expected between analysis and measured data for blast series 1 due to depth

misalignment as discussed in Chapter 9. In spite of the expected errors, results for blast series 1 are presented in this chapter for completeness and for verifying the soundness of the proposed bulk transition enhancements.

11.2 Application of the Bulk Transition Relationship

The bulk modulus transition relationship described in Chapter 10 was the pivotal improvement made to the final version of the baseline analysis model. Ideally as discussed in Chapter 10, the bulk modulus transition equation would work best if incorporated directly into the existing *MAT_FHWA_SOIL model for the following reasons:

1. Bulk modulus could be updated in each element, resulting in much smoother transitioning of the moduli across the geometry of the entire soil model.
2. Bulk moduli for each element could be updated as often as every iteration. An input option could be added to allow users the ability to specify an update frequency that is suitable for the analysis of interest. More frequent updates of the bulk modulus would mean smaller changes in bulk modulus per update, which could also reduce the generation of potentially undesirable shocks.
3. Pore pressure and pre-existing overburden conditions could be computed and applied automatically within the material model's calculation routines. Thereby reducing potential errors caused by manual inputs and changes between bulk modulus updates.

Due to difficulties in obtaining the material model for modifications, a proof-of-concept approximation approach was developed to demonstrate the functionality and validity of the bulk transition relationship.

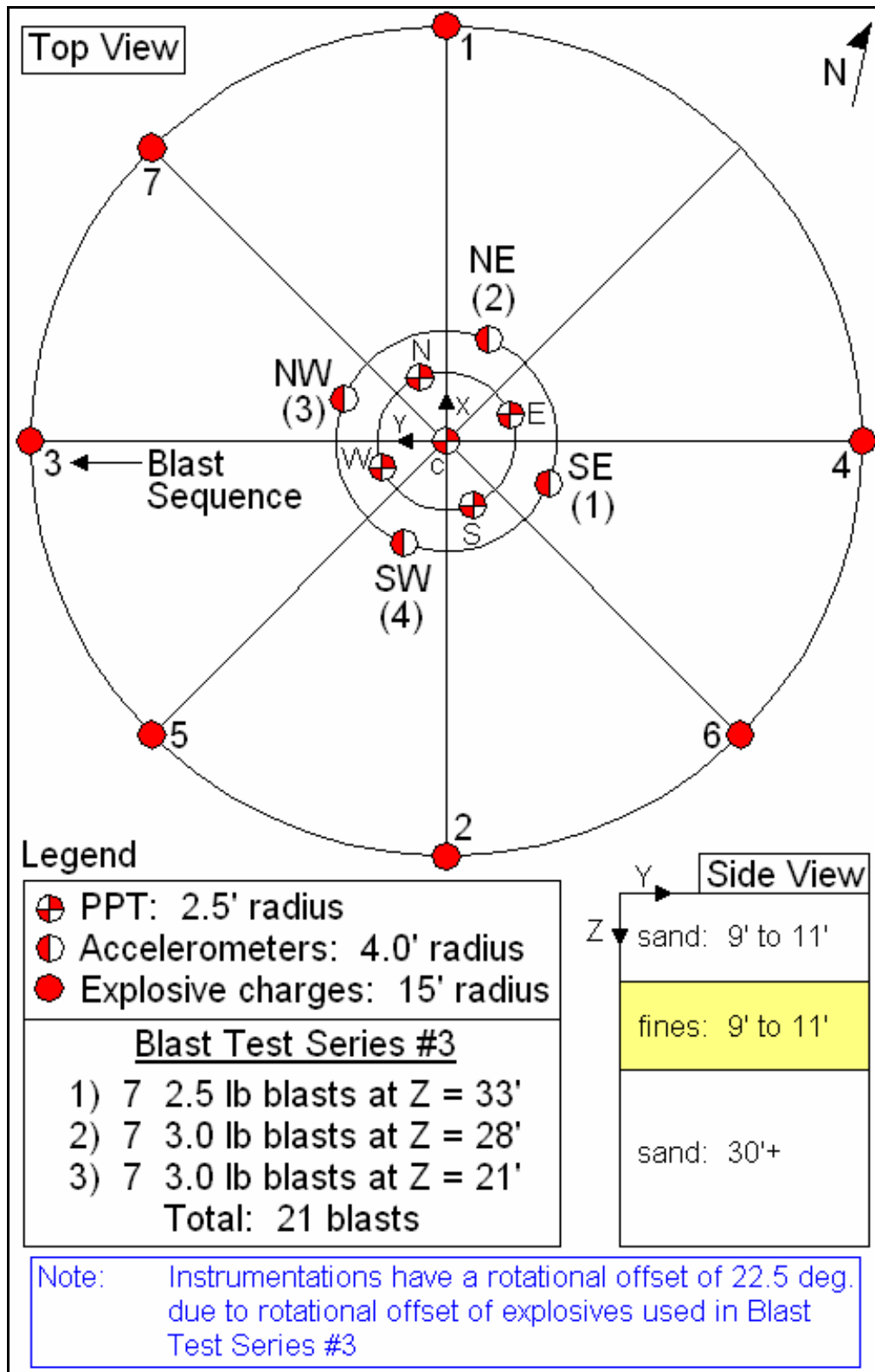


Figure 11-1 May 2005 Test Blast Order and Instrumentation Layout

11.3 Proof-of-Concept Evaluation Assumptions and Limitations

Since the baseline material model was not readily available for enhancements, it was simply infeasible to perform manual modifications to the bulk modulus for each element during each analysis iteration. Any attempt to do so would significantly increase analysis run time and monitoring time required to complete the tasks by orders of magnitudes. To ensure a feasible analysis, the incorporation of the bulk transition effects to prove the viability and applicability of the concept were performed manually with the following limitations:

1. The model was divided into several sections with respect to depths and location of instrumentation. Each type of instrumentation (i.e. PPT's, accelerometers) was located within a section by itself to minimize cross smearing of results between two instruments.
2. Since it is not feasible to manually extract average volumetric stresses from each analysis iteration to compute bulk moduli for the next time step, an estimated bulk transition relationship was applied for the proof-of-concept analysis. Instead of updating the bulk modulus for each element after each analysis iteration, bulk moduli for sections defined in 1 above were updated at the end of each blast at a time just prior to the next blast. Although this assumption provides a coarse approximation of the more comprehensive and frequent updates as proposed in Section 11.2, it should be sufficient to demonstrate the merits and soundness of the proposed bulk transition concept.
3. Computations of the estimated bulk modulus for simulating blast series 3 were based on the assumption that full liquefaction was achieved by the end of the

21-blast sequence in blast series 3. As such, water in the soil was expected to take over the full volumetric load carrying responsibility by the end of blast series 3.

4. Analysis on blast series 1 was based on the assumption that blast series 1 produced approximately 50% to 60% of impulsive volumetric loading effects in the soil within the blast circle width and depth of interest. This assumption was based on a “ball-park” estimate of blast series 1 using cube root of explosive weights, plus considerations for one of eight blast holes’ depth misalignment. Similar to the estimate made in Item 3 above, this estimate is necessary without the bulk transition method being implemented directly into the material model where updates on bulk moduli are based on current computed volumetric stresses. After comparing the computed results against measured data for blast series 1, this assumption appears to provide a good first order estimate of the event.
5. Modifications to the bulk moduli were made via the full restart feature of LS-DYNA using custom developed self-modifying input controlling routines and batch job submission scripts.
6. In order to account for additional uncertainties and errors induced by discretizing the large model into a limited number of sections along its depth, an iterative approach was applied to calibrate and fine-tune the uncertainty factor. The uncertainty factor that was calibrated for blast series 3 and was applied to blast series 1 without modifications.

7. Without the transitional changes of bulk modulus among all elements using more frequent iterations as discussed in Chapter 10, slight changes in bulk moduli in one section of the model have greater effects on neighboring sections. Although changes in the exponents are not significant for each run, an iterative approach to account for discretization errors is warranted to converge to the desired solution.
8. The discretization and simplifying assumptions made in this analysis are recommended only for demonstrating the validity, soundness and applicability of the bulk transition concept. It is preferred to have the features incorporated directly into the material model for greater consistency and uniformity with less potential for errors and undesirable transient effects.

11.4 Proof-of-Concept Analysis Steps

The analysis performed to demonstrate the application of the bulk transition relationship was made possible by a custom developed C++ program to perform self-modifications and updates of the input deck containing the latest soil material properties. A summary of the steps required to perform the analysis is presented below while the corresponding input decks and controlling software are presented in Appendix D of this dissertation.

1. Subdivide the LS-DYNA model input deck into the following modules: First, the control deck containing fundamental LS-DYNA commands used to define the problem and the corresponding analysis parameters. Second, the geometry deck containing elemental and nodal information of the model's geometry as well as nodal and elemental constraints and sets. Third, soil material

properties deck used to allow updates of each soil layer's input parameters such as bulk moduli. Fourth, a stress initialization deck containing ANSYS (or other implicit FEA software) results of the soil model subjected to gravity load. Stress results from this deck become the initial values for each element in the full analysis. This is done to represent the pre-load in the soil due to pre-existing stresses in the soil mass due to gravity and prior to any blasting operations.

2. Develop a custom batch script as presented in Appendix D of this dissertation.
3. Develop a custom self-modifying controller similar to the one presented in Appendix D of this dissertation.
4. Submit the analysis and the run will follow the steps listed below:
 - a. Call self-modifying program to generate the initial soil material input deck for analysis. Self-modifying program also updates the input deck for itself in preparation for the next analysis call (or step).
 - b. Call LS-DYNA to perform the analysis due to the first blast using soil properties generated by step 1.
 - c. Terminate LS-DYNA run just prior to the next blast.
 - d. Call self-modifying program to generate the next set of soil properties.
 - e. Call LS-DYNA via a full restart to incorporate results from the previous run from step 3, and material inputs from the current self-modifying controller run listed in step d.
 - f. Repeat steps c to e until all blasts have taken place.

The remaining subsections in this chapter of the dissertation present the results from the analyses of the final baseline model with bulk transition enhancements.

11.5 Analysis Input Parameters

Table 7-2 summarizes the mechanical properties and most of the input parameters required for the baseline analysis. Corresponding detonation properties and hydrodynamic parameters are presented in Table 8-1. Remaining input parameters used to define the bulk transition effects are summarized in Table 11-1 for blast series 3 and Table 11-2 for blast series 1. Equations used to compute input parameters for the bulk transition effects are located in Section 10.9.4.

Table 11-1 Summary of Bulk Transition Input Parameters for Blast Series 3

Blast circle radius	15 ft	Explosive Type			Pentex
Bottom level charge depth	33 ft	Bottom level explosive wt. (each)			2.50 lb
Mid level charge depth	28 ft	Mid level explosive weight (each)			3.00 lb
Top level charge depth	21 ft	Top level explosive weight (each)			3.00 lb
No. of explosives per level	7	Weighted average explosive depth			27.2 ft
Factor of uncertainties f	0.153	TNT equivalency (energy based)			1.12
PPT Location	East	Center	South	North	Center
Depth	18 ft	25 ft	31 ft	38 ft	45 ft
Depth Factor z_r	1.0	1.0	1.1	1.4	1.7
Exponent n	0.67	0.58	0.98	2.16	4.51
Equivalent distance to blast source	17.6 ft	15.2 ft	15.5 ft	18.5 ft	23.3 ft
Scaled distance to blast source (SD)	4.9	4.3	4.3	5.2	6.5
Volumetric strain factor (K_{sk}) (Calibrated to Blast Series 3)	0.162	0.150	0.120	0.120	0.120

The baseline volumetric strain factor (K_{sk_3}), which was introduced in Section 7.4, was calibrated for blast series 3 with an average explosive weight (W_{avg_3}) of 2.833 lbs. This average explosive weight was based on seven 2.5-lb charges at bottom level and a

total of fourteen 3.0-lb charges at mid and top levels. As with any explosive related scaled parameters, volumetric strain factor for other explosive weights (K_{sk_i}) can be scaled from K_{sk_3} using Equation 11-1 as a cube-root function of the average explosive weight of interest (W_{avg_i}) and W_{avg_3} from blast series 3.

Table 11-2 Summary of Bulk Transition Input Parameters for Blast Series 1

Blast circle radius	15 ft	Explosive Type			Pentex
Bottom level charge depth	33 ft	Bottom level explosive wt. (each)			1,00 lb
Mid level charge depth	28 ft	Mid level explosive weight (each)			1.00 lb
Top level charge depth	21 ft	Top level explosive weight (each)			1.00 lb
No. of explosives per level	8	Weighted average explosive depth			27.3 ft
Factor of uncertainties f	0.153	TNT equivalency (energy based)			1.12
PPT Location	East	Center	South	North	West
Depth	18 ft	25 ft	31 ft	38 ft	45 ft
Depth Factor z_r	1.0	1.0	1.1	1.4	1.6
Exponent n	0.67	0.58	0.98	2.16	4.51
Equivalent distance to blast source	17.7 ft	15.2 ft	15.4 ft	18.4 ft	23.2 ft
Scaled distance to blast source (SD)	7.0	6.0	6.1	7.3	9.2
Volumetric strain factor (K_{sk})	0.1145	0.1060	0.0848	0.0848	0.0848

$$K_{sk_i} = K_{sk_3} \cdot \left(\frac{W_{avg_i}}{W_{avg_3}} \right)^{\frac{1}{3}} \quad (11-1)$$

11.6 Blast Sequence Snap Shots

Figure 11-2 illustrates a plan (top) view of the blast wave propagation sequence at the bottom level as computed by LS-DYNA for the simulation of blast series 3. Blast order is shown from top down while across from left to right are three consecutive snap-

shots in time at an output interval of 0.01 seconds upon first sign of the corresponding blast initiations. Corresponding mid- and top-level blast sequence snap shots are summarized in Figure 11-3 and Figure 11-4, respectively, to complete the entire set of tri-level sequential blasts conducted for blast series 3.

One can easily visualize the blast wave propagation emanating from the center of each blast source upon detonation. Meanwhile, one can also visualize the effects of having fairly wide output saving intervals as discussed in Section 10.6. The baseline result output interval was set to approximately 0.01 seconds. An approximate value is declared since LS-DYNA does not and cannot guarantee an exact output saving interval due to the dynamic and ever changing time step sizes being used in the analysis. LS-DYNA can only output at the time closest to the saving intervals specified by the user.

At the beginning of the blast series, detonation is initiated in the bottom level. The output saving interval of 0.01 seconds captured a large portion of nearly every blast-pressure spike associated with each blast initiation as shown in Figure 11-2. Toward the end of the bottom level blast, results began to show the effects of a slight cumulative offset in both detonation initiation and shock wave output interval time. This accumulation of time offset eventually led to a noticeable shift of the output interval from capturing within the detonation spike time frame to barely missing the spikes altogether toward the end of the blast series in the top level. Fortunately, the capturing of spikes during output is more of a cosmetic annoyance rather than an erroneous effect. This is because the underlying analysis iteration time step is in the range of 2 to 3 microseconds down to ten's of nanoseconds, which is more than adequate to capture each transient spike experienced during the course of the analysis as discussed in Section 10.6.

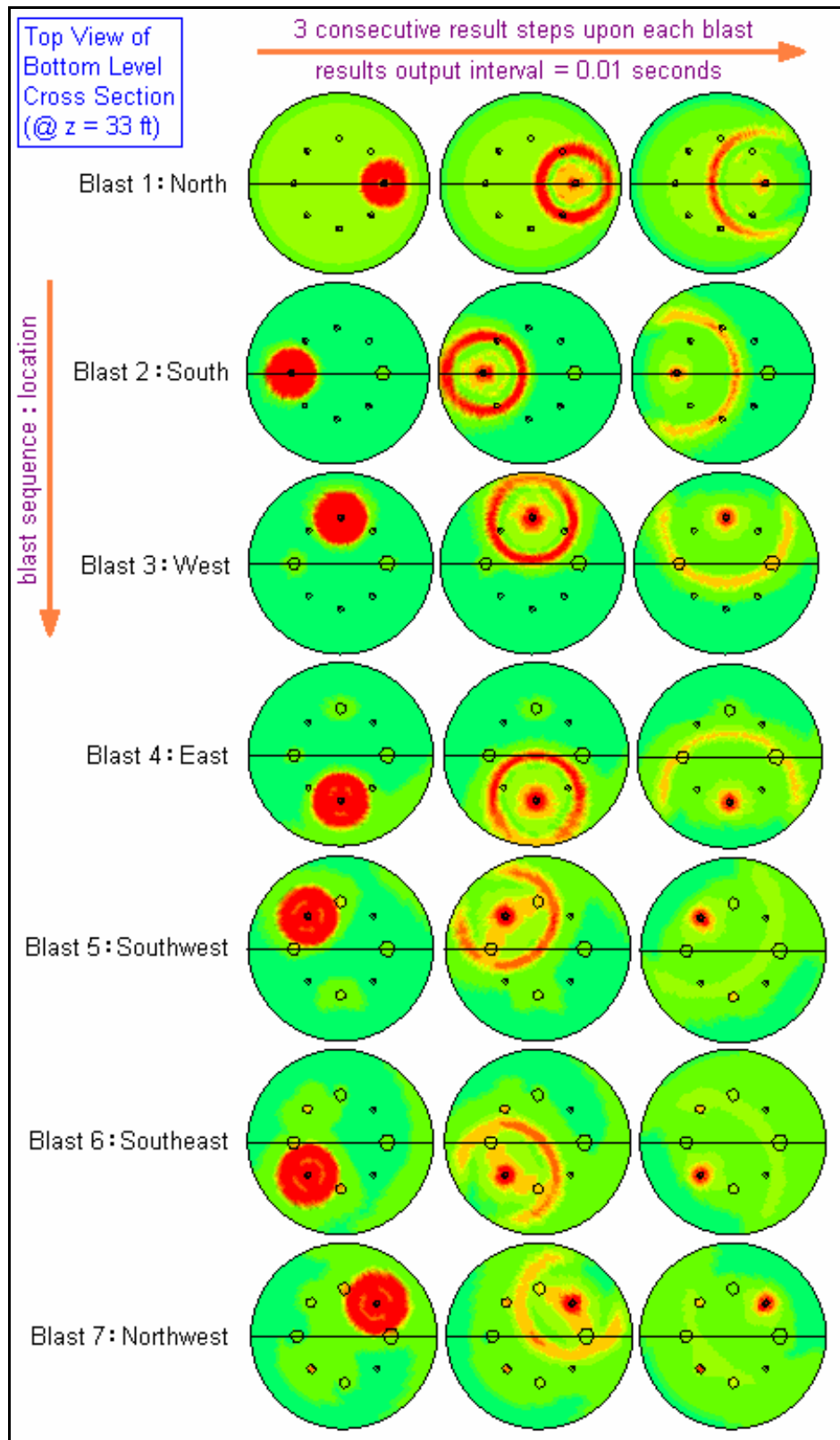


Figure 11-2 Blast Series 3 Bottom Level Blast Wave Propagation Summary

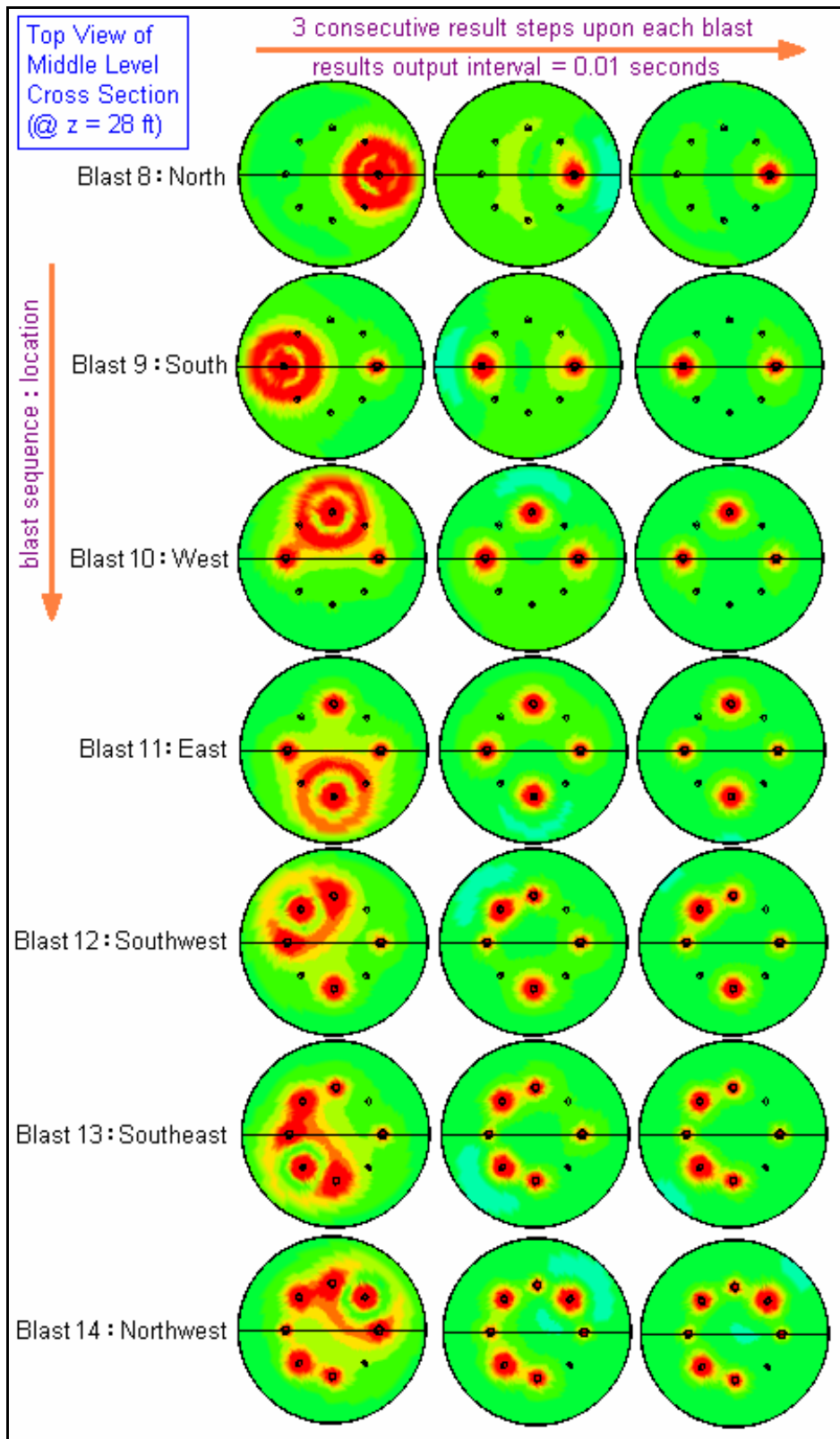


Figure 11-3 Blast Series 3 Mid-Level Blast Wave Propagation Summary

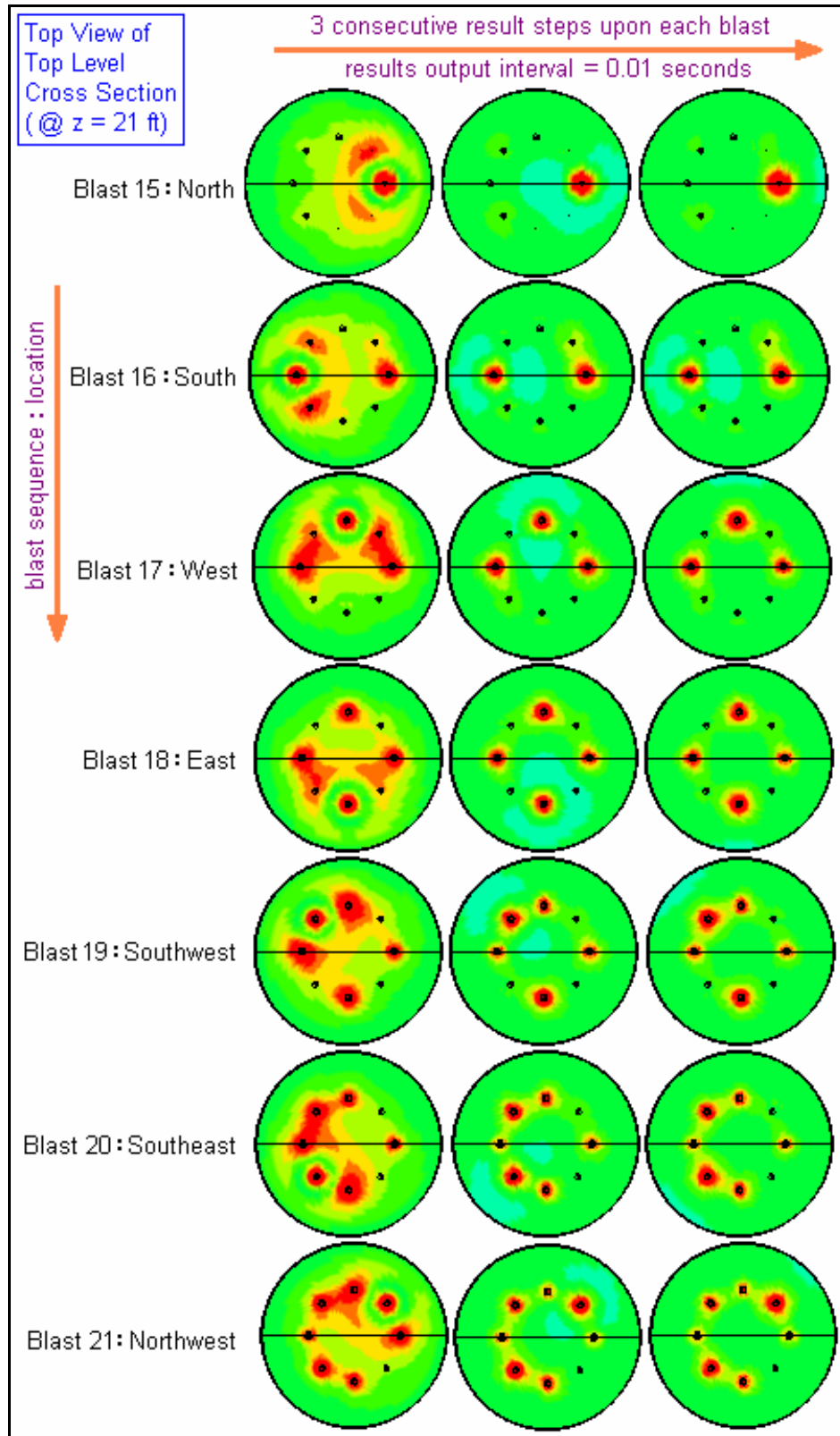


Figure 11-4 Blast Series 3 Top Level Blast Wave Propagation Summary

More succinctly stated, the frequency of output interval is nothing more than a way to provide snapshots of a nearly continuous event being evaluated in the background by the software. There are potential solutions that would increase the probability of capturing more transient spikes in the output by utilizing manually defined time step increments. Given that the analysis run time is significant and the actual distance between each blast source to each observation or instrumentation point is different for each blast and for each location, significant manual effort and multiple reruns of the same analysis would be necessary to capture every spike associated with each blast. Such amount of time spent on retrieving spike information that does not affect the overall results is not cost effective, necessary, nor recommended. As such, results are presented as shown in this dissertation.

11.7 Pore Water Pressure Results

Results showing excess pore water pressure development at each of the pre-designated PPT locations for both the baseline blast series 3 and the additional analysis of blast series 1 are presented in this section of the dissertation in the following order: North PPT at depth of 38 feet; south PPT at depth of 31 feet; west PPT at depth of 45 feet; east PPT at depth of 18 feet; and center PPT at depth of 25 feet (Corresponding to Figure 11-5 through Figure 11-9, respectively). The order used here represents the order of data acquisition channels used at the May 2005 Vancouver blast-induced liquefaction experiment. Each figure is presented with an overlay of measured data and computed results at a specific PPT location for both blast series 3 and blast series 1. Annotations were added into each figure of results to enhance clarity and to minimize confusions.

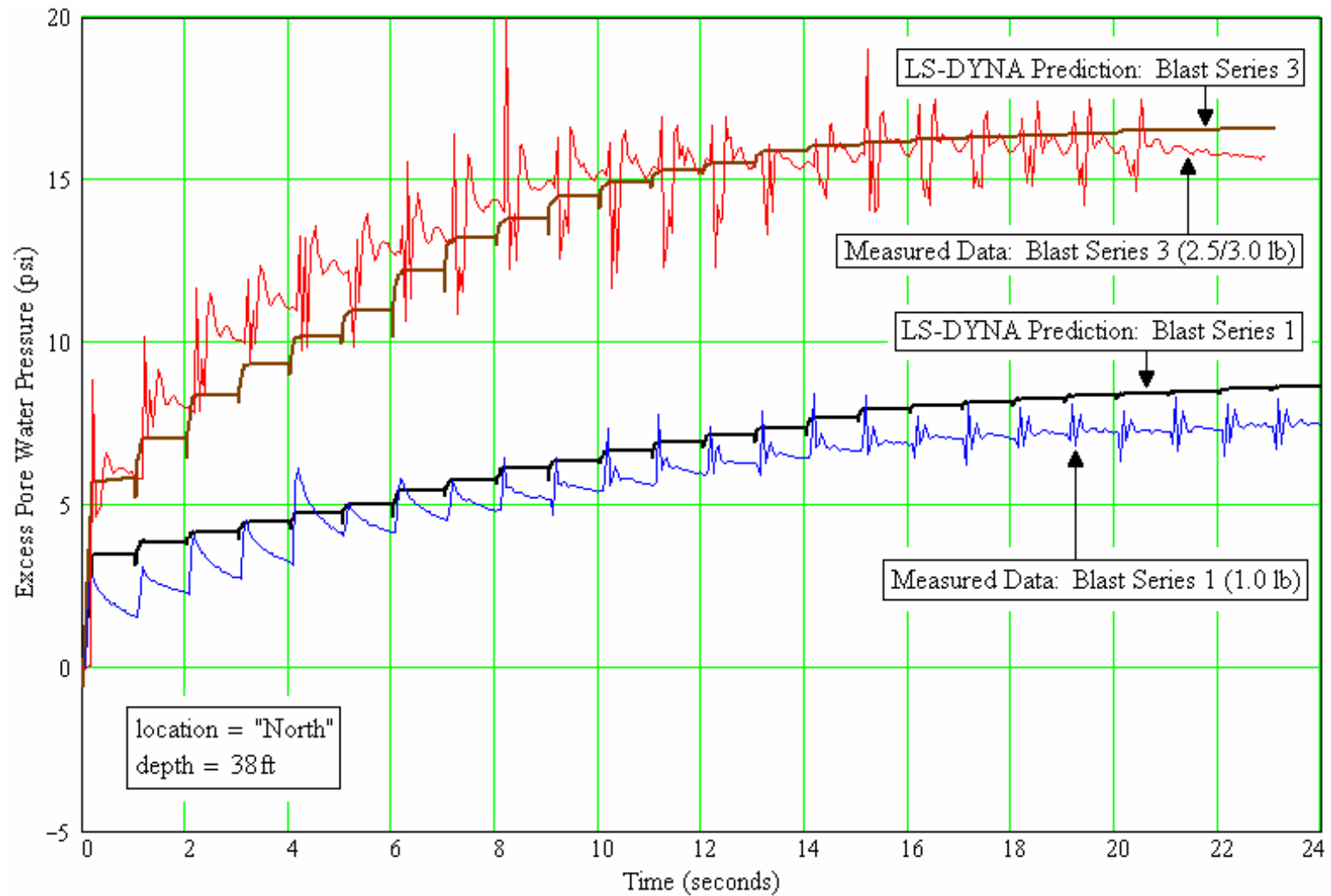


Figure 11-5 Excess Pore Pressure Histories (North PPT at Z = 38 ft)

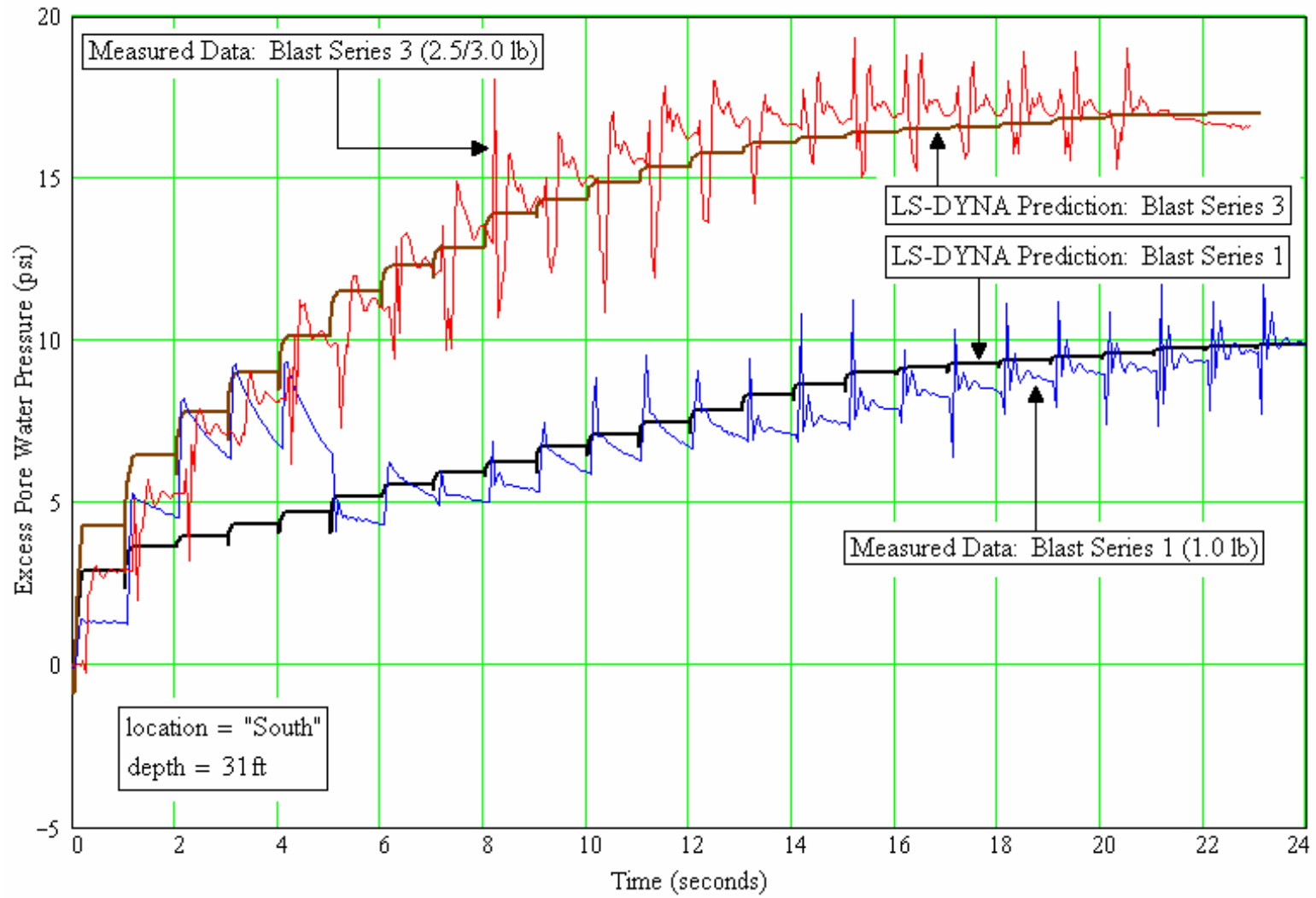


Figure 11-6 Excess Pore Pressure Histories (South PPT at Z = 31 ft)

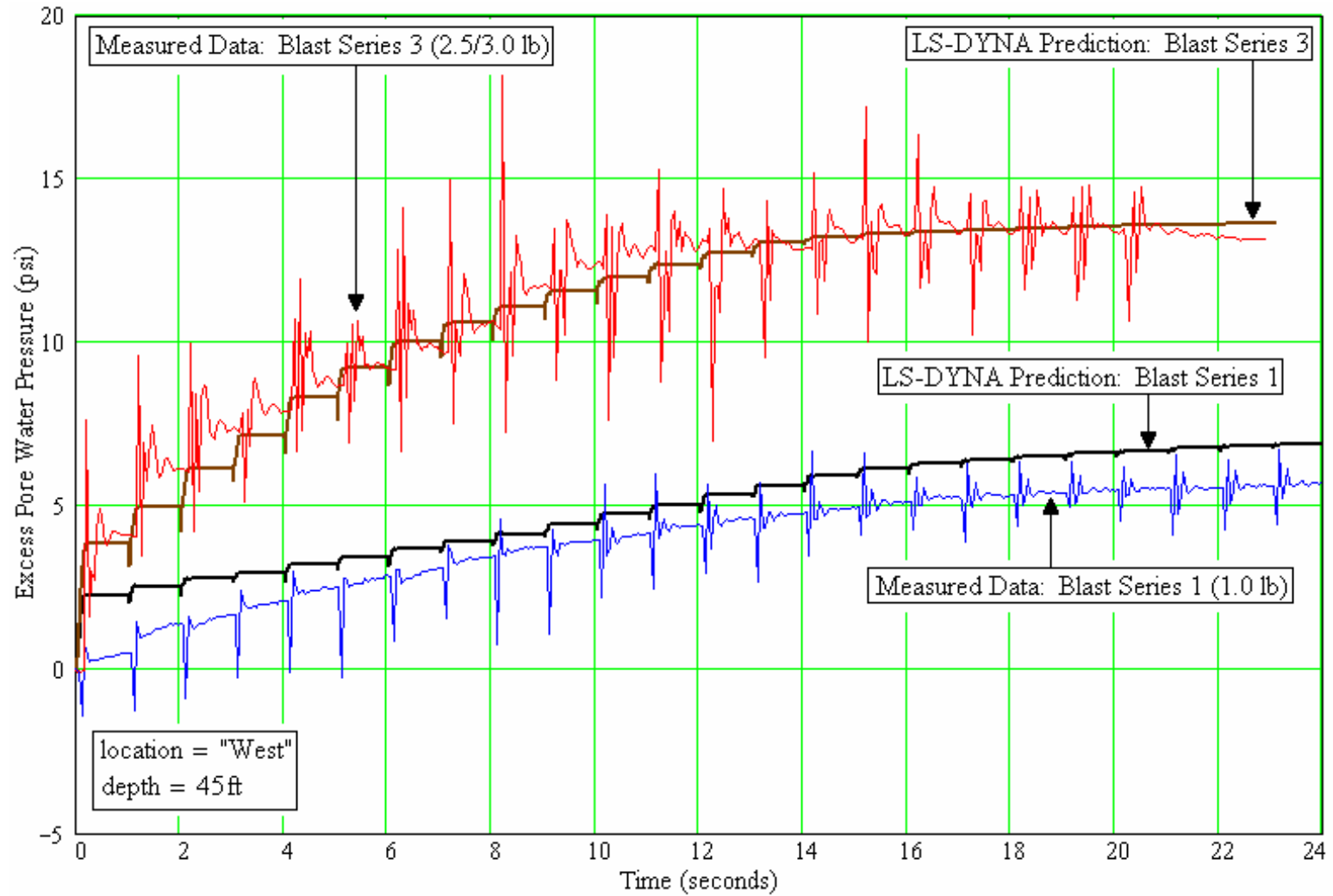


Figure 11-7 Excess Pore Pressure Histories (West PPT at Z = 45 ft)

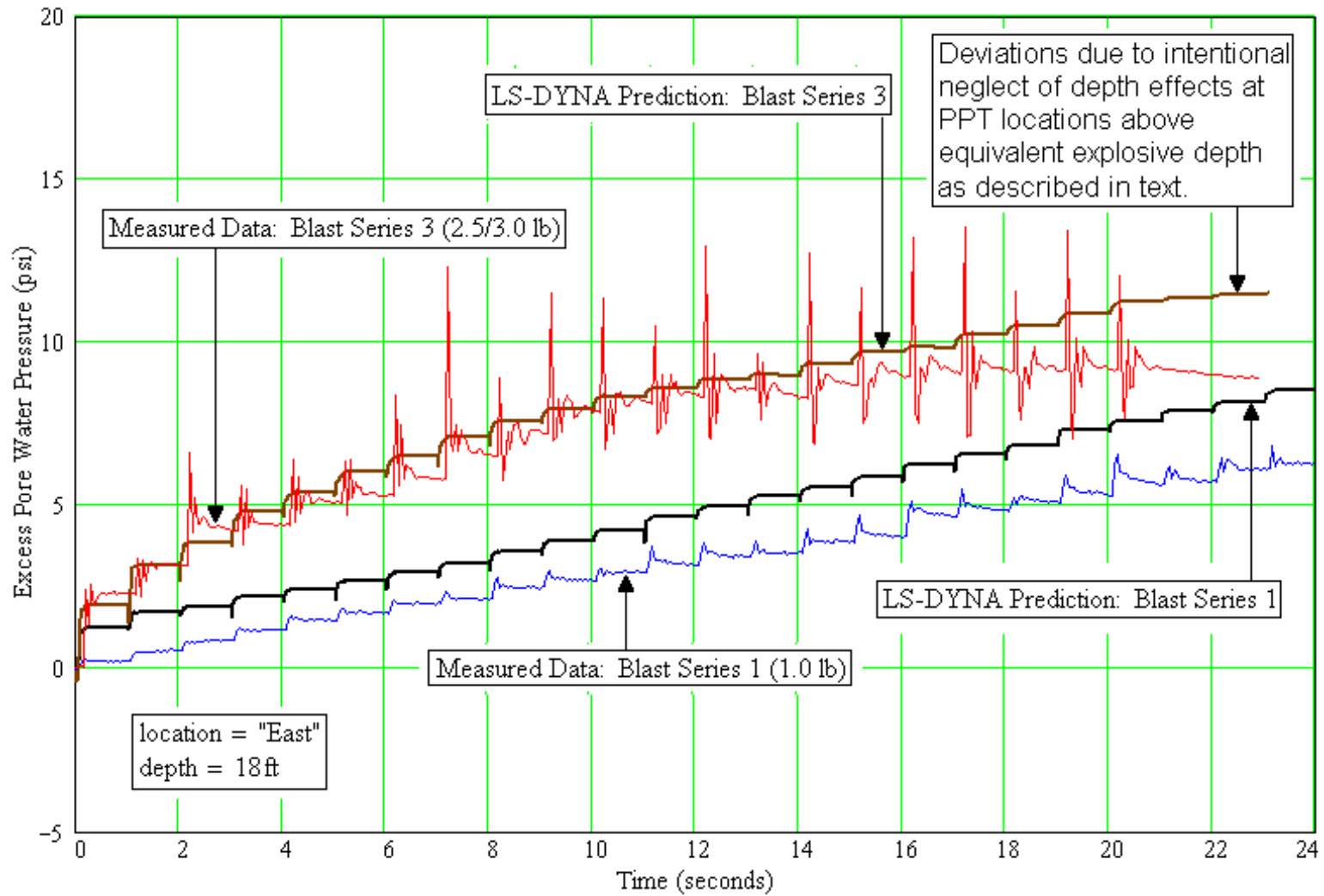


Figure 11-8 Excess Pore Pressure Histories (East PPT at Z = 18 ft)

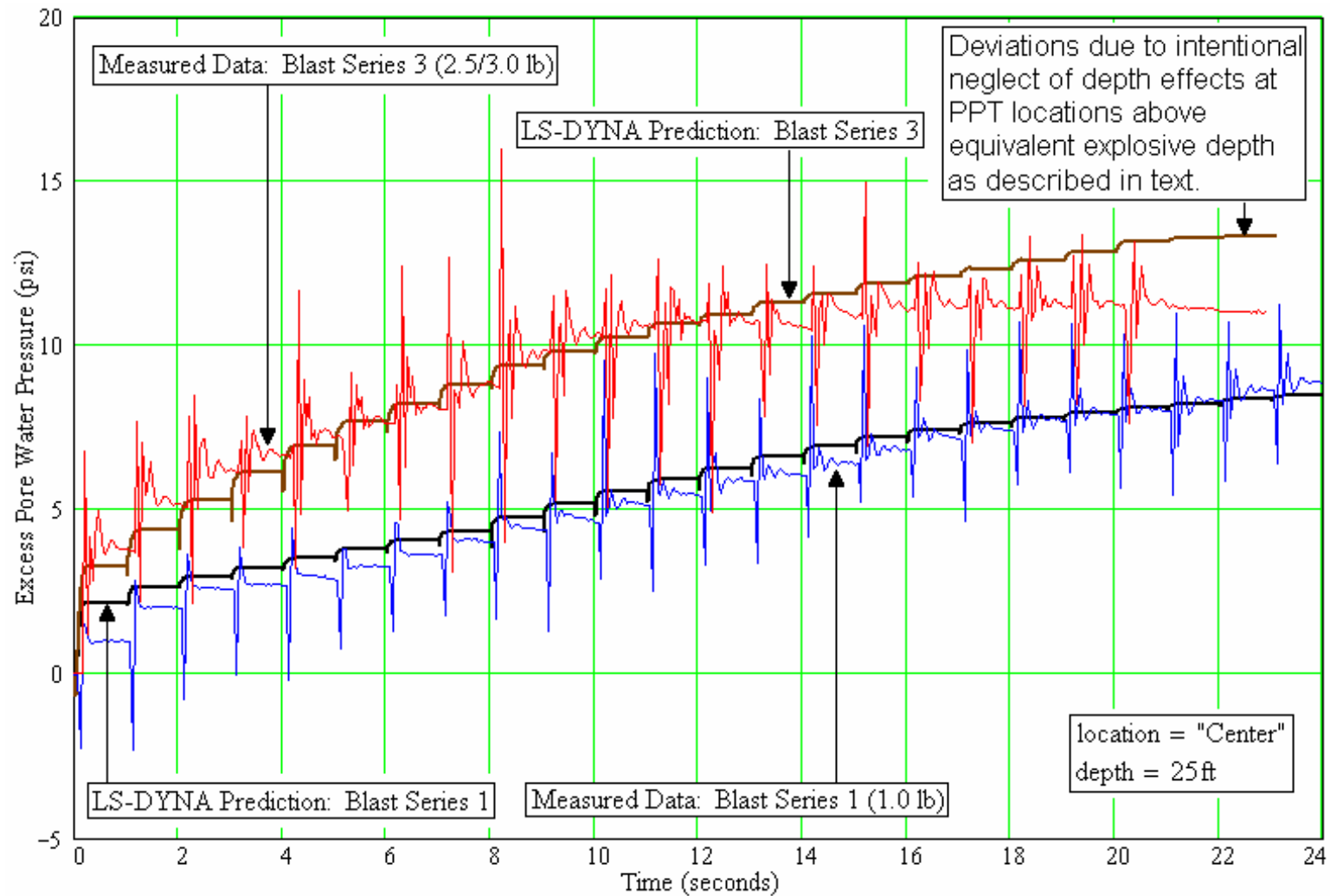


Figure 11-9 Excess Pore Pressure Histories (Center PPT at Z = 25 ft)

Initial effective stress for each PPT location as shown in Table 11-3 were computed from the depths and estimated unit weights of the corresponding soil layers provided by Professor Rollins. Pore water pressure ratios (R_u) obtained from dividing the pore pressure values by the corresponding initial effective stress were computed and plotted in Figure 11-10 through Figure 11-14.

Table 11-3 Initial Effective Stress at Each PPT Location

Location	Depth (ft)	σ' (psi)
East PPT	18	10.1
Center PPT	25	12.7
South PPT	31	14.9
North PPT	38	17.4
West PPT	45	20.0

As described in Section 10.6, a coarse output interval of 0.01 seconds was necessary to maintain a reasonable amount of hard disk space consumption (i.e. less than a total of 5 GB per analysis run). The wide output interval comes with a cost of potentially missing pressure spikes, especially toward the end of the simulation where time value round off is more prominent (i.e. analysis time in terms of seconds while time steps in terms of microseconds) as discussed in Section 11.6. Nevertheless, one can readily see the trends of the pore pressure build-up throughout both blast series 1 and blast series 3 as observed at each of the pre-designated PPT locations.

For a proof-of-concept analysis using rough sections of bulk transition assignments, the proposed bulk transition relationship described in this section reasonably predicted pore pressure development for both blast series 3 and blast series 1.

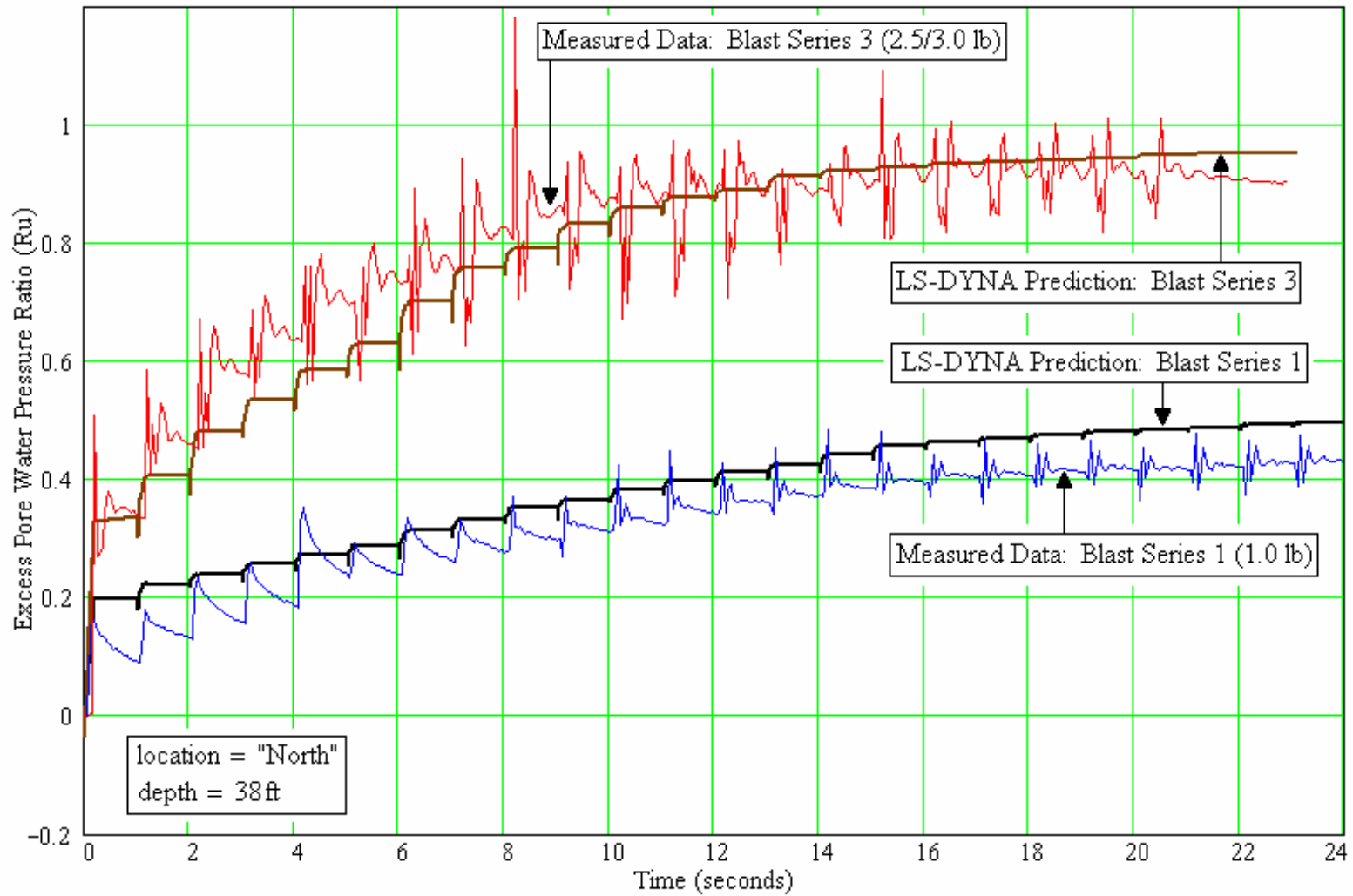


Figure 11-10 Excess Pore Pressure Ratio (North PPT at Z = 38 ft)

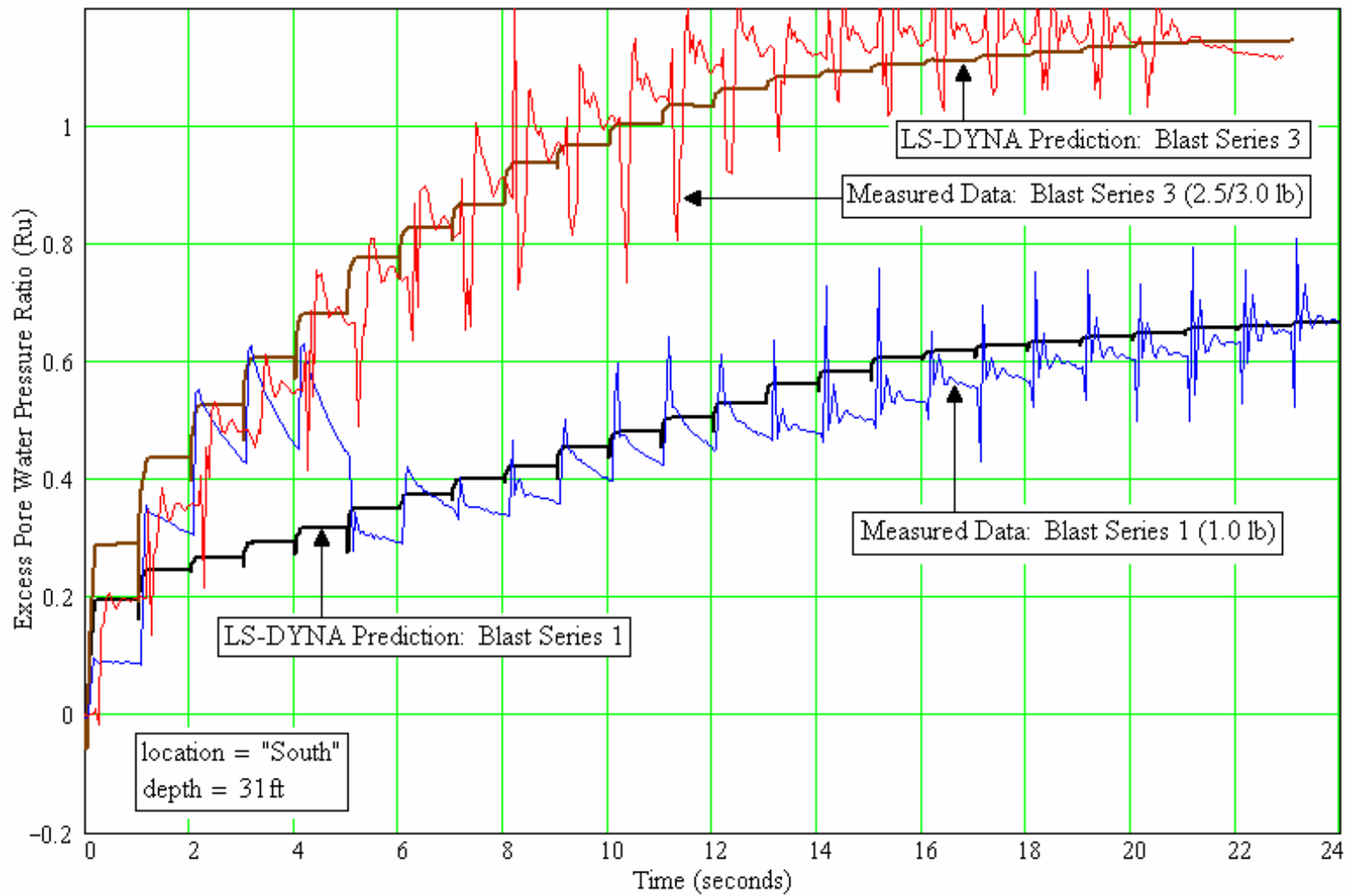


Figure 11-11 Excess Pore Pressure Ratio (South PPT at Z = 31 ft)

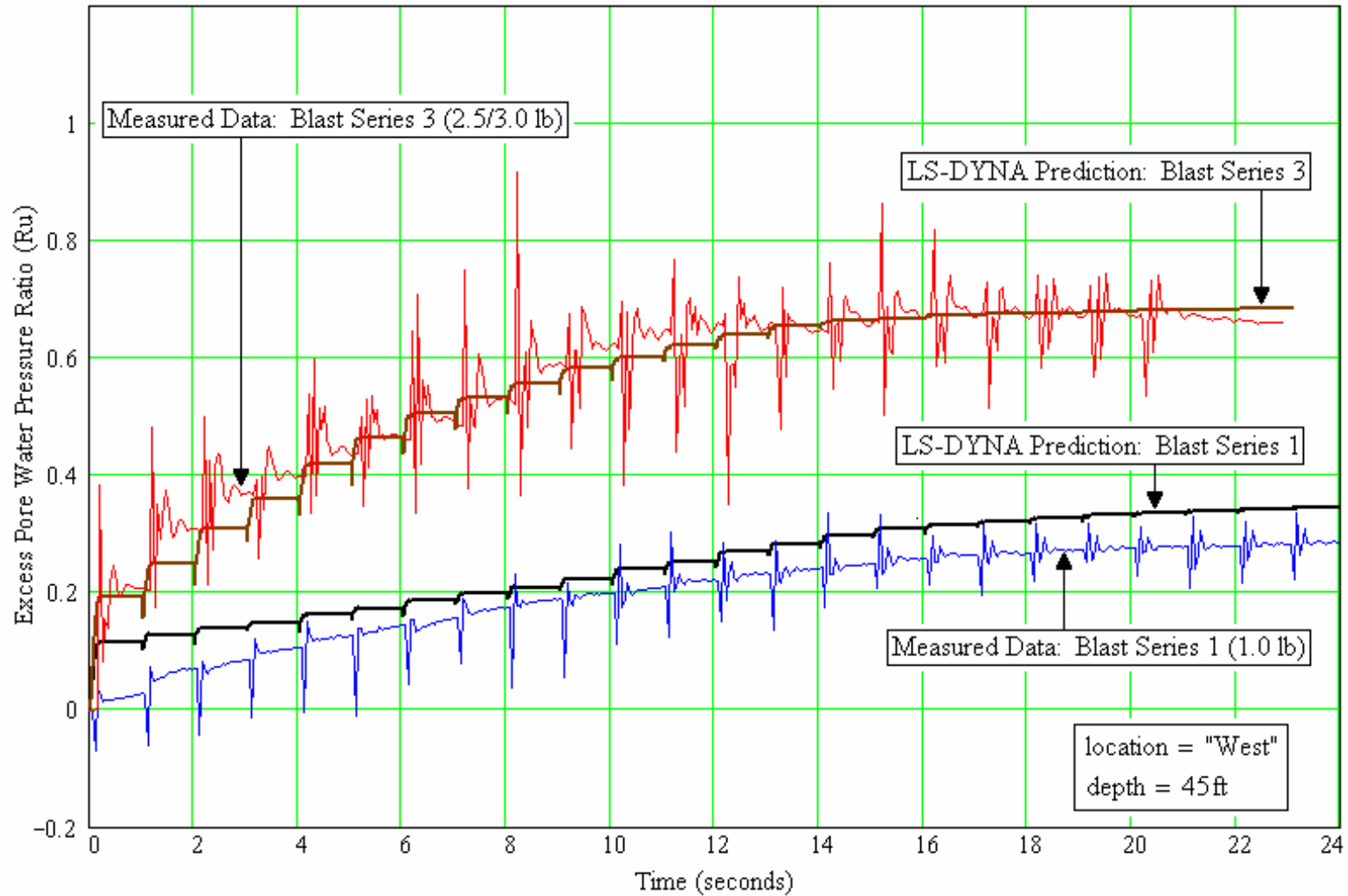


Figure 11-12 Excess Pore Pressure Ratio (West PPT at Z = 45 ft)

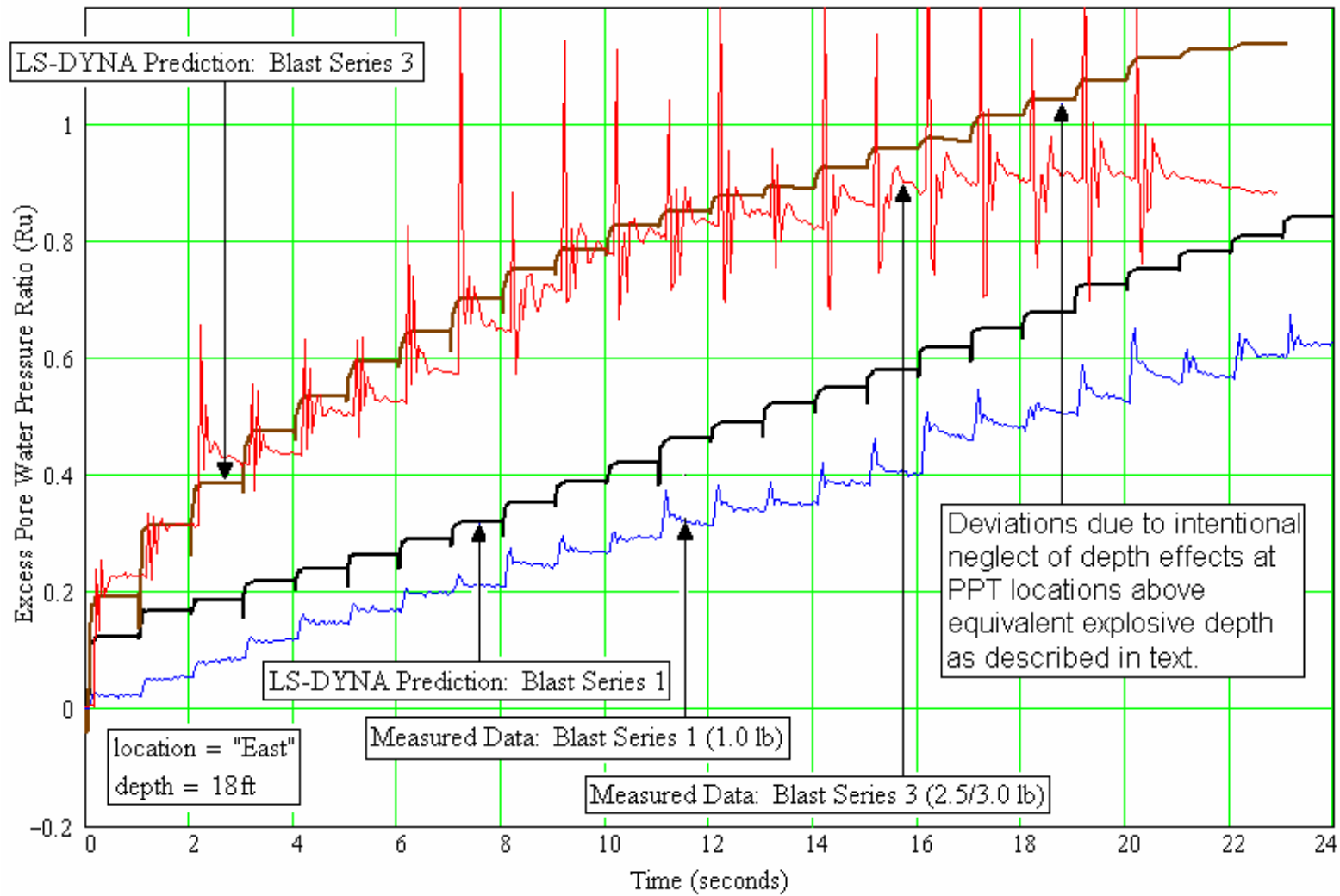


Figure 11-13 Excess Pore Pressure Ratio (East PPT at Z = 18 ft)

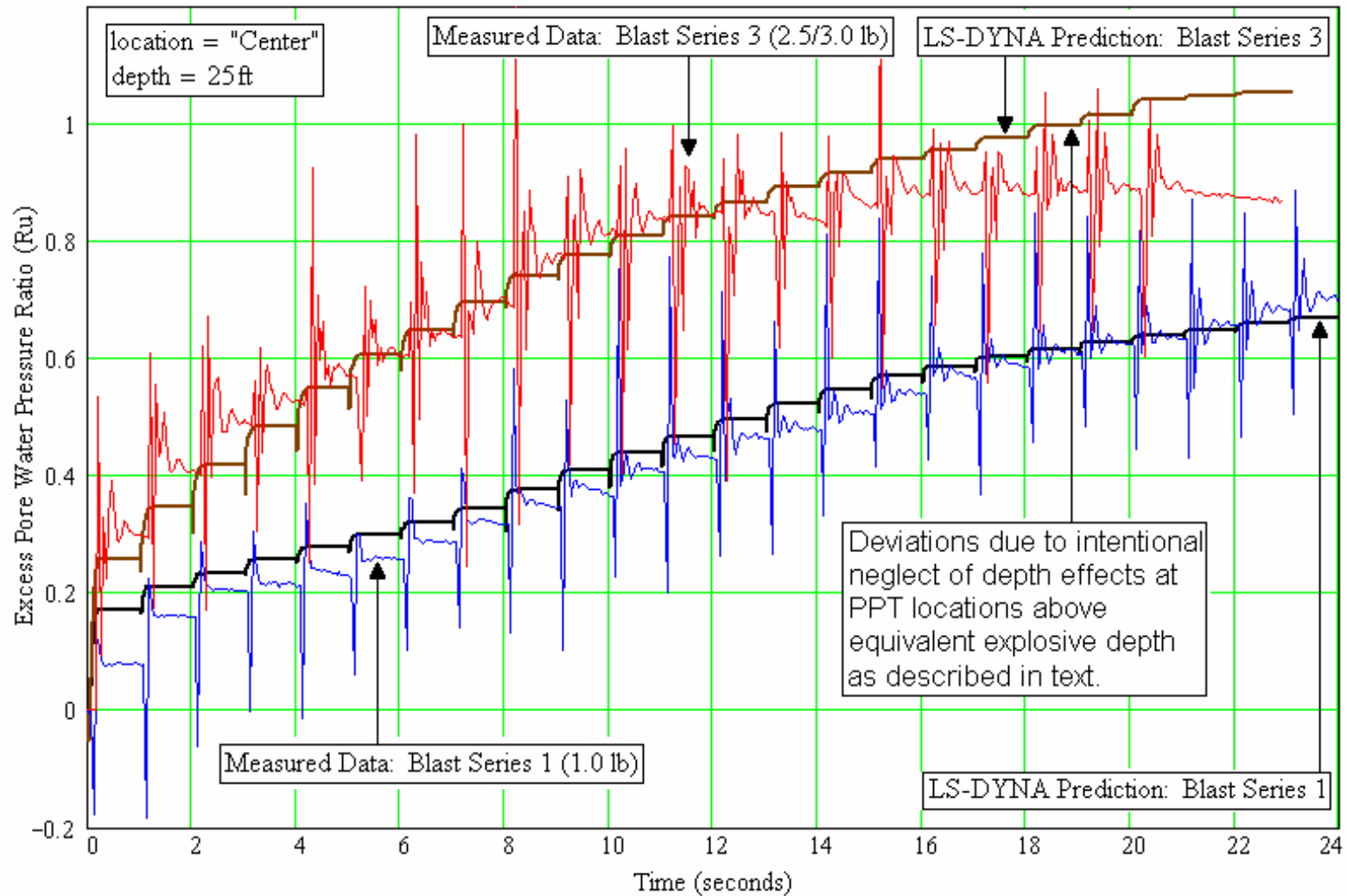


Figure 11-14 Excess Pore Pressure Ratio (Center PPT at Z = 25 ft)

For the baseline analysis, essentially the same set of input parameters calibrated for blast series 3 were used for both blast series 3 and blast series 1 at all PPT locations. No attempt was made to custom fit each individual curve for each PPT location and for each blast series during the final analysis. Differences observed in some of the input parameters were driven by different test environments between blast series 1 and blast series 3. Variables that influenced the differences in input parameters include the number of explosives per level (i.e. 8 in blast series 1, and 7 in blast series 3) and the corresponding explosive weights. The non-uniform explosive weights and number of explosives per level in blast series 3 resulted in a slight shift of values in the equivalent explosive depth and average explosive weight, which propagated through the calculations of many of the input parameters.

During the course of the research, minor adjustments using an iterative process were used to calibrate the data against blast series 3 in order to help achieve the desired level of confidence in the data fitting process. This is especially true when discrete approximations were used for the proof-of-concept analysis. To illustrate the effects and necessity of iterative input parameter adjustments during data calibration, depth effects at PPT depths of 18 and 25 feet (i.e. above the corresponding centroidal explosive depth) were intentionally ignored as discussed in Section 10.9.4. This is done by assuming the value of the depth factor to be 1.00, one can easily observe that the curvatures of the computed results at the depths of 18 feet (Figure 11-8) and 25 feet (Figure 11-9) deviate from the measured data toward the end of the blast series. This type of behavior can easily be corrected by accounting for depth effects. Depth effect adjustments were not applied in the research for two simple reasons. First, to demonstrate the existence of

depth effects. Second, since a slight improvement in a proof-of-concept analysis did not justify the additional time required to improve results that may require further iterations once integration and implementation of the approach into the material model is completed in future research. Nevertheless, a brief description of the effects of depth is provided in the following paragraph for future references.

A slight increase in the depth factor can slow down the rise rate of the bulk modulus, thereby inducing a more concave downward trend as exhibited by the predicted curves computed at greater depths such as those shown in Figure 11-5 through Figure 11-7 and Figure 11-10 through Figure 11-12. Other similar minor fine tuning adjustments and calibrations for parameters such as the depth factor described in this paragraph can also be made to further improve the computed results observed in Figure 11-5 through Figure 11-14.

A general form of the bulk transition relationship as analyzed during this research is proposed for implementation to soil material models, further research of the relationship is expected to yield greater insight that can lead to overall improvement in the bulk modulus transition concept's predictive capabilities.

11.8 Acceleration, Velocity and Displacement Results

Acceleration, velocity and displacement time histories at the locations of the four accelerometers shown previously in Figure 10-1 were extracted from the baseline analysis. The following pages summarize the acceleration time histories as computed by LS-DYNA at each of the accelerometer locations, followed by velocity and displacement time history results, respectively.

Recall from Figure 11-1, locations of the accelerometers used in both blast series 1 and blast series 3, in the respective data acquisition order, are:

1. Accelerometer located northwest of blast circle center axis at depth $Z = 25$ ft.
2. Accelerometer located northeast of blast circle center axis at depth $Z = 25$ ft.
3. Accelerometer located southwest of blast circle center axis at depth $Z = 25$ ft.
4. Accelerometer located southeast of blast circle center axis at depth $Z = 25$ ft.

Due to excessive noise and magnitude drifts observed in the acceleration data measured at the Vancouver blast-induced liquefaction site, the author made an attempt to filter the data by subtracting the mean value curves of each blast segment to determine if the acceleration data were salvageable. Gohl et al. (2001) and Chang (2002) were able to successfully apply this filtering approach to reduce a majority of their undesirable noise and/or deviant data from its mean. Unfortunately, as a result of excessive deviations and uncharacteristic jumps and shifts in the measured data, only a small group of the acceleration time histories were salvageable (i.e. data that make sense). Even within the group of salvageable data, unexpected and unexplained characteristics such as directions of accelerations continue to shadow the data with uncertainties. As such, comparisons between measured and computed acceleration are expected to be at best within the same order of magnitude. Figure 11-15 shows an example of a comparison between accelerations computed by LS-DYNA and the corresponding measured/filtered accelerations at each of the accelerometer locations during the first 0.04 seconds upon the initiation of the first blast. Although both amplitudes and pulse width between computed and measured accelerations are within the same order of magnitude, there remains unanswered questions concerning certain characteristics observed in the measured data.

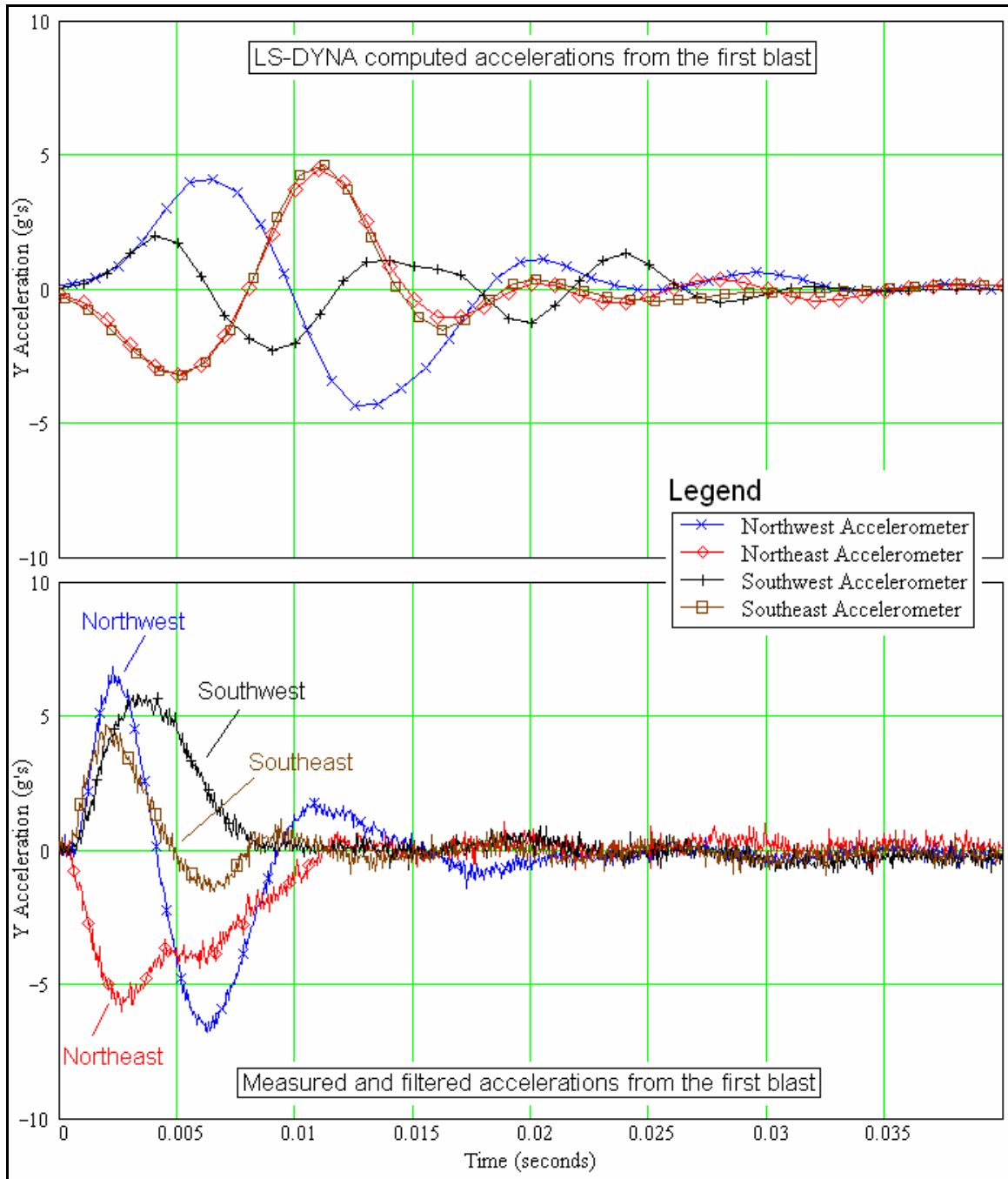


Figure 11-15 Comparison Between Computed and Measured Acceleration Data

For example, Y-axis is along the East-West direction. Since the first blast was located on the X axis and north of Y axis, one would expect that the accelerometers on the east side of the X axis would have opposite acceleration directions as the

accelerometers on the west side of the X axis as shown in the LS-DYNA computed results shown in the top of Figure 11-15. Measured data shown in the bottom of Figure 11-15 indicated that accelerometers in the northwest, southwest and southeast directions all have positive accelerations during the first pulse, whereas the northeast accelerometer has a negative first pulse. Furthermore, all but the northwest accelerometer have mostly one-sided accelerations with small or no rebounds, thus exhibiting an apparent over damped trend. As a result of excessive noise and multiple one-sided pulses (i.e. no rebound in the opposite direction), numerical integrations that were applied to obtain velocities and displacements produced results with excessive and undesirable amplitudes as explained in Section 9.5. Therefore, the author was unable to compare the LS-DYNA computed velocities and displacements against measured data.

Two major positive observations were deduced from Figure 11-15. First, amplitude and pulse width between computed and measured data are within the same “ball-park” region, providing a certain degree of confidence that the computed LS-DYNA results are at least within reason. Second, acceleration amplitudes dampened well within the 0.2-second blast interval time used (versus 1.0 second in actual tests) for the analysis as discussed in Section 10.2. This provides a visual confirmation of the validity of the assumptions used to shorten the blast interval time in order to allow each analysis to be conducted within a more feasible and acceptable time frame.

An important note concerning the computed acceleration data shown in the top of Figure 11-15 is that the data as shown was obtained from a run of the first 0.2 seconds of blast series 3 with the result output interval set to 1 milliseconds, instead of the 0.01 second used for all other analyses. By reducing the output interval, one effectively

increases the corresponding disk usage. In the case of this refined analysis, approximately 2 gigabytes of disk space were required to simulate the first 0.2 seconds of blast series 3. Although it is not advisable to perform a full duration blast series simulation using the refined output interval described above, the 0.2-second blast simulation analysis was conducted to allow a higher quality direct comparison against the measured data. Other than the mentioned refinement made to the output interval, the rest of the analysis used to produce Figure 11-15, including all input parameters and data, were identical to the baseline full-duration analysis for blast series 3.

Figure 11-16 shows the full-duration computed component/resultant accelerations at the northwest accelerometer location. Due to short blast-pulses (< 0.10 seconds) within a long time duration (25 seconds), widths of transient blast pulse as shown in Figure 11-16 are difficult to discern. To help improve legibility of the acceleration results, the last 0.8 seconds of each blast interval were truncated, while the first 0.2 seconds of each blast interval were plotted using the width of a 1 second interval in the original graph as shown in Figure 11-17 through Figure 11-20. By so doing, one effectively produces composite plots that stretched across each blast pulse's width direction by a factor of 5 for visualization purposes. With the number of accelerometers and acceleration components to be plotted for both blast series 1 and blast series 3, along with page size limitations, it is not feasible to show each individual blast interval with an enlarged plot as shown in Figure 11-15.

The corresponding velocity and displacement time history results computed by LS-DYNA for both blast series 1 and blast series 3 are presented in Figure 11-21 through Figure 11-24 and Figure 11-25 through Figure 11-28, respectively.

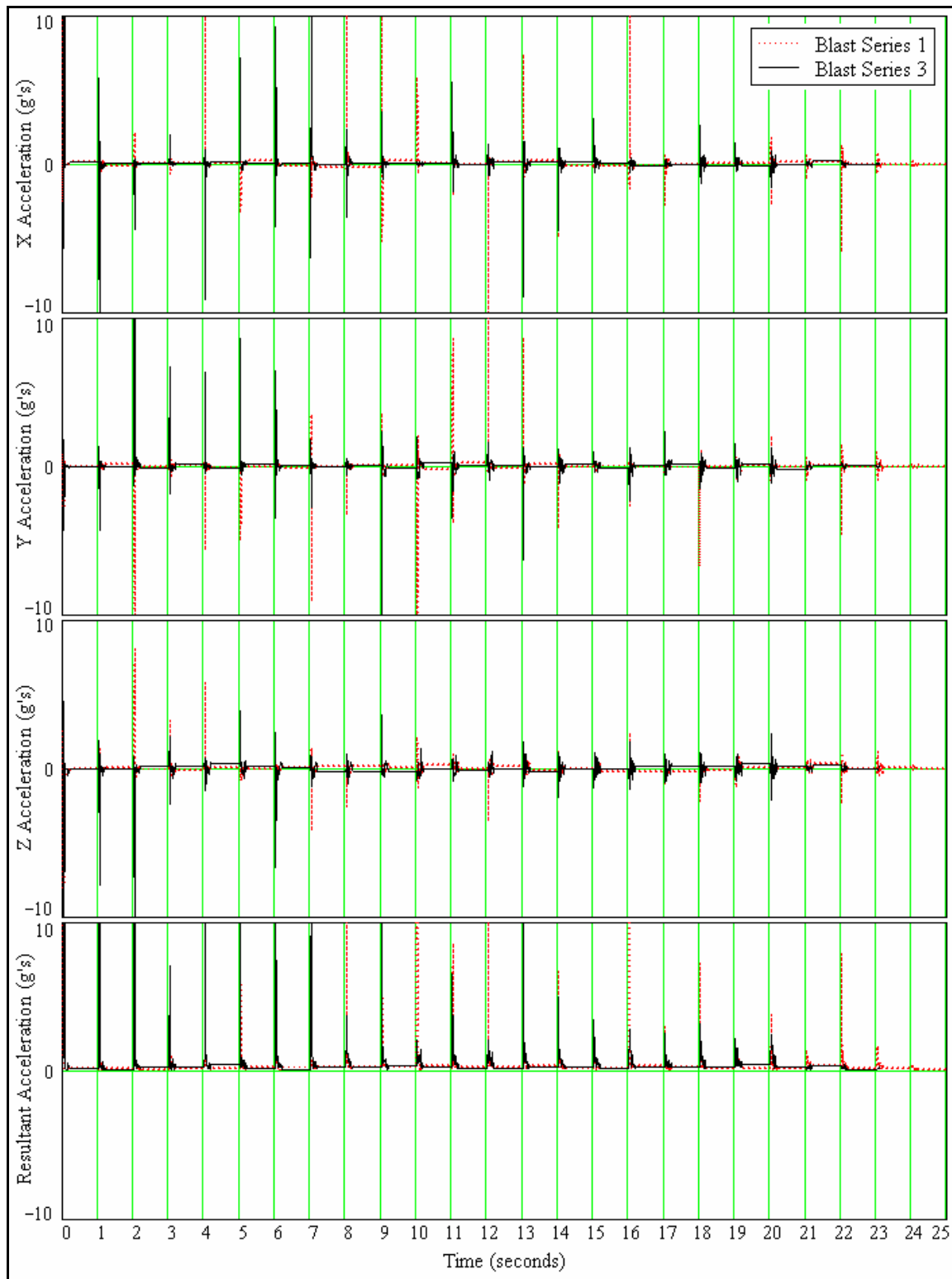


Figure 11-16 Sample of a Full-Duration Computed Accelerations

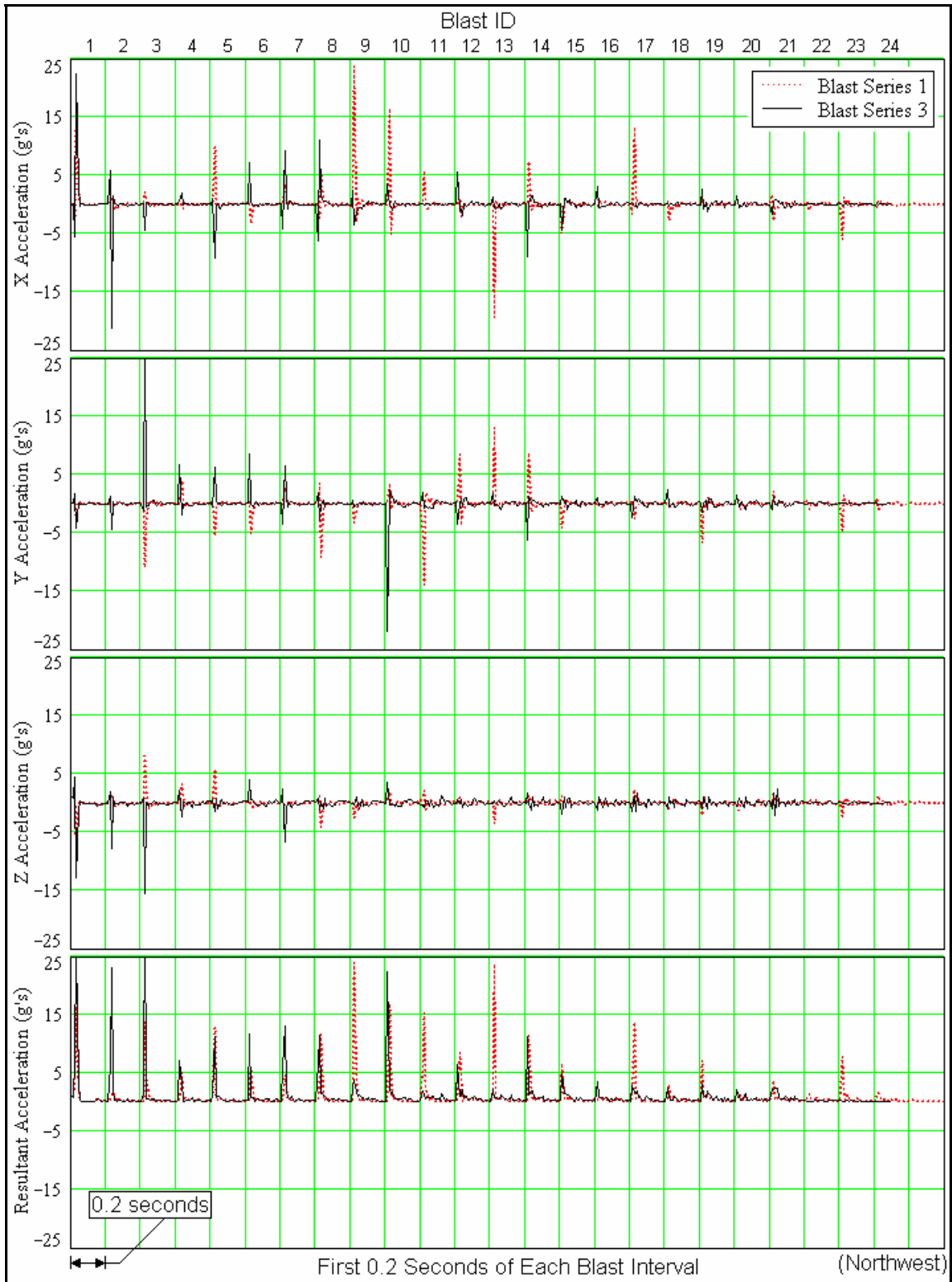


Figure 11-17 Compressed-Duration Acceleration at Northwest Accelerometer

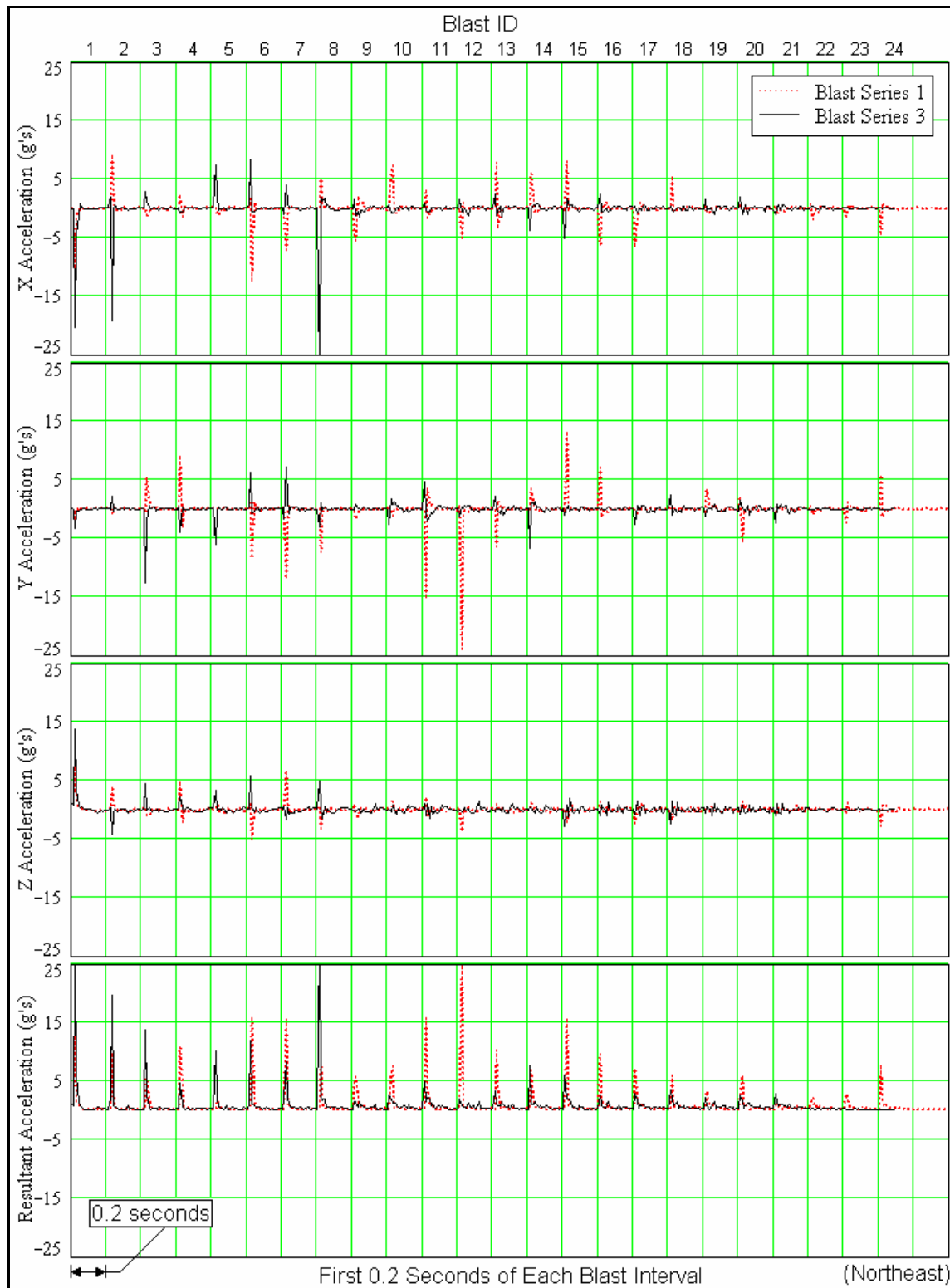


Figure 11-18 Compressed-Duration Acceleration at Northeast Accelerometer

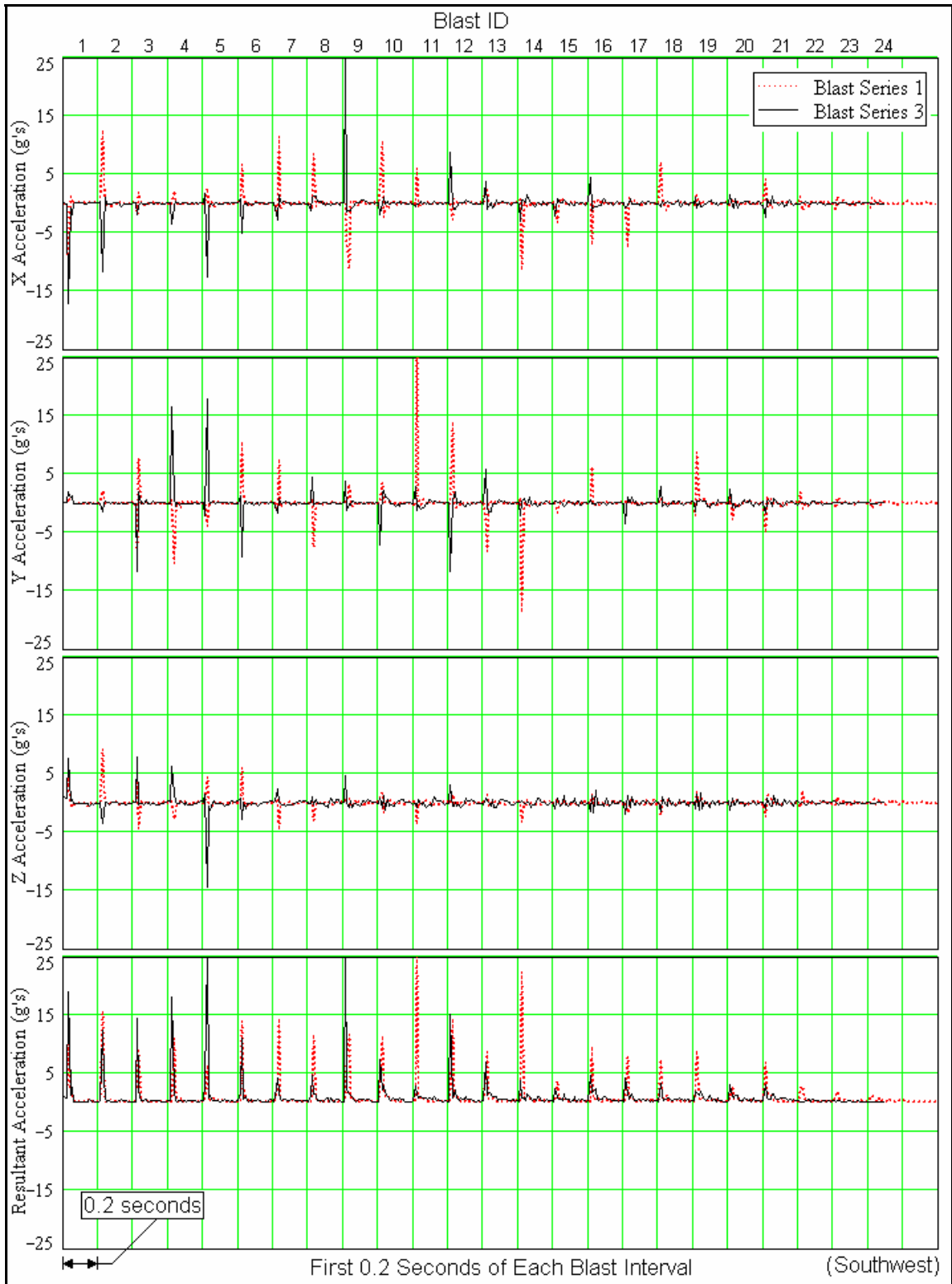


Figure 11-19 Compressed-Duration Acceleration at Southwest Accelerometer

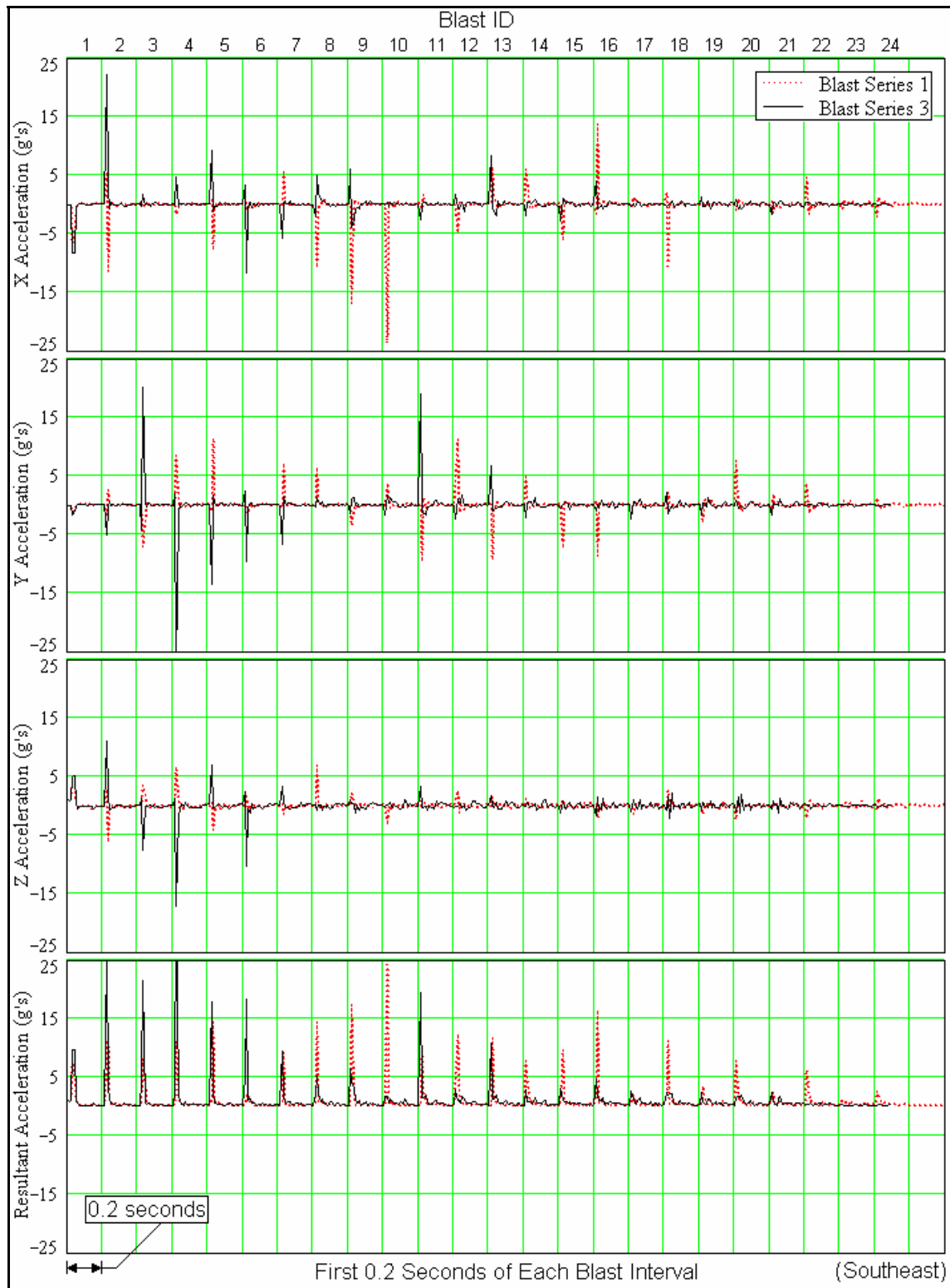


Figure 11-20 Compressed-Duration Acceleration at Southeast Accelerometer

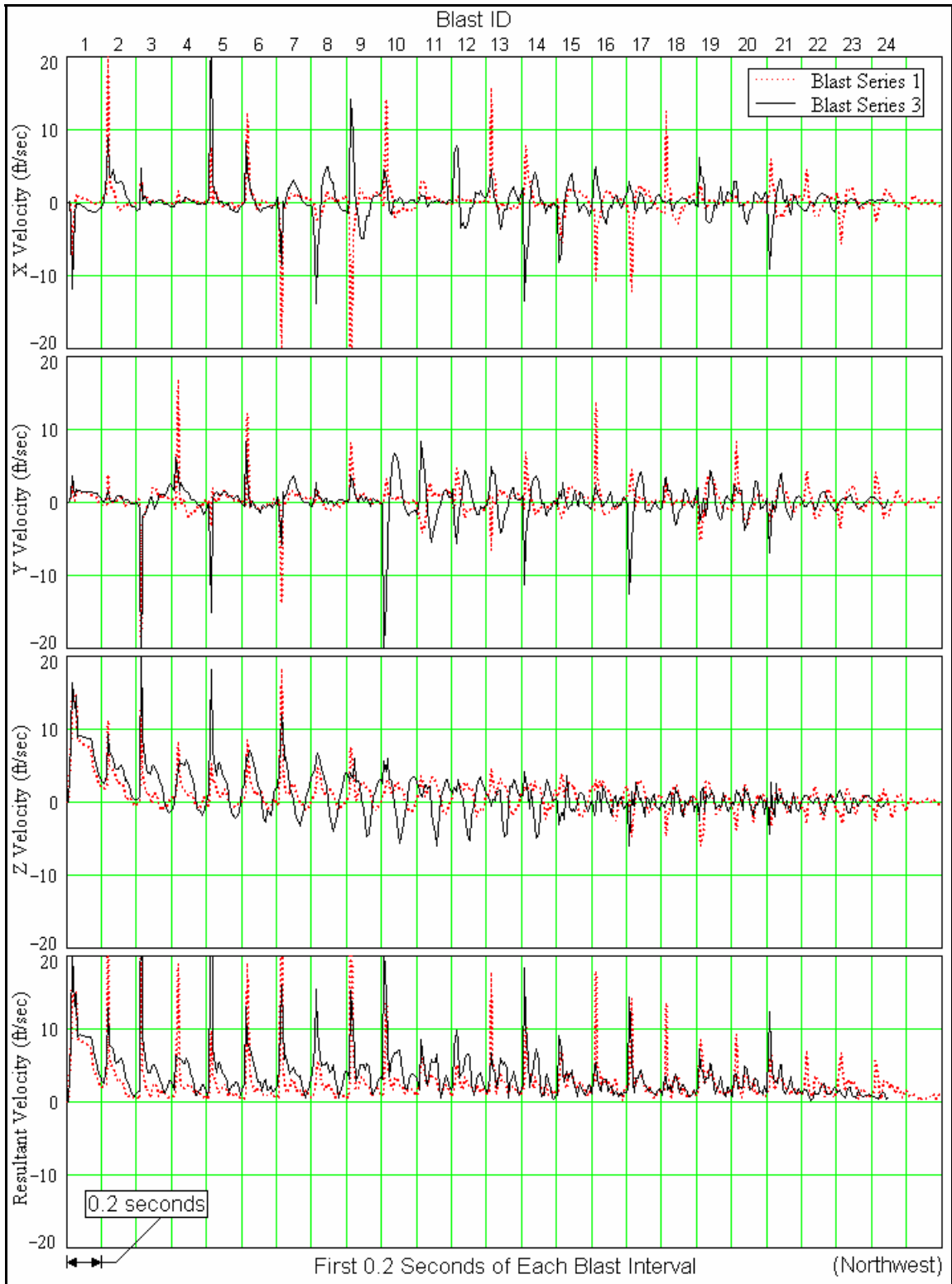


Figure 11-21 Compressed-Duration Velocity at Northwest Accelerometer

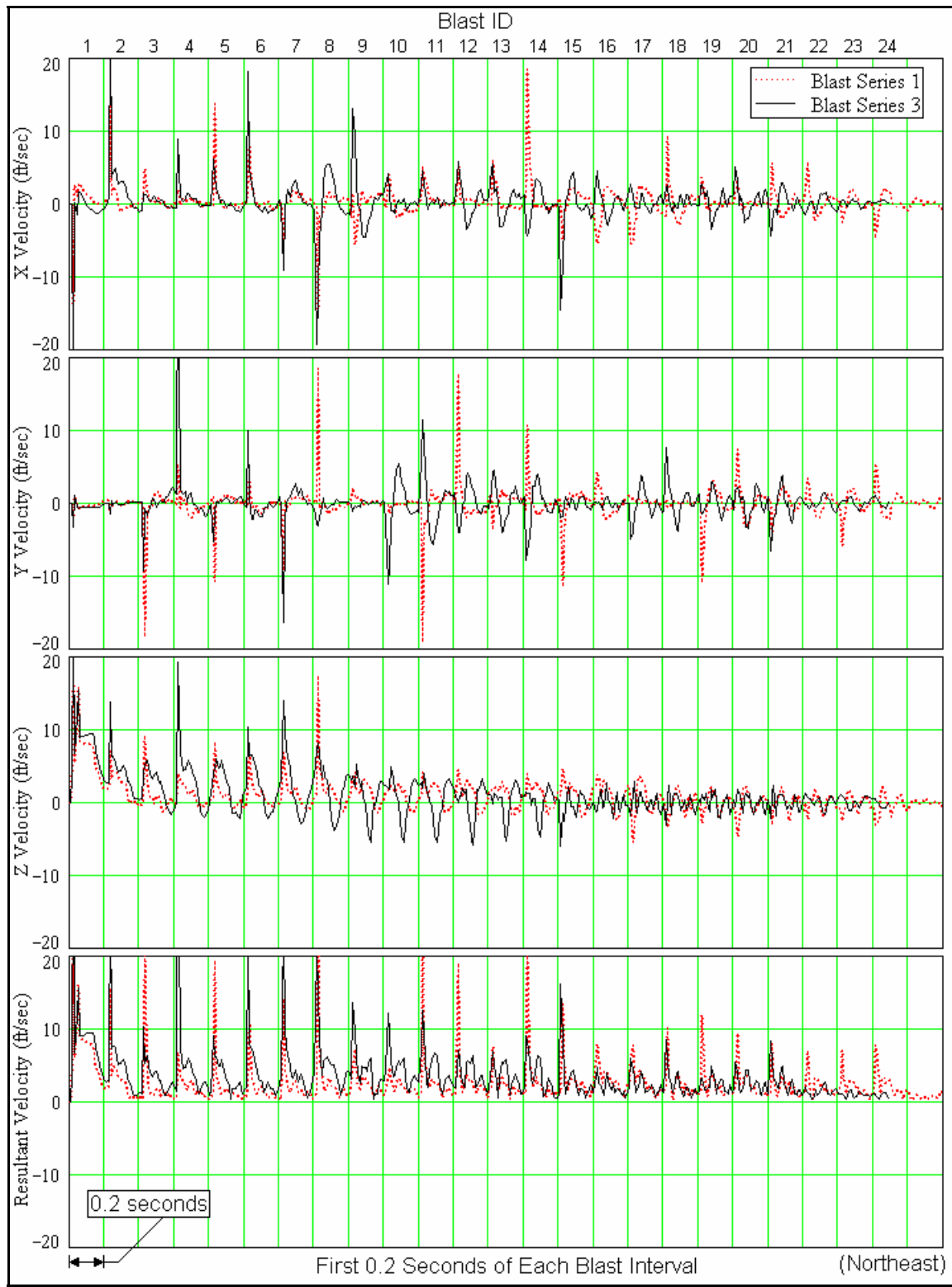


Figure 11-22 Compressed-Duration Velocity at Northeast Accelerometer

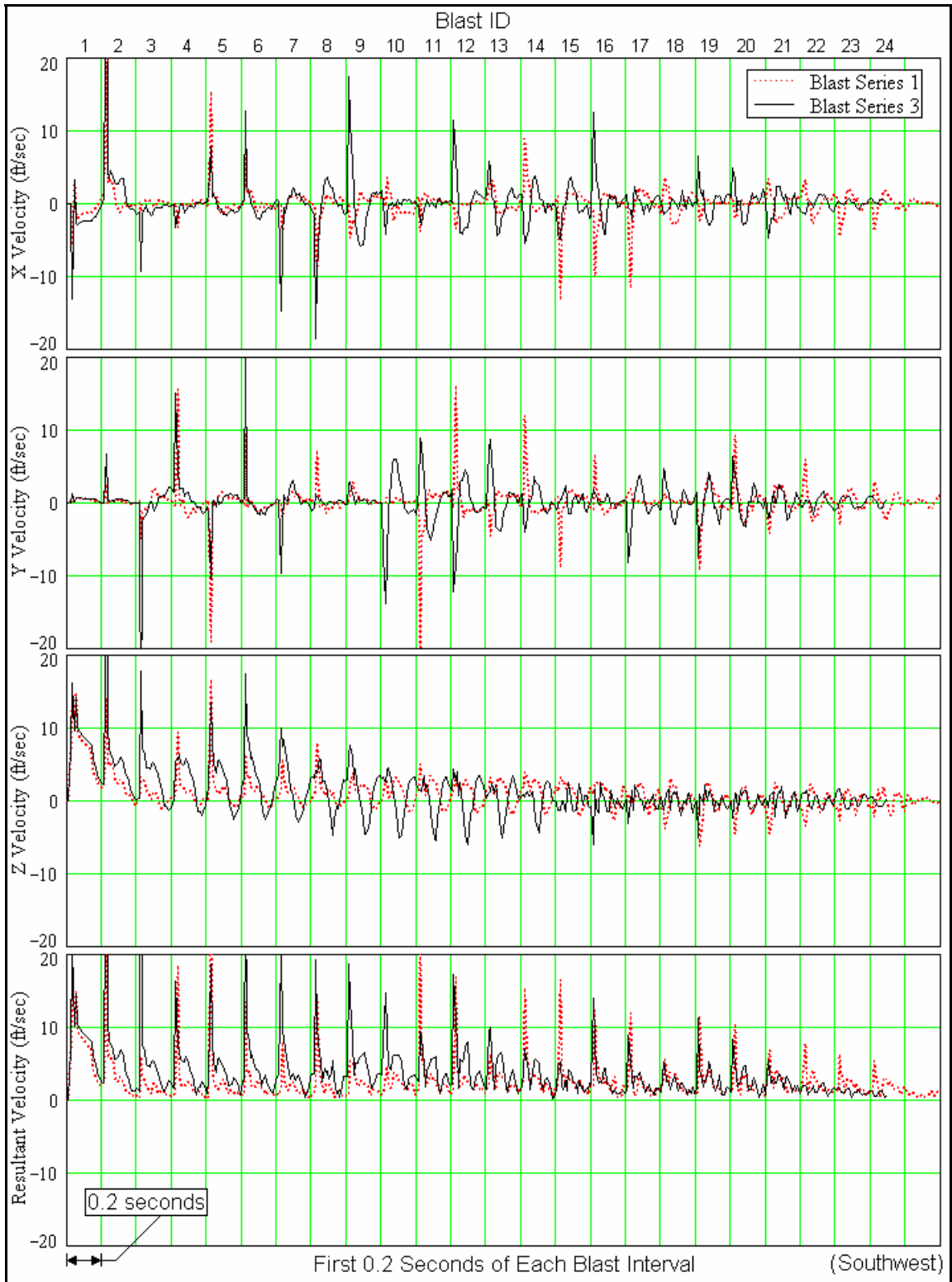


Figure 11-23 Compressed-Duration Velocity at Southwest Accelerometer

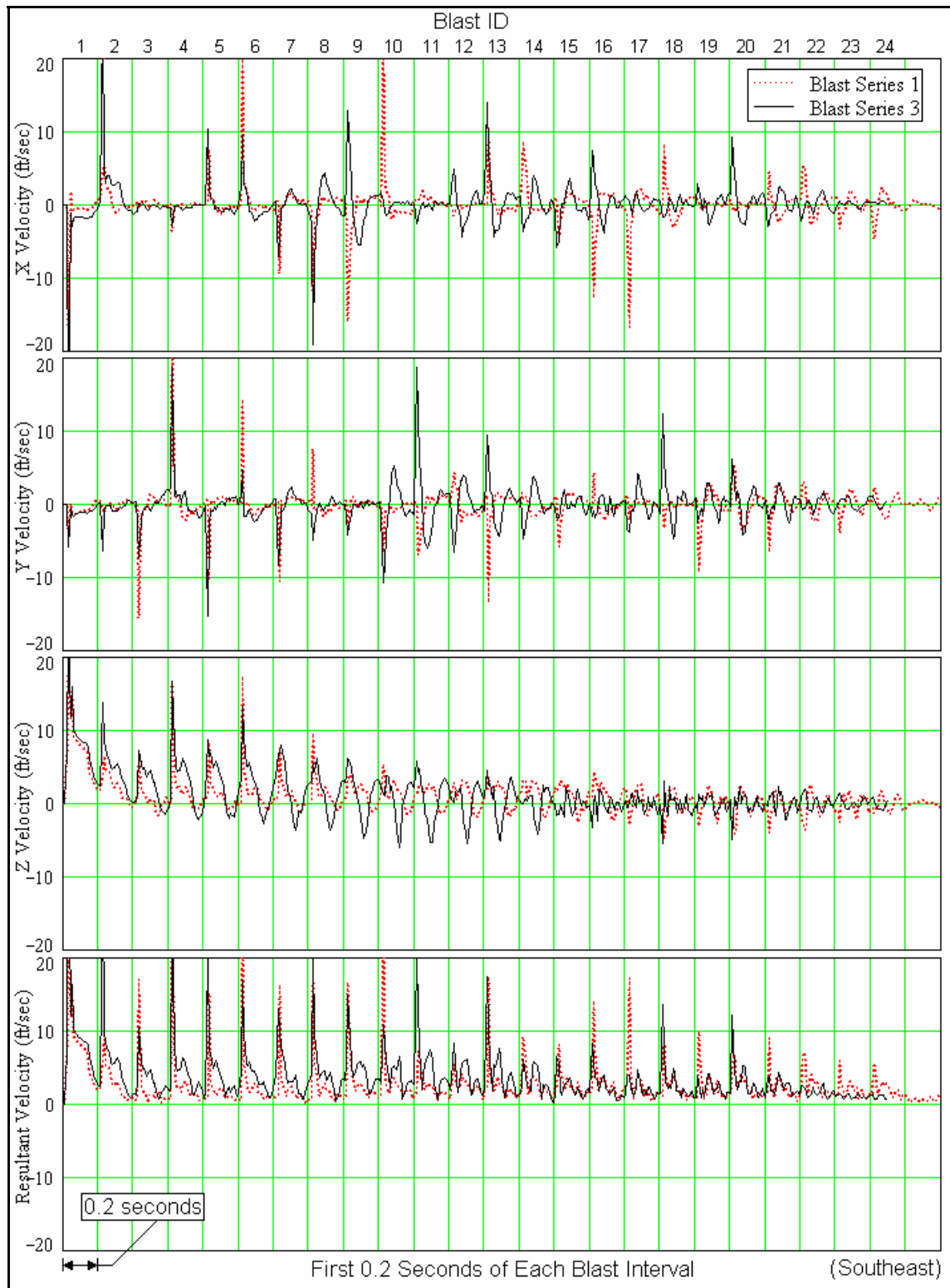


Figure 11-24 Compressed-Duration Velocity at Southeast Accelerometer

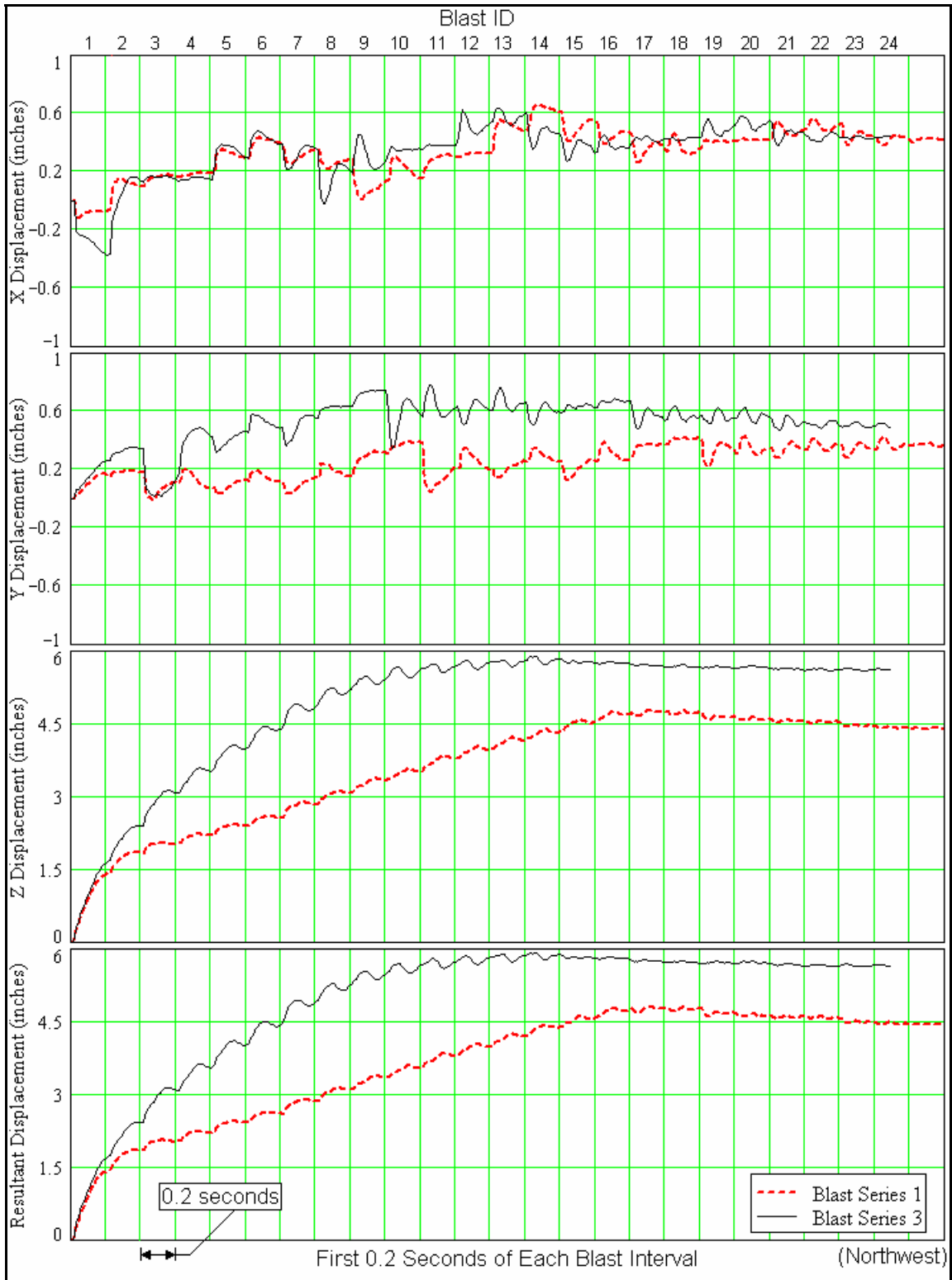


Figure 11-25 Compressed-Duration Displacement at Northwest Accelerometer

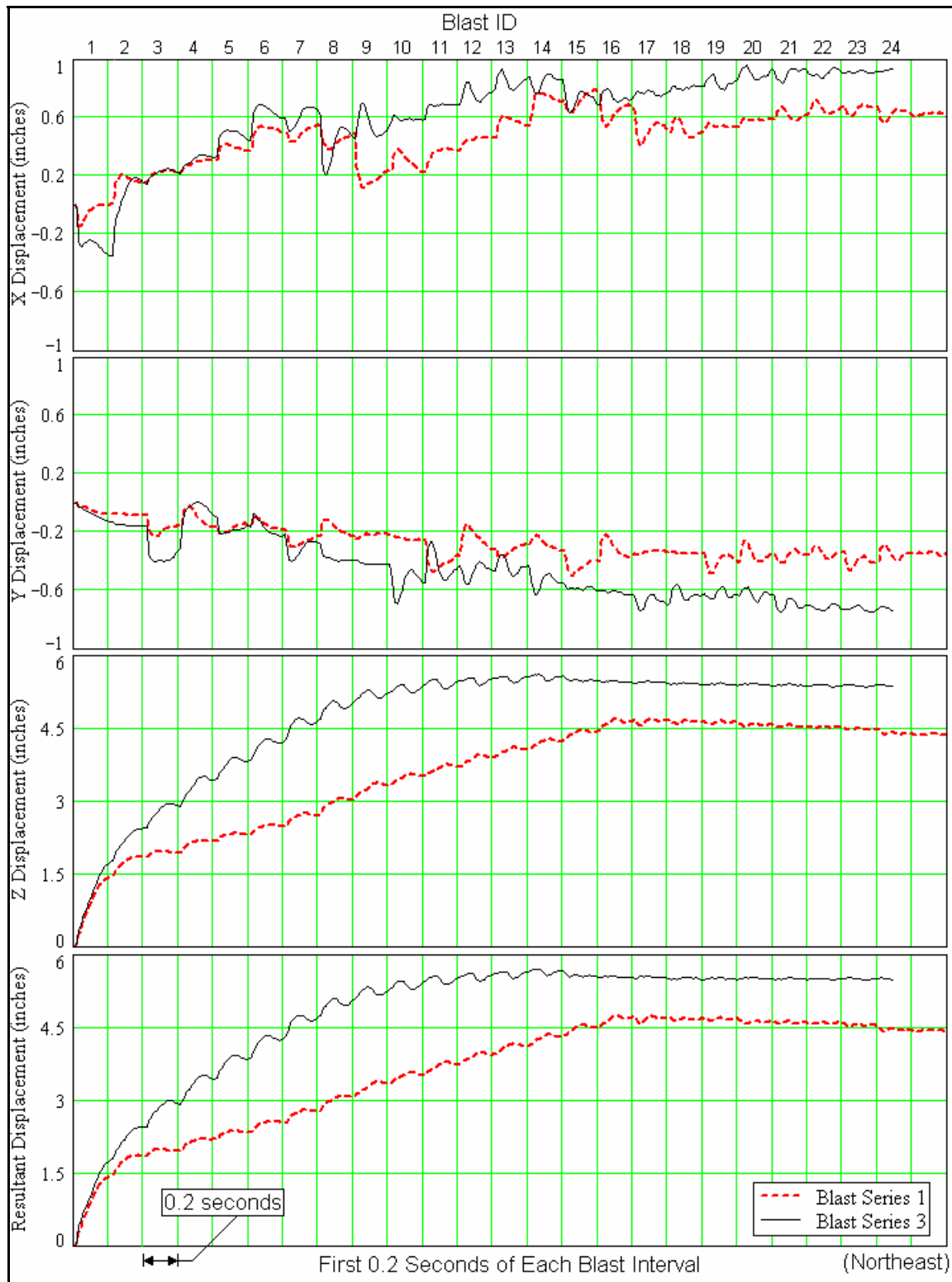


Figure 11-26 Compressed-Duration Displacement at Northeast Accelerometer

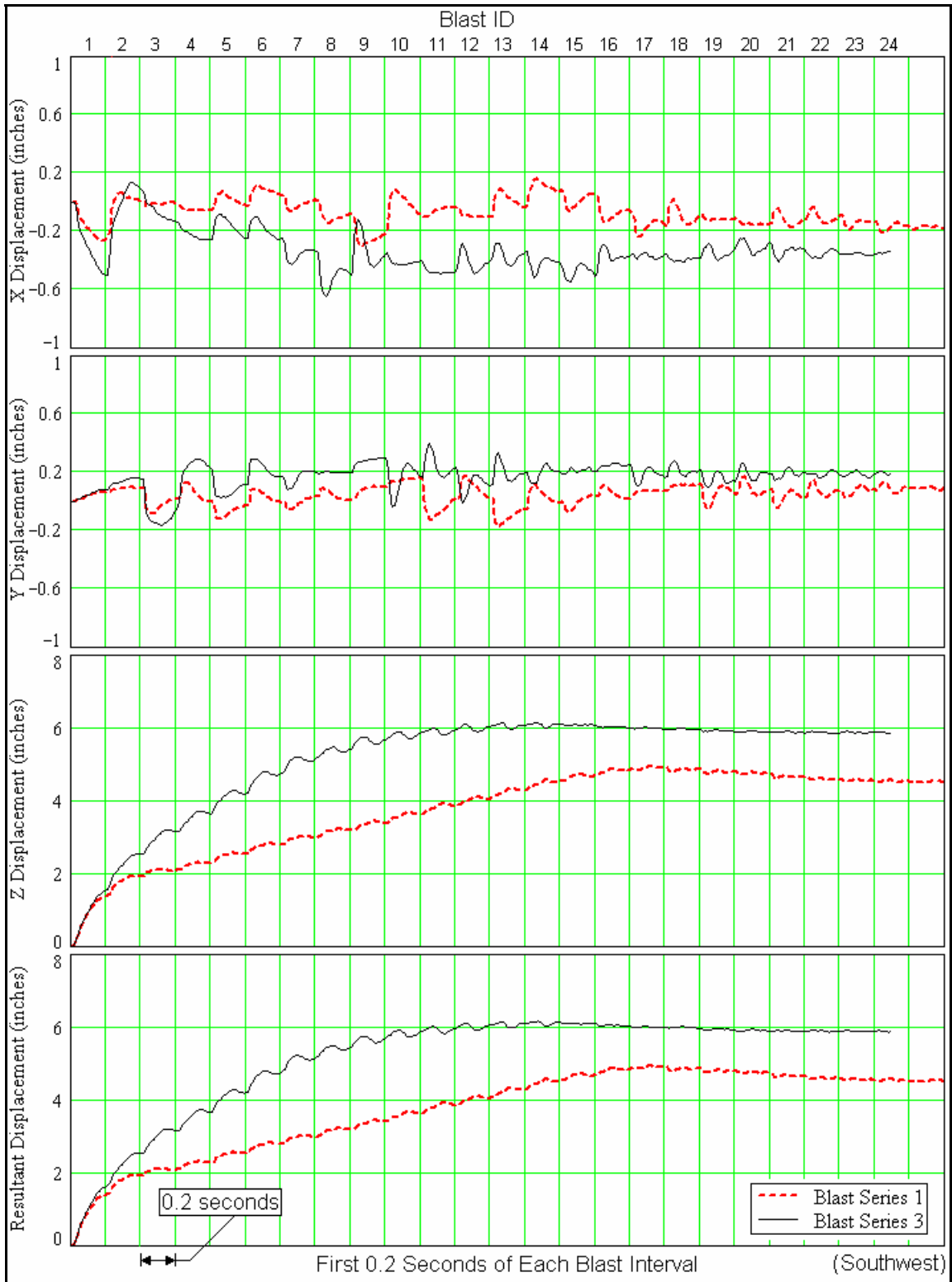


Figure 11-27 Compressed-Duration Displacement at Southwest Accelerometer

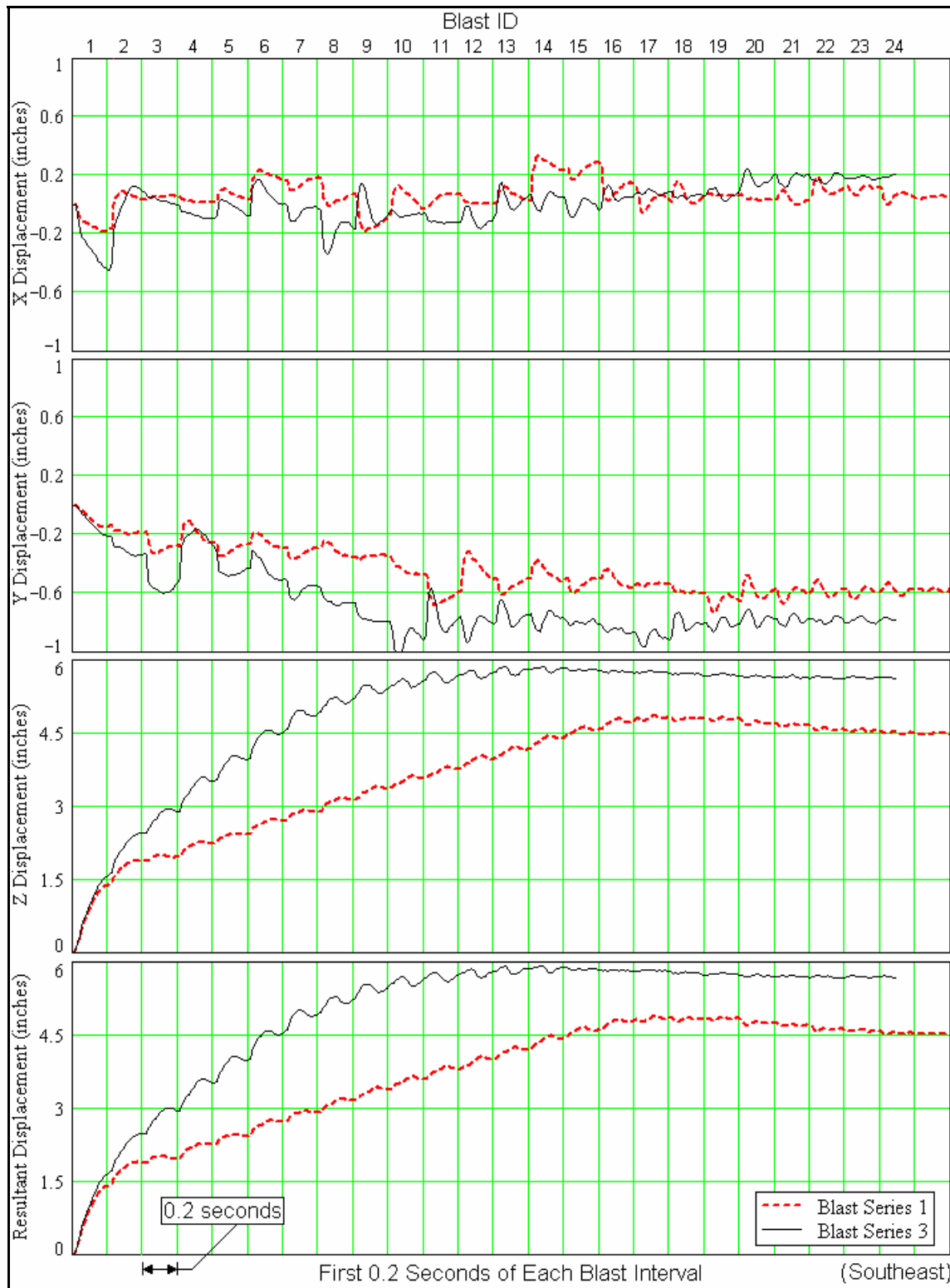


Figure 11-28 Compressed-Duration Displacement at Southeast Accelerometer

An interesting observation can be made through the computed acceleration, velocity and displacement results as presented in Figure 11-17 through Figure 11-28. Through the process of numerical integrations, averaging effects are manifested through the smoothing of peak values (i.e. spikes) from accelerations to velocities, then from velocities to displacements. Since stresses and strains in finite elements are computed from interpolations and extrapolations of displacement results, it follows that peaks and spikes associated with acceleration time histories become significantly less apparent in stress and strain results.

Theoretically, as the time step for each analysis iteration approaches zero, the corresponding averaging effects as a by-product of numerical integration diminish, thereby producing increasingly accurate results that mimic more closely to high-speed measured data. However, as the time step is reduced, the feasibility of completing the analysis within a reasonable amount of time is also reduced in proportion to time step sizes. Therefore, a balance between run time feasibility and accuracy of the results must be considered prior to performing a long duration analysis.

11.9 Pore Water Pressure Ratio and Shear Strains

An important aspect of this research effort is to study the relationship between shear strains generated by the numerical model and the corresponding pore pressure ratio. Figure 11-29 and Figure 11-30 show the relationship between pore water pressure ratio and average shear strain for both blast series 3 and blast series 1, respectively, at the five PPT locations described in this dissertation. Average shear strain is defined as 0.65 times the maximum shear strains computed by the numerical model.

An overlay of data digitized from cyclic triaxial tests published by Dobry et al. (1982) and from blast-induced experiments by Gohl et al. (2001) were incorporated into Figure 11-29 and Figure 11-30 for comparisons against LS-DYNA computed results. Dobry's data shown in Figure 11-29 and Figure 11-30 included all six data sets that were tested for 10 cycles at a relative density of 60% as presented in Dobry et al. (1982).

Since cyclic shear strain tests and blast tests are fundamentally different in load application rates, magnitudes, load type, load repetitiveness, and durations, one cannot expect results from the two tests to be identical. However, one can expect the overall shape and characteristics of the results from cyclic shear tests and blast tests to be similar at the macroscopic level. The repetitive nature of cyclic shear tests mimics the cyclic portion of an earthquake, while blast tests mimics the sudden shocks one encounters from the initiation of a large earthquake induced by sudden release of stored energy in the soil. Both are important within their own respective area of contributions to the understanding of the nature and effects of earthquakes.

One can readily see from Figure 11-29 and Figure 11-30 that the computed results from LS-DYNA are more in-line with blast test results from Gohl et al. (2001) than cyclic shear test data from Dobry et al. (1982). Both computed results and observed results from blast tests produced greater shear strains at the same pore water pressure ratio (R_u) level than results from the cyclic shear tests. One can expect such behaviors to occur due to the more sudden and damaging compressive and distortional effects from detonations of explosives.

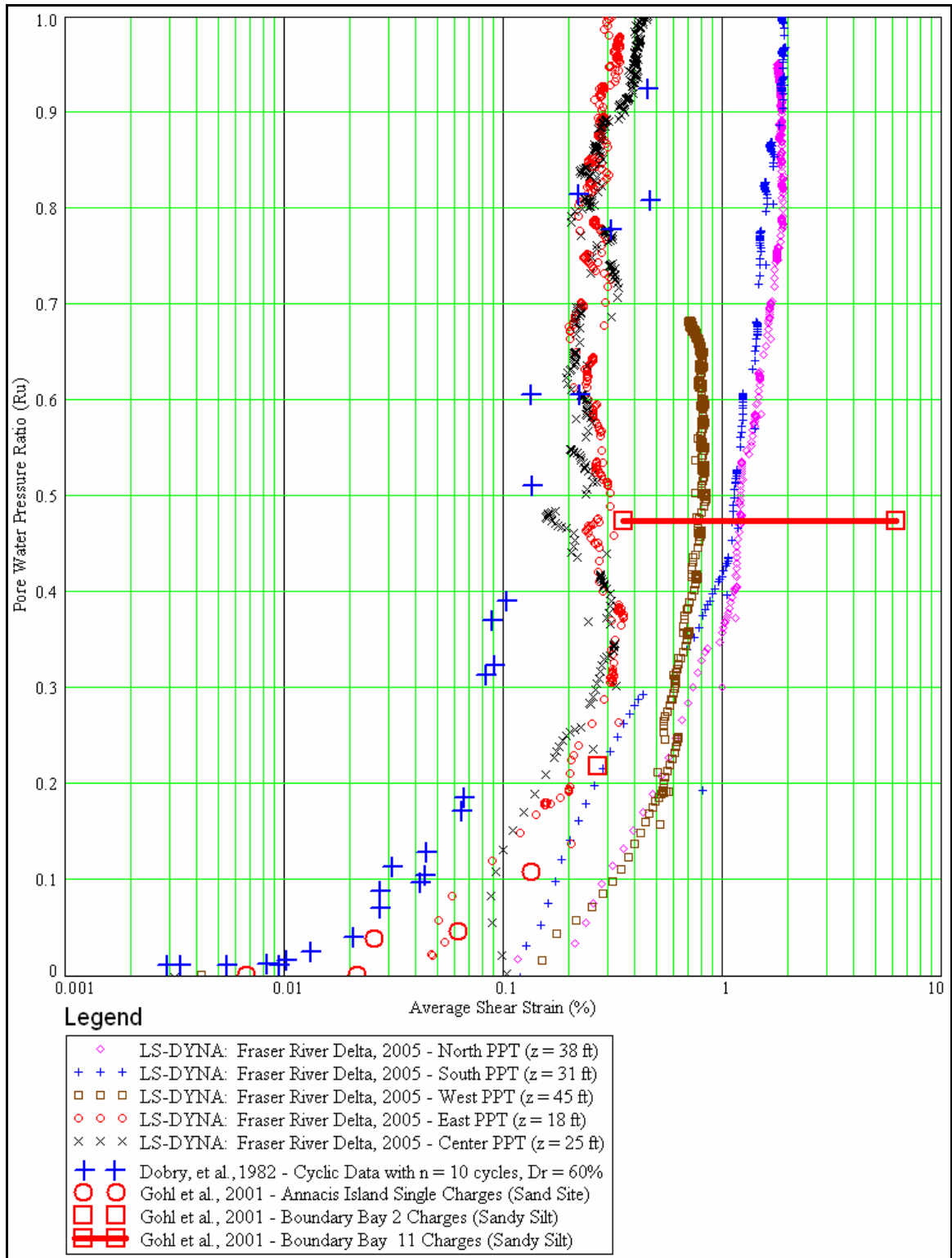


Figure 11-29 Blast Series 3 Pore Pressure - Shear Strain Relationship

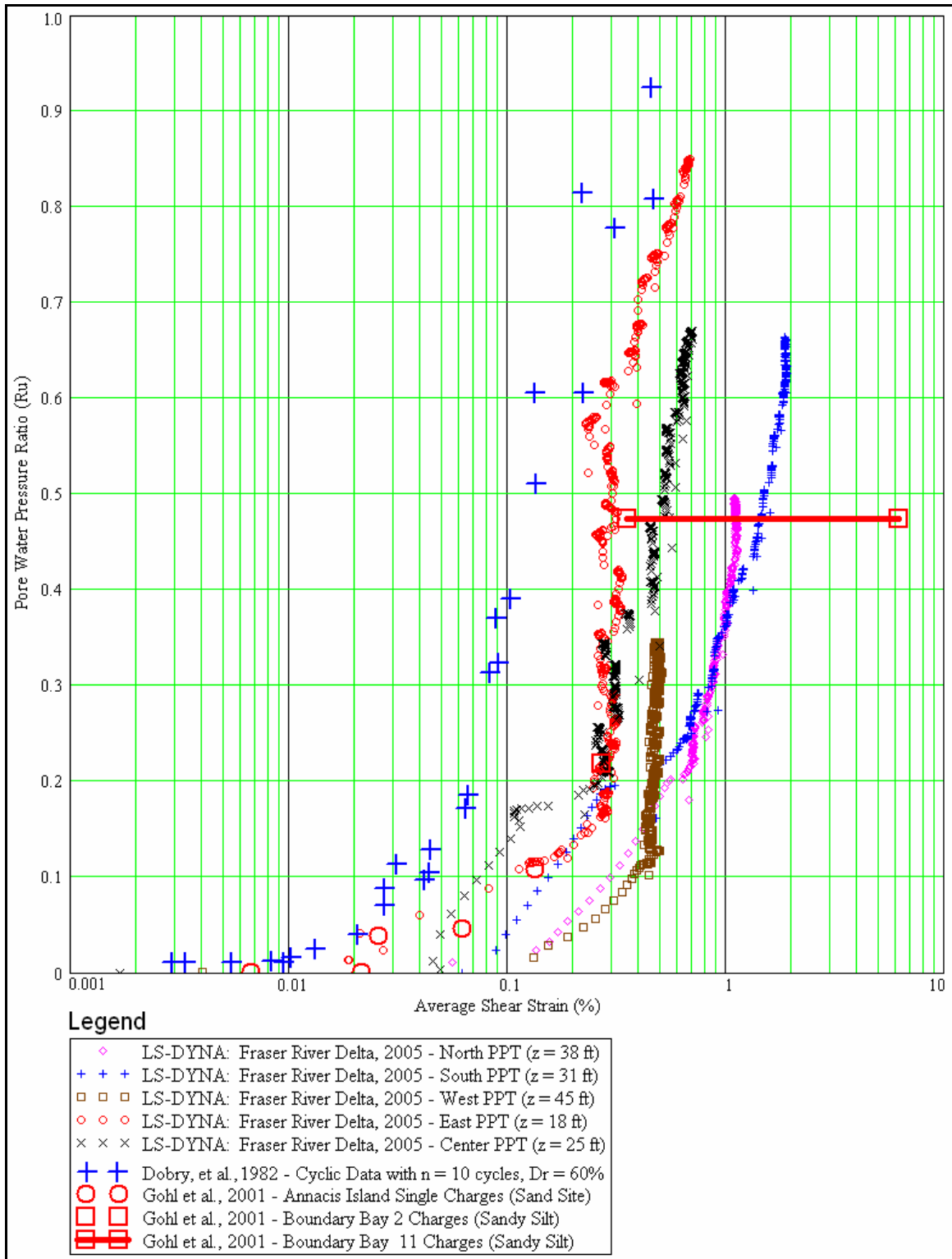


Figure 11-30 Blast Series 1 Pore Pressure - Shear Strain Relationship

Overall trend of the computed results using an approximate proof-of-concept approach are in reasonable agreement with measured data as shown in Figure 11-29 and Figure 11-30. Two areas of known deficiencies intentionally introduced into the proof-of-concept approach manifest themselves rather clearly in the results presented in both Figure 11-29 and Figure 11-30.

The two deficiencies, depth effects and degradations of shear moduli, were introduced to the analyses of blast series 3 and blast series 1 as discussed earlier in this Chapter as well as in Chapter 10. Depth effects were ignored in soil above the weighted equivalent depth of the explosives to demonstrate the existence and effects of soil depth and to reduce the number of iterations required for the calibration of the approximate model against blast series 3. Degradation of shear moduli were not accounted for in order to isolate and to demonstrate bulk transition effects. Effects due to soil depth are manifested in Figure 11-29 and Figure 11-30 through the separation of the results between PPT locations that account for depth and PPT locations that do not account for depth. Effects of ignoring shear modulus degradations manifested in Figure 11-29 and Figure 11-30 through the more vertically inclined trends observed in the upper half of the computed shear strain results as one would expect. An explanation of the behaviors exhibited by the computed results due to neglect of shear modulus degradations is presented below.

From elementary mechanics of materials, modulus is inversely proportional to strain. As the shear modulus reduces due to degradation, the corresponding shear strains increase in proportion to the decrease in shear modulus. Therefore, one would expect the upper half of the computed shear strains shown in Figure 11-29 and Figure 11-30 would

lean more toward the right with respect to decreasing (or degrading) shear moduli, indicating an increase in shear strains as the soil liquefies. As explained previously in this Chapter, shear modulus degradations would best be accounted for when both shear and bulk transition effects are incorporated directly into the corresponding soil material model where adjustments and extensive bookkeeping are performed internally by the software. Until then, approximating both bulk and shear transitions simultaneously can be prohibitively expensive and infeasible to accomplish within a reasonable amount of time due to complexities introduced by the interactions of both bulk and shear parameters in the analysis. Nevertheless, results as shown in Figure 11-29 and Figure 11-30 indicate that the proposed bulk transition concept can provide reasonable representations of the soil liquefaction development process subjected to controlled blast environments.

12 Conclusions and Improvement Recommendations

12.1 Conclusions

The original objective of producing a predictive numerical model was revised due to the lack of access to the baseline *MAT_FHWA_SOIL material model in LS-DYNA where a noticeable amount of improvements including bulk transition effects are recommended. Nevertheless, a proof of concept evaluation was conducted to demonstrate the viability, feasibility and soundness of the proposed bulk transitioning relationship defined in this dissertation.

During the proof of concept evaluation, a single set of input parameters were calibrated to predict the shapes and characteristics of the pore pressure development process at 5 different locations and depths in a 3-D non-symmetrical, sequential, multi-level blast-induced liquefaction simulation. Pore water pressure results from the analysis provided reasonable fits to the measured data at all 5 PPT locations and depths applied in blast series 3 conducted in May 2005 at south Vancouver's Fraser River Delta region. Additionally, the baseline model calibrated to blast series 3 was applied to predict liquefaction development for blast series 1 with non-uniformly placed and nearly one-third of the explosives relative to blast series 3. Minor and expected deviations were observed in the comparison between predicted and measured test data due to faulty placement of certain explosives in blast series 1. This provides an additional source of

verification for the proposed model. Nevertheless, minor adjustments to the proposed bulk transitional relationships would be helpful in refining the proposed approach to evaluate liquefaction development in saturated sandy soils.

Shear strains computed by the baseline numerical model appear to be consistent both in shapes and in magnitudes with blast-induced liquefaction data published by Gohl, et al. (2001). When compared against cyclic shear test data published by Dobry et al. (1982), the overall shape of the strain distribution with respect to pore pressure ratio is consistent, while the strain magnitudes are slightly greater than those obtained by cyclic shear tests. Such an observation appears to contradict the theory that blast-induced liquefactions do not produce sufficient shear strains to accurately represent a large earthquake event.

Although compressive waves are prominent near each blast source during a blast-induced liquefaction experiment, imbalances of normal and shear stresses from explosive shocks cause noticeable distortional behaviors in regions not immediately adjacent to blast source. These distortional behaviors are similar to those produced by a large earthquake in an in-situ environment. The existence of large shear strains computed by the numerical model using typical sand and water properties appear to support the distortional phenomenon that one expects in soil subjected to a large earthquake.

Acceleration, velocity and displacement components computed by the model also exhibit, magnitudes, and characteristics similar to those observed during the blast-induced liquefaction experiment.

12.2 Improvement Recommendations

12.2.1 Soil Properties

Soil properties are often difficult and expensive to determine, but are critical and essential for a sound understanding of the ground characteristics, and for reliable and accurate analyses. For instance, little is known concerning the clay layer between the partially saturated sand layer above and fully saturated sand layer below at the May 2005 Vancouver blast-liquefaction site. This lack of information concerning the clay layer added a significant degree of uncertainty into the numerical modeling analysis, especially in regions near the clay layer and along the clay-sand interfaces above and below the clay layer. To help minimize uncertainties, it is recommended that more extensive in-situ or laboratory tests of all non-liquefiable soil layers present at the site be performed prior to liquefaction tests.

12.2.2 Blast-Induced Liquefaction Test Instrumentation

Uncharacteristic “jumps” and “magnitude shifts” observed in the May 2005 Vancouver liquefaction test data make it extremely difficult to compare against analysis results that are more “well behaved.” This is especially true for the high-speed acceleration data; no one has yet been able to determine the actual, underlying source that caused the uncharacteristic and random jumps and shifts observed through the measured data set.

Although some “jumps” and “shifts” may be typical of geo-materials due to their particulate and non-homogeneous nature, they may still be reduced to a manageable level. All available data indicated that the observed acceleration and pressure magnitudes

are well below the limits of the instrumentation used in the May 2005 Vancouver test series. Perhaps much of the “jumps” and “shifts” are due to noise and other characteristics associated with the high-amplitude capacity of the devices. One potential solution in reducing the “jumps” and “shifts” is to apply transducers and accelerometers with reduced amplitude limits than those used in the May 2005 Vancouver test series.

Further investigations in data capturing techniques, equipment calibrations, instrumentation installation processes, and choice of instrumentation are recommended. The outcome of this work should be reduced amplitude limits that still satisfy the need for data stability, reliability, repeatability, and noise reduction.

12.2.3 Degradations of Shear Modulus

It is a well-established fact in the geotechnical field that the shear modulus degrades as cyclic strain increases. As cohesionless soil liquefies, water, which cannot resist shear strains, becomes the primary compressive load carrier with significantly reduced shear strain resistance remaining in the soil-water composite material. This transition is a significant event, which needs to be accounted for in order to accurately simulate the liquefaction event.

The current *MAT_FHWA_SOIL material model assumes a constant shear modulus in its calculations. Accounting for shear modulus degradation using relationships defined in published documents such as Kramer (1996) can simulate non-linear characteristics of soil behaviors subjected to large impulsive or cyclic loading environments. Such non-linear characteristics are not likely to be captured by an analysis utilizing a constant, non-degraded shear modulus.

To estimate the effects of shear modulus degradations, an approach similar to the bulk modulus transition method used in this research can be applied. That is, one can utilize the restart feature in LS-DYNA to allow the alterations of the shear moduli in the soil layers between blasts. One must be reminded that the restart approach mentioned here can only provide a simple estimate of the actual shear modulus degradation effects. The author recommends that shear modulus degradation defined in the literature such as Kramer (1996), as well as the corresponding bulk modulus transitions used in this research, be implemented in future releases of the existing or new soil material models. Such implementations provide an avenue for users to properly consider pore-water pressure development in geomaterials.

12.2.4 Pore Water Pressure Definition

The baseline *MAT_FHWA_SOIL material model in LS-DYNA computes the amount of pore water pressure (u) in accordance with Equation 12-1 (Lewis, 2004).

$$u = \frac{K_{sk}}{1 + K_{sk} \cdot D_2 \cdot n_{cur}} \cdot \varepsilon_v \quad (12-1)$$

The equation's behavior is a direct function of the current porosity (n_{cur}) and volumetric strains (ε_v) for partially saturated soil. If porosity and volumetric strains change non-linearly, then the resulting pore water pressure is a non-linear function. However, in a fully saturated environment, the value of D_2 must be zero in accordance with the definition presented in the material model's theoretical and user's manuals (Lewis, 2004). Therefore, in fully saturated cohesionless soils where liquefaction

potential is greatest, the “as defined” pore water relationship in the *MAT_FHWA_SOIL model is linearly proportional to the volumetric strain ε_v . It is proposed that the pore pressure relationship be modified to account for the relationship between excess pore pressure build-up and the corresponding degradation of the shear modulus observed in the corresponding soil material.

12.2.5 Pore Water Pressure Results Extraction

Currently the baseline *MAT_174 or *MAT_FHWA_SOIL material model does not output pore water pressure computed in saturated soil during the course of analysis. The material model presently outputs the effective pressure, which is obtained from the difference between computed total pressure and computed pore water pressure. To obtain the pore water pressure, one must apply reverse engineering to back-calculate it from volumetric strains and the corresponding skeleton bulk modulus, iteratively if soil is partially saturated. Such reverse engineering is not necessary since pore water pressure is an essential parameter in determining the development of liquefaction, and is computed by the model internally in LS-DYNA. Yvonne Murray of Aptek sent in a request to LSTC in September 2005 to add the pore water pressure as an output parameters from LS-DYNA. It is uncertain how long it will take for LSTC to implement such a request.

12.2.6 Fluid-Structure Interactions of Explosive Detonations in Soils

The baseline analysis conducted for this research consists of an integrated model where the explosive elements are embedded into the soil model at pre-defined locations. The accuracy of such an approach is generally sufficient for macroscopic evaluations of the liquefaction potential of the soils at regions away from the explosives. When refined

evaluations at regions at or adjacent to explosives are desired, it is recommended that a fluid-structure approach be utilized in defining the explosives and their interactions with the surrounding soil regions. However, prior to applying the advanced fluid-structure technology for a more detailed look at the blast-interaction, one must consider potential issues such as computing resources and run time requirements. Based on past experience, the fluid-structure approach was intentionally avoided during this research due to a significant increase in complexity and run time. With presently available computing resources, it is simply not feasible to complete the research tasks within a reasonable amount of time using analysis methods that can require up to an order of magnitude longer run times, plus additional storage / memory resources.

Also at the present time, for some undetermined reasons, LS-DYNA version 970 has trouble computing the detonation initiation time for a sequential blast series correctly when using Eulerian, rather than ALE or LaGrangian, analysis method. Multiple charges were initiated at the start of an Eulerian analysis instead of a user-defined sequential pattern. This problem does not occur when the analysis type is switched to ALE or LaGrangian. Since the Eulerian analysis method was not used during the course of this research, no further action was undertaken to resolve this issue. However, further investigation into this matter concerning sequential initiation time during future research is recommended prior to running an Eulerian analysis.

12.2.7 Soil Interactions with Structures and Foundations

When evaluating soil interactions with foundations and structures during blast-liquefaction tests, one may accomplish the tasks by one of two available approaches in LS-DYNA. First, interactions can be simulated via advanced contact and sliding

elements between soils and structures. This is the less demanding of the two approaches. Second, interactions can be modeled via fluid-structure analysis. Fluid-structure is significantly more complicated and time consuming. However, it is also a more generalized approach that is appropriate for problems involving large deformations and material plasticity, especially when the Eulerian method is recommended or required. The rocket-powered static test for the evaluations of pile foundations subjected to lateral load in liquefied soils is an excellent example that can be evaluated using either the advanced contact analysis approach or the fluid-structure analysis approach.

12.2.8 Dual-Phase Soil Material Model

To properly account for the build-up of pore water pressure in partially or fully saturated sandy soil, a dual-phase soil material model is required. Dual-phase behaviors are directly related to the degradations of shear modulus described in Section 12.2.3 of this dissertation. A dual-phase soil material model is a mathematical representation of the solid mass (i.e. sand particles) while there is strength transfer among solid soil particles. When pore water pressure has increased sufficiently to a point where solid soil particles no longer carry or transfer loads between adjacent particles, the material model transforms into and behaves like a viscous fluid continuum. When excess pore water pressure has reduced sufficiently that the solid particles can carry and transfer loads, the model can transition back to a solid continuum.

To account for such “phase-switching” behaviors, two sets of hydrodynamic and EOS input parameters are necessary for the model: one for the definition of the solid soil particles and the other for the fluid (i.e. water) embedded in the soil. If the soil is unsaturated or dry, then the fluid-portion of the parameters is ignored in the analysis.

Taylor (2004) presented a paper on this type of soil model which he developed at Sandia National Laboratories for explicit analyses that accounts for the development of pore water pressure subjected to impulsive hydrodynamic loading environments.

The baseline model applied for the current dissertation research utilized a “ball-park” type approximation method with a half-sine pulse function to simulate the transitioning of solid bulk (and potentially shear) modulus behavior to the nearly incompressible behavior one expects to observe in saturated soils during liquefaction. The approximate method was applied mainly to demonstrate the existence of the dual phase phenomenon one expects to observe in liquefying soil.

In order to incorporate the dual phase capabilities in *MAT_FHWA_SOIL or similar material models that can be used internationally without restrictions, extensive enhancements and/or overhaul is required for the existing model(s). This task requires extensive research and validations. Co-operation and funding from FHWA or other government agencies are essential for the success of such a development effort.

12.2.9 Multi-Material Advections and Interactions

During the early stage of the research, an attempt was made to apply the Eulerian method for the simulation of the blast-induced liquefaction event. Techniques involving multi-material advections and interactions were tested. However, undesirable behaviors in the both the explosive and soil material models, including interactions between the two, caused suspicions that the baseline *MAT_FHWA_SOIL material model had not been implemented for Eulerian multi-material analyses. The Eulerian or the Eulerian–LaGrangian fluid structure method with multi-material mixing capabilities is probably the most appropriate method for simulating blast interactions in the explosives and their

immediately surrounding regions due to its stability under high deformations and high magnitude loads. If continual numerical modeling of liquefiable soils subjected to highly impulsive loading environments is desired, then it is justifiable to implement the baseline soil material model for Eulerian method.

12.2.10 Parallelized Soil Material Model

The baseline *MAT_174 or *MAT_FHWA_SOIL material model does not appear to be parallelized to take advantage of the computing power of CPU clusters. To improve the feasibility of making long duration, multi-level sequential blast simulations, the soil material model itself must be “vectorized” or “parallelized” for multiple processor computations.

12.2.11 Seepage, Settlement and, Slope Stability Considerations

Currently neither the baseline *MAT_FHWA_SOIL soil material model nor Taylor’s dual phase model (Taylor, 2004) account for seepage in soils. Since the focus of the analysis used for this research is on the immediate blasting effects in the soils when the time duration is short (i.e. seconds), pressure build-up rate are much greater than soil seepage rate. As such, the amount of seepage is negligible. However, for liquefaction studies involving longer duration loads (i.e. earthquakes), and drainage effects due to artificial improvements (i.e. drain tubes), seepage effects are expected to be important in providing an accurate representation of the actual environment. According to Lewis, “hooks” were incorporated into the *MAT_FHWA_SOIL material model during development in preparation for future implementations of seepage effects (Lewis, 2004). To ensure that seepage is accounted for in future numerical liquefaction research, funding

from the Federal Highway Administration (FHWA) or other agencies should be secured to complete the implementation of seepage into the soil model.

Without the ability to account for seepage in saturated sandy soil, the *MAT_FHWA_SOIL model cannot relieve internal pressure induced by detonations. As long as internal pressure remains within the model, settlements cannot take place. Implementation of seepage capability into the *MAT_FHWA_SOIL material model as discussed previously may provide the ability to also account for settlement in liquefied soils. Since settlement is a “long term” (i.e. minutes to hours) effect in comparison with “short term” (i.e. microseconds to seconds) blast-induced liquefaction load, settlements can be treated as a quasi-static loading environment.

One potential approach that can evaluate the “long term” settlement effects is to transfer the explicit blast-induced liquefaction analysis results to the implicit solver seamlessly in LS-DYNA for an implicit seepage and settlement analysis. Additional implicit analysis that follows the explicit analysis will require enhancements to the existing *MAT_FHWA_SOIL model. Perhaps funding can be secured from FHWA or other agencies for such types of enhancements.

12.2.12 Meshless Modeling with Probabilistic Material Property Definition

A promising technology being developed by Sandia National Laboratories called peridynamic that can model random fractures and particle separations can potentially be very useful in simulating saturated cohesionless soils subjected to impulsive or shock environments. It is the opinion of the author that the peridynamic approach, when coupled with probabilistic distributions in defining both material characteristics and loading environments, may hold the key in accurately modeling earthquake and blast-

induced liquefaction events in cohesionless soils. Applied Research Associates' Southeast Division in Raleigh, NC has developed probabilistic technology embedded into a software system called ProFES to interface finite element and other analysis techniques. When coupled with advanced analysis techniques under development, software like ProFES may provide the means for geotechnical engineers to perform probabilistic evaluations and predictions of soil liquefaction potential.

12.2.13 Depth Effects

During the course of this research, it was observed that effects of depth pivoted about the equivalent depth of the entire set of explosives placed in-situ. Further observations revealed that effects of depth below the equivalent depth are non-linear, while effects of depth above the equivalent depth are relatively constant. Additional study of depth effects is recommended to provide greater understanding on how shock wave propagates in both blast-induced liquefaction tests as well as in large earthquakes.

References

- Al-Qasimi, E. M. A., Charlie, W. A, and Woeller, D. J. (2005). "Canadian Liquefaction Experiment (CANLEX) Blast-Induced Ground Motion and Pore Pressure Experiments." *Geotechnical Testing Journal*. ASTM International, Vol. 28, No. 1, pp. 1-13.
- Anderson, E. (1993). "Explosives." *Progress in Astronautics and Aeronautics*. American Institute of Aeronautics and Astronautics, Inc. Washington, DC., Vol. 155, pp. 81-163.
- Ashford, S. A. and Rollins, K. M. (2000). "TILT: The Treasure Island Liquefaction Test." Report No. SSRP 2001/17. Department of Structural Engineering, School of Engineering, University of California, San Diego. Final Report. January.
- Ashford, S. A. and Rollins, K. M. (2004). "Blast-Induced Liquefaction for Full-Scale Foundation Testing." *Journal of Geotechnical and Geoenvironmental Engineering*. American Society of Civil Engineers, Vol. 130, No. 8, pp. 798-806.
- Baker, W. E. (1973). "Explosions in Air." University of Texas Press, Austin, TX.
- Bathe, K. J. (1982). "Finite Element Procedures in Engineering Analysis.", Prentice-Hall, Inc. New Jersey.
- Bell, R. L., Baer M. R., Brannon, R. M., Crawford, D. A., Elrick, M. G., Hertel, E. S. Jr., Schmitt, R. G., Silling, S. A., and Taylor P. A. (2005). "CTH User's Manual and Input Instructions." Version 7.0. Sandia National Laboratories, Albuquerque, NM.
- Belytschko, T., Liu, W. K., Moran, B. (2000). "Nonlinear Finite Elements for Continua and Structures." John Wiley & Sons, Ltd. West Sussex PO19 1UD, England.

- Bolt, B. A. (1993). "Earthquakes and Geological Discovery." Scientific American Library, New York.
- Byrne, P. M., and Park, S. S. (2003). "Numerical Modeling of Fraser River Sand and RPI Centrifuge Tests." University of British Columbia Earthquake Induced Damage Mitigation from Soil Liquefaction Project Power-Point Presentation.
- Byrne, P. M., Park, S. S., Beaty, M., Sharp, M., Gonzalez, L., and Abdoun T. (2004a). "Numerical Modeling of Liquefaction and Comparison with Centrifuge Tests". Canadian Geotechnical Journal. National Research Council of Canada. Vol. 41, pp. 193-211.
- Byrne, P. M., Park, S. S., Beaty, M., Sharp, M., Gonzalez, L., and Abdoun T. (2004b). "Numerical Modeling of Dynamic Centrifuge Tests". Proceeding of the 13th World Conference on Earthquake Engineering. Vancouver, B.C. Paper No. 3387.
- Byrne, P. M., Park, S. S., and Beaty, M. (2003). "Seismic Liquefaction: Centrifuge and Numerical Modeling." FLAC and Numerical Modeling in Geomechanics, pp. 321-331.
- Byrne, P.M., Puebla, H., Chan, D. H., Soroush A., Morgenstern, N. R., Cathro, D. C., Gu, W. H., Phillips, R., Robertson, P. K., Hofmann, B. A., Wride, C. E., Segoo, D. C., Plewes, H. D., List, B. R., and Tan, S. (2000). "CANLEX: Full-Scale Experiment and Modeling." Canadian Geotechnical Journal. National Research Council of Canada. Vol. 37, pp. 543-562.
- Carleone, J. (1993). "Tactical Missile Warheads.", Progress in Astronautics and Aeronautics. American Institute of Aeronautics and Astronautics, Inc. Washington, DC. Vol. 155.
- Chang, W. J. (2002). "Development of an In Situ Dynamic Liquefaction Test." PhD Dissertation. University of Texas at Austin. Austin, TX.
- Charlie, W. A., Dowden, N. A., Villano, E. J., Veyera, G. E., and Doehring, D. O. (2005). "Blast-Induced Stress Wave Propagation and Attenuation: Centrifuge Model Versus Prototype Tests." Geotechnical Testing Journal, Vol. 28, No. 2, pp. 1-10.
- Cooper, P. W., and Kurowski, S. R. (1996). "Introduction to the Technology of Explosives." Wiley-VCH, Inc., New York, NY.

- Cooper, P. W. (1996). "Explosives Engineering." Wiley-VCH, Inc., New York, NY.
- Das, B. M. (2002). "Principles of Geotechnical Engineering." Fifth Edition. Brooks/Cole, Pacific Grove, CA.
- Denny, M. W. (1993). "Air and Water: The Biology and Physics of Life's Media." Princeton University Press, Princeton, NJ.
- Dobratz, B. M. and Crawford, P.C. (1985). "LLNL Explosives Handbook: Properties of Chemical Explosives and Explosive Simulants." Lawrence Livermore National Laboratory, Livermore, CA.
- Dobry, R., Ladd, R. S., Yokel, F. Y., Chung, R. M., and Powell, D., 1982. "Prediction of pore water pressure buildup and liquefaction of sands during earthquake by the cyclic strain method." NBS Building Science Series 138, National Bureau of Standards, Gaithersburg, Maryland.
- Drake, J. D. and Little, C. D., (1983). "Ground Shock from Penetrating Conventional Weapons." Proceedings of the Symposium on Interaction of Non-Nuclear Munitions with Structures. U. S. Air Force Academy, Colorado Springs, CO.
- EQE (1995). "The January 17, 1995 Kobe Earthquake." Summary Report, www.eqe.com/publications/kobe/economic.htm.
- Fung, Y. C. (1977). "A First Course In Continuum Mechanics." Second Edition. Prentice-Hall, Inc., Englewood Cliffs, NJ.
- Gohl, W. B. (2005). Forwarded E-mail communications from Professor Kyle M. Rollins. Pacific Geodynamics Inc., Vancouver, B.C.
- Gohl, W. B., Howie, J. A., Rea, C. E. (2001). "Use of Controlled Detonation of Explosives for Liquefaction Testing." Proceedings: Fourth International Conference on Recent Advances in Geotechnical Earthquake Engineering and Soil Dynamics and Symposium in Honor of Professor W. D. Liam Finn. San Diego, CA.
- Hallquist, J. O. (2003). "LS-DYNA Keyword User's Manual." Version 970. Livermore Software Technology Corporation, Livermore, CA.

- Hallquist, J. O. (1998). "LS-DYNA Theoretical Manual." Livermore Software Technology Corporation, Livermore, CA.
- Hallquist, J. O. (2002). "LS-Pre/Post User's Manual." Version 1.0. Livermore Software Technology Corporation, Livermore, CA.
- Holzer, T. L. (1998). "Introduction: The Loma Prieta, California, Earthquake of October 17, 1989 – Liquefaction." U. S. Geological Survey Professional Paper 1551-B. U. S. Government Printing Office.
- Housner, G. W. (1985). "Liquefaction of Soils During Earthquakes." Report by the Committee on Earthquake Engineering, Commission on Engineering and Technical Systems, National Research Council. National Academy Press, Washington D.C.
- Idriss, I. M. (2001). "The Role of Modeling in Geotechnical Earthquake Engineering." Proceedings of NSF International Workshop on Earthquake Simulation in Geotechnical Engineering. Case Western Reserve University, Cleveland, OH.
- Kerley, G. I. (2001). "Equations of State: A Course in Modeling Techniques for Hydrocode Calculations." Kerley Publishing Services, Albuquerque, NM.
- Kramer, S. L. (1996). "Geotechnical Earthquake Engineering." Prentice Hall, Inc., Upper Saddle River, NJ.
- Lane, J. D. (2004). "Static and Cyclic Lateral Load Testing of a Full-Scale Pile Group During Blast-Induced Liquefaction." Ph.D. Dissertation. Department of Civil and Environmental Engineering, Brigham Young University, Provo, UT.
- Lee, K. L. (1974). "Earthquake Induced Settlements in Saturated Sands.", Journal of the Geotechnical Engineering Division, ASEC. Vol. 100, No. GT4., pp. 387 – 406.
- Lee, W. Y. (2003). "Shock and Detonation Calculations for Fiber Composites Structures Subjected to Undersea Blast Environments." Unpublished Work and Independent Research. Engineering and Technical Computing Consultations, Mesa, AZ.
- Lewis, B. A. (2004). "Manual for LS-DYNA Soil Material Model 147." Federal Highway Administration. Publication No. FHWA-HRT-095. McLean, VA.

- Li, X. S. (2001). "Unified Critical State Sand Model in Flow-Liquefaction Deformation Analysis." Proceedings of NSF International Workshop on Earthquake Simulation in Geotechnical Engineering. Case Western Reserve University, Cleveland, OH.
- Mader, C. L. (1979). "Numerical Modeling of Explosives and Propellants." University of California Press. Berkeley, CA.
- Mader, C. L. (1998). "Numerical Modeling of Explosives and Propellants." Second edition. CRC Press, LLC. Boca Raton, FL.
- Murray, Y. D. (2005). E-mail communications. APTEK Inc. Colorado Springs, CO.
- Murray, Y. D. (1997). "Modeling Rate Effects in Rock and Concrete," Proceedings of the 8th International Symposium on the Interaction of the Effects of Munitions with Structures, Defense Special Weapons Agency, McLean, VA.
- National Research Council (1985). "Liquefaction of Soils During Earthquakes," National Academy Press.
- Orica Brazil Inc. (2002). "Pentex Boosters Material Safety Data Sheet." MSDS Number 60000. Orica Canada Inc., Brownsburg, QC.
- Orica Canada Inc. (2003). "Pentex[®] AP Cast Boosters Technical Data Sheet." Orica Canada Inc., Brownsburg, QC.
- Park, S. S., and Byrne, P. M. (2004a). "Numerical Modeling of Soil Liquefaction at Slope Site." The 2004 International Conference on Cyclic Behaviour of Soils and Liquefaction Proceedings.
- Park, S. S., and Byrne, P. M. (2004b). "Practical Constitutive Model for Soil Liquefaction." The 9th International Symposium on Numerical Models in Geomechanics. NUMOG IX Proceedings.
- Popov, E. P. (1976). "Mechanics of Materials." Second Edition. Prentice-Hall, Inc. Englewood Cliffs, N.J.

- Rathje, E. M., Chang, W. J., and Stokoe, K. H. II (2005). "Development of an In Situ Dynamic Liquefaction Test." *Geotechnical Testing Journal*. ASTM, Vol. 28, No. 1, pp. 50-60.
- Rathje, E. M., Chang, W. J., Stokoe, K. H. II, and Cox, B. R. (2004). "Evaluation of Ground Strain From In Situ Dynamic Response." *Proceeding of the 13th World Conference on Earthquake Engineering*. Vancouver, B.C. Paper No. 3099.
- Reid, J. D. and Coon, B. A. (2004). "Evaluation of LS-DYNA Soil Material Model 147." *Federal Highway Administration*. Publication No. FHWA-HRT-04-094. McLean, VA.
- Robertson, P. K., Wride, C. E., List, B. R., Atukorala, U., Biggar, K. W., Byrne, P. M., Campanella, R. G., Cathro, D. C., Chan, D. H., Czajewski, K., Finn, W. D. L., Gu, W. H., Hammamji, Y., Hofmann, B. A., Howie, J. A., Hughes, J., Imrie, A. S., Konrad, J. M., Küpper, A., Law, T., Lord, E. R. F., Monahan, P. A., Morgenstern, N. R., Phillips R., Piché, R., Plewes, H. D., Scott, D., Sego, D. C., Sobkowicz, J., Stewart, R. A., Watts, B. D., Woeller, D. J., Youd, T. L., and Zavodni, Z. (2000a). "The Canadian Liquefaction Experiment: An Overview." *Canadian Geotechnical Journal*. National Research Council of Canada. Vol. 37, pp. 499-504.
- Robertson, P. K., Wride, C. E., List, B. R., Atukorala, U., Biggar, K. W., Byrne, P. M., Campanella, R. G., Cathro, D. C., Chan, D. H., Czajewski, K., Finn, W. D. L., Gu, W. H., Hammamji, Y., Hofmann, B. A., Howie, J. A., Hughes, J., Imrie, A. S., Konrad, J. M., Küpper, A., Law, T., Lord, E. R. F., Monahan, P. A., Morgenstern, N. R., Phillips R., Piché, R., Plewes, H. D., Scott, D., Sego, D. C., Sobkowicz, J., Stewart, R. A., Watts, B. D., Woeller, D. J., Youd, T. L., and Zavodni, Z. (2000b). "The CANLEX Project: Summary and Conclusions." *Canadian Geotechnical Journal*. National Research Council of Canada. Vol. 37, pp. 563-591.
- Rollins, K. M., Anderson, J. K. S., Goughnour, R. R., McCain, A. K. (2004). "Liquefaction Hazard Mitigation Using Vertical Composite Drains." *The 13th World Conference on Earthquake Engineering*. Vancouver B. C., Canada.
- Rollins, K. M., Gerber, T. M., Lane, J. D., and Ashford, S. A. (2005a). "Lateral Resistance of a Full-Scale Pile Group in Liquefied Sand." *Journal of Geotechnical and Geoenvironmental Engineering*. American Society of Civil Engineers, Vol. 131, No. 1, pp. 115-125.

- Rollins, K. M., Lane, J. D., and Gerber T. M. (2005b). "Measured and Computed Lateral Response of a Pile Group in Sand." *Journal of Geotechnical and Geoenvironmental Engineering*. American Society of Civil Engineers, Vol. 131, No. 1, pp. 103-114.
- Schwer, L. (2003) "Geomaterial Modeling with LS-DYNA." Course Notes. Schwer Engineering & Consulting Services. Windsor, CA.
- Schwer, L. (2001). "Laboratory Tests for Characterizing Geomaterials." Schwer Engineering & Consulting Services. Windsor, CA.
- Seid-Karbasi, M., and Byrne, P. M. (2004). "Embankment Dams and Earthquakes." *The International Journal on Hydropower & Dams*. Aqua~Media International Ltd., Sutton, U.K. Issue 2, pp. 96-102.
- Silling, S. (2005). "Peridynamic Modeling of Material Failure". Computational Physics Department. Sandia National Laboratories. Albuquerque, NM.
- Souli, M'hamed (2000). "LS-DYNA: Advanced Course in ALE and Fluid / Structure Coupling." Livermore Software Technology Corporation. Livermore, CA.
- Souli, M'hamed (2005). E-mail communications on ALE and Eulerian capabilities in LS-DYNA. Livermore Software Technology Corporation. Livermore, CA.
- Stone, R. (1967). "High Explosive Handbook. Volume I." Lawrence Radiation Laboratory. Publication No. UCRL-6759. Livermore, CA.
- Swisdak, M. M. (1975). "Explosion Effects and Properties. Part I: Explosion Effects in Air." Naval Surface Weapons Center, White Oak Division. Publication No. NSWC/WOL/TR-75-116. Silver Spring, MD.
- Swisdak, M. M. (1978). "Explosion Effects and Properties. Part II: Explosion Effects in Water." Naval Surface Weapons Center, White Oak Division. Publication No. NSWC/WOL/TR-76-116. Silver Spring, MD.
- Taylor, P. A. (2004). "Modeling the Response of Variably Saturated Geomaterials to Large Strain Rate Loading." Department of Computational Physics & Simulation Frameworks Presentation. Sandia National Laboratories. Albuquerque, NM.

- Walters, W. P. and Held, M. (2003). *Fundamentals of Shaped Charges Seminar Notes*. Computational Mechanics Associates, Baltimore, MD.
- Walters, W. P. and Zukas, J. A. (1989). "Fundamentals of Shaped Charges". CMC Press. Baltimore, MD.
- Wride, C. E., Hofmann, B. A., D. C. Seago, Plewes, H. D., Konrad, J.-M., Biggar, K. W., Robertson, P. K., and Monahan, P. A. (2000a). "Ground Sampling Program at the CANLEX Test Sites." *Canadian Geotechnical Journal*. National Research Council of Canada. Vol. 37, No. 3, pp. 530-542.
- Wride, C. E., Robertson, P. K., Biggar, K. W., Campanella, R. G., Hofmann, B. A., Hughes, J. M. O., Küpper, A., Woeller, D. J. (2000b). "Interpretation of In Situ Test Results from the CANLEX Sites." *Canadian Geotechnical Journal*. National Research Council of Canada. Vol. 37, No. 3, pp. 505-529.
- Youd, T. L., Idriss, I. M., Andrus, R. D., Arango, I., Castro, G., Christian, J. T., Dobry, R., Liam Finn, W. D., Harder, L., F. Jr., Hynes, M. E., Ishihara, K., Koester, J. P., Liao, S. C., Marcuson, W. F. III, Martin, G. R., Mitchell, J. K., Moriwaki, Y., Power, M. S., Robertson, P. K., Seed, R. B., Stokoe, K. H. II. (2001). "Liquefaction Resistance of Soils: Summary Report From the 1996 NCEER and 1998 NCEER/NSF Workshops on Evaluation of Liquefaction Resistance of Soils." *Journal of Geotechnical and Geoenvironmental Engineering*. American Society of Civil Engineers, Vol. 127, No. 10, pp. 817-832.
- Zienkiewicz, O.C. and Taylor, R. L. (2000a). "The Finite Element Method Volume 1: The Basis." Fifth Edition. Butterworth-Heinemann. Woburn, MA.
- Zienkiewicz, O.C. and Taylor, R. L. (2000b). "The Finite Element Method Volume 2: Solid Mechanics." Fifth Edition. Butterworth-Heinemann. Woburn, MA.
- Zienkiewicz, O.C. and Taylor, R. L. (2000c). "The Finite Element Method Volume 3: Fluid Dynamics." Fifth Edition. Butterworth-Heinemann. Woburn, MA.

Appendix A ANSYS® Parametric Model Development

To facilitate construction of the 3-D blast-induced liquefaction numerical model, ANSYS® pre-processor (PREP7) version 9.0 was used due to its extensive parametric programming and modeling capabilities. The baseline model consists of three levels of explosives with eight charges per level. Listed below is the tri-level parametric input decks used to generate the final baseline blast-induced liquefaction model for this dissertation.

```
/prep7
/triad,off
*afun, deg      ! model coordinates defined in degrees
!----+----1----+----2----+----3----+----4----+----5----+----6----+----7----+----8
! parametric deck to generate full cylinder blast model
! Author: Wayne Y. Lee (May, 2005)
! Improved / enhanced: December, 2005
!----+----1----+----2----+----3----+----4----+----5----+----6----+----7----+----8
! define parameters
f2i=12         ! conversion factor from feet to inches
toler=1.000E-04 ! geometric tolerance to account for round off
pie=3.1415926536 ! circle constant

mexpid=11     ! starting material id of explosive
nlevel=3      ! number of levels of explosives

nexp=8        ! number of explosives per level
dens=0.0607   ! density of explosive (pci)
hexp=12.000   ! total height of explosive column
exsz=12.000   ! height of explosive element
bhole=3.00    ! blast hole radius

d1=21.00*f2i  ! depth at first level of explosives
d2=28.00*f2i  ! depth at second level of explosives
d3=33.00*f2i  ! depth at third level of explosives
nl=19         ! number of plane meshes at specific depths

!----+----1----+----2----+----3----+----4----+----5----+----6----+----7----+----8
! define parameters / arrays for geometry generation
```

```

! syntax:  genlayer, mexp, dens, hexp, nexp, bhole, z0
!---+---1---+---2---+---3---+---4---+---5---+---6---+---7---+---8
*dim, matexp, ,nl  $ *dim, zz, ,nl  $ *dim, dzz, ,nl-1 $ *dim, de, ,nl-1
*dim, ast, ,nl+1  $ *dim, lst, ,nl+1 $ *dim, kst, ,nl+1

d1b1=-d1-f2i      $ d1b=d1b1+f2i    $ d1t=d1b+hexp    $ d1t1=d1t+f2i
d2b1=-d2-f2i      $ d2b=d2b1+f2i    $ d2t=d2b+hexp    $ d2t1=d2t+f2i
d3b1=-d3-f2i      $ d3b=d3b1+f2i    $ d3t=d3b+hexp    $ d3t1=d3t+f2i

zz(1)=(-61.0*f2i), (-49.0*f2i), (-46.0*f2i), (-39.0*f2i), d3b1, d3b, d3t, d3t1
zz(9)=d2b1, d2b, d2t, d2t1, d1b1, d1b, d1t, d1t1, (-15.0*f2i), (-9.00*f2i), (0.00*f2i)

mex1=30.0          $ mex2=2.5          $ mex3=3.0
matexp(1)=mex1, mex1, mex1, mex1, mex1, mex2, mex2, mex1, mex1, mex3
matexp(11)=mex3, mex1, mex1, mex3, mex3, mex1, mex1, mex1, mex1

de(1)=24.0, 12.0, 12.0, 12.0, 12.0, exsz, 12.0, 12.0, 12.0, exsz
de(11)=12.0, 12.0, 12.0, exsz, 12.0, 12.0, 24.0, 24.0

nummrg, all
numcmp, all
allsel, all

!---+---1---+---2---+---3---+---4---+---5---+---6---+---7---+---8
! call macro (subroutine) genlayer to generate plane meshes at specific depths
!---+---1---+---2---+---3---+---4---+---5---+---6---+---7---+---8
*get, ast(1), area, , num, max
*get, lst(1), line, , num, max
*get, kst(1), kp, , num, max

!*do, i, 1, nl
*do, i, 1, nl
    genlayer, matexp(i), dens, hexp, nexp, bhole, zz(i)
    *get, ast(i+1), area, , num, max
    *get, lst(i+1), line, , num, max
    *get, kst(i+1), kp, , num, max
*enddo

nummrg, all
numcmp, all
allsel, all

!---+---1---+---2---+---3---+---4---+---5---+---6---+---7---+---8
! generate volumes and brick elements
!---+---1---+---2---+---3---+---4---+---5---+---6---+---7---+---8
!*do, i, 1, nl-1
*do, i, 1, nl-1
    dk=kst(2)-kst(1)
    kk0=(i-1)*dk $ kk1=i*dk
    dzz(i)=zz(i+1)-zz(i)
    esize, , dzz(i)/de(i)

    ! no transition, perform extrusion only
    *if, matexp(i), eq, matexp(i+1), then
        vext, ast(i)+1, ast(i+1), 1, 0.0, 0.0, dzz(i)

    ! transition, perform both extrusion and manual generation
    *else
        *get, vs, volu, , num, max
        vext, ast(i)+5, ast(i)+18, 1, 0.0, 0.0, dzz(i)

    allsel, all
    nummrg, all

```

```

numcmp,all

*get,vs1,volu,,num,max
v,kk0+7 ,kk0+8 ,kk0+9 ,kk0+10,kk1+7 ,kk1+8, kk1+9, kk1+10
v,kk0+7 ,kk0+11,kk0+12,kk0+8 ,kk1+7 ,kk1+11,kk1+12,kk1+8
v,kk0+8 ,kk0+12,kk0+13,kk0+9 ,kk1+8 ,kk1+12,kk1+13,kk1+9
v,kk0+9 ,kk0+13,kk0+14,kk0+10,kk1+9 ,kk1+13,kk1+14,kk1+10

*get,ve,volu,,num,max
vsel,s,volu,,vs+1,ve $ aslv,s,1 $ lsla,s,1 $ ksll,s,1

vsweep,all
allsel,all

*get,ve,volu,,num,max
vsel,s,volu,,vs+1,ve $ cm,v1,volu

! generate eighth model
local,12,0, 0.0,0.0,0.0, 22.5
csys,12
cmsel,s,v1
vsymm,y,all
csys,0
allsel,all
nummrg,all
numcmp,all
*get,ve,volu,,num,max
vsel,s,volu,,vs+1,ve $ cm,v1,volu
allsel,all

! generate quarter model
local,12,0, 0.0,0.0,0.0, 45.0
csys,12
cmsel,s,v1
vsymm,y,all
csys,0
allsel,all
nummrg,all
numcmp,all

! now extrude the center
vext,ast(i)+73,, ,0.0,0.0,dzz(i)

allsel,all
nummrg,all
numcmp,all

! generate half model
*get,ve,volu,,num,max
vsel,s,volu,,vs+1,ve $ cm,v1,volu
allsel,all

csys,0
cmsel,s,v1
vsymm,x,all
allsel,all
nummrg,all
numcmp,all

! generate full model
*get,ve,volu,,num,max
vsel,s,volu,,vs+1,ve $ cm,v1,volu
allsel,all

```

```

    csys,0
    cmsel,s,v1
    vsymm,y,all
    allsel,all
    nummrg,all
    numcmp,all
*endif

    nsel,s,loc,z,zz(i)-toler,zz(i)+toler $ ksln,s,1 $ lslk,s,1 $ asll,s,1
    aclear,all
    allsel,all
    nummrg,all
    numcmp,all
*enddo

!---+---1---+---2---+---3---+---4---+---5---+---6---+---7---+---8
! clean up plane mesh templates
!---+---1---+---2---+---3---+---4---+---5---+---6---+---7---+---8
aclear,all
allsel,all
nummrg,all
numcmp,all

!---+---1---+---2---+---3---+---4---+---5---+---6---+---7---+---8
! define material property id's by layers
!---+---1---+---2---+---3---+---4---+---5---+---6---+---7---+---8
csys,0
nsel,s,loc,y,-toler,10000.0          $ cm,n1,node
nsel,s,loc,y,-10000.0-toler,toler $ cm,n2,node
allsel,all

! partially saturated sand
cmsel,s,n1 $ nsel,r,loc,z,((-9.00*f2i)-toler),((0.000*f2i)+toler) $ esln,s,1
emodif,all,mat,1

! fully saturated clay
cmsel,s,n1 $ nsel,r,loc,z,((-17.0*f2i)-toler),((-9.00*f2i)+toler) $ esln,s,1
emodif,all,mat,2

! fully saturated sand
cmsel,s,n1 $ nsel,r,loc,z,((-23.0*f2i)-toler),((-17.0*f2i)+toler) $ esln,s,1
emodif,all,mat,3

! fully saturated sand
cmsel,s,n1 $ nsel,r,loc,z,((-29.0*f2i)-toler),((-23.0*f2i)+toler) $ esln,s,1
emodif,all,mat,35

! fully saturated sand
cmsel,s,n1 $ nsel,r,loc,z,((-35.0*f2i)-toler),((-29.0*f2i)+toler) $ esln,s,1
emodif,all,mat,37

! fully saturated sand
cmsel,s,n1 $ nsel,r,loc,z,((-41.0*f2i)-toler),((-35.0*f2i)+toler) $ esln,s,1
emodif,all,mat,39

! fully saturated sand
cmsel,s,n1 $ nsel,r,loc,z,((-61.0*f2i)-toler),((-41.0*f2i)+toler) $ esln,s,1
emodif,all,mat,41

! #####
! partially saturated sand
cmsel,s,n2 $ nsel,r,loc,z,((-9.00*f2i)-toler),((0.000*f2i)+toler) $ esln,s,1

```

```

emodif,all,mat,6

! fully saturated clay
cmsel,s,n2 $ nsel,r,loc,z,((-17.0*f2i)-toler),((-9.00*f2i)+toler) $ esln,s,1
emodif,all,mat,7

! fully saturated sand
cmsel,s,n2 $ nsel,r,loc,z,((-23.0*f2i)-toler),((-17.0*f2i)+toler) $ esln,s,1
emodif,all,mat,8

! fully saturated sand
cmsel,s,n2 $ nsel,r,loc,z,((-29.0*f2i)-toler),((-23.0*f2i)+toler) $ esln,s,1
emodif,all,mat,36

! fully saturated sand
cmsel,s,n2 $ nsel,r,loc,z,((-35.0*f2i)-toler),((-29.0*f2i)+toler) $ esln,s,1
emodif,all,mat,38

! fully saturated sand
cmsel,s,n2 $ nsel,r,loc,z,((-41.0*f2i)-toler),((-35.0*f2i)+toler) $ esln,s,1
emodif,all,mat,40

! fully saturated sand
cmsel,s,n2 $ nsel,r,loc,z,((-61.0*f2i)-toler),((-41.0*f2i)+toler) $ esln,s,1
emodif,all,mat,42

allsel,all

!----+----1----+----2----+----3----+----4----+----5----+----6----+----7----+----8
! define explosive surround - (i.e. sacrificial layer)
!----+----1----+----2----+----3----+----4----+----5----+----6----+----7----+----8
diam=25.0          $ radius=0.5*diam
dtheta=360.0/nexp  $ ht=atan(radius/rb)
rmin=rb-radius    $ rmax=rb+radius
zbmin=-d3-f2i-toler  $ zbmax=-d3+(f2i+hexp+toler)
zmmin=-d2-f2i-toler  $ zmmax=-d2+(f2i+hexp+toler)
ztmin=-d1-f2i-toler  $ ztmax=-d1+(f2i+hexp+toler)

csys,1
nsel,s,loc,x,rmin,rmax $ nsel,r,loc,z,zbmin,zbmax $ cm,nsacb,node
nsel,s,loc,x,rmin,rmax $ nsel,r,loc,z,zmmin,zmmax $ cm,nsacm,node
nsel,s,loc,x,rmin,rmax $ nsel,r,loc,z,ztmin,ztmax $ cm,nsact,node
allsel,all
csys,0

*do,i,1,nexp
  theta=(i-1)*dtheta

  csys,1      $ cmsel,s,nsacb
  nsel,r,loc,y,theta-ht,theta+ht      $ esln,s,1 $ emodif,all,mat,5
  csys,0
  nsel,r,loc,y,-10000.0-toler,toler $ esln,s,1 $ emodif,all,mat,10

  csys,1      $ cmsel,s,nsacm
  nsel,r,loc,y,theta-ht,theta+ht      $ esln,s,1 $ emodif,all,mat,5
  csys,0
  nsel,r,loc,y,-10000.0-toler,toler $ esln,s,1 $ emodif,all,mat,10

  csys,1      $ cmsel,s,nsact
  nsel,r,loc,y,theta-ht,theta+ht      $ esln,s,1 $ emodif,all,mat,5
  csys,0
  nsel,r,loc,y,-10000.0-toler,toler $ esln,s,1 $ emodif,all,mat,10
*enddo

```



```

allsel,all
csys,0
!---+---1---+---2---+---3---+---4---+---5---+---6---+---7---+---8
! define blast holes
!---+---1---+---2---+---3---+---4---+---5---+---6---+---7---+---8
dtheta=360.0/nexp

csys,1
diam=8.50      $ radius=0.5*diam $ haftheta=atan(radius/rb)
rmin=rb-radius $ rmax=rb+radius
zmin=-33.0
nsel,s,loc,x,rmin,rmax $ nsel,r,loc,z,-d3-toler,+toler $ cm,nhole,node
allsel,all
csys,0

cmsel,s,nhole $ nsel,r,loc,y,-toler,10000.0 $ cm,nhole1,node
esln,s,1      $ emodif,all,mat,4

cmsel,s,nhole $ nsel,r,loc,y,-10000.0-toler,toler $ cm,nhole2,node
esln,s,1      $ emodif,all,mat,9

allsel,all

!---+---1---+---2---+---3---+---4---+---5---+---6---+---7---+---8
! define explosives
!---+---1---+---2---+---3---+---4---+---5---+---6---+---7---+---8
dtheta=360.0/nexp

diam=3.00      $ radius=0.5*diam
haftheta=atan(radius/rb)
rmin=rb-radius $ rmax=rb+radius
zbmin=-d3-toler $ zbmax=-d3+(hexp+toler)
zmmin=-d2-toler $ zmmax=-d2+(hexp+toler)
ztmin=-d1-toler $ ztmax=-d1+(hexp+toler)

csys,1      $ matnum=11

! bottom level of explosives
nsel,s,loc,x,rmin,rmax $ nsel,r,loc,z,zbmin,zbmax $ cm,nexpb,node

*do,i,1,nexp
  theta=(i-1)*dtheta $ cmsel,s,nexpb
  nsel,r,loc,y,theta-haftheta,theta+haftheta
  esln,s,1          $ emodif,all,mat,matnum
  matnum=matnum+1
*enddo

! middle level of explosives
nsel,s,loc,x,rmin,rmax $ nsel,r,loc,z,zmmin,zmmax $ cm,nexpm,node

*do,i,1,nexp
  theta=(i-1)*dtheta $ cmsel,s,nexpm
  nsel,r,loc,y,theta-haftheta,theta+haftheta
  esln,s,1          $ emodif,all,mat,matnum
  matnum=matnum+1
*enddo

! top level of explosives
nsel,s,loc,x,rmin,rmax $ nsel,r,loc,z,ztmin,ztmax $ cm,nexpt,node

*do,i,1,nexp
  theta=(i-1)*dtheta $ cmsel,s,nexpt

```

```

    nsel,r,loc,y,theta-haftheta,theta+haftheta
    esln,s,1          $ emodif,all,mat,matnum
    matnum=matnum+1
*enddo

allsel,all
csys,0

!---+---1---+---2---+---3---+---4---+---5---+---6---+---7---+---8
! define nodes for non-reflecting (or impedance matching) boundary
! condition
!---+---1---+---2---+---3---+---4---+---5---+---6---+---7---+---8
! OD of model
csys,1
nsel,s,loc,x,(ro-toler),(ro+toler)
csys,0
cm,nidod,node
sf,all,pres,1.0
/output,prrOD,lis
sflist,all,pres
/output
sfdele,all,pres
allsel,all

! bottom of model
nsel,s,loc,z,(zz(1)-toler),(zz(1)+toler)
cm,nidb,node
sf,all,pres,1.0
/output,prrB,lis
sflist,all,pres
/output
sfdele,all,pres
allsel,all

! above air on top
!zz=(0.0*f2i)
!nsel,s,loc,z,-toler,toler
!cm,nidt,node
!sf,all,pres,1.0
!/output,prrT,lis
!sflist,all,pres
!/output
!allsel,all

!---+---1---+---2---+---3---+---4---+---5---+---6---+---7---+---8
! extract nodes at bottom of model typically used for vertical
! constraints against vertical motions. Do not apply constraints
! to these nodes. Just save them to be translated for the ls-dyna
! deck if we need it for debugging purposes
!---+---1---+---2---+---3---+---4---+---5---+---6---+---7---+---8
nsel,s,loc,z,(zz(1)-toler),(zz(1)+toler)
nwrite,dznodes,dat,,0
!d,all,uz,0.0 ! uncomment out this line for debugging
allsel,all

!---+---1---+---2---+---3---+---4---+---5---+---6---+---7---+---8
! write out elements, nodes and boundary conditions for translation
! to ls-dyna
!---+---1---+---2---+---3---+---4---+---5---+---6---+---7---+---8
ewrite,elem,dat,,0,SHORT
nwrite,node,dat,,0
/output,dlist,lis
dlist,all

```

```

/output
fini
/exit

```

The baseline parametric input deck listed above calls a macro (or subroutine) named genlayer to generate the various soil layers. Listed below is the listing for the macro genlayer.mac.

```

! genlayer.mac
! syntax: genlayer,mexp,dens,hexp,nexp,bhole,z0
!-----1-----2-----3-----4-----5-----6-----7-----8
mexp=arg1          ! material mass
dens=arg2          ! material density
hexp=arg3          ! material height
nexp=arg4          ! number of explosives
bhole=arg5         ! blast hole radius
z0=arg6           ! current layer depth
!-----1-----2-----3-----4-----5-----6-----7-----8
ra1=2.50*f2i      ! PPT radial location
ra2=4.00*f2i      ! accelerometer radial location
ra3=5.50*f2i      ! transition circle
ra4=11.0*f2i      ! transition circle
ra=12.00*f2i      ! transition circle
rb=15.00*f2i      ! blast circle radius in feet, converted to inches
rc=19.50*f2i      ! intermediate diameter
rd=24.00*f2i      ! intermediate diameter
ro=30.00*f2i      ! outer diameter of circular area

xc=0.0            ! center point x or radial coordinate
dz=12.0           ! change in z coordinates
!-----1-----2-----3-----4-----5-----6-----7-----8
! compute parameters
Dexp=sqrt((4.0*mexp)/((dens*hexp)*pie))
bhex=((12*(pie*pie))*0.25)/3.0)*Dexp
ahex=bhex/2.0     $ hhex=(sqrt(3.0)/4.0)*bhex
arcleng=360/(nexp*2) ! arclength of 1/2 angular distance between explosive
influ=bhole*5.0   ! zone of influence
!-----1-----2-----3-----4-----5-----6-----7-----8
allsel,all
*get,kk,kp,,num,max
*get,ll,line,,num,max
*get,aa,area,,num,max
!-----1-----2-----3-----4-----5-----6-----7-----8
! surface #1 - explosive slots
!-----1-----2-----3-----4-----5-----6-----7-----8
! basic keypoints
k,kk+1,xc,0.0,z0 $ k,kk+2,xc,0.0,z0+1.0 $ k,kk+3,xc+1.0,0.0,z0
k,kk+4,rb,0.0,z0 $ k,kk+5,rb,0.0,z0+1.0 $ k,kk+6,rb+1.0,0.0,z0

circle,kk+4,ahex*1.000,kk+5,kk+6,180.0,3
circle,kk+4,bhole*4.00,kk+5,kk+6,180.0,3
circle,kk+4,bhole*10.0,kk+5,kk+6,180.0,3

xr=rc*cos(arcleng)          $ yr=rc*sin(arcleng)

```

```

xra= xr+(rc-xr)*(4.0/8.0)   $ yra=yr*(4.0/8.0)
k,kk+19, rc,0.0, z0   $ k,kk+20,xra,yra,z0 $ k,kk+21,xr,yr,z0

nummrg,all
numcmp,all

csys,1
k,kk+22,ro*(0.586),arcleng,z0 $ k,kk+23,ro*(0.496),arcleng,z0
csys,0

xr=ra*cos(arcleng) $ yr=ra*sin(arcleng) $ yra=yr*(3.0/5.0)
k,kk+24, xr,0.0, z0   $ k,kk+25, xr,yra, z0   $ k,kk+26, xr, yr, z0

nummrg,all
numcmp,all

theta=arcleng*(0.500)
circle,kk+1, ro,kk+2,kk+3,theta,1
circle,kk+1, ro,kk+2,kk+28,(arcleng-theta),1
nummrg,all
numcmp,all

xr=ra4*cos(arcleng) $ yr=ra4*sin(arcleng)
k,kk+30, xr,0.0, z0   $ k,kk+31, xr,yr, z0

circle,kk+1, ra3,kk+2,kk+3,arcleng,1
circle,kk+1, ra2,kk+2,kk+3,arcleng,1
circle,kk+1, ral,kk+2,kk+3,arcleng,1

nummrg,all
numcmp,all
/pnum,kp,1

1,kk+24,kk+18 $ 1,kk+18,kk+14 $ 1,kk+14,kk+10 $ 1,kk+10, kk+7
1, kk+7,kk+11 $ 1,kk+11,kk+15 $ 1,kk+15,kk+19
1,kk+25,kk+17 $ 1,kk+23,kk+17 $ 1,kk+17,kk+13 $ 1,kk+13, kk+9
1,kk+22,kk+16 $ 1,kk+16,kk+12 $ 1,kk+12, kk+8 $ 1,kk+16,kk+20
1,kk+22,kk+21 $ 1,kk+23,kk+22 $ 1,kk+26,kk+23 $ 1,kk+24,kk+25 $ 1,kk+25,kk+26

1,kk+19,kk+27 $ 1,kk+20,kk+28 $ 1,kk+21,kk+29

1,kk+30,kk+31
1,kk+36,kk+34 $ 1,kk+34,kk+32 $ 1,kk+32,kk+30 $ 1,kk+30,kk+24
1,kk+37,kk+35 $ 1,kk+35,kk+33 $ 1,kk+33,kk+31 $ 1,kk+31,kk+26

a, kk+7, kk+8, kk+9,kk+10 $ a, kk+7,kk+11,kk+12, kk+8
a, kk+8,kk+12,kk+13, kk+9 $ a, kk+9,kk+13,kk+14,kk+10
a,kk+11,kk+15,kk+16,kk+12 $ a,kk+12,kk+16,kk+17,kk+13
a,kk+13,kk+17,kk+18,kk+14

a,kk+15,kk+19,kk+20,kk+16 $ a,kk+16,kk+20,kk+21,kk+22
a,kk+17,kk+16,kk+22,kk+23 $ a,kk+25,kk+17,kk+23,kk+26
a,kk+24,kk+18,kk+17,kk+25

a,kk+19,kk+27,kk+28,kk+20 $ a,kk+20,kk+28,kk+29,kk+21

ksel,s,kp,,kk+24,kk+26 $ ksel,a,kp,,kk+30,kk+31 $ lslk,s,1 $ al,all
allsel,all

a,kk+32,kk+30,kk+31,kk+33 $ a,kk+34,kk+32,kk+33,kk+35
a,kk+36,kk+34,kk+35,kk+37

!---+---1---+---2---+---3---+---4---+---5---+---6---+---7---+---8

```

kssel,s,kp,,kk+19,kk+20,20-19	\$ lslk,s,1
kssel,s,kp,,kk+15,kk+16,16-15	\$ lslk,a,1
kssel,s,kp,,kk+16,kk+17,17-16	\$ lslk,a,1
kssel,s,kp,,kk+22,kk+23,23-22	\$ lslk,a,1
kssel,s,kp,,kk+17,kk+18,18-17	\$ lslk,a,1
lesize,all,,, 3, 1.000/1.000,1	
kssel,s,kp,,kk+20,kk+21,21-20	\$ lslk,s,1
lesize,all,,, 3, 1.500/1.000,1	
kssel,s,kp,,kk+16,kk+22,22-16	\$ lslk,s,1
lesize,all,,, 3, 1.000/2.000,1	
kssel,s,kp,,kk+17,kk+23,23-17	\$ lslk,s,1
lesize,all,,, 3, 1.000/1.300,1	
kssel,s,kp,,kk+23,kk+26,26-23	\$ lslk,s,1
lesize,all,,, 3, 1.000/1.000,1	
kssel,s,kp,,kk+17,kk+25,25-17	\$ lslk,s,1
lesize,all,,, 2, 1.000/1.750,1	
kssel,s,kp,,kk+25,kk+26,26-25	\$ lslk,s,1
lesize,all,,, 2, 1.000/1.000,1	
kssel,s,kp,,kk+24,kk+25,25-24	\$ lslk,s,1
lesize,all,,, 3, 1.000/1.000,1	
kssel,s,kp,,kk+18,kk+24,24-18	\$ lslk,s,1
lesize,all,,, 2, 1.000/1.000,1	
kssel,s,kp,,kk+15,kk+19,19-15	\$ lslk,s,1
lesize,all,,, 2, 1.000/1.000,1	
kssel,s,kp,,kk+16,kk+20,20-16	\$ lslk,s,1
lesize,all,,, 2, 1.500/1.000,1	
kssel,s,kp,,kk+21,kk+22,22-21	\$ lslk,s,1
lesize,all,,, 2, 1.000/1.000,1	
kssel,s,kp,,kk+19,kk+27,27-19	\$ lslk,s,1
lesize,all,,, 7, 2.000/1.000,1	
kssel,s,kp,,kk+20,kk+28,28-20	\$ lslk,s,1
lesize,all,,, 7, 2.000/1.000,1	
kssel,s,kp,,kk+21,kk+29,29-21	\$ lslk,s,1
lesize,all,,, 7, 2.000/1.000,1	
kssel,s,kp,,kk+27,kk+28,28-27	\$ lslk,s,1
lesize,all,,, 3, 1.000/1.000,1	
kssel,s,kp,,kk+28,kk+29,29-28	\$ lslk,s,1
lesize,all,,, 3, 1.000/1.000,1	
kssel,s,kp,,kk+30,kk+31,31-30	\$ lslk,s,1
lesize,all,,, 5, 1.000/1.000,1	
kssel,s,kp,,kk+32,kk+33,33-32	\$ lslk,s,1
lesize,all,,, 3, 1.000/1.000,1	
kssel,s,kp,,kk+34,kk+35,35-34	\$ lslk,s,1
lesize,all,,, 1, 1.000/1.000,1	
kssel,s,kp,,kk+36,kk+37,37-36	\$ lslk,s,1
lesize,all,,, 1, 1.000/1.000,1	
kssel,s,kp,,kk+24,kk+30,30-24	\$ lslk,s,1
kssel,s,kp,,kk+26,kk+31,31-26	\$ lslk,a,1
lesize,all,,, 1, 1.000/1.000,1	
kssel,s,kp,,kk+30,kk+32,32-30	\$ lslk,s,1
kssel,s,kp,,kk+31,kk+33,33-31	\$ lslk,a,1
lesize,all,,, 4, 1.000/1.000,1	
kssel,s,kp,,kk+32,kk+34,34-32	\$ lslk,s,1

```

ksel,s,kp,,kk+33,kk+35,35-33      $ lslk,a,1
lesize,all,,, 1, 1.000/1.000,1

ksel,s,kp,,kk+34,kk+36,36-34      $ lslk,s,1
ksel,s,kp,,kk+35,kk+37,37-35      $ lslk,a,1
lesize,all,,, 2, 1.000/1.000,1
!---+---1---+---2---+---3---+---4---+---5---+---6---+---7---+---8
et,1,SHELL63
et,2,SOLID45
! mesh selected areas
!MOPT,AMESH,ALTERNATE
!MOPT,QMESH,ALTERNATE
esize,,1
type,1 $ real,3 $ mat,3 $ amesh, aa+1,aa+18
allsel,all
nummrg,all $ numcmp,all
!---+---1---+---2---+---3---+---4---+---5---+---6---+---7---+---8
*get,aaa,area,,num,max
asel,s,area,,aa+1,aaa
cm,aal,area
allsel,all

! generate eighth model
local,12,0, 0.0,0.0,0.0, 22.5
csys,12
cmsel,s,aal
arsymm,y,all
csys,0
allsel,all
nummrg,all
numcmp,all

*get,aaa,area,,num,max
asel,s,area,,aa+1,aaa
cm,aal,area
allsel,all

! generate quarter model
local,12,0, 0.0,0.0,0.0, 45.0
csys,12
cmsel,s,aal
arsymm,y,all
csys,0
allsel,all
nummrg,all
numcmp,all
!---+---1---+---2---+---3---+---4---+---5---+---6---+---7---+---8
ksel,s,loc,x,ral-toler,ral+toler
ksel,r,loc,y,-toler,toler
ksel,r,loc,z,z0-toler,z0+toler
*get,k1,kp,,num,max

ksel,s,loc,y,ral-toler,ral+toler
ksel,r,loc,x,-toler,toler
ksel,r,loc,z,z0-toler,z0+toler
*get,k2,kp,,num,max

allsel,all
l,kk+1,k1 $ l,kk+1,k2
ksel,s,kp,,kk+1 $ ksel,a,kp,,k1,k2,k2-k1 $ lslk,s,1
lesize,all,,,3, 1.000/1.000,1

allsel,all

```

```

csys,1
ksel,s,loc,x,ra1-toler,ra1+toler
ksel,r,loc,z,z0-toler,toler
ksel,a,kp,,kk+1
csys,0
lslk,s,1 $ a1,all
*get,a1,area,,num,max
amesh,a1
!---+----1----+----2----+----3----+----4----+----5----+----6----+----7----+----8
!generate half model
*get,aaa,area,,num,max
asel,s,area,,aa+1,aaa
cm,aa1,area
allsel,all

csys,0
cmsel,s,aa1
arsymm,x,all
allsel,all
nummrg,all
numcmp,all
!---+----1----+----2----+----3----+----4----+----5----+----6----+----7----+----8
! generate full model
*get,aaa,area,,num,max
asel,s,area,,aa+1,aaa
cm,aa1,area
allsel,all

csys,0
cmsel,s,aa1
arsymm,y,all
allsel,all
nummrg,all
numcmp,all
!---+----1----+----2----+----3----+----4----+----5----+----6----+----7----+----8

```

Use of the parametric input approach such as the one documented above to generate ANSYS® solid models, and keeping only the parametric input deck, is recommended for documentation and time/disk space saving purposes. ANSYS® tends to have huge overhead costs (i.e. generate huge database and output files for reasonably sized models). As such, files generated by ANSYS® for non-parametric, interactively built models require a significant amount of disk space which may not be a luxury one can afford, especially when working with multiple projects and/or multiple designs of moderately sized models. For example, the output and model database and other files generated by the input deck listed above require more than 500+ megabytes (MB) on an

HP-UX desktop computer. In contrast, the parametric input deck listed above requires less than 50 kilobytes (kB) of disk space. When considering the fact that it takes less 5 minutes to re-generate the above model on an HP-UX desktop computer, it is obviously more economical, efficient, and cost effective to save just the small parametric input deck.

Appendix B Tracers and Pore Water Pressure Extraction

Tracers represent particles located within a continuum (i.e. current numerical model) that are specified by the user to track results computed by the corresponding analysis software. Tracers can be placed anywhere within a given model. Their locations do not have to coincide with any specific geometric entities such as nodes. There are two types of tracers available in shock wave analysis.

One type of tracer represents spatial points or particles that remain fixed in space (i.e. in Eulerian coordinates) for tracking numerical quantities such as velocities and stress waves that pass through the particle in time. This type of tracer is typically used to simulate test-data capturing devices such as pore pressure transducers or accelerometers that are installed at pre-defined and fixed spatial locations.

A second type of tracer represents material points or particles that follow the movements (i.e. in Lagrangian coordinates) of the material located at the initial position of the respective tracer point. This type of tracer is typically used for tracking the trajectory or instantaneous position and state of stress of a given material with respect to time.

For the Vancouver blast series conducted in May of 2005, there are five pore pressure transducers and four accelerometers installed in a circumferential pattern around

the center of the blast circle. Table 9-1 summarizes the locations and depths of the pressure transducers and accelerometers.

In LS-DYNA, tracers are available only for ALE, Eulerian and coupled Eulerian-LaGrangian (fluid-structure) analysis options. Unfortunately, tracers are currently unavailable for LaGrangian analysis option. When tracers are specified for solid elements, positions, velocities, and stress components of the tracers with respect to time are saved in addition to the normal set of result data. From the velocity results saved for the tracer points, one can easily compute the corresponding accelerations by taking the time derivatives of the respective velocities. LS-PrePost has built-in capabilities to perform time derivatives and time integrations of variables stored in the tracer history file. As such, extracting acceleration time histories are relatively simple through LS-PrePost.

On the other hand, pore pressure results for the FHWA Mat 147 soil material model are not currently available in standard analysis output or tracer history output per information provided by APTEK Inc., the developer of the soil material model (Murray, 2005). One must back-calculate the pore pressure from the volumetric strains computed by LS-DYNA. Since volumetric strain is simply the average principal strains, volumetric strains are readily available in LS-PrePost as a part of the normal analysis results with respect to time, or “state” as defined in LS-DYNA terminology. However, strain results are not directly available in tracer results. As such, they must be computed from stress results listed in the tracer output file and the corresponding material properties. Computing material properties are simple when their values are unchanged (i.e. linear, elastic) during the course of the analysis. However, computations become challenging

when material properties such as bulk modulus are updated as material deforms as in the baseline soil material model. Therefore, to extract the pore water pressure from soil material FHWA Mat 147, it is recommended to use LS-PrePost computed volumetric strains instead of computing the volumetric strains via tracers. The major draw back in using LS-PrePost is that one may not obtain the results at the exact locations as one would desire due to discrete locations of nodes and elements. This is where careful planning in meshing the model in such a way that the desired tracer positions coincide with nodes in the model.

To extract volumetric strains for the calculations of pore-water pressure, one must locate from the tracer points of interest, the nearest node(s) or element(s) where the volumetric strains with respect to time are presented in LS-PrePost. To facilitate the extraction of volumetric strains in LS-PrePost for the determination of pore water pressure, a special C/C++ utility software was written to perform the necessary determinations of the node(s) and element(s) nearest to the tracer points (or measurement device locations) of interest. The software was compiled on Cygwin (a Linux emulator for MS Windows operating system) GNU as well as Linux GNU C/C++ compilers. With 1GB of internal memory, the software can easily handle up to 150,000 elements, 150,000 nodes, and up to 100 tracer points with ease. Presented below is a full listing of the utility software's source code.

```
//--+-1-----2-----3-----4-----5-----6-----7-----8
// FILE:      program to find nearest nodes and elements of given tracers
// AUTHOR:    W.Y.Lee
// DATE:     August 06, 2005
//--+-1-----2-----3-----4-----5-----6-----7-----8
#include"findne.h"

#define      DEBUGON
#undef       DEBUGON
```

```

//--+-1-----2-----3-----4-----5-----6-----7-----8
// define local routine prototypes
//--+-1-----2-----3-----4-----5-----6-----7-----8
Static void   ReadStr   (FILE *fptr, char *s, int mxsz);
static void   TrimStr   (char *s);
static FILE   *OpenFile (char *s, char *rw);
static void   ProcTR    (TRACERS& tr, FILE* fptr);
static void   ProcNE    (NODES& n, ELEMS& e, FILE *fptr);
static void   SeekNE    (TRACERS& tr, NODES& n, ELEMS& e, FILE* fptr);
static double CalcDist  (double x1, double y1, double z1,
                        double x2, double y2, double z2);
//--+-1-----2-----3-----4-----5-----6-----7-----8
//--+-1-----2-----3-----4-----5-----6-----7-----8
// ReadStr    read and trim a string
// author:    W. Y. Lee
// date:      August 06, 2005
//--+-1-----2-----3-----4-----5-----6-----7-----8
static void ReadStr(FILE *fptr, char *s, int mxsz)
{
    if (s != (char *) NULL)
    {
        fgets(s, mxsz, fptr);
        TrimStr(s);
    }
}
//--+-1-----2-----3-----4-----5-----6-----7-----8
// TrimStr    trim all leading/trailing control characters from a string
// author:    W. Y. Lee
// date:      August 06, 2005
//--+-1-----2-----3-----4-----5-----6-----7-----8
static void TrimStr(char *s)
{
    int   indx = 0;
    unsigned int   i, j;

    if (s != (char *) NULL)
    {
        for (;;)
        {
            if (s[indx] == '\0')
            {
                break;
            }
            else if (s[indx] == '\n')
            {
                s[indx] = '\0';
                break;
            }
            else if (iscntrl(s[indx]))
            {
                s[indx] = ' ';
            }

            indx++;
        }

        indx = strlen(s) - 1;

        for (;;)
        {
            if (indx <= 0)
                break;

```

```

        if (iscntrl(s[indx]) || s[indx] == ' ')
        {
            s[indx] = '\\0';
        }
        else
        {
            break;
        }

        indx--;
    }

    for (i = 0; i < strlen(s); i++)
    {
        if (s[i] != ' ')
        {
            for (j = i; j <= strlen(s); j++)
            {
                s[j - i] = s[j];
            }

            break;
        }
    }
}

//-----1-----2-----3-----4-----5-----6-----7-----8
// OpenFile routine to open a specific file
// author: W. Y. Lee
// date: August 06, 2005
//-----1-----2-----3-----4-----5-----6-----7-----8
static FILE *OpenFile(char *s, char *rw)
{
    int i, j, leng;
    FILE *fptr = (FILE *) NULL;

    if (s != (char *) NULL)
    {
        if (strlen(s) <= 0)
        {
            fptr = (FILE *) NULL;
        }
        else
        {
            fptr = fopen(s, rw);
        }
    }

    return(fptr);
}

//-----1-----2-----3-----4-----5-----6-----7-----8
// ProcTR routine to read in and store tracer points
// author: W. Y. Lee
// date: August 06, 2005
//
// format of tracer file:
// comment
// tracer location x, y, z
// comment
// tracer location x, y, z
// . . .
// . . .
// . . .

```

```

// comment
// tracer location x, y, z
//--+-1---+---2---+---3---+---4---+---5---+---6---+---7---+---8
static void ProcTR(TRACERS& tr, FILE* fptr)
{
    long    i, j;
    char    s    [MXSTRSZ];

    tr.ntr = 0;
    fprintf(stdout, "\n*** Reading tracer location file ***\n");
    for (i = 0; i < MXTR; i++)
    {
        fgets(s, MXSTRSZ, fptr);
        if (feof(fptr))
            break;
        TrimStr(s);

        // set tracer id and save tracer comment
        tr.tr[tr.ntr].id = tr.ntr + 1;
        strcpy(tr.tr[tr.ntr].loc, s);

        fgets(s, MXSTRSZ, fptr);
        if (feof(fptr))
            break;
        TrimStr(s);

        // save x, y, z coordinates
        tr.tr[tr.ntr].x = atof(strtok(s, "    ,;\n"));
        tr.tr[tr.ntr].y = atof(strtok('\0', "    ,;\n"));
        tr.tr[tr.ntr].z = atof(strtok('\0', "    ,;\n"));

        tr.tr[tr.ntr].nn = 0;
        tr.tr[tr.ntr].ne = 0;
        tr.tr[tr.ntr].ndist = 1.0E+20;
        tr.tr[tr.ntr].edist = 1.0E+20;

        tr.ntr ++;
    }
    fprintf(stdout, "*** Tracer location file process completed ***\n\n");
}
//--+-1---+---2---+---3---+---4---+---5---+---6---+---7---+---8
// dyna node and element section types
//--+-1---+---2---+---3---+---4---+---5---+---6---+---7---+---8
enum DynaSectType
{
    UNKNOWN = 0,
    NODESECT, // dyna node section
    ESOLID,   // dyna solid element section
    ESHELL,   // dyna shell element section
    EBELM     // dyna beam element section
};
//--+-1---+---2---+---3---+---4---+---5---+---6---+---7---+---8
// ProcNE routine to read in nodes & elements from a dyna file
// author: W. Y. Lee
// date: August 06, 2005
//--+-1---+---2---+---3---+---4---+---5---+---6---+---7---+---8
static void ProcNE(NODES& n, ELEMS& e, FILE *fptr)
{
    Long    i;
    DynaSectType idx = UNKNOWN;
    char    s    [MXSTRSZ];
    char    s1   [MXSTRSZ];

```

```

n.nn = 0;
e.ne = 0;
fprintf(stdout, "\n*** Reading / processing LS-DYNA input file ***\n");
for (;;)
{
    fgets(s, MXSTRSZ, fptr);
    strcpy(s1, s);
    if (feof(fptr))
        break;

    TrimStr(s);
    if (s[0] == '*')
    {
        fprintf(stdout, "%s\n", s);
        fprintf(fptr, "%s", s1);
        if (strcmp(s, "*END") == 0)
        {
            break;
        }
        else if (strcmp(s, "*NODE") == 0)
        {
            idx = NODESECT;
        }
        else if (strcmp(s, "*ELEMENT_SOLID") == 0)
        {
            idx = ESOLID;
        }
        else if (strcmp(s, "*ELEMENT_SHELL") == 0)
        {
            idx = ESHELL;
        }
        else if (strcmp(s, "*ELEMENT_BEAM") == 0)
        {
            idx = EBEAM;
        }
        else
        {
            idx = UNKNOWN;
        }
    }
    else if (s[0] == '$')
    {
        // ignore comments
    }
    else
    {
        switch(idx)
        {
            case UNKNOWN:
            default:
                break;
            case NODESECT:
                strcpy(n.n[n.nn].loc, "");
                n.n[n.nn].id = atol(strtok(s, " ,;\n"));
                n.n[n.nn].x = atof(strtok('\0', " ,;\n"));
                n.n[n.nn].y = atof(strtok('\0', " ,;\n"));
                n.n[n.nn].z = atof(strtok('\0', " ,;\n"));
                n.n[n.nn].t = atol(strtok('\0', " ,;\n"));
                n.n[n.nn].r = atol(strtok('\0', " ,;\n"));
                n.nn ++;
                break;
            case ESOLID:
            case ESHELL:

```



```

case EBEAM:
    e.e[e.ne].eid = atol(strtok(s, " ,;\n"));
    e.e[e.ne].pid = atol(strtok('\0', " ,;\n"));

    e.e[e.ne].nne = ((idx == ESOLID) ? 8 :
                     ((idx == ESHELL) ? 4 :
                      ((idx == EBEAM) ? 3 : 0)));

    for (i = 0; i < e.e[e.ne].nne; i++)
    {
        e.e[e.ne].nc[i] = atol(strtok('\0', " ,;\n"));
    }

    e.ne ++;
    break;
}
}
}
    fprintf(stdout, "*** LS-DYNA input file process completed ***\n\n");
}
//-----1-----2-----3-----4-----5-----6-----7-----8
// SeekNE routine to seek nearest nodes and elements from given tracers
// author: W. Y. Lee
// date: August 06, 2005
//-----1-----2-----3-----4-----5-----6-----7-----8
static void SeekNE(TRACERS& tr, NODES& n, ELEMS& e, FILE* fptr)
{
    Long i, j;
    long nne;
    double d, dd;
    double xavg, yavg, zavg;

    fprintf(fptr, "*** Program to seek nearest node(s) and element(s) to\n"
            "*** a given set of tracer points for LS-DYNA result\n"
            "*** extraction purposes.\n\n"
            "*** written by W. Y. Lee (August 06, 2005)\n\n");

    fprintf(fptr, "Total number of nodes in model: %-#ld\n", n.nn);
    fprintf(fptr, "Total number of elements in model: %-#ld\n", e.ne);
    fprintf(fptr, "Total number of tracer points: %-#ld\n\n", tr.ntr);

    // seek nearest node(s)
    for (i = 0; i < n.nn; i++)
    {
        for (j = 0; j < tr.ntr; j++)
        {
            dd = CalcDist(tr.tr[j].x, tr.tr[j].y, tr.tr[j].z,
                          n.n[i].x, n.n[i].y, n.n[i].z);
            if (dd < tr.trsj.ndist)
            {
                tr.trsj.nn = 1;
                tr.trsj.n[tr.trsj.nn - 1] = n.n[i];
                tr.trsj.ndist = dd;
            }
            else if (dd == tr.trsj.ndist)
            {
                tr.trsj.nn ++;
                tr.trsj.n[tr.trsj.nn - 1] = n.n[i];
            }
        }
    }

    // seek nearest element(s)

```

```

for (i = 0; i < e.ne; i++)
{
    xavg = 0.0;          yavg = 0.0;          zavg = 0.0;
    nne = e.e[i].nne;

    // estimate element centroid
    for (j = 0; j < nne; j++)
    {
        xavg += n.n[e.e[i].nc[j] - 1].x;
        yavg += n.n[e.e[i].nc[j] - 1].y;
        zavg += n.n[e.e[i].nc[j] - 1].z;
    }

    xavg /= ((nne > 0) ? ((double) nne) : 1);
    yavg /= ((nne > 0) ? ((double) nne) : 1);
    zavg /= ((nne > 0) ? ((double) nne) : 1);

    for (j = 0; j < tr.ntr; j++)
    {
        dd = CalcDist(tr.tr[j].x, tr.tr[j].y, tr.tr[j].z, xavg, yavg, zavg);
        if (dd < tr.tr[s[j]].edist)
        {
            tr.tr[s[j]].ne = 1;
            tr.tr[s[j]].e[tr.tr[s[j]].ne - 1] = e.e[i];
            tr.tr[s[j]].edist = dd;
        }
        else if (dd == tr.tr[s[j]].edist)
        {
            tr.tr[s[j]].ne ++;
            tr.tr[s[j]].e[tr.tr[s[j]].ne - 1] = e.e[i];
        }
    }
}

fprintf(fp, "$$$ Summary of nearest node(s) and element(s):\n\n");
for (i = 0; i < tr.ntr; i++)
{
    fprintf(fp, "\nTracer Point #%-ld (%s)\n",
            i+1,
            "located at (%-#14.6lG, %-#14.6lG, %-#14.6lG):\n",
            tr.tr[i].loc, tr.tr[i].x, tr.tr[i].y, tr.tr[i].z);

    fprintf(fp, " Distance to nearest node is %-#14.6lG\n",
            tr.tr[s[i]].ndist);
    for (j = 0 ; j < tr.tr[s[i]].mn; j++)
    {
        fprintf(fp, " Node #%-#8.0ld at (%-#14.6lG, %-#14.6lG, "
                "%-#14.6lG)\n", tr.tr[s[i]].n[j].id, tr.tr[s[i]].n[j].x,
                tr.tr[s[i]].n[j].y, tr.tr[s[i]].n[j].z);
    }

    fprintf(fp, " Distance to nearest element is %-#14.6lG\n",
            tr.tr[s[i]].edist);
    for (j = 0 ; j < tr.tr[s[i]].ne; j++)
    {
        fprintf(fp, " Element #%-#8.0ld (Part #%-ld)\n",
                tr.tr[s[i]].e[j].eid, tr.tr[s[i]].e[j].pid);
    }
}
}
//--+-1-----2-----3-----4-----5-----6-----7-----8
// CalcDist routine to compute distance between two points
// author: W. Y. Lee
// date: August 06, 2005

```

```

//--+-----1-----+-----2-----+-----3-----+-----4-----+-----5-----+-----6-----+-----7-----+-----8
static double CalcDist(double x1, double y1, double z1,
                      double x2, double y2, double z2)
{
    return(sqrt((x2-x1)*(x2-x1) + (y2-y1)*(y2-y1) + (z2-z1)*(z2-z1)));
}
//--+-----1-----+-----2-----+-----3-----+-----4-----+-----5-----+-----6-----+-----7-----+-----8
// main driver
// author:    W. Y. Lee
// date:      August 06, 2005
//--+-----1-----+-----2-----+-----3-----+-----4-----+-----5-----+-----6-----+-----7-----+-----8
int main()
{
    char    s    [MXSTRSZ];
    char    *p;
    NODES   n;
    ELEMS   e;
    TRACERS tr;
    FILE    *fptr;

    n.n = new NODE[MXNN];
    e.e = new ELEM[MXNE];

    fprintf(stdout, "\nProgram to find nearest nodes and "
               "elements for tracers\n\n");

    fprintf(stdout, "Enter name of tracer location file: "
               "(max # of tracers = %d): ", MXTR);
    fgets(s, MXSTRSZ, stdin);
    p = strtok(s, " ,;\n");
    fptr = OpenFile(p, "r");
    ProcTR(tr, fptr);
    fclose(fptr);

    fprintf(stdout, "Enter existing LS-DYNA input file name: ");
    fgets(s, MXSTRSZ, stdin);
    p = strtok(s, " ,;\n");
    fptr = OpenFile(p, "r");
    ProcNE(n, e, fptr);
    fclose(fptr);

    fprintf(stdout, "Enter name of output summary file: ");
    fgets(s, MXSTRSZ, stdin);
    p = strtok(s, " ,;\n");
    fptr = OpenFile(p, "w");
    SeekNE(tr, n, e, fptr);
    fclose(fptr);

    fprintf(stdout, "\n*** Process completed ***\n\n");

    delete[] n.n;
    delete[] e.e;

    return(0);
}
//--+-----1-----+-----2-----+-----3-----+-----4-----+-----5-----+-----6-----+-----7-----+-----8

```

Listing for the header file associated with the source code listed above is provided

below:

```
// *****
// findne.h  header file for findne.cpp
// Author:   W.Y. Lee
// DATE:     August 6, 2005
// *****
#ifndef    FINDNE_H
#define    FINDNE_H

#include   <stdlib.h>
#include   <stdio.h>
#include   <math.h>
#include   <string.h>
#include   <ctype.h>

//-----
// define string parameters and local routine prototypes
//-----
#define    SHORTFORMAT
#define    LONGFORMAT
#undef     LONGFORMAT

#define    RNDERR      1.0E-08
#define    MXSTRLEN    255
#define    MXSTRSZ     (MXSTRLEN + 1)
#define    Boolean     int
#define    bool        int
#define    TRUE        1
#define    FALSE       0
#define    true        1
#define    false       0
#define    MXNE        150000
#define    MXNN        150000
#define    MXNNE       8
#define    MXTR        100
#define    MXTRNE      10

//-----
typedef struct  node
{
    Char    loc[MXSTRSZ]; // node location identifier
    Long    id;           // node id
    double  x, y, z;     // node location coordinate
    long    t, r;        // nodal transformation flag
} NODE, *NODE_PTR;

typedef struct  elem
{
    long    eid;         // element id
    long    pid;         // part id
    long    nne;         // number of nodes in element
    long    nc[MXNNE];  // nodal connectivity
} ELEM, *ELEM_PTR;

typedef struct  nodes
{
    long    nn;
    NODE    *n;
}
```

```

    } NODES, *NODES_PTR;

typedef struct elems
{
    long ne;
    ELEM *e;
} ELEMS, *ELEMS_PTR;

typedef struct trsum
{
    Long    nn;                // number of nodes
    long    ne;                // number of elements
    double  ndist;            // shortest distance of node from tracer
    double  edist;            // shortest distance of element from tracer
    NODE    n [MXTRNE];       // array of nodes nearest to tracer
    ELEM    e [MXTRNE];       // array of elements nearest to tracer
} TRSUM, *TRSUM_PTR;

typedef struct tracers
{
    Long    ntr;                // actual number of tracers
    NODE    tr [MXTR];         // array of tracers
    TRSUM    trs [MXTR];
} TRACERS, *TRACERS_PTR;
//-----
#endif

```

Inputs to the utility software consist of a tracer definition file, the LS-DYNA input deck containing nodal coordinates and element connectivities. The program saves a summary of its findings to a user specified output file. Format for the tracer definition file consists of alternating one line of comment/description of a tracer followed by one line containing the x, y, and z coordinates of the same tracer.

The tracer definition file used to describe the locations of the data capturing devices used in the May, 2005 Vancouver blast series is presented below. Distance units presented in the tracer definition file below are in inches and are defined in the standard finite element analysis (FEA) modeling coordinates (i.e. +Z measured up from ground surface).

```

PPT 859105 (N) - z=38' (38')
30.00000  0.000000  -456.0000

```

```

PPT 883032 (S) - z=31' (31')
-30.00000  0.0000000  -372.0000
PPT 859120 (W) - z=45' (45')
 0.000000  30.00000  -540.0000
PPT 859215 (E) - z=18' (18') - clay
 0.000000 -30.00000  -216.0000
PPT 856610 (C) - z=25' (25')
 0.000000  0.000000  -300.0000
accelerometers NW - z=25' (25')
 33.94113  33.94113  -300.0000
accelerometers NE - z=25' (25')
 33.94113 -33.94113  -300.0000
accelerometers SW - z=25' (25')
-33.94113  33.94113  -300.0000
accelerometers SE - z=25' (25')
-33.94113 -33.94113  -300.0000

```

Finally, a summary of the extracted ID numbers of the nodes and elements nearest to the respective tracers as computed by the utility software is presented below.

```

#####
### Program to extract nearest node(s) and element(s)
### for a set of tracer points located within a
### given LS-DYNA model for post-processing.
###
### Author: Wayne Y. Lee (Date: August 06, 2005)
### (C) 2005 by Wayne Y. Lee. All rights reserved.
###
### Current date / time: Tue Jan 24 17:06:43 2006
### Tracer location file: tracers.inp
### LS-DYNA input deck: soil1.dyn
### Output summary file: tracersum.prn
#####
Total number of nodes in model: 103537
Total number of elements in model: 99072
Total number of tracer points: 9

$$$ Summary of nearest node(s) and element(s):

Tracer Point #1 (PPT 859105 (N) - z=38' (38'))
  Rotation Angle: 22.5000 deg.
  Original non-rotated Coordinates: (30.0000 , 0.00000 , -456.000 )
  Actual rotated Coordinates used: (27.7164 , 11.4805 , -456.000 ):
  Distance to nearest node above tracer is 3.81039E-08
    Node #68225 at (27.7164 , 11.4805 , -456.000 )
  Distance to nearest node below tracer is 3.81039E-08
    Node #68225 at (27.7164 , 11.4805 , -456.000 )
  Distance to nearest element is 9.51036
    Element #35575 (Part #3)
    Element #35576 (Part #3)

```

Element #35600 (Part #3)
Element #35601 (Part #3)

Tracer Point #2 (PPT 883032 (S) - z=31' (31'))

Rotation Angle: 22.5000 deg.
Original non-rotated Coordinates: (-30.0000 , 0.00000 , -372.000)
Actual rotated Coordinates used: (-27.7164 , -11.4805 , -372.000):
Distance to nearest node above tracer is 3.81039E-08
Node #16532 at (-27.7164 , -11.4805 , -372.000)
Distance to nearest node below tracer is 3.81039E-08
Node #16532 at (-27.7164 , -11.4805 , -372.000)
Distance to nearest element is 9.51036
Element #49531 (Part #8)
Element #49536 (Part #8)
Element #53653 (Part #8)
Element #53663 (Part #8)

Tracer Point #3 (PPT 859120 (W) - z=45' (45'))

Rotation Angle: 22.5000 deg.
Original non-rotated Coordinates: (0.00000 , 30.0000 , -540.000)
Actual rotated Coordinates used: (-11.4805 , 27.7164 , -540.000):
Distance to nearest node above tracer is 3.81039E-08
Node #60759 at (-11.4805 , 27.7164 , -540.000)
Distance to nearest node below tracer is 3.81039E-08
Node #60759 at (-11.4805 , 27.7164 , -540.000)
Distance to nearest element is 9.50744
Element #25752 (Part #3)
Element #25753 (Part #3)
Element #25787 (Part #3)
Element #25788 (Part #3)

Tracer Point #4 (PPT 859215 (E) - z=18' (18') - clay)

Rotation Angle: 22.5000 deg.
Original non-rotated Coordinates: (0.00000 , -30.0000 , -216.000)
Actual rotated Coordinates used: (11.4805 , -27.7164 , -216.000):
Distance to nearest node above tracer is 3.81039E-08
Node #89012 at (11.4805 , -27.7164 , -216.000)
Distance to nearest node below tracer is 3.81039E-08
Node #89012 at (11.4805 , -27.7164 , -216.000)
Distance to nearest element is 9.50744
Element #80469 (Part #7)
Element #80470 (Part #7)
Element #80489 (Part #7)
Element #80490 (Part #7)

Tracer Point #5 (PPT 856610 (C) - z=25' (25'))

Rotation Angle: 22.5000 deg.
Original non-rotated Coordinates: (0.00000 , 0.00000 , -300.000)
Actual rotated Coordinates used: (0.00000 , 0.00000 , -300.000):
Distance to nearest node above tracer is 0.00000
Node #79823 at (0.00000 , 0.00000 , -300.000)
Distance to nearest node below tracer is 0.00000
Node #79823 at (0.00000 , 0.00000 , -300.000)
Distance to nearest element is 8.98860
Element #61901 (Part #3)
Element #61902 (Part #3)
Element #63965 (Part #3)
Element #63966 (Part #3)
Element #66029 (Part #8)
Element #66030 (Part #8)
Element #68093 (Part #8)
Element #68094 (Part #8)

Tracer Point #6 (accelerometers NW - z=25' (25'))
 Rotation Angle: 22.5000 deg.
 Original non-rotated Coordinates: (33.9411 , 33.9411 , -300.000)
 Actual rotated Coordinates used: (18.3688 , 44.3462 , -300.000):
 Distance to nearest node above tracer is 6.31409E-06
 Node #79484 at (18.3688 , 44.3462 , -300.000)
 Distance to nearest node below tracer is 6.31409E-06
 Node #79484 at (18.3688 , 44.3462 , -300.000)
 Distance to nearest element is 13.3991
 Element #61369 (Part #3)
 Element #61370 (Part #3)
 Element #61873 (Part #3)
 Element #61874 (Part #3)
 Element #61877 (Part #3)
 Element #61878 (Part #3)

Tracer Point #7 (accelerometers NE - z=25' (25'))
 Rotation Angle: 22.5000 deg.
 Original non-rotated Coordinates: (33.9411 , -33.9411 , -300.000)
 Actual rotated Coordinates used: (44.3462 , -18.3688 , -300.000):
 Distance to nearest node above tracer is 6.31409E-06
 Node #81809 at (44.3462 , -18.3688 , -300.000)
 Distance to nearest node below tracer is 6.31409E-06
 Node #81809 at (44.3462 , -18.3688 , -300.000)
 Distance to nearest element is 13.3991
 Element #64481 (Part #8)
 Element #64482 (Part #8)
 Element #64985 (Part #8)
 Element #64986 (Part #8)
 Element #64989 (Part #8)
 Element #64990 (Part #8)

Tracer Point #8 (accelerometers SW - z=25' (25'))
 Rotation Angle: 22.5000 deg.
 Original non-rotated Coordinates: (-33.9411 , 33.9411 , -300.000)
 Actual rotated Coordinates used: (-44.3462 , 18.3688 , -300.000):
 Distance to nearest node above tracer is 6.31409E-06
 Node #80294 at (-44.3462 , 18.3688 , -300.000)
 Distance to nearest node below tracer is 6.31409E-06
 Node #80294 at (-44.3462 , 18.3688 , -300.000)
 Distance to nearest element is 13.3991
 Element #62417 (Part #3)
 Element #62418 (Part #3)
 Element #62921 (Part #3)
 Element #62922 (Part #3)
 Element #62925 (Part #3)
 Element #62926 (Part #3)

Tracer Point #9 (accelerometers SE - z=25' (25'))
 Rotation Angle: 22.5000 deg.
 Original non-rotated Coordinates: (-33.9411 , -33.9411 , -300.000)
 Actual rotated Coordinates used: (-18.3688 , -44.3462 , -300.000):
 Distance to nearest node above tracer is 6.31409E-06
 Node #84176 at (-18.3688 , -44.3462 , -300.000)
 Distance to nearest node below tracer is 6.31409E-06
 Node #84176 at (-18.3688 , -44.3462 , -300.000)
 Distance to nearest element is 13.3991
 Element #67561 (Part #8)
 Element #67562 (Part #8)
 Element #68065 (Part #8)
 Element #68066 (Part #8)
 Element #68069 (Part #8)
 Element #68070 (Part #8)

One may discover from the output that the closest nodes are coincident to the locations of the corresponding pore water pressure transducers and accelerometers. This was done in purpose during the model generation research to help reduce unnecessary additional extrapolations and / or interpolations that could become the source of unacceptable numerical errors.

With the nodes and elements nearest to the tracer points of interest defined, one can extract the corresponding average volumetric strains directly from LS-PrePost for calculating pore-water pressure results, which are then used to determine the soil's progress toward liquefaction.

Appendix C Cauchy's Infinitesimal Strain

Rathje, Chang, and Stokoe developed a procedure for measuring liquefaction and pore pressure generation characteristics of soil from data measured in situ (Rathje et al., 2004, Rathje et al., 2005 and Chang, 2002). The concept by Rathje et al. begins by measuring velocities via geophones placed strategically in a rectangular pattern vertically within a pre-determined volume of liquefiable soil deposit, followed by the application of dynamic cyclic loads from a near-by location. A vibroseis truck (Rathje et al., 2004, Rathje et al., 2005 and Chang, 2002) is utilized to generate the desired vertical dynamic cyclic loads. The measured velocities are integrated to obtain the corresponding displacement data used to compute shear and normal strains located within the rectangular data measured grid using a displacement-based approach. Wave-propagation methods are also presented in the development. However, only the displacement-based method utilized by Rathje et al. is applicable to the May 2005 Vancouver blast-induced liquefaction test due to limited availability of data.

Cauchy's infinitesimal strain theory forms the basis of the strain computations in the displacement-based method by Rathje et al. Chang's dissertation (Chang, 2002) summarizes the concept by which the strains are computed. One should note that shear strains presented by Rathje et al. in their papers that were published in 2004 and 2005 were applicable only for the following conditions:

1. Pattern of displacement inputs is rectangular with edges parallel to the coordinate axes and center at the origin of the same coordinate system.
2. Iso-parametric strain distribution within the rectangular region is linear, elastic.
3. Strains are infinitesimal in that the first derivatives of the displacements with respect to the corresponding coordinate directions are so small that the squares or the products of the derivatives are negligible. By eliminating the products and squares of the first derivatives of the displacements, the Almansi strains from which strains were derived becomes Cauchy's infinitesimal strains.

In the May, 2005 Vancouver blast-induced liquefaction test, accelerometers are placed horizontally at a depth of 25 feet from the surface. Although the accelerometers are placed in a square pattern, they are rotated with respect to the global x, y coordinates, with x due north and y due west. Out-of-plane (depth or z direction) is not considered since only four (or planar) tri-axial accelerometers in a rectangular pattern were available for data measurement. Furthermore, one of the four z-direction acceleration measurement devices became inoperative prior to test. As a result, only x and y (or horizontal planar) data is available for strain computations.

Due to the rotated orientation with displacements measured in the non-rotated orientation, the limited form of the strain computation approach presented by Rathje et al. in 2004 and 2005 is not directly applicable. The following pages present a listing of the MathCad[®] derivation of the infinitesimal strains in a quadrilateral element that is applicable to the May 2005 Vancouver test.

Iso-parametric Quadrilateral Element Strain Function Derivation

2-D tensor Indices

Fung, Y. C., "A First Course in Continuum Mechanics" (1977), 2nd Edition, Prentice-Hall, Inc., Englewood Cliffs, NJ., pp. 125-129.

$i = 1..2 \quad \kappa = 1..2$

$\alpha = 1..2$

LaGrangian strain tensor (by Green - St. Venant)

2-D displacements u_i (or u, v) in **unstrained** configuration / coordinates of r_i (or r, s)

$$\epsilon_{gsv_{i\kappa}} = \frac{1}{2} \left(\frac{\delta u_{\kappa}}{\delta r_i} + \frac{\delta u_i}{\delta r_{\kappa}} + \frac{\delta u_{\alpha}}{\delta r_i} \frac{\delta u_{\alpha}}{\delta r_{\kappa}} \right)$$

In unabridged forms:

$$\epsilon_{gsv_{rr}} = \frac{\delta u}{\delta r} + \frac{1}{2} \left[\left(\frac{\delta u}{\delta r} \right)^2 + \left(\frac{\delta v}{\delta r} \right)^2 \right]$$

$$\epsilon_{gsv_{ss}} = \frac{\delta v}{\delta s} + \frac{1}{2} \left[\left(\frac{\delta u}{\delta s} \right)^2 + \left(\frac{\delta v}{\delta s} \right)^2 \right]$$

$$\gamma_{gsv_{rs}} = 2 \cdot \epsilon_{gsv_{rs}} = \frac{\delta v}{\delta r} + \frac{\delta u}{\delta s} + \left(\frac{\delta u}{\delta r} \cdot \frac{\delta u}{\delta s} + \frac{\delta v}{\delta r} \cdot \frac{\delta v}{\delta s} \right)$$

Eulerian strain tensor (by Cauchy for infinitesimal strains, by Almansi and Hamel for finite strains)

2 - D displacements u_i (or u, v) in **strained** configuration / coordinates of x_i (or x, y)

$$\epsilon_{alm_{i\kappa}} = \frac{1}{2} \left(\frac{\delta u_{\kappa}}{\delta x_i} + \frac{\delta u_i}{\delta x_{\kappa}} - \frac{\delta u_{\alpha}}{\delta x_i} \frac{\delta u_{\alpha}}{\delta x_{\kappa}} \right)$$

In unabridged forms:

$$\epsilon_{alm_{rr}} = \frac{\delta u}{\delta x} - \frac{1}{2} \left[\left(\frac{\delta u}{\delta x} \right)^2 + \left(\frac{\delta v}{\delta x} \right)^2 \right]$$

$$\epsilon_{alm_{ss}} = \frac{\delta v}{\delta y} - \frac{1}{2} \left[\left(\frac{\delta u}{\delta y} \right)^2 + \left(\frac{\delta v}{\delta y} \right)^2 \right]$$

$$\gamma_{alm_{rs}} = 2 \epsilon_{alm_{rs}} = \frac{\delta v}{\delta x} + \frac{\delta u}{\delta y} - \left(\frac{\delta u}{\delta x} \frac{\delta u}{\delta y} + \frac{\delta v}{\delta x} \frac{\delta v}{\delta y} \right)$$

Now if the first derivatives of the displacement components are small such that their squares and products become negligible, then both LaGrangian & Eulerian strain tensors reduce to the following equations

Green - St. Venant (LaGrangian) Strain Tensor

Almasi (Eulerian) Strain Tensor

Cauchy's (Eulerian) infinitesimal strain tensor is defined as

$$\epsilon_{gsv_{i\kappa}} = \frac{1}{2} \left(\frac{\delta u_{\kappa}}{\delta r_i} + \frac{\delta u_i}{\delta r_{\kappa}} \right)$$

$$\epsilon_{alm_{i\kappa}} = \frac{1}{2} \left(\frac{\delta u_{\kappa}}{\delta x_i} + \frac{\delta u_i}{\delta x_{\kappa}} \right)$$

$$\epsilon_{i\kappa} = \frac{1}{2} \left(\frac{\delta u_{\kappa}}{\delta x_i} + \frac{\delta u_i}{\delta x_{\kappa}} \right)$$

$$\epsilon_{gsv_{rr}} = \frac{\delta u}{\delta r}$$

$$\epsilon_{alm_{rr}} = \frac{\delta u}{\delta x}$$

$$\epsilon_{rr} = \frac{\delta u}{\delta x}$$

$$\epsilon_{gsv_{ss}} = \frac{\delta v}{\delta s}$$

$$\epsilon_{alm_{ss}} = \frac{\delta v}{\delta y}$$

$$\epsilon_{ss} = \frac{\delta v}{\delta y}$$

$$\gamma_{gsv_{rs}} = 2 \cdot \epsilon_{gsv_{rs}} = \frac{\delta v}{\delta r} + \frac{\delta u}{\delta s}$$

$$\gamma_{alm_{rs}} = 2 \epsilon_{alm_{rs}} = \frac{\delta v}{\delta x} + \frac{\delta u}{\delta y}$$

$$\gamma_{rs} = 2 \epsilon_{rs} = \frac{\delta v}{\delta x} + \frac{\delta u}{\delta y}$$

Therefore, the reduced Almansi Eulerian strain tensor is nothing more than Cauchy's infinitesimal strain tensor. Also note that in the infinitesimal case, distinction between LaGrangian (Green - St. Venant) and Eulerian (Almansi and Cauchy) strains is negligible.

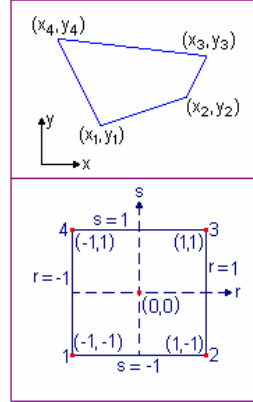
2-D Bi-linear LaGrange polynomials based isoparametric shape function:

$$N_i = \frac{(1 + r \cdot rs_i, 0)(1 + s \cdot rs_i, 1)}{4}$$

where i = node index (1 to 4)

rs = nodal coordinates of a quad element in (r, s) coordinate system

$$rs \equiv \begin{pmatrix} -1 & -1 \\ 1 & -1 \\ 1 & 1 \\ -1 & 1 \end{pmatrix} \implies \begin{matrix} N_1 = \frac{(1-r)(1-s)}{4} & N_2 = \frac{(1+r)(1-s)}{4} \\ N_3 = \frac{(1+r)(1+s)}{4} & N_4 = \frac{(1-r)(1+s)}{4} \end{matrix}$$



Global coordinates of points within a 2-D isoparametric quad element:

$$x = \sum_{i=1}^4 N_i \cdot x_i = N_1 \cdot x_1 + N_2 \cdot x_2 + N_3 \cdot x_3 + N_4 \cdot x_4$$

$$y = \sum_{i=1}^4 N_i \cdot y_i = N_1 \cdot y_1 + N_2 \cdot y_2 + N_3 \cdot y_3 + N_4 \cdot y_4$$

"QuadElem.bmp"

Displacements of a point (u, v) anywhere within the element are also defined in terms of the corresponding nodal displacements (u_i, v_i) in the global (x, y) directions, respectively.

$$u = \sum_{i=1}^4 N_i \cdot u_i = N_1 \cdot u_1 + N_2 \cdot u_2 + N_3 \cdot u_3 + N_4 \cdot u_4 \quad v = \sum_{i=1}^4 N_i \cdot v_i = N_1 \cdot v_1 + N_2 \cdot v_2 + N_3 \cdot v_3 + N_4 \cdot v_4$$

where (x, y) = global coordinates of any point inside the element (x_i, y_i) = global coordinates of the ith node in the element. Now expand the coordinates:

Expand Cauchy's (Eulerian) infinitesimal strains' partial derivatives

$$\begin{aligned} \epsilon_x &= \frac{\delta u}{\delta x} = \left(\frac{\delta N_1}{\delta x} \cdot u_1 + N_1 \cdot \frac{\delta u_1}{\delta x} \right) + \left(\frac{\delta N_2}{\delta x} \cdot u_2 + N_2 \cdot \frac{\delta u_2}{\delta x} \right) + \left(\frac{\delta N_3}{\delta x} \cdot u_3 + N_3 \cdot \frac{\delta u_3}{\delta x} \right) + \left(\frac{\delta N_4}{\delta x} \cdot u_4 + N_4 \cdot \frac{\delta u_4}{\delta x} \right) \\ \epsilon_y &= \frac{\delta v}{\delta y} = \left(\frac{\delta N_1}{\delta y} \cdot v_1 + N_1 \cdot \frac{\delta v_1}{\delta y} \right) + \left(\frac{\delta N_2}{\delta y} \cdot v_2 + N_2 \cdot \frac{\delta v_2}{\delta y} \right) + \left(\frac{\delta N_3}{\delta y} \cdot v_3 + N_3 \cdot \frac{\delta v_3}{\delta y} \right) + \left(\frac{\delta N_4}{\delta y} \cdot v_4 + N_4 \cdot \frac{\delta v_4}{\delta y} \right) \\ \gamma_{xy} &= \frac{\delta u}{\delta y} + \frac{\delta v}{\delta x} = \left(\frac{\delta N_1}{\delta y} \cdot u_1 + N_1 \cdot \frac{\delta u_1}{\delta y} \right) + \left(\frac{\delta N_2}{\delta y} \cdot u_2 + N_2 \cdot \frac{\delta u_2}{\delta y} \right) + \left(\frac{\delta N_3}{\delta y} \cdot u_3 + N_3 \cdot \frac{\delta u_3}{\delta y} \right) + \left(\frac{\delta N_4}{\delta y} \cdot u_4 + N_4 \cdot \frac{\delta u_4}{\delta y} \right) \\ &\quad + \left(\frac{\delta N_1}{\delta x} \cdot v_1 + N_1 \cdot \frac{\delta v_1}{\delta x} \right) + \left(\frac{\delta N_2}{\delta x} \cdot v_2 + N_2 \cdot \frac{\delta v_2}{\delta x} \right) + \left(\frac{\delta N_3}{\delta x} \cdot v_3 + N_3 \cdot \frac{\delta v_3}{\delta x} \right) + \left(\frac{\delta N_4}{\delta x} \cdot v_4 + N_4 \cdot \frac{\delta v_4}{\delta x} \right) \end{aligned}$$

Since u_i and v_i are known displacements, their derivatives with respect to x and y are zero.

Simplify the strain equations:

$$\epsilon_x = \frac{\delta u}{\delta x} = \frac{\delta N_1}{\delta x} \cdot u_1 + \frac{\delta N_2}{\delta x} \cdot u_2 + \frac{\delta N_3}{\delta x} \cdot u_3 + \frac{\delta N_4}{\delta x} \cdot u_4 \quad \epsilon_y = \frac{\delta v}{\delta y} = \frac{\delta N_1}{\delta y} \cdot v_1 + \frac{\delta N_2}{\delta y} \cdot v_2 + \frac{\delta N_3}{\delta y} \cdot v_3 + \frac{\delta N_4}{\delta y} \cdot v_4$$

$$\gamma_{xy} = \frac{\delta u}{\delta y} + \frac{\delta v}{\delta x} = \frac{\delta N_1}{\delta y} \cdot u_1 + \frac{\delta N_1}{\delta x} \cdot v_1 + \frac{\delta N_2}{\delta y} \cdot u_2 + \frac{\delta N_2}{\delta x} \cdot v_2 + \frac{\delta N_3}{\delta y} \cdot u_3 + \frac{\delta N_3}{\delta x} \cdot v_3 + \frac{\delta N_4}{\delta y} \cdot u_4 + \frac{\delta N_4}{\delta x} \cdot v_4$$

Rewrite the strain equations in matrix form, we'll have

$$\epsilon = \begin{pmatrix} \epsilon_x \\ \epsilon_y \\ \gamma_{xy} \end{pmatrix} = \begin{pmatrix} \frac{\delta N_1}{\delta x} & 0 & \frac{\delta N_2}{\delta x} & 0 & \frac{\delta N_3}{\delta x} & 0 & \frac{\delta N_4}{\delta x} & 0 \\ 0 & \frac{\delta N_1}{\delta y} & 0 & \frac{\delta N_2}{\delta y} & 0 & \frac{\delta N_3}{\delta y} & 0 & \frac{\delta N_4}{\delta y} \\ \frac{\delta N_1}{\delta y} & \frac{\delta N_1}{\delta x} & \frac{\delta N_2}{\delta y} & \frac{\delta N_2}{\delta x} & \frac{\delta N_3}{\delta y} & \frac{\delta N_3}{\delta x} & \frac{\delta N_4}{\delta y} & \frac{\delta N_4}{\delta x} \end{pmatrix} \begin{pmatrix} u_1 \\ v_1 \\ u_2 \\ v_2 \\ u_3 \\ v_3 \\ u_4 \\ v_4 \end{pmatrix}$$

Recall shape functions

$$N_i = \frac{(1+r \cdot rs_i, 0)(1+s \cdot rs_i, 1)}{4}$$

$$rs = \begin{pmatrix} -1 & -1 \\ 1 & -1 \\ 1 & 1 \\ -1 & 1 \end{pmatrix}$$

Recall that N_i are functions of (r, s) , need to define a relationship between (r, s) and (x, y)

$$\begin{pmatrix} \frac{\delta N_i}{\delta r} \\ \frac{\delta N_i}{\delta s} \end{pmatrix} = \begin{pmatrix} \frac{\delta x}{\delta r} & \frac{\delta y}{\delta r} \\ \frac{\delta x}{\delta s} & \frac{\delta y}{\delta s} \end{pmatrix} \cdot \begin{pmatrix} \frac{\delta N_i}{\delta x} \\ \frac{\delta N_i}{\delta y} \end{pmatrix} = J \cdot \begin{pmatrix} \frac{\delta N_i}{\delta x} \\ \frac{\delta N_i}{\delta y} \end{pmatrix} \quad \text{where } J \text{ is called the Jacobian} \quad \implies \begin{pmatrix} \frac{\delta N_i}{\delta x} \\ \frac{\delta N_i}{\delta y} \end{pmatrix} = J^{-1} \cdot \begin{pmatrix} \frac{\delta N_i}{\delta r} \\ \frac{\delta N_i}{\delta s} \end{pmatrix}$$

Symbolic inverse of a 2×2 matrix: $\begin{pmatrix} a & b \\ c & d \end{pmatrix}^{-1} = \frac{1}{a \cdot d - b \cdot c} \begin{pmatrix} d & -b \\ -c & a \end{pmatrix} = \xi \cdot \begin{pmatrix} d & -b \\ -c & a \end{pmatrix}$ $\xi = \frac{1}{a \cdot d - b \cdot c} = \frac{1}{\eta - \zeta}$

Now define the inverse of the Jacobian: $J^{-1} = \begin{pmatrix} \frac{\delta x}{\delta r} & \frac{\delta y}{\delta r} \\ \frac{\delta x}{\delta s} & \frac{\delta y}{\delta s} \end{pmatrix}^{-1} = \begin{pmatrix} \frac{\delta r}{\delta x} & \frac{\delta s}{\delta x} \\ \frac{\delta r}{\delta y} & \frac{\delta s}{\delta y} \end{pmatrix} = \frac{1}{\frac{\delta x}{\delta r} \frac{\delta y}{\delta s} - \frac{\delta y}{\delta r} \frac{\delta x}{\delta s}} \begin{pmatrix} \frac{\delta y}{\delta s} & -\frac{\delta y}{\delta r} \\ -\frac{\delta x}{\delta s} & \frac{\delta x}{\delta r} \end{pmatrix} = \xi \cdot \begin{pmatrix} \frac{\delta y}{\delta s} & -\frac{\delta y}{\delta r} \\ -\frac{\delta x}{\delta s} & \frac{\delta x}{\delta r} \end{pmatrix}$

where $\xi = \frac{1}{\frac{\delta x}{\delta r} \frac{\delta y}{\delta s} - \frac{\delta y}{\delta r} \frac{\delta x}{\delta s}} = \frac{1}{\eta - \zeta}$ with $\eta = \frac{\delta x}{\delta r} \frac{\delta y}{\delta s}$ and $\zeta = \frac{\delta y}{\delta r} \frac{\delta x}{\delta s}$

Substitute inverse of Jacobian into relationship: $\begin{pmatrix} \frac{\delta N_i}{\delta x} \\ \frac{\delta N_i}{\delta y} \end{pmatrix} = J^{-1} \cdot \begin{pmatrix} \frac{\delta N_i}{\delta r} \\ \frac{\delta N_i}{\delta s} \end{pmatrix} = \xi \cdot \begin{pmatrix} \frac{\delta y}{\delta s} & -\frac{\delta y}{\delta r} \\ -\frac{\delta x}{\delta s} & \frac{\delta x}{\delta r} \end{pmatrix} \cdot \begin{pmatrix} \frac{\delta N_i}{\delta r} \\ \frac{\delta N_i}{\delta s} \end{pmatrix} = \xi \cdot \begin{pmatrix} \frac{\delta y}{\delta s} \frac{\delta N_i}{\delta r} - \frac{\delta y}{\delta r} \frac{\delta N_i}{\delta s} \\ \frac{\delta x}{\delta r} \frac{\delta N_i}{\delta s} - \frac{\delta x}{\delta s} \frac{\delta N_i}{\delta r} \end{pmatrix}$

Recall global coordinates in terms of the bi-linear shape function N : $x = \sum_{t=1}^4 N_t \cdot x_t$ and $y = \sum_{t=1}^4 N_t \cdot y_t$

$$\frac{\delta x}{\delta r} = \sum_{t=1}^4 \frac{\delta N_t}{\delta r} \cdot x_t \quad \frac{\delta x}{\delta s} = \sum_{t=1}^4 \frac{\delta N_t}{\delta s} \cdot x_t \quad \frac{\delta y}{\delta r} = \sum_{t=1}^4 \frac{\delta N_t}{\delta r} \cdot y_t \quad \frac{\delta y}{\delta s} = \sum_{t=1}^4 \frac{\delta N_t}{\delta s} \cdot y_t$$

Recall shape function and compute its derivatives:

$$N_1 = \frac{(1+r \cdot rs_{i,0})(1+s \cdot rs_{i,1})}{4} \quad \frac{\delta N_1}{\delta r} = \frac{rs_{i,0} \cdot (1+s \cdot rs_{i,1})}{4} \quad \frac{\delta N_1}{\delta s} = \frac{rs_{i,1} \cdot (1+r \cdot rs_{i,0})}{4}$$

When expanded, shape function and its derivatives take the forms:

$$N_1 = \frac{(1-r) \cdot (1-s)}{4} \quad N_2 = \frac{(1+r) \cdot (1-s)}{4} \quad N_3 = \frac{(1+r) \cdot (1+s)}{4} \quad N_4 = \frac{(1-r) \cdot (1+s)}{4}$$

$$\begin{matrix} \frac{\delta N_1}{\delta r} = -\frac{1-s}{4} & \frac{\delta N_2}{\delta r} = \frac{1-s}{4} & \frac{\delta N_3}{\delta r} = \frac{1+s}{4} & \frac{\delta N_4}{\delta r} = -\frac{1+s}{4} \\ \frac{\delta N_1}{\delta s} = -\frac{1-r}{4} & \frac{\delta N_2}{\delta s} = -\frac{1+r}{4} & \frac{\delta N_3}{\delta s} = \frac{1+r}{4} & \frac{\delta N_4}{\delta s} = \frac{1-r}{4} \end{matrix} \quad \text{where } rs = \begin{pmatrix} -1 & -1 \\ 1 & -1 \\ 1 & 1 \\ -1 & 1 \end{pmatrix}$$

Expand the partial derivatives of the components that define the shape functions:

$$\frac{\delta x}{\delta r} = \sum_{t=1}^4 \frac{\delta N_t}{\delta r} \cdot x_t = \frac{\delta N_1}{\delta r} \cdot x_1 + \frac{\delta N_2}{\delta r} \cdot x_2 + \frac{\delta N_3}{\delta r} \cdot x_3 + \frac{\delta N_4}{\delta r} \cdot x_4 = -\frac{1-s}{4} \cdot x_1 + \frac{1-s}{4} \cdot x_2 + \frac{1+s}{4} \cdot x_3 + -\frac{1+s}{4} \cdot x_4$$

$$\frac{\delta y}{\delta r} = \sum_{t=1}^4 \frac{\delta N_t}{\delta r} \cdot y_t = \frac{\delta N_1}{\delta r} \cdot y_1 + \frac{\delta N_2}{\delta r} \cdot y_2 + \frac{\delta N_3}{\delta r} \cdot y_3 + \frac{\delta N_4}{\delta r} \cdot y_4 = -\frac{1-s}{4} \cdot y_1 + \frac{1-s}{4} \cdot y_2 + \frac{1+s}{4} \cdot y_3 + -\frac{1+s}{4} \cdot y_4$$

$$\frac{\delta x}{\delta s} = \sum_{t=1}^4 \frac{\delta N_t}{\delta s} \cdot x_t = \frac{\delta N_1}{\delta s} x_1 + \frac{\delta N_2}{\delta s} x_2 + \frac{\delta N_3}{\delta s} x_3 + \frac{\delta N_4}{\delta s} x_4 = -\frac{1-r}{4} x_1 + -\frac{1+r}{4} x_2 + \frac{1+r}{4} x_3 + \frac{1-r}{4} x_4$$

$$\frac{\delta y}{\delta s} = \sum_{t=1}^4 \frac{\delta N_t}{\delta s} \cdot y_t = \frac{\delta N_1}{\delta s} y_1 + \frac{\delta N_2}{\delta s} y_2 + \frac{\delta N_3}{\delta s} y_3 + \frac{\delta N_4}{\delta s} y_4 = -\frac{1-r}{4} y_1 + -\frac{1+r}{4} y_2 + \frac{1+r}{4} y_3 + \frac{1-r}{4} y_4$$

$$\frac{\delta x}{\delta r} = \sum_{t=1}^4 \frac{\delta N_t}{\delta r} \cdot x_t = \sum_{t=1}^4 \frac{rs_{t,0} \cdot (1 + s \cdot rs_{t,1})}{4} \cdot x_t \quad \frac{\delta y}{\delta r} = \sum_{t=1}^4 \frac{\delta N_t}{\delta r} \cdot y_t = \sum_{t=1}^4 \frac{rs_{t,0} \cdot (1 + s \cdot rs_{t,1})}{4} \cdot y_t$$

$$\frac{\delta x}{\delta s} = \sum_{t=1}^4 \frac{\delta N_t}{\delta s} \cdot x_t = \sum_{t=1}^4 \frac{rs_{t,1} \cdot (1 + r \cdot rs_{t,0})}{4} \cdot x_t \quad \frac{\delta y}{\delta s} = \sum_{t=1}^4 \frac{\delta N_t}{\delta s} \cdot y_t = \sum_{t=1}^4 \frac{rs_{t,1} \cdot (1 + r \cdot rs_{t,0})}{4} \cdot y_t$$

Substitute, expand, and simplify to obtain

$$\frac{\delta x}{\delta r} = \frac{(1-s) \cdot (x_2 - x_1) - (1+s) \cdot (x_4 - x_3)}{4} \quad \frac{\delta y}{\delta r} = \frac{(1-s) \cdot (y_2 - y_1) - (1+s) \cdot (y_4 - y_3)}{4} \quad \frac{\delta N_i}{\delta r} = \frac{rs_{i,0} \cdot (1 + s \cdot rs_{i,1})}{4}$$

$$\frac{\delta x}{\delta s} = \frac{(1-r) \cdot (x_4 - x_1) + (1+r) \cdot (x_3 - x_2)}{4} \quad \frac{\delta y}{\delta s} = \frac{(1-r) \cdot (y_4 - y_1) + (1+r) \cdot (y_3 - y_2)}{4} \quad \frac{\delta N_i}{\delta s} = \frac{rs_{i,1} \cdot (1 + r \cdot rs_{i,0})}{4}$$

$$\eta = \frac{\delta x}{\delta r} \cdot \frac{\delta y}{\delta s} = \left[\frac{(1-s) \cdot (x_2 - x_1) - (1+s) \cdot (x_4 - x_3)}{4} \right] \left[\frac{(1-r) \cdot (y_4 - y_1) + (1+r) \cdot (y_3 - y_2)}{4} \right]$$

$$\zeta = \frac{\delta y}{\delta r} \cdot \frac{\delta x}{\delta s} = \left[\frac{(1-s) \cdot (y_2 - y_1) - (1+s) \cdot (y_4 - y_3)}{4} \right] \left[\frac{(1-r) \cdot (x_4 - x_1) + (1+r) \cdot (x_3 - x_2)}{4} \right]$$

Derive the parameter ξ for defining the inverse of the Jacobian:

$$\xi = \frac{1}{\eta - \zeta} = \frac{1}{\frac{\delta x}{\delta r} \cdot \frac{\delta y}{\delta s} - \frac{\delta y}{\delta r} \cdot \frac{\delta x}{\delta s}}$$

$$\xi = \frac{1}{\left[\sum_{t=1}^4 \frac{r_t \cdot (1 + s \cdot rs_{t,1})}{4} \cdot x_t \right] \left[\sum_{t=1}^4 \frac{s_t \cdot (1 + r \cdot rs_{t,0})}{4} \cdot y_t \right] - \left[\sum_{t=1}^4 \frac{r_t \cdot (1 + s \cdot rs_{t,1})}{4} \cdot y_t \right] \left[\sum_{t=1}^4 \frac{s_t \cdot (1 + r \cdot rs_{t,0})}{4} \cdot x_t \right]}$$

Substitute and simplify expression for ξ :

$$\xi = \frac{1}{\left[\frac{(1-s) \cdot (y_2 - y_1) - (1+s) \cdot (y_4 - y_3)}{4} \cdot \frac{(1-r) \cdot (x_4 - x_1) + (1+r) \cdot (x_3 - x_2)}{4} \right] - \left[\frac{(1-s) \cdot (x_2 - x_1) - (1+s) \cdot (x_4 - x_3)}{4} \cdot \frac{(1-r) \cdot (y_4 - y_1) + (1+r) \cdot (y_3 - y_2)}{4} \right]}$$

$$\xi = \frac{8}{\left[(y_4 - y_1) \cdot (x_3 - x_2) - (y_3 - y_2) \cdot (x_4 - x_1) \right] \cdot s + \left[(y_2 - y_1) \cdot (x_4 - x_3) - (y_4 - y_3) \cdot (x_2 - x_1) \right] \cdot r - \left[(y_4 - y_2) \cdot (x_3 - x_1) - (y_3 - y_1) \cdot (x_4 - x_2) \right]}$$

Recall partial derivative of the shape function:

$$\begin{pmatrix} \frac{\delta N_i}{\delta x} \\ \frac{\delta N_i}{\delta y} \end{pmatrix} = J^{-1} \cdot \begin{pmatrix} \frac{\delta N_i}{\delta r} \\ \frac{\delta N_i}{\delta s} \end{pmatrix} = \begin{pmatrix} \frac{\delta r}{\delta x} & \frac{\delta s}{\delta x} \\ \frac{\delta r}{\delta y} & \frac{\delta s}{\delta y} \end{pmatrix} \begin{pmatrix} \frac{\delta N_i}{\delta r} \\ \frac{\delta N_i}{\delta s} \end{pmatrix} = \xi \cdot \begin{pmatrix} \frac{\delta y}{\delta s} & -\frac{\delta y}{\delta r} \\ -\frac{\delta x}{\delta s} & \frac{\delta x}{\delta r} \end{pmatrix} \begin{pmatrix} \frac{\delta N_i}{\delta r} \\ \frac{\delta N_i}{\delta s} \end{pmatrix} = \xi \cdot \begin{pmatrix} \frac{\delta y}{\delta s} \cdot \frac{\delta N_i}{\delta r} - \frac{\delta y}{\delta r} \cdot \frac{\delta N_i}{\delta s} \\ \frac{\delta x}{\delta r} \cdot \frac{\delta N_i}{\delta s} - \frac{\delta x}{\delta s} \cdot \frac{\delta N_i}{\delta r} \end{pmatrix}$$

$$\begin{pmatrix} \frac{\delta N_1}{\delta x} \\ \frac{\delta N_1}{\delta y} \end{pmatrix} = \xi \cdot \begin{bmatrix} \left[\sum_{i=1}^4 \frac{s_i \cdot (1 + r \cdot r_{s_i,0})}{4} \cdot y_i \right] \cdot \frac{r_{s_i,0} \cdot (1 + s \cdot r_{s_i,1})}{4} - \left[\sum_{i=1}^4 \frac{r_i \cdot (1 + s \cdot r_{s_i,1})}{4} \cdot y_i \right] \cdot \frac{r_{s_i,1} \cdot (1 + r \cdot r_{s_i,0})}{4} \\ \left[\sum_{i=1}^4 \frac{r_i \cdot (1 + s \cdot r_{s_i,1})}{4} \cdot x_i \right] \cdot \frac{r_{s_i,1} \cdot (1 + r \cdot r_{s_i,0})}{4} - \left[\sum_{i=1}^4 \frac{s_i \cdot (1 + r \cdot r_{s_i,0})}{4} \cdot x_i \right] \cdot \frac{r_{s_i,0} \cdot (1 + s \cdot r_{s_i,1})}{4} \end{bmatrix}$$

with $\xi = \frac{8}{\left[(y_4 - y_1) \cdot (x_3 - x_2) - (y_3 - y_2) \cdot (x_4 - x_1) \right] \cdot s + \left[(y_2 - y_1) \cdot (x_4 - x_3) - (y_4 - y_3) \cdot (x_2 - x_1) \right] \cdot r + \left[(y_4 - y_2) \cdot (x_3 - x_1) - (y_3 - y_1) \cdot (x_4 - x_2) \right]}$

Substitute partial derivatives of the coordinates, we'll have:

$$\begin{pmatrix} \frac{\delta N_1}{\delta x} \\ \frac{\delta N_1}{\delta y} \end{pmatrix} = \frac{\xi}{4} \begin{bmatrix} \left[(1-r) \cdot (y_4 - y_1) + (1+r) \cdot (y_3 - y_2) \right] \left(\frac{\delta N_1}{\delta r} \right) - \left[(1-s) \cdot (y_2 - y_1) - (1+s) \cdot (y_4 - y_3) \right] \left(\frac{\delta N_1}{\delta s} \right) \\ \left[(1-s) \cdot (x_2 - x_1) - (1+s) \cdot (x_4 - x_3) \right] \left(\frac{\delta N_1}{\delta s} \right) - \left[(1-r) \cdot (x_4 - x_1) + (1+r) \cdot (x_3 - x_2) \right] \left(\frac{\delta N_1}{\delta r} \right) \end{bmatrix}$$

where $\frac{\delta N_1}{\delta r} = -\frac{1-s}{4}$ $\frac{\delta N_2}{\delta r} = \frac{1-s}{4}$ $\frac{\delta N_3}{\delta r} = \frac{1+s}{4}$ $\frac{\delta N_4}{\delta r} = -\frac{1+s}{4}$
 $\frac{\delta N_1}{\delta s} = -\frac{1-r}{4}$ $\frac{\delta N_2}{\delta s} = -\frac{1+r}{4}$ $\frac{\delta N_3}{\delta s} = \frac{1+r}{4}$ $\frac{\delta N_4}{\delta s} = \frac{1-r}{4}$

Solve for partial derivative of shape functions with respect to global coordinates (x, y):

$$\begin{aligned} \frac{\delta N_1}{\delta x} &= \frac{\xi}{4} \cdot \left[\left[(1-r) \cdot (y_4 - y_1) + (1+r) \cdot (y_3 - y_2) \right] \cdot \left(-\frac{1-s}{4} \right) - \left[(1-s) \cdot (y_2 - y_1) - (1+s) \cdot (y_4 - y_3) \right] \cdot \left(-\frac{1-r}{4} \right) \right] \\ \frac{\delta N_2}{\delta x} &= \frac{\xi}{4} \cdot \left[\left[(1-r) \cdot (y_4 - y_1) + (1+r) \cdot (y_3 - y_2) \right] \cdot \left(\frac{1-s}{4} \right) - \left[(1-s) \cdot (y_2 - y_1) - (1+s) \cdot (y_4 - y_3) \right] \cdot \left(-\frac{1+r}{4} \right) \right] \\ \frac{\delta N_3}{\delta x} &= \frac{\xi}{4} \cdot \left[\left[(1-r) \cdot (y_4 - y_1) + (1+r) \cdot (y_3 - y_2) \right] \cdot \left(\frac{1+s}{4} \right) - \left[(1-s) \cdot (y_2 - y_1) - (1+s) \cdot (y_4 - y_3) \right] \cdot \left(\frac{1+r}{4} \right) \right] \\ \frac{\delta N_4}{\delta x} &= \frac{\xi}{4} \cdot \left[\left[(1-r) \cdot (y_4 - y_1) + (1+r) \cdot (y_3 - y_2) \right] \cdot \left(-\frac{1+s}{4} \right) - \left[(1-s) \cdot (y_2 - y_1) - (1+s) \cdot (y_4 - y_3) \right] \cdot \left(\frac{1-r}{4} \right) \right] \\ \frac{\delta N_1}{\delta y} &= \frac{\xi}{4} \cdot \left[\left[(1-s) \cdot (x_2 - x_1) - (1+s) \cdot (x_4 - x_3) \right] \cdot \left(-\frac{1-r}{4} \right) - \left[(1-r) \cdot (x_4 - x_1) + (1+r) \cdot (x_3 - x_2) \right] \cdot \left(-\frac{1-s}{4} \right) \right] \\ \frac{\delta N_2}{\delta y} &= \frac{\xi}{4} \cdot \left[\left[(1-s) \cdot (x_2 - x_1) - (1+s) \cdot (x_4 - x_3) \right] \cdot \left(-\frac{1+r}{4} \right) - \left[(1-r) \cdot (x_4 - x_1) + (1+r) \cdot (x_3 - x_2) \right] \cdot \left(\frac{1-s}{4} \right) \right] \\ \frac{\delta N_3}{\delta y} &= \frac{\xi}{4} \cdot \left[\left[(1-s) \cdot (x_2 - x_1) - (1+s) \cdot (x_4 - x_3) \right] \cdot \left(\frac{1+r}{4} \right) - \left[(1-r) \cdot (x_4 - x_1) + (1+r) \cdot (x_3 - x_2) \right] \cdot \left(\frac{1+s}{4} \right) \right] \\ \frac{\delta N_4}{\delta y} &= \frac{\xi}{4} \cdot \left[\left[(1-s) \cdot (x_2 - x_1) - (1+s) \cdot (x_4 - x_3) \right] \cdot \left(\frac{1-r}{4} \right) - \left[(1-r) \cdot (x_4 - x_1) + (1+r) \cdot (x_3 - x_2) \right] \cdot \left(-\frac{1+s}{4} \right) \right] \end{aligned}$$

Partial derivatives of shape function can be simplified to:

$$\begin{aligned} \frac{\delta N_1}{\delta x} &= \frac{\xi}{8} \cdot \left[(y_4 - y_3) \cdot r + (y_3 - y_2) \cdot s - (y_4 - y_2) \right] & \frac{\delta N_1}{\delta y} &= \frac{\xi}{8} \cdot \left[-(x_4 - x_3) \cdot r - (x_3 - x_2) \cdot s + (x_4 - x_2) \right] \\ \frac{\delta N_2}{\delta x} &= \frac{\xi}{8} \cdot \left[-(y_4 - y_3) \cdot r - (y_4 - y_1) \cdot s + (y_3 - y_1) \right] & \frac{\delta N_2}{\delta y} &= \frac{\xi}{8} \cdot \left[(x_4 - x_3) \cdot r + (x_4 - x_1) \cdot s - (x_3 - x_1) \right] \end{aligned}$$

$$\frac{\delta N_3}{\delta x} = \frac{\xi}{8} [-(y_2 - y_1)r + (y_4 - y_1)s + (y_4 - y_2)]$$

$$\frac{\delta N_3}{\delta y} = \frac{\xi}{8} [(x_2 - x_1)r - (x_4 - x_1)s - (x_4 - x_2)]$$

$$\frac{\delta N_4}{\delta x} = \frac{\xi}{8} [(y_2 - y_1)r - (y_3 - y_2)s - (y_3 - y_1)]$$

$$\frac{\delta N_4}{\delta y} = \frac{\xi}{8} [-(x_2 - x_1)r + (x_3 - x_2)s + (x_3 - x_1)]$$

Recall from the definition of Cauchy's infinitesimal strains in deformed configuration (Eulerian based)

$$\epsilon_x = \frac{\delta u}{\delta x} = \frac{\delta N_1}{\delta x} \cdot u_1 + \frac{\delta N_2}{\delta x} \cdot u_2 + \frac{\delta N_3}{\delta x} \cdot u_3 + \frac{\delta N_4}{\delta x} \cdot u_4 \quad \epsilon_y = \frac{\delta v}{\delta y} = \frac{\delta N_1}{\delta y} \cdot v_1 + \frac{\delta N_2}{\delta y} \cdot v_2 + \frac{\delta N_3}{\delta y} \cdot v_3 + \frac{\delta N_4}{\delta y} \cdot v_4$$

$$\gamma_{xy} = \frac{\delta u}{\delta y} + \frac{\delta v}{\delta x} = \frac{\delta N_1}{\delta y} \cdot u_1 + \frac{\delta N_1}{\delta x} \cdot v_1 + \frac{\delta N_2}{\delta y} \cdot u_2 + \frac{\delta N_2}{\delta x} \cdot v_2 + \frac{\delta N_3}{\delta y} \cdot u_3 + \frac{\delta N_3}{\delta x} \cdot v_3 + \frac{\delta N_4}{\delta y} \cdot u_4 + \frac{\delta N_4}{\delta x} \cdot v_4$$

Degenerate Cauchy's infinitesimal case for a rectangular element with edges a and b parallel to x and y axes and center at (0, 0)

Define coordinates and mapping from (r, s) to (x, y):

$$y_1 = y_2 = -b \quad y_3 = y_4 = b \quad x_1 = x_4 = -a \quad x_2 = x_3 = a$$

where

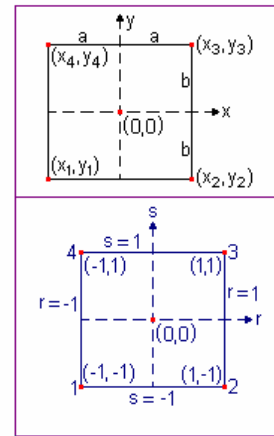
$$x_4 - x_1 = x_3 - x_2 = y_4 - y_3 = y_2 - y_1 = 0$$

$$x_3 - x_4 = x_2 - x_1 = x_3 - x_1 = x_2 - x_4 = 2a$$

$$y_4 - y_1 = y_4 - y_2 = y_3 - y_1 = y_3 - y_2 = 2b$$

$$\frac{s - (-1)}{2} = \frac{s + 1}{2} = \frac{y - (-b)}{2b} = \frac{y + b}{2b} \implies s = \left(1 + \frac{y}{b}\right) - 1 = \frac{y}{b}$$

$$\frac{r - (-1)}{2} = \frac{r + 1}{2} = \frac{x - (-a)}{2a} = \frac{x + a}{2a} \implies r = \left(1 + \frac{x}{a}\right) - 1 = \frac{x}{a}$$



"rectelem.bmp"

Define shape function parameters / derivatives:

$$\xi = \frac{8}{[(y_4 - y_1) \cdot (0) - (y_3 - y_2) \cdot (0)] \cdot s + [(0) \cdot (x_4 - x_3) - (0) \cdot (x_2 - x_1)] \cdot r + [(2b) \cdot (2a) - (2b) \cdot (-2a)]} = \frac{1}{a \cdot b}$$

$$\frac{\delta N_1}{\delta x} = \frac{\xi}{8} \cdot (2 \cdot b \cdot s - 2b) = \frac{s - 1}{4a} = \frac{-1}{4a} \left(1 - \frac{y}{b}\right)$$

$$\frac{\delta N_1}{\delta y} = \frac{\xi}{8} \cdot (2 \cdot a \cdot r - 2a) = \frac{r - 1}{4b} = \frac{-1}{4b} \left(1 - \frac{x}{a}\right)$$

$$\frac{\delta N_2}{\delta x} = \frac{\xi}{8} \cdot (-2 \cdot b \cdot s + 2b) = \frac{1 - s}{4a} = \frac{1}{4a} \left(1 - \frac{y}{b}\right)$$

$$\frac{\delta N_2}{\delta y} = \frac{\xi}{8} \cdot (-2 \cdot a \cdot r - 2a) = \frac{-(r + 1)}{4b} = \frac{-1}{4b} \left(1 + \frac{x}{a}\right)$$

$$\frac{\delta N_3}{\delta x} = \frac{\xi}{8} \cdot (2 \cdot b \cdot s + 2b) = \frac{s + 1}{4a} = \frac{1}{4a} \left(1 + \frac{y}{b}\right)$$

$$\frac{\delta N_3}{\delta y} = \frac{\xi}{8} \cdot (2 \cdot a \cdot r + 2a) = \frac{r + 1}{4b} = \frac{1}{4b} \left(1 + \frac{x}{a}\right)$$

$$\frac{\delta N_4}{\delta x} = \frac{\xi}{8} \cdot (-2 \cdot b \cdot s - 2b) = \frac{-(s + 1)}{4a} = \frac{-1}{4a} \left(1 + \frac{y}{b}\right)$$

$$\frac{\delta N_4}{\delta y} = \frac{\xi}{8} \cdot [-(2 \cdot a) \cdot r + 2a] = \frac{1 - r}{4b} = \frac{1}{4b} \left(1 - \frac{x}{a}\right)$$

Define strains in terms of shape function and parametric coordinates:

$$\epsilon_x = \frac{\delta u}{\delta x} = \frac{\delta N_1}{\delta x} \cdot u_1 + \frac{\delta N_2}{\delta x} \cdot u_2 + \frac{\delta N_3}{\delta x} \cdot u_3 + \frac{\delta N_4}{\delta x} \cdot u_4 \quad \epsilon_y = \frac{\delta v}{\delta y} = \frac{\delta N_1}{\delta y} \cdot v_1 + \frac{\delta N_2}{\delta y} \cdot v_2 + \frac{\delta N_3}{\delta y} \cdot v_3 + \frac{\delta N_4}{\delta y} \cdot v_4$$

$$\gamma_{xy} = \frac{\delta u}{\delta y} + \frac{\delta v}{\delta x} = \frac{\delta N_1}{\delta y} \cdot u_1 + \frac{\delta N_1}{\delta x} \cdot v_1 + \frac{\delta N_2}{\delta y} \cdot u_2 + \frac{\delta N_2}{\delta x} \cdot v_2 + \frac{\delta N_3}{\delta y} \cdot u_3 + \frac{\delta N_3}{\delta x} \cdot v_3 + \frac{\delta N_4}{\delta y} \cdot u_4 + \frac{\delta N_4}{\delta x} \cdot v_4$$

Substitute into Cauchy's infinitesimal strain equations, we'll have the Rathje - Chang expressions

$$\varepsilon_x = \frac{1}{4a} \left[-\left(1 - \frac{y}{b}\right) \cdot u_1 + \left(1 - \frac{y}{b}\right) \cdot u_2 + \left(1 + \frac{y}{b}\right) \cdot u_3 - \left(1 + \frac{y}{b}\right) \cdot u_4 \right]$$

$$\varepsilon_y = \frac{1}{4b} \left[-\left(1 - \frac{x}{a}\right) \cdot v_1 - \left(1 + \frac{x}{a}\right) \cdot v_2 + \left(1 + \frac{x}{a}\right) \cdot v_3 + \left(1 - \frac{x}{a}\right) \cdot v_4 \right]$$

$$\gamma_{xy} = \frac{1}{4} \cdot \left[\frac{1}{a} \cdot \left[-\left(1 - \frac{y}{b}\right) \cdot v_1 + \left(1 - \frac{y}{b}\right) \cdot v_2 + \left(1 + \frac{y}{b}\right) \cdot v_3 - \left(1 + \frac{y}{b}\right) \cdot v_4 \right] \dots \right. \\ \left. + \frac{1}{b} \cdot \left[-\left(1 - \frac{x}{a}\right) \cdot u_1 - \left(1 + \frac{x}{a}\right) \cdot u_2 + \left(1 + \frac{x}{a}\right) \cdot u_3 + \left(1 - \frac{x}{a}\right) \cdot u_4 \right] \right]$$

Appendix D Baseline Tri-Level Model

This section presents the LS-DYNA control decks used for the baseline tri-level sequential blasting model. The control deck consists of operation commands and instructions for LS-DYNA to perform the appropriate analysis tasks. It is also a driver for the geometry deck. Details and descriptions of the commands and instructions used in the deck listed below are presented in the LS-DYNA Version 970 Keyword Manual (Hallquist, 2003).

The baseline blast-induced liquefaction model consists of modularized input decks driven by the corresponding control deck. Input modules include a soil material property deck called `soilmat.dyn`, a soil geometry input file called `soil3.dyn`, and a file called `siginit.dyn`, which describes the initial stress state within the soil mass due to gravity at time zero (i.e. prior to blasts).

There are two control decks for the baseline blast-induced liquefaction analysis involving the simulation of material phase change process (i.e. from solid soil particles to liquid or water). The LS-DYNA full restart with material property altering capabilities was utilized to provide a quarter sine-pulse material transitioning simulation of solid to liquid bulk behaviors.

Listed below is the initial run control deck (`ctrl.dyn`), followed by the restart control deck (`rectrl.dyn`).

```

$---+---1---+---2---+---3---+---4---+---5---+---6---+---7---+---8
$ ctrl.dyn - initial run control deck - ls-dyna
$---+---1---+---2---+---3---+---4---+---5---+---6---+---7---+---8
*KEYWORD 3000000
$---+---1---+---2---+---3---+---4---+---5---+---6---+---7---+---8
$ include soil material properties
$---+---1---+---2---+---3---+---4---+---5---+---6---+---7---+---8
*INCLUDE
soilmat.dyn
$*CONTROL_STRUCTURED_TERM
$---+---1---+---2---+---3---+---4---+---5---+---6---+---7---+---8
*TITLE
May 2005 Vancouver Blast
$---+---1---+---2---+---3---+---4---+---5---+---6---+---7---+---8
*CONTROL_TERMINATION
0.1999
*CONTROL_TIMESTEP
1.000E-03 0.500
*CONTROL_CONTACT
0.500 0.0 2 0 4 0 1 1
0 0 1 1 10.000 0 0
*CONTROL_ENERGY
2 2 1 1
*CONTROL_PARALLEL
$ NCPU NUMRHS CONST PARA
2 2 1 1
$---+---1---+---2---+---3---+---4---+---5---+---6---+---7---+---8
$ NOTE: ALE is not used in final analysis to reduce run time and numerical
$ errors due to material instabilities
$---+---1---+---2---+---3---+---4---+---5---+---6---+---7---+---8
$*CONTROL_ALE
$ DCT NADV METH AFAC BFAC CFAC DFAC EFAC
$ 3 1 2 -1.0 0.0 0.0 0.0
0.0
$ START END AAFAC VFACT PRIT EBC PREF NSIDEBC
$ 0.000 1.000E+20 1.0 1.000E-06 0.0 0 0.0
$---+---1---+---2---+---3---+---4---+---5---+---6---+---7---+---8
$*ALE_REFERENCE_SYSTEM_GROUP
$ SID STYPE RPTYPE PRID BCTRAN BCEXP BCROT ICOORD
$ 1 0 1 1 0 0 0
0
$ XC YC ZC EXPLIM EFAC
$ 0.000000 0.000000 0.000000 1.200E+00 0.5
$
$*ALE_REFERENCE_SYSTEM_GROUP
$ SID STYPE RPTYPE PRID BCTRAN BCEXP BCROT ICOORD
$ 2 0 1 1 0 0 0
0
$ XC YC ZC EXPLIM EFAC
$ 0.000000 0.000000 0.000000 1.200E+00 0.5
$---+---1---+---2---+---3---+---4---+---5---+---6---+---7---+---8
$*SECTION_SOLID_ALE
$ SECID ELFORM AET
$ 1 5
$ AFAC BFAC CFAC DFAC START END AAFAC
$ -1.000000 0.000000 0.000000 0.000000 0.000000 1.00E+20 1.000000
*SECTION_SOLID
1 1
$---+---1---+---2---+---3---+---4---+---5---+---6---+---7---+---8
*SET_PART_LIST
1
1 2 3 4 5 6 7 8
9 10 35 36 37 38 39 40

```

```

$
*SET_PART_LIST
  2
    11      12      13      14      15      16      17      18
    19      20      21      22      23      24      25      26
    27      28      29      30      31      32      33      34
$---+---1---+---2---+---3---+---4---+---5---+---6---+---7---+---8
$*CONTROL_EXPLOSIVE_SHADOW
*DATABASE_BINARY_D3PLOT
  1.000E-02
*DATABASE_BINARY_D3DUMP
  2.000E-01
$---+---1---+---2---+---3---+---4---+---5---+---6---+---7---+---8
$ curve data not used
*DEFINE_CURVE
  102      0  1.000000  1.000000  0.000000  0.000000      0
$ blast 1
  0.0000000000000000      1.000E+00
  100.0000000000000000      1.000E+00
*DEFINE_CURVE
  103      0  1.000000  1.000000  0.000000  0.000000      0
$ blast 1
  0.0000000000000000      1.000E+00
  100.0000000000000000      1.000E+00
$---+---1---+---2---+---3---+---4---+---5---+---6---+---7---+---8
*DATABASE_TRHIST
  1.000E-03      1
*DATABASE_TRACER
$
$ PPT 859105 (N) - 38' depth
$0.000E+00      1  30.00000  0.000000 -456.0000
$ rotated 22.5 deg
  0.000E+00      1  27.71640  11.48050 -456.0000
$
$ PPT 883032 (S) - 31' depth
$0.000E+00      1 -30.00000  0.0000000 -372.0000
$ rotated 22.5 deg
  0.000E+00      1 -27.71640 -11.48050 -372.0000
$
$ PPT 859120 (W) - 45' depth
$0.000E+00      1  0.000000  30.00000 -540.0000
$ rotated 22.5 deg
  0.000E+00      1 -11.48050  27.71640 -540.0000
$
$ PPT 859215 (E) - 18' depth
$0.000E+00      1  0.000000 -30.00000 -216.0000
$ rotated 22.5 deg
  0.000E+00      1  11.48050 -27.71640 -216.0000
$
$ PPT 856610 (C) - 25' depth
$0.000E+00      1  0.000000  0.000000 -300.0000
$ rotated 22.5 deg
  0.000E+00      1  0.000000  0.000000 -300.0000
$ accelerometers (NW, NE, SW, SE)
  0.000E+00      1  18.36880  44.34620 -300.0000
  0.000E+00      1  44.34620 -18.36880 -300.0000
  0.000E+00      1 -44.34620  18.36880 -300.0000
  0.000E+00      1 -18.36880 -44.34620 -300.0000
$
$0.000E+00      1  33.94113  33.94113 -300.0000
$0.000E+00      1  33.94113 -33.94113 -300.0000
$0.000E+00      1 -33.94113  33.94113 -300.0000
$0.000E+00      1 -33.94113 -33.94113 -300.0000

```

```

$---+---1---+---2---+---3---+---4---+---5---+---6---+---7---+---8
*HOURGLASS
$      HGID      IHQ      QM      IBQ      Q2      Q1      QB      QW
      1          5          0.10
      2          3          0.10
$---+---1---+---2---+---3---+---4---+---5---+---6---+---7---+---8
$ top sand
*PART
  PART PID = 1
$      PID      SID      MID      EOSID      HGID
      1          1          6          EOSID      2
$ clay
*PART
  PART PID = 2
      2          1          5          2
$ sand
*PART
  PART PID = 3
      3          1          3          2
$ gravel
*PART
  PART PID = 4
      4          1          4          2
$ water / air / gravel
*PART
  PART PID = 5
      5          1          7          2
$      5          1          8          3          2
$---+---1---+---2---+---3---+---4---+---5---+---6---+---7---+---8
$ top sand
*PART
  PART PID = 6
$      PID      SID      MID      EOSID      HGID
      6          1          6          EOSID      2
$ clay
*PART
  PART PID = 7
      7          1          5          2
$ sand
*PART
  PART PID = 8
      8          1          3          2
$ gravel
*PART
  PART PID = 9
      9          1          4          2
$ water / air / gravel
*PART
  PART PID = 10
      10         1          7          2
$      10         1          8          3          2
$---+---1---+---2---+---3---+---4---+---5---+---6---+---7---+---8
$ explosives
*PART
  PART PID = 11
$      PID      SID      MID      EOSID      HGID
      11         1          2          2          2
$
*PART
  PART PID = 12
      12         1          2          2          2
$
*PART

```

	PART PID = 13				
	13	1	2	2	2
\$					
*PART					
	PART PID = 14				
	14	1	2	2	2
\$					
*PART					
	PART PID = 15				
	15	1	2	2	2
\$					
*PART					
	PART PID = 16				
	16	1	2	2	2
\$					
*PART					
	PART PID = 17				
	17	1	2	2	2
\$					
*PART					
	PART PID = 18				
	18	1	4		2
\$					
*PART					
	PART PID = 19				
	19	1	2	2	2
\$					
*PART					
	PART PID = 20				
	20	1	2	2	2
\$					
*PART					
	PART PID = 21				
	21	1	2	2	2
\$					
*PART					
	PART PID = 22				
	22	1	2	2	2
\$					
*PART					
	PART PID = 23				
	23	1	2	2	2
\$					
*PART					
	PART PID = 24				
	24	1	2	2	2
\$					
*PART					
	PART PID = 25				
	25	1	2	2	2
\$					
*PART					
	PART PID = 26				
	26	1	4		2
\$					
*PART					
	PART PID = 27				
	27	1	2	2	2
\$					
*PART					
	PART PID = 28				
	28	1	2	2	2
\$					


```

*PART
  PART PID = 29
    29      1      2      2      2
$
*PART
  PART PID = 30
    30      1      2      2      2
$
*PART
  PART PID = 31
    31      1      2      2      2
$
*PART
  PART PID = 32
    32      1      2      2      2
$
*PART
  PART PID = 33
    33      1      2      2      2
$
*PART
  PART PID = 34
    34      1      4      2
$---+---1---+---2---+---3---+---4---+---5---+---6---+---7---+---8
$ sand
*PART
  PART PID = 35
    35      1      8      2
$ sand
*PART
  PART PID = 36
    36      1      8      2
$ sand
*PART
  PART PID = 37
    37      1      9      2
$ sand
*PART
  PART PID = 38
    38      1      9      2
$ sand
*PART
  PART PID = 39
    39      1     10      2
$ sand
*PART
  PART PID = 40
    40      1     10      2
$ sand
*PART
  PART PID = 41
    41      1     11      2
$ sand
*PART
  PART PID = 42
    42      1     11      2
$---+---1---+---2---+---3---+---4---+---5---+---6---+---7---+---8
$ Air
*MAT_NULL
  1 1.148E-07 -14.69590 2.901E-09
$ Air
*EOS_LINEAR_POLYNOMIAL
  1 0.000E+00 2.104E+01 0.000E+00 0.000E+00 0.000E+00 0.000E+00 0.000E+00

```

```

0.000E+00 1.000E+00
$-----1-----2-----3-----4-----5-----6-----7-----8
$ explosive hydro-dynamic properties
*MAT_HIGH_EXPLOSIVE_BURN
$      MID      RHO      D      PCJ      BETA      K      G      SIGY
$ Pentolite (Pentex)
      2 1.572E-04 2.965E+05 3.698E+06      0.0000 1.000E+06 1.000E+05 1.000E+04
*EOS_JWL
$      EOSID      A      B      R1      R2      OMEGA      E0      V0
$ Pentolite (Pentex)
      2 7.846E+07 1.359E+06      4.5000      1.1000      0.3500 1.175E+06 1.000E+00
$-----1-----2-----3-----4-----5-----6-----7-----8
$ Initiate at bottom of explosive
*INITIAL_DETONATION
$      PID      X      Y      Z      LT
      11 180.0000 0.000000 -390.0000 0.0000000
      15 -180.0000 0.000000 -390.0000 0.2000000
      13 0.000000 180.0000 -390.0000 0.4000000
      17 0.000000 -180.0000 -390.0000 0.6000000
      14 -127.2792 127.2792 -390.0000 0.8000000
      16 -127.2792 -127.2792 -390.0000 1.0000000
      12 127.2792 127.2792 -390.0000 1.2000000
$      18 127.2792 -127.2792 -390.0000 1.4000000
$
      19 180.0000 0.000000 -330.0000 1.4000000
      23 -180.0000 0.000000 -330.0000 1.6000000
      21 0.000000 180.0000 -330.0000 1.8000000
      25 0.000000 -180.0000 -330.0000 2.0000000
      22 -127.2792 127.2792 -330.0000 2.2000000
      24 -127.2792 -127.2792 -330.0000 2.4000000
      20 127.2792 127.2792 -330.0000 2.6000000
$      26 127.2792 -127.2792 -330.0000 2.8000000
$
      27 180.0000 0.000000 -246.0000 2.8000000
      31 -180.0000 0.000000 -246.0000 3.0000000
      29 0.000000 180.0000 -246.0000 3.2000000
      33 0.000000 -180.0000 -246.0000 3.4000000
      30 -127.2792 127.2792 -246.0000 3.6000000
      32 -127.2792 -127.2792 -246.0000 3.8000000
      28 127.2792 127.2792 -246.0000 4.0000000
$      34 127.2792 -127.2792 -246.0000 4.2000000
$
$-----1-----2-----3-----4-----5-----6-----7-----8
$ semi-infinite (continuum) boundary (dilatational / shear waves: 0 to turn on)
$ to model half space (DYNA generates proper impedance function at boundary)
*BOUNDARY_NON_REFLECTING
$      SSID      AD      AS
      1      0.0      0.0
      2      0.0      0.0
$-----1-----2-----3-----4-----5-----6-----7-----8
$ symmetry boundary along oblique plane - not needed for full model
*$DEFINE_COORDINATE_SYSTEM
$      CID      X0      Y0      Z0      XX      YX      ZX
$      1      0.0      0.0      0.0      1.0      0.0      -1.0
$      X_XY_PL      Y_XY_PL      Z_XY_PL
$      0.0      1.0      0.0
$
*$BOUNDARY_SPC_SET
$      NSID      CID      DOFX      DOFY      DOFZ      DOFRX      DOFRY      DOFRZ
$      1      1      0      0      1      1      1      0
$-----1-----2-----3-----4-----5-----6-----7-----8
*$LOAD_BODY_Z
$      LCID      SF      LCIDDR      XC      YC      ZC

```

```

$      201      386.088
$*DEFINE_CURVE
$      201      0      1.000000      1.000000      0.000000      0.000000      0
$      0.0000000      1.0000000
$      1000.0000000      1.0000000
$---+---1---+---2---+---3---+---4---+---5---+---6---+---7---+---8
$ include 3-D soil material geometry deck
*INCLUDE
soil3.dyn
$---+---1---+---2---+---3---+---4---+---5---+---6---+---7---+---8
$ initial stresses due to gravity as computed by ANSYS implicit analysis
$ using the same 3-D model for a one to one mapping
*INCLUDE
siginit.dyn
$---+---1---+---2---+---3---+---4---+---5---+---6---+---7---+---8
*END

```

The corresponding LS-DYNA analysis “full-restart” control deck used for the baseline model in this research is listed below.

```

$---+---1---+---2---+---3---+---4---+---5---+---6---+---7---+---8
$ rectrl.dyn - analysis restart control deck - ls-dyna
$---+---1---+---2---+---3---+---4---+---5---+---6---+---7---+---8
*KEYWORD 30000000
*STRESS_INITIALIZATION
*INCLUDE
soilmat.dyn
$*CONTROL_STRUCTURED_TERM
$---+---1---+---2---+---3---+---4---+---5---+---6---+---7---+---8
*TITLE
May 2005 Vancouver Blast
$---+---1---+---2---+---3---+---4---+---5---+---6---+---7---+---8
*CONTROL_TIMESTEP
1.000E-03      0.500
*CONTROL_CONTACT
0.500      0.0      2      0      4      0      1      1
0      0      1      1      10.000      0      0
*CONTROL_ENERGY
2      2      1      1
*CONTROL_PARALLEL
$      NCPU      NUMRHS      CONST      PARA
2      2      1      1
$---+---1---+---2---+---3---+---4---+---5---+---6---+---7---+---8
$ NOTE: ALE is not used in final analysis to reduce run time and numerical
$ errors due to material instabilities
$---+---1---+---2---+---3---+---4---+---5---+---6---+---7---+---8
$*CONTROL_ALE
$      DCT      NADV      METH      AFAC      BFAC      CFAC      DFAC      EFAC
$      3      1      2      -1.0      0.0      0.0      0.0
0.0
$      START      END      AAFAC      VFACT      PRIT      EBC      PREF      NSIDEB
$      0.000      1.000E+20      1.0      1.000E-06      0.0      0      0.0
$---+---1---+---2---+---3---+---4---+---5---+---6---+---7---+---8
$*ALE_REFERENCE_SYSTEM_GROUP
$      SID      STYPE      RPTYPE      PRID      BCTAN      BCEXP      BCROT      ICOOR

```

```

$      1      0      1      1      0      0      0
0
$      XC      YC      ZC      EXPLIM      EFAC
$ 0.000000  0.000000  0.000000  1.200E+00      0.5
$
$*ALE_REFERENCE_SYSTEM_GROUP
$      SID      STYPE      RPTYPE      PRID      BCTRAN      BCEXP      BCROT      ICOORD
$      2      0      1      1      0      0      0
0
$      XC      YC      ZC      EXPLIM      EFAC
$ 0.000000  0.000000  0.000000  1.200E+00      0.5
$---+---1---+---2---+---3---+---4---+---5---+---6---+---7---+---8
$*SECTION_SOLID_ALE
$      SECID      ELFORM      AET
$      1      5
$      AFAC      BFAC      CFAC      DFAC      START      END      AAFAC
$ -1.000000  0.000000  0.000000  0.000000  0.000000  1.00E+20  1.000000
*SECTION_SOLID
      1      1
$---+---1---+---2---+---3---+---4---+---5---+---6---+---7---+---8
*SET_PART_LIST
      1
      1      2      3      4      5      6      7      8
      9      10     35     36     37     38     39     40
$
*SET_PART_LIST
      2
      11     12     13     14     15     16     17     18
      19     20     21     22     23     24     25     26
      27     28     29     30     31     32     33     34
$---+---1---+---2---+---3---+---4---+---5---+---6---+---7---+---8
$*CONTROL_EXPLOSIVE_SHADOW
*DATABASE_BINARY_D3PLOT
1.000E-02
*DATABASE_BINARY_D3DUMP
2.000E-01
$---+---1---+---2---+---3---+---4---+---5---+---6---+---7---+---8
$ curve data not used
*DEFINE_CURVE
      102      0  1.000000  1.000000  0.000000  0.000000      0
$ blast 1
      0.0000000000000000      1.000E+00
      100.0000000000000000      1.000E+00
*DEFINE_CURVE
      103      0  1.000000  1.000000  0.000000  0.000000      0
$ blast 1
      0.0000000000000000      1.000E+00
      100.0000000000000000      1.000E+00
$---+---1---+---2---+---3---+---4---+---5---+---6---+---7---+---8
*DATABASE_TRHIST
1.000E-03      1
*DATABASE_TRACER
$
$ PPT 859105 (N) - 38' depth
$0.000E+00      1  30.00000  0.000000 -456.0000
$ rotated 22.5 deg
0.000E+00      1  27.71640  11.48050 -456.0000
$
$ PPT 883032 (S) - 31' depth
$0.000E+00      1 -30.00000  0.000000 -372.0000
$ rotated 22.5 deg
0.000E+00      1 -27.71640 -11.48050 -372.0000
$
$

```

```

$ PPT 859120 (W) - 45' depth
$0.000E+00      1  0.000000  30.00000 -540.0000
$ rotated 22.5 deg
  0.000E+00      1 -11.48050  27.71640 -540.0000
$
$ PPT 859215 (E) - 18' depth
$0.000E+00      1  0.000000 -30.00000 -216.0000
$ rotated 22.5 deg
  0.000E+00      1  11.48050 -27.71640 -216.0000
$
$ PPT 856610 (C) - 25' depth
$0.000E+00      1  0.000000  0.000000 -300.0000
$ rotated 22.5 deg
  0.000E+00      1  0.000000  0.000000 -300.0000
$ accelerometers (NW, NE, SW, SE)
  0.000E+00      1  18.36880  44.34620 -300.0000
  0.000E+00      1  44.34620 -18.36880 -300.0000
  0.000E+00      1 -44.34620  18.36880 -300.0000
  0.000E+00      1 -18.36880 -44.34620 -300.0000
$
$0.000E+00      1  33.94113  33.94113 -300.0000
$0.000E+00      1  33.94113 -33.94113 -300.0000
$0.000E+00      1 -33.94113  33.94113 -300.0000
$0.000E+00      1 -33.94113 -33.94113 -300.0000
$-----1-----2-----3-----4-----5-----6-----7-----8
*HOURLASS
$      HGID      IHQ      QM      IBQ      Q2      Q1      QB      QW
      1      5      0.10
      2      3      0.10
$-----1-----2-----3-----4-----5-----6-----7-----8
$ top sand
*PART
  PART PID = 1
$      PID      SID      MID      EOSID      HGID
      1      1      6
$ clay
*PART
  PART PID = 2
      2      1      5      2
$ sand
*PART
  PART PID = 3
      3      1      3      2
$ gravel
*PART
  PART PID = 4
      4      1      4      2
$ water / air / gravel
*PART
  PART PID = 5
      5      1      7      2
$      5      1      8      3      2
$-----1-----2-----3-----4-----5-----6-----7-----8
$ top sand
*PART
  PART PID = 6
$      PID      SID      MID      EOSID      HGID
      6      1      6      2
$ clay
*PART
  PART PID = 7
      7      1      5      2
$ sand

```

```

*PART
  PART PID = 8
    8          1          3          2
$ gravel
*PART
  PART PID = 9
    9          1          4          2
$ water / air / gravel
*PART
  PART PID = 10
    10         1          7          2
$    10         1          8          3          2
$---+---1---+---2---+---3---+---4---+---5---+---6---+---7---+---8
$ explosives
*PART
  PART PID = 11
$    PID      SID      MID      EOSID      HGID
    11         1         2         2         2
$
*PART
  PART PID = 12
    12         1         2         2         2
$
*PART
  PART PID = 13
    13         1         2         2         2
$
*PART
  PART PID = 14
    14         1         2         2         2
$
*PART
  PART PID = 15
    15         1         2         2         2
$
*PART
  PART PID = 16
    16         1         2         2         2
$
*PART
  PART PID = 17
    17         1         2         2         2
$
*PART
  PART PID = 18
    18         1         4         2         2
$
*PART
  PART PID = 19
    19         1         2         2         2
$
*PART
  PART PID = 20
    20         1         2         2         2
$
*PART
  PART PID = 21
    21         1         2         2         2
$
*PART
  PART PID = 22
    22         1         2         2         2
$

```

```

*PART
  PART PID = 23
    23      1      2      2      2
$
*PART
  PART PID = 24
    24      1      2      2      2
$
*PART
  PART PID = 25
    25      1      2      2      2
$
*PART
  PART PID = 26
    26      1      4      2
$
*PART
  PART PID = 27
    27      1      2      2      2
$
*PART
  PART PID = 28
    28      1      2      2      2
$
*PART
  PART PID = 29
    29      1      2      2      2
$
*PART
  PART PID = 30
    30      1      2      2      2
$
*PART
  PART PID = 31
    31      1      2      2      2
$
*PART
  PART PID = 32
    32      1      2      2      2
$
*PART
  PART PID = 33
    33      1      2      2      2
$
*PART
  PART PID = 34
    34      1      4      2
$-----1-----2-----3-----4-----5-----6-----7-----8
$ sand
*PART
  PART PID = 35
    35      1      8      2
$ sand
*PART
  PART PID = 36
    36      1      8      2
$ sand
*PART
  PART PID = 37
    37      1      9      2
$ sand
*PART
  PART PID = 38

```

```

38          1          9          2
$ sand
*PART
PART PID = 39
39          1          10         2
$ sand
*PART
PART PID = 40
40          1          10         2
$ sand
*PART
PART PID = 41
41          1          11         2
$ sand
*PART
PART PID = 42
42          1          11         2
$---+---1---+---2---+---3---+---4---+---5---+---6---+---7---+---8
$ Air
*MAT_NULL
1 1.148E-07 -14.69590 2.901E-09
$ Air
*EOS_LINEAR_POLYNOMIAL
1 0.000E+00 2.104E+01 0.000E+00 0.000E+00 0.000E+00 0.000E+00 0.000E+00
0.000E+00 1.000E+00
$---+---1---+---2---+---3---+---4---+---5---+---6---+---7---+---8
$ explosive hydro-dynamic properties
*MAT_HIGH_EXPLOSIVE_BURN
$ MID RHO D PCJ BETA K G SIGY
$ Pentolite (Pentex)
2 1.572E-04 2.965E+05 3.698E+06 0.0000 1.000E+06 1.000E+05 1.000E+04
*EOS_JWL
$ EOSID A B R1 R2 OMEGA E0 V0
$ Pentolite (Pentex)
2 7.846E+07 1.359E+06 4.5000 1.1000 0.3500 1.175E+06 1.000E+00
$---+---1---+---2---+---3---+---4---+---5---+---6---+---7---+---8
$ Initiate at bottom of explosive
*INITIAL_DETONATION
$ PID X Y Z LT
11 180.0000 0.000000 -390.0000 0.000000
15 -180.0000 0.000000 -390.0000 0.200000
13 0.000000 180.0000 -390.0000 0.400000
17 0.000000 -180.0000 -390.0000 0.600000
14 -127.2792 127.2792 -390.0000 0.800000
16 -127.2792 -127.2792 -390.0000 1.000000
12 127.2792 127.2792 -390.0000 1.200000
$ 18 127.2792 -127.2792 -390.0000 1.400000
$
19 180.0000 0.000000 -330.0000 1.400000
23 -180.0000 0.000000 -330.0000 1.600000
21 0.000000 180.0000 -330.0000 1.800000
25 0.000000 -180.0000 -330.0000 2.000000
22 -127.2792 127.2792 -330.0000 2.200000
24 -127.2792 -127.2792 -330.0000 2.400000
20 127.2792 127.2792 -330.0000 2.600000
$ 26 127.2792 -127.2792 -330.0000 2.800000
$
27 180.0000 0.000000 -246.0000 2.800000
31 -180.0000 0.000000 -246.0000 3.000000
29 0.000000 180.0000 -246.0000 3.200000
33 0.000000 -180.0000 -246.0000 3.400000
30 -127.2792 127.2792 -246.0000 3.600000
32 -127.2792 -127.2792 -246.0000 3.800000

```



```

28 127.2792 127.2792 -246.0000 4.0000000
$ 34 127.2792 -127.2792 -246.0000 4.2000000
$
$---+---1---+---2---+---3---+---4---+---5---+---6---+---7---+---8
$ semi-infinite (continuum) boundary (dilatational / shear waves: 0 to turn on)
$ to model half space (DYNA generates proper impedance function at boundary)
*BOUNDARY_NON_REFLECTING
$  SSID      AD      AS
$    1      0.0    0.0
$    2      0.0    0.0
$---+---1---+---2---+---3---+---4---+---5---+---6---+---7---+---8
$ symmetry boundary along oblique plane - not needed for full model
*$DEFINE_COORDINATE_SYSTEM
$  CID      X0      Y0      Z0      XX      YX      ZX
$    1      0.0    0.0    0.0    1.0    0.0   -1.0
$  X_XY_PL  Y_XY_PL  Z_XY_PL
$    0.0    1.0    0.0
$
$
*$BOUNDARY_SPC_SET
$  NSID     CID     DOFX     DOFY     DOFZ     DOFRX     DOFRY     DOFRZ
$    1      1      0        0        1        1        1        0
$---+---1---+---2---+---3---+---4---+---5---+---6---+---7---+---8
*$LOAD_BODY_Z
$  LCID     SF     LCIDDR     XC     YC     ZC
$    201    386.088
*$DEFINE_CURVE
$    201     0  1.000000  1.000000  0.000000  0.000000  0
$          0.000000          1.000000
$          1000.000000          1.000000
$---+---1---+---2---+---3---+---4---+---5---+---6---+---7---+---8
*INCLUDE
soil3.dyn
$---+---1---+---2---+---3---+---4---+---5---+---6---+---7---+---8
*END

```

A half sine-pulse method was implemented to simulate the phase change process from solid soil mass to liquid. This simulation process requires LS-DYNA's full restart (with material property changes) capabilities, as well as self-modify job control files with modularized material property input deck to be altered by a custom C++ routine designed to apply necessary changes in material properties. The self-modifying process is necessary due to the current lack of availability and accessibility for the implementation of the phase change process directly into the soil material model in LS-DYNA. This process can be eliminated once the proposed phase change process is implemented directly into LS-DYNA's soil material model.

A short C++ program was developed to apply the half sine-pulse simulation of bulk behavior phase change. This program basically takes the user-defined soil FHWA_SOIL material model inputs and updates the necessary input properties to represent the transition process from soil to liquid materials. The software was developed and compiled using GNU's C++ compiler for Cygwin, which is a free Linux overlay developed by GNU for Microsoft Windows. Cygwin allows the users to develop/evaluate software in a Linux environment using a regular PC with Windows operating system. Since softwares developed in Cygwin is essentially identical to those developed in Linux or UNIX, one can port softwares developed in Cygwin to Linux or UNIX seamlessly.

Upon completion of the debugging/validation process, the bulk modulus transition software was then ported to BYU's Dell cluster in Linux and recompiled using GNU's C++ compiler for Linux without difficulties. The source listing of the C++ routine is listed below for reference.

```
//-----
// genmat.cpp:  file to generate an ls-dyna material input deck for restarts
//              quarter sine pulse phase transitioning approach
// AUTHOR: W.Y.Lee
// DATE: February 3, 2006
//-----
// arguments to main:
// 1 name of file containing material properties of the original deck
// 2 1st run termination time
// 3 time increment for subsequent runs
// 4 max. run time to set last run to
// 5 total number of runs
// 6 next run id (i.e. current run id + 1)
//
// format of file containing material properties of the original deck:
// each input value must be spaced at 10 spaces to be consistent with LS-DYNA
//
// line 1:          kB, kG, me, ne, sigpm, Pa, Kmax, nmat,
// line 2:          sc[0], nexp[0]
// ...
// line 1 + nmat   sc[nmat-1], nexp[nmat-1]
// line 2 + nmat
```

```

//      3 lines of 8 inputs and 4th line with 1 input for each material
// line 1 + 2*nmat
//
//   where:
//   nmat is the number of *FHWA_MAT_147 materials
//   sc is the G to Ksk scale factor for each of 9 material
//   nexpt is the exponent of the respective curves for defining K
// i.e.  genmat mat.inp 0.1999 0.2 5.0 20 1
//-----
#include<stdlib.h>
#include<stdio.h>
#include<math.h>
#include<string.h>
#include<ctype.h>
//-----
// define string parameters and local routine prototypes
//-----
#define   MXSTRLEN  255
#define   MXSTRSZ   (MXSTRLEN + 1)
//-----
// OpenFile routine to open a specific file
//-----
static FILE *OpenFile(char *s, char *rw)
{
    FILE *fptr = (FILE *) NULL;

    if (s != (char *) NULL)
    {
        if (strlen(s) <= 0)
        {
            fptr = (FILE *) NULL;
        }
        else
        {
            fptr = fopen(s, rw);
        }
    }

    return(fptr);
}
//-----
static void PrnComment(FILE *fout)
{
    fprintf(fout, "$---+---1---+---2---+---3---+---4"
            "-----5-----6-----7-----8\n");
}
//-----
int main(int argc, char *argv[])
{
    // get material properties deck
    FILE *finp = OpenFile(argv[1], "r");
    if (finp == (FILE *) NULL)
        return(1);

    // set program calling parameters
    double tend0 = atof(argv[2]);
    double tinc = atof(argv[3]);
    double tendmax = atof(argv[4]);
    int numruns = atoi(argv[5]);
    int runid = atoi(argv[6]);

    // make sure run id doesn't exceed max. no. of runs
    // or interpolation will be messed up...

```

```

if (runid > numruns)
    runid = numruns;

// read in processing parameters
double    kB, kG, me, ne, sigpm, Pa, Kmax;
int       nmat;
fscanf(finp, "%10lf%10lf%10lf%10lf%10lf%10lf%10lf%10d\n",
        &kB, &kG, &me, &ne, &sigpm, &Pa, &Kmax, &nmat);

if (nmat < 1) return(1);

double *G2Ksk = new double[nmat]; // Ksk scale factor
double *nexp= new double[nmat]; // bulk modulus exponents
double *K    = new double[nmat]; // bulk moduli
double *nu   = new double[nmat]; // poisson's ratio
double *E    = new double[nmat]; // Young's modulus
double *G    = new double[nmat]; // Shear modulus

// determine initial shear modulus in accordance with UBC method...
double Kmin = kB * Pa * pow((sigpm/Pa), me); // initial bulk modulus
double Go   = kG * Pa * pow((sigpm/Pa), ne); // initial shear modulus

// parameters for computing quarter sine pulse fit in log scale
double logKmin = log10(Kmin);
double logKmax = log10(Kmax);
double logDK = logKmax - logKmin;
double logdK = logDK / (((double) numruns) - 1);
double pie   = 3.14159;
double term; // temporary term for computation purposes

// read and process each bulk modulus value
int    i;
for (i = 0; i < nmat; i++)
{
    fscanf(finp, "%10lf%10lf\n", &(G2Ksk[i]), &(nexp[i]));

    // shear modulus is currently un-altered due to the fact that
    // changes in bulk is so much more significant that reduce in
    // shear modulus is negligible... Hook is added here for such
    // changes if desired...
    G[i] = Go;

    // update bulk modulus using quarter sine pulse in log scale
    term = pow((((double) runid)-1) * logdK / logDK, nexp[i]) * pie / 2.0;
    K[i] = pow(10.0, (logKmin + logDK * sin(term)));

    // update poisson's ratio and Young's modulus for references
    nu[i] = ((3.0 * K[i]) - (2.0 * G[i])) / (2 * ((3.0 * K[i]) + G[i]));
    E[i] = (9.0 * G[i] * K[i]) / ((3.0 * K[i]) + G[i]);
}

// run id and current segment of analysis' termination time
runid = ((runid < 1) ? 1 : runid);
double t_term = ((runid >= numruns) ? tendmax : (tend0+(runid-1)*tinc));

// dump results to ls-dyna material input deck ...
char    s[MXSTRSZ];
sprintf(s, "soilmat.dyn");
FILE    *fout = OpenFile(s, "w");

// ls-dyna overhead stuff...
fprintf(fout, "*KEYWORD 3000000\n"
        " *CONTROL_TERMINATION\n%#10.7lf\n", t_term);

```

```

PrnComment(fout);

fprintf(fout, "$ kB=%-#12.4lG, kG=%-#12.4lG, me=%-#12.4lG, "
        "ne=%-#12.4lG\n"
        "$ sigpm=%-#12.4lG, Pa=%-#12.4lG, Kmax=%-#12.4lG, "
        "Kmin=%-#12.4lG\n", kB, kG, me, ne, sigpm, Pa, Kmax, Kmin);

fprintf(fout, "$ run number %d of %d runs with %d materials\n",
        runid, numruns, nmat);

// now process and update each material card...
double v1[8], v2[8], v3[8], v4;
for(i = 0; i < nmat; i++)
{
    // read in material properties
    fscanf(finp, "%10lf%10lf%10lf%10lf"
            "%10lf%10lf%10lf%10lf\n"
            "%10lf%10lf%10lf%10lf"
            "%10lf%10lf%10lf%10lf\n"
            "%10lf%10lf%10lf%10lf"
            "%10lf%10lf%10lf%10lf\n%10lf\n",
            &(v1[0]), &(v1[1]), &(v1[2]), &(v1[3]),
            &(v1[4]), &(v1[5]), &(v1[6]), &(v1[7]),
            &(v2[0]), &(v2[1]), &(v2[2]), &(v2[3]),
            &(v2[4]), &(v2[5]), &(v2[6]), &(v2[7]),
            &(v3[0]), &(v3[1]), &(v3[2]), &(v3[3]),
            &(v3[4]), &(v3[5]), &(v3[6]), &(v3[7]), &v4);

    // adjust bulk, shear and pore pressure scale (skeleton bulk)
    v2[0] = K[i];
    v2[1] = G[i];
    v3[2] = G[i] * G2Ksk[i];
    PrnComment(fout);
    fprintf(fout,
            "$ G to Ksk scale factor: %-#12.4lG, "
            "K exponent: %-#12.4lG\n"
            "$ K=%-#12.4lG, G=%-#12.4lG, "
            "E=%-#12.4lG, nu=%-12.4lG\n",
            G2Ksk[i], nexp[i], K[i], G[i], E[i], nu[i]);

    // print updated (modified) material deck for ls-dyna
    fprintf(fout, "MAT_FHWA_SOIL\n"
            "%10d%10.3lE%10d%10.3lf%10.3lE%10.3lf%10.3lE%10d\n"
            "%#10.3lE%#10.3lE%10.3lf%10.3lf%10.5lf%10.3lf%10.3lf\n"
            "%10.5lf%10.3lf%#10.3lE%10.3lf%10.5lf%10.3lf%10.3lf\n"
            "%10.3lf\n", int(v1[0]), v1[1], int(v1[2]), v1[3],
            v1[4], v1[5], v1[6], int(v1[7]),
            v2[0], v2[1], v2[2], v2[3], v2[4], v2[5], v2[6], v2[7],
            v3[0], v3[1], v3[2], v3[3], v3[4], v3[5], v3[6], v3[7],
            v4);
}

// finishing touch of ls-dyna deck
PrnComment(fout);
fprintf(fout, "*END\n");
fclose(fout);
fclose(finp);

// self modify input deck
fout = OpenFile(".genmat", "w");
fprintf(fout, "./genmat %s %lf %lf %lf %d %d\n", argv[1], tend0,
        tinc, tendmax, numruns, runid+1);
fclose(fout);

```

```

// self modify ls-dyna input director file
if (runid > 1)
{
  fout = OpenFile(".rerun", "w");
  fprintf(fout, "i=rectrl.dyn r=d3dump%2.2d", runid-1);
  fclose(fout);
}
else
{
  fout = OpenFile(".run", "w");
  fprintf(fout, "i=ctrl.dyn");
  fclose(fout);
}

// time to clean up
delete [] G2Ksk;   delete [] nexp;       delete [] K;
delete [] nu;     delete [] E;         delete [] G;

return(0);
}

//-----
//-----

```

The above software takes its inputs from two sources. First, a one-line program execution command with six input parameters as shown below:

```
./genmat mat.inp 0.199900 0.200000 5.000000 21 1
```

Descriptions of the input parameters are provided at the top of the C++ software listing above. The command line was designed to be altered by the software as a part of the self-modifying feature. As such, it was stored in a file called `.genmat` as required by the C++ software.

The second program execution inputs are obtained from a material definition input deck named by the user. In the example above, it was named `mat.inp`. The material definition input consists of input material properties to the LS-DYNA's `FHWA_SOIL` material model, quarter-sine pulse equation parameters, and the initial bulk and shear

moduli definition parameters using the UBC soil property definition as described in Chapter 7 of this dissertation. The file mat.inp as described here is listed below for references. Details on the format of the file is listed at the beginning of the C++ software listing provided earlier in this Appendix.

```

300.00    180.00    0.5000    0.5000  16.679340  14.695949  1.000E+06          9
0.2200    1.0000
0.2200    1.0000
0.2200    1.0000
0.2200    1.0000
0.2200    1.0000
0.2300    0.5000
0.2100    0.5000
0.2300    1.0000
0.1500    2.2000
  3 1.723E-04          1    2.684 9.357E-05    10.0 1.00E-04    20
4696.880  2818.130    0.7854  0.00500  0.89923    1.00    0.25    0.01
0.37254  0.0000000  140.3430  0.000E+00  0.52360  1.000E+00  1000.000    0.0
1.000
  4 1.723E-04          1    2.684 9.357E-05    10.0 1.00E-04    20
4696.880  2818.130    0.7854  0.00500  0.89923    1.00    0.25    0.01
0.37254    0.0    0.0    0.0    0.52360  1.000E+00  1000.000    0.0
1.000
  5 1.768E-04          1    2.780 9.357E-05    10.0 1.00E-04    20
4696.880  2818.130    0.7854  0.00500  2.0000    1.00    0.25    0.01
0.35967    0.0  140.3430    0.0    0.52360  1.000E+00  1000.000    0.0
1.000
  6 1.364E-04          1    2.684 9.357E-05    10.0 1.00E-04    20
4696.880  2818.130    0.7854  0.00500  0.89923    1.00    0.25    0.01
0.06991  0.000E+00  140.3430  0.000E+00  0.52360  1.000E+00  1000.000    0.0
1.000
  7 1.723E-04          1    2.684 9.357E-05    10.0 1.00E-04    20
4696.880  2818.130    0.7854  0.00500  0.89923    1.00    0.25    0.01
0.37254  0.000E+00  140.3430  0.000E+00  0.52360  1.000E+00  1000.000    0.0
1.000
  8 1.723E-04          1    2.684 9.357E-05    10.0 1.00E-04    20
4696.880  2818.130    0.7854  0.00500  0.89923    1.00    0.25    0.01
0.37254  0.000E+00  359.3110  0.000E+00  0.52360  1.000E+00  1000.000    0.0
1.000
  9 1.723E-04          1    2.684 9.357E-05    10.0 1.00E-04    20
4696.880  2818.130    0.7854  0.00500  0.89923    1.00    0.25    0.01
0.37254  0.000E+00  546.9990  0.000E+00  0.52360  1.000E+00  1000.000    0.0
1.000
 10 1.723E-04          1    2.684 9.357E-05    10.0 1.00E-04    20
4696.880  2818.130    0.7854  0.00500  0.89923    1.00    0.25    0.01
0.37254  0.000E+00  765.9670  0.000E+00  0.52360  1.000E+00  1000.000    0.0
1.000
 11 1.723E-04          1    2.684 9.357E-05    10.0 1.00E-04    20
4696.880  2818.130    0.7854  0.00500  0.89923    1.00    0.25    0.01
0.37254  0.000E+00  984.9360  0.000E+00  0.52360  1.000E+00  1000.000    0.0
1.000

```

The C++ bulk transitioning software provides output to three separate files. First, a one-liner file called .run for initial run of the analysis (or .rerun for subsequent runs of the analysis) containing the input and restart parameters necessary to execute LS-DYNA. Second, the software alters or updates the .genmat input deck in preparation for the next restart iteration. Third, the software generates the necessary LS-DYNA FHWA_SOIL material model input deck containing the updated material properties determined by the phase transitioning software as required for a successful LS-DYNA run of the current blast scenario. A sample of the LS-DYNA soil material definition deck to be altered by the phase change input software is provided below for reference. Highlighted in red are the values altered by the phase transitioning software.

```

$---+---1---+---2---+---3---+---4---+---5---+---6---+---7---+---8
$ LS-DYNA FHWA_SOIL material model input deck
$---+---1---+---2---+---3---+---4---+---5---+---6---+---7---+---8
*KEYWORD 30000000
*CONTROL_TERMINATION
0.9999000
$---+---1---+---2---+---3---+---4---+---5---+---6---+---7---+---8
$ kB=300          , kG=180          , me=0.5          , ne=0.5
$ sigpm=16.68    , Pa=14.7         , Kmax=1E+06    , Kmin=4697
$ K=9950         , G=2818          , E=7725       , nu=0.3706
$ G2Ksk: 0.220, 0.220, 0.220, 0.220, 0.220, 0.220, 0.220, 0.220, 0.220
$ run number 5 of 21.000000 runs, K curve exponent: 1.500000
$---+---1---+---2---+---3---+---4---+---5---+---6---+---7---+---8
*MAT_FHWA_SOIL
   3 1.723E-04          1      2.684 9.357E-05      10.000 1.000E-04          20
   9950.30 2818.13      0.785 0.005 0.89923      1.000 0.250 0.010
   0.37254 0.000 619.988 0.000 0.52360      1.000 1000.000 0.000
   1.000
$---+---1---+---2---+---3---+---4---+---5---+---6---+---7---+---8
*MAT_FHWA_SOIL
   4 1.723E-04          1      2.684 9.357E-05      10.000 1.000E-04          20
   9950.30 2818.13      0.785 0.005 0.89923      1.000 0.250 0.010
   0.37254 0.000 619.988 0.000 0.52360      1.000 1000.000 0.000
   1.000
$---+---1---+---2---+---3---+---4---+---5---+---6---+---7---+---8
*MAT_FHWA_SOIL
   5 1.768E-04          1      2.780 9.357E-05      10.000 1.000E-04          20
   9950.30 2818.13      0.785 0.005 2.00000      1.000 0.250 0.010
   0.35967 0.000 619.988 0.000 0.52360      1.000 1000.000 0.000
   1.000
$---+---1---+---2---+---3---+---4---+---5---+---6---+---7---+---8
*MAT_FHWA_SOIL
   6 1.364E-04          1      2.684 9.357E-05      10.000 1.000E-04          20

```



```

    9950.30  2818.13    0.785    0.005    0.89923    1.000    0.250    0.010
    0.06991    0.000  619.988    0.000    0.52360    1.000  1000.000    0.000
    1.000
$---+---1---+---2---+---3---+---4---+---5---+---6---+---7---+---8
*MAT_FHWA_SOIL
    7 1.723E-04    1    2.684 9.357E-05    10.000 1.000E-04    20
    9950.30  2818.13    0.785    0.005    0.89923    1.000    0.250    0.010
    0.37254    0.000  619.988    0.000    0.52360    1.000  1000.000    0.000
    1.000
$---+---1---+---2---+---3---+---4---+---5---+---6---+---7---+---8
*MAT_FHWA_SOIL
    8 1.723E-04    1    2.684 9.357E-05    10.000 1.000E-04    20
    9950.30  2818.13    0.785    0.005    0.89923    1.000    0.250    0.010
    0.37254    0.000  619.988    0.000    0.52360    1.000  1000.000    0.000
    1.000
$---+---1---+---2---+---3---+---4---+---5---+---6---+---7---+---8
*MAT_FHWA_SOIL
    9 1.723E-04    1    2.684 9.357E-05    10.000 1.000E-04    20
    9950.30  2818.13    0.785    0.005    0.89923    1.000    0.250    0.010
    0.37254    0.000  619.988    0.000    0.52360    1.000  1000.000    0.000
    1.000
$---+---1---+---2---+---3---+---4---+---5---+---6---+---7---+---8
*MAT_FHWA_SOIL
   10 1.723E-04    1    2.684 9.357E-05    10.000 1.000E-04    20
    9950.30  2818.13    0.785    0.005    0.89923    1.000    0.250    0.010
    0.37254    0.000  619.988    0.000    0.52360    1.000  1000.000    0.000
    1.000
$---+---1---+---2---+---3---+---4---+---5---+---6---+---7---+---8
*MAT_FHWA_SOIL
   11 1.723E-04    1    2.684 9.357E-05    10.000 1.000E-04    20
    9950.30  2818.13    0.785    0.005    0.89923    1.000    0.250    0.010
    0.37254    0.000  619.988    0.000    0.52360    1.000  1000.000    0.000
    1.000
$---+---1---+---2---+---3---+---4---+---5---+---6---+---7---+---8
*END

```

On BYU's Dell cluster, all jobs are controlled and submitted via a pre-defined job control process as specified by BYU's Supercomputing Laboratory. Listed below is the batch script used to execute both the initial and subsequent restart runs for the simulation of the sequential blast-induced liquefaction event. The batch script was written for Linux's default "bash" (Bourne-Again Shell) script language which is used on BYU's Dell cluster.

```

#!/bin/bash
#PBS -l nodes=1:ppn=2,walltime=2000:00:00
#PBS -N run0

```

```

#PBS -m n
#PBC -M leewy@byu.edu
export LSTC_LICENSE=network
export LSTC_LICENSE_SERVER_PORT=13373
export LSTC_LICENSE_SERVER=m4a.et.byu.edu
cd $PBS_O_WORKDIR

/opt/mpich/intel/bin/mpirun \
# -machinefile $PBS_NODEFILE\
# -np 2 \
source .genmat
/ibrix/apps/lsdyna/ls970_5434a_sp < .run
source .genmat
/ibrix/apps/lsdyna/ls970_5434a_sp < .rerun
rm d3dump01
source .genmat
/ibrix/apps/lsdyna/ls970_5434a_sp < .rerun
rm d3dump02
source .genmat
/ibrix/apps/lsdyna/ls970_5434a_sp < .rerun
rm d3dump03
source .genmat
/ibrix/apps/lsdyna/ls970_5434a_sp < .rerun
rm d3dump04
source .genmat
/ibrix/apps/lsdyna/ls970_5434a_sp < .rerun
rm d3dump05
source .genmat
/ibrix/apps/lsdyna/ls970_5434a_sp < .rerun
rm d3dump06
source .genmat
/ibrix/apps/lsdyna/ls970_5434a_sp < .rerun
rm d3dump07
source .genmat
/ibrix/apps/lsdyna/ls970_5434a_sp < .rerun
rm d3dump08
source .genmat
/ibrix/apps/lsdyna/ls970_5434a_sp < .rerun
rm d3dump09
source .genmat
/ibrix/apps/lsdyna/ls970_5434a_sp < .rerun
rm d3dump10
source .genmat
/ibrix/apps/lsdyna/ls970_5434a_sp < .rerun
rm d3dump11
source .genmat
/ibrix/apps/lsdyna/ls970_5434a_sp < .rerun
rm d3dump12
source .genmat
/ibrix/apps/lsdyna/ls970_5434a_sp < .rerun
rm d3dump13

```

```
source .genmat
/ibrix/apps/lsdyna/ls970_5434a_sp < .rerun
rm d3dump14
source .genmat
/ibrix/apps/lsdyna/ls970_5434a_sp < .rerun
rm d3dump15
source .genmat
/ibrix/apps/lsdyna/ls970_5434a_sp < .rerun
rm d3dump16
source .genmat
/ibrix/apps/lsdyna/ls970_5434a_sp < .rerun
rm d3dump17
source .genmat
/ibrix/apps/lsdyna/ls970_5434a_sp < .rerun
rm d3dump18
source .genmat
/ibrix/apps/lsdyna/ls970_5434a_sp < .rerun
rm d3dump19
source .genmat
/ibrix/apps/lsdyna/ls970_5434a_sp < .rerun
rm d3dump20
exit 0
```

The script basically takes the inputs generated by the phase transition software and applies them in executing the corresponding LS-DYNA runs. Since there are 21 blasts in the baseline blast event to be simulated, there are 20 restart runs immediately following an initial analysis run as listed in the “bash” script.

Since the soil material geometry deck (soil3.dyn) and the soil mass initial stress deck (siginit.dyn) contain 100,000+ nodes, ~100,000 elements and hundreds of boundary and other definitions, these items are not presented in this dissertation. However, the corresponding control deck listed in this section can be used as is or can be modified to drive other blast-induced liquefaction geometry decks with consistent component id’s and unit notations. The basic features of the control deck can also be extracted for other applications.